High-Energy-Density Field-Reversed Configurations for Sub-Microsecond Magnetized Target Fusion

by

Brendan J. Sporer

A dissertation submitted in partial fulfillment
of the requirements for the degree of
Doctor of Philosophy
(Nuclear Engineering and Radiological Sciences)
in the University of Michigan
2023

Doctoral Committee:

Professor Ryan D. McBride, Chair
Professor Ronald M. Gilgenbach
Research Associate Professor Nicholas M. Jordan
Associate Professor Benjamin A. Jorns
Stephen A. Slutz, Sandia National Laboratories
Thomas E. Weber, Los Alamos National Laboratory

Brendan J. Sporer

bsporer@umich.edu

ORCID iD: 0000-0001-6290-699X

Acknowledgments

I would like to start by thanking Dr. Igor Jovanovic, Dr. John Foster, and Garnette Roberts for their advocacy in getting me accepted to the University of Michigan graduate program, despite my decidedly poor application essays. Were it not for them, I might have been forced into a very different career path. Of course, many thanks to my advisor Dr. Ryan McBride, who was able to find a spot for me in his lab. His teaching and mentoring over the next five years would turn me from a naïve, wide-eyed tinkerer to an actual scientist. I am especially grateful that he always made me feel comfortable proposing and pursuing new and exotic ideas for the lab or for my research, eventually allowing me to pursue the topic of this dissertation. I would also like to thank the other UM members of my committee: Dr. Ron Gilgenbach, an excellent teacher and lab director who procured most of the machines and equipment detailed in this dissertation; Dr. Nick Jordan, my invaluable everyday mentor and manager who was always there to field my questions or random ideas; and Dr. Ben Jorns, who provided excellent physics perspective from outside the pulsed-power field. Also, a shoutout to Senior Electronics Technician Mark Perrault (now retired), who always kept our lab safe, clean, maintained, and well-stocked, and assisted with (or solely performed) countless electrical projects for the lab over the years.

I also want to thank all the other students of the PPML – past and present, graduate and undergraduate. I could not have performed or even imagined the experiments detailed in this thesis without the countless helpful conversations and assistance from my fellow students. They also made coming to the lab everyday a lot more fun. A special shoutout to Drs. Akash Shah and George Dowhan, and future Drs. Trevor Smith and Joe Chen. We will always share a bond in toiling over MAIZE together!

Next, I would like to thank all those that worked with me from Sandia who were so kind and helpful to me, both as a student and during my residency: Drs. Matt Gomez, Gabe Shipley, Steve Slutz, Kris Beckwith, Brian Hutsel, and Chris Jennings. A special thanks to Gabe, who was always available to help me and mentor me through experimental and computational procedures/issues – despite having no administrative affiliation with my residency! I hope I have a chance to work with you all again in the future. I want to thank Chris Jennings for getting me started with the Kraken code, and also Dr. Aidan Crilly from Imperial College London for being so helpful with the SpK code and providing some input files. This produced the synthetic images that really tied together my simulations and experiments.

Finally, I could not be where I am today without the nurturing and opportunities provided by my parents, Jill and Drew. Thank you for always believing in me and supporting me. To my best friend and wife Emily, thank you for being there for me, as you always have been, through some of the most uncertain and stressful years of our lives. Thank you for loving me and believing in me enough to move your life to Michigan (and now to California). And, of course, I need to thank our three black kitties, Simba, Nala, and Meeko, for always being there to relieve stress, and also for their insightful edits to this dissertation when I left my computer on the couch. I think I wrote most of this thesis with a cat on my lap.

TABLE OF CONTENTS

LIST OF FIGURES

FIGURE

LIST OF TABLES

TABLE

LIST OF APPENDICES

ABSTRACT

Magnetized target fusion (MTF) has gained popularity in recent decades as potentially a more economic route to fusion gain greater than unity in the laboratory. The magnetized liner inertial fusion (MagLIF) program on the Z-machine (20 MA, 100 ns) at Sandia National Laboratories has successfully integrated and demonstrated the principles of MTF, and several other organizations are pursuing MTF approaches to fusion energy.

The "field-reversed configuration", or FRC, is a popular magnetized plasma target, favored for its closed-field lines and high average plasma beta (ratio of particle pressure to magnetic field pressure), among other attributes. The work detailed in this thesis explores the nascent idea of producing and compressing high-energy-density (HED), centimeter-scale FRCs on the Z-machine, for the purposes of large fusion yield and other fundamental plasma/code-benchmarking studies like magnetic reconnection. In practice, this would be done using bias coils and liner compression hardware similar to that used for the MagLIF program. The *in-situ* formation concept for the FRC requires axial field production by both external coils and a helically slotted (i.e. "AutoMag"-type) liner.

To inform FRC physics at this novel hydrodynamic scale, a platform has been developed on the MAIZE linear transformer driver (1 MA, 100 ns) to form high-applied-field (10–15 T), solenoidal FRCs with physics similar to those desired for compression on the Z-facility. To the author's knowledge, this represents the first time FRCs have been formed using two separate field sources (external slow coils and a helical fast coil) as well as on a linear transformer driver system. The claim of FRC formation on MAIZE will be justified by analysis of visible light imaging, magnetic probe data, and the appearance of expected FRC instabilities. The high-density FRCs are studied for stability and lifetime, and compared with simulation and the predictions found in the existing FRC literature. As predicted by historical experiments, it appears that low-density FRCs are more well-formed and stable than higher-density ones. Furthermore, the density limit for successful formation does not seem to be related to gross stability, but to non-uniformities in Z-discharge pre-ionization (ZPI) of the high-pressure deuterium gas fill. Alternative methods of pre-ionization are recommended to be explored. As expected with no active stabilization, the wobble and rotational instabilities appear in MAIZE FRCs with small radius. Large radius FRCs do not show rotational instability; it is theorized that the asymmetry and finite azimuthal fields inherent to solenoidal fields

near the coil stabilize the rotational instability.

To complement the experimental effort on MAIZE, numerical simulations were run using the two-dimensional axisymmetric version of the resistive magnetohydrodynamics (MHD) code, Kraken. The code was initialized with an analytic FRC profile and used to study relaxation and decay, including two treatments of anomalous resistivity. The effects of field-flare (or the finite length of the AutoMag axial field), are shown to affect FRC decay but not significantly. These simulations further suggest that high-density FRC lifetimes are the minimum of those predicted by classical and anomalous theory from the literature, the latter of which being more accurate for hot, high-flux FRCs. Thermonuclear FRCs initialized with extreme elongation, as would be the case near peak liner compression, are found to quickly lose thermal energy and tear into smaller plasmoids within a few Alfvén times. It is unclear how much this effect reduces the burn time or is itself reduced in growth by kinetic effects not captured in the MHD code. Additionally, it is shown that a significant gradient in axial field produced by the AutoMag liner can be tolerated without risk of the FRC being ejected axially during the liner compression.

An interesting feature observed in the MAIZE experiments was an extremely hollow visible emission profile within the FRC radius, inconsistent with the density profiles predicted from initial simulation attempts. To understand this experimental observation in the specific hardware of the MAIZE platform, a scheme was implemented in 2D Kraken using an applied field shape similar to that produced during a typical MAIZE shot. FRCs are successfully formed under a wide range of conditions. A simulation post-processing package was then used to produce synthetic images of the formation and relaxation process in the photon sensitivity range of the fast-framing camera used in the MAIZE experiments. Unlike those of previous simulations, these synthetic images are shown to qualitatively agree with the experimental images. It is believed this further justifies the claim of FRC production. However, the comparisons also suggest a lower-than-expected plasma density in the experiments, which was likely caused by gas exhausting into the fill tube during the pre-ionization process. The low density and the effects of the specific applied field shape are shown to cause the hollowing observed in some of the FRC visible emission profiles – a result that may be unique to the MAIZE experimental configuration.

Finally, the work presented in this thesis is summarized, and suggestions for future work are presented. Prospects for a Z-machine shot proposal are bright, but a great deal of work remains – particularly in simulation. Full 3D simulations with anomalous resistivity and a driving electrical circuit will be needed to model FRC formation processes and match future experiments. Optimization of Z-machine energy coupling to large liners remains an open question requiring parameter scans with a detailed Z-machine circuit code. It is speculated that the Z-machine's pulse-shaping and self-crowbarring capabilities could be used to further improve FRC MTF performance. Results from such optimizations are sure to influence the desired FRC parameters. Additionally,

alternative methods of pre-ionization should be investigated and characterized to improve uniformity and energy coupling. Hardware for pressurizing and pre-ionizing a deuterium-filled, dielectric-coated, implodeable AutoMag liner installed in the Z-machine should be designed and implemented on a mega-ampere facility of higher impedance than MAIZE (e.g., Mykonos at Sandia), to explore the formation of high-density FRCs at the large fast-field strengths desired for Z (>60 T). Once the ideal FRC starting parameters for a well-characterized liner implosion trajectory on Z have been identified, and once such an FRC has been successfully formed and diagnosed on a mega-ampere machine, hardware for the first HED FRC shot on the Z-machine can then be confidently designed.

CHAPTER 1

Introduction

1.1 Approaches to Fusion Gain

The zoology of concepts for achieving fusion energy gain from a thermonuclear plasma represent diverse approaches to exceeding the Lawson criterion [1], which can be simplified to a minimum limit on the product of a plasma's particle density and energy confinement time: $n\tau_E$. Tenuous (low-n) thermonuclear plasmas have manageable pressures that can be contained by the strongest superconducting electromagnets – but they must be confined for τ_E of several seconds, requiring very large plasmas and machines. This field of magnetic confinement fusion (MCF) includes devices such as tokamaks, stellerators, magnetic mirrors, and many others. A renaissance of sorts is occurring in MCF at the time of this dissertation's writing: recent advances in high-temperature superconducting (HTS) tape manufacture have allowed the engineering of very high field strength, fusion-scale magnets [2] and thus more compact, medium-power reactor prospects [3] [4] [5]. For example, this author has published [6] on the advantages of modern HTS technology for the magnetic electrostatic confinement reactor concept, as detailed in Appendix A.

On the other end of the Lawson spectrum, extremely high pressure (high-n) plasmas can be confined by their own inertia for long enough to satisfy the correspondingly short τ_E criterion. This field of inertial confinement fusion (ICF) has also seen a recent breakthrough, as the team at the National Ignition Facility (NIF) achieved robust fusion burn and ignition [7] [8] for the first time without the assistance of a fission weapon. While inertial fusion energy (IFE) power-plants are an alluring prospect, ICF and the NIF have historically benefitted resource-wise from the field of nuclear weapons physics and stockpile stewardship. Both the Z-machine and the NIF, located at U.S. DOE-NNSA laboratories, help answer questions about stockpile aging and modernization [9] [10]. They help enable stockpile certification without resorting to full-scale underground testing (which the U.S. has not done since 1992). Given the violent nature of high-gain ICF experiments, IFE is generally regarded as a less practical path to fusion-based electricity production. However, this has not hindered serious investment from legitimate entities [11] [12], and IFE may also see a revival this decade with rapid advancements in laser and computational technology.

A third distinct approach to satisfying the Lawson criterion is represented by a moderate density plasma (medium-n), containing strong magnetic fields applied in some transient, pulsed fashion so as to compress and heat the plasma as in ICF, but over a longer timescale (intermediate τ_E to that of ICF and MCF). The magnetic field of the plasma is compressed along with the plasma, and it serves two purposes: 1) to conserve adiabaticity for the longer compression/burn time and 2) to bend fusion alpha particle trajectories to assist in ignition at lower values of fuel ρR. It has been argued recently [13] that this field of magnetized target, a.k.a. magneto-inertial fusion (MTF or MIF), may represent the most economical route to achieving controlled fusion gain greater than unity, in terms of capital cost of the specialized facility required [14] [15]. Ironically, MCF and ICF have purpose-built, flagship ignition facilities (ITER and NIF, respectively), but MTF does not.

To increase research efforts in MTF, the ARPA-E ALPHA program [16] was launched in 2014. This program included funding for the MagLIF program on the Z-machine at Sandia National Laboratories (SNL). MagLIF has rigorously demonstrated the principles of MTF, as discussed in Chapter 2. This dissertation concerns an alternate approach to MTF on the Z-machine—one that uses field-reversed configurations (FRCs).

1.2 Field-Reversed Configurations

As the name implies, MTF requires a magnetized plasma target for compression. The chosen magnetic confinement topology must confine the plasma for longer than the compression time, almost always requiring a closed-field line configuration (with the exception of very fast MagLIF, to be discussed in Chapter 2). Furthermore, if no solid conductors are to penetrate the MTF plasma core, this leaves as target options the so-called compact toroids (CTs): spheromaks and field-reversed configurations (FRCs). An FRC, depicted in Fig. 1.1, is (ideally) axisymmetric, defined by a purely toroidal current producing purely poloidal magnetic field lines. Spheromaks are superficially similar to FRCs, with the addition of a poloidal current component producing a toroidal field component. This introduces helicity and force-free currents, making spheromaks unique from FRCs and more closely affiliated with the family of Taylor states [17]. Spheromaks are thus unstable to many of the macro- and micro- modes pertinent to other toroidal helicity devices and have a plasma beta (ratio of plasma pressure to magnetic field pressure) experimentally limited to a few tens of percent at best [18]. By contrast, FRCs can have an average beta near unity due to a lack of helicity and a favorable magnetic pressure topology. Large beta is desired in MTF to maximize the fraction of compressional energy coupling to the plasma. For this reason, FRCs are usually the preferred MTF plasma target.

FRCs are typically formed using the reversed θ-pinch method, as shown in Fig. 1.2. First, neutral gas is introduced into a dielectric (usually quartz) discharge tube and axially magnetized by a coil
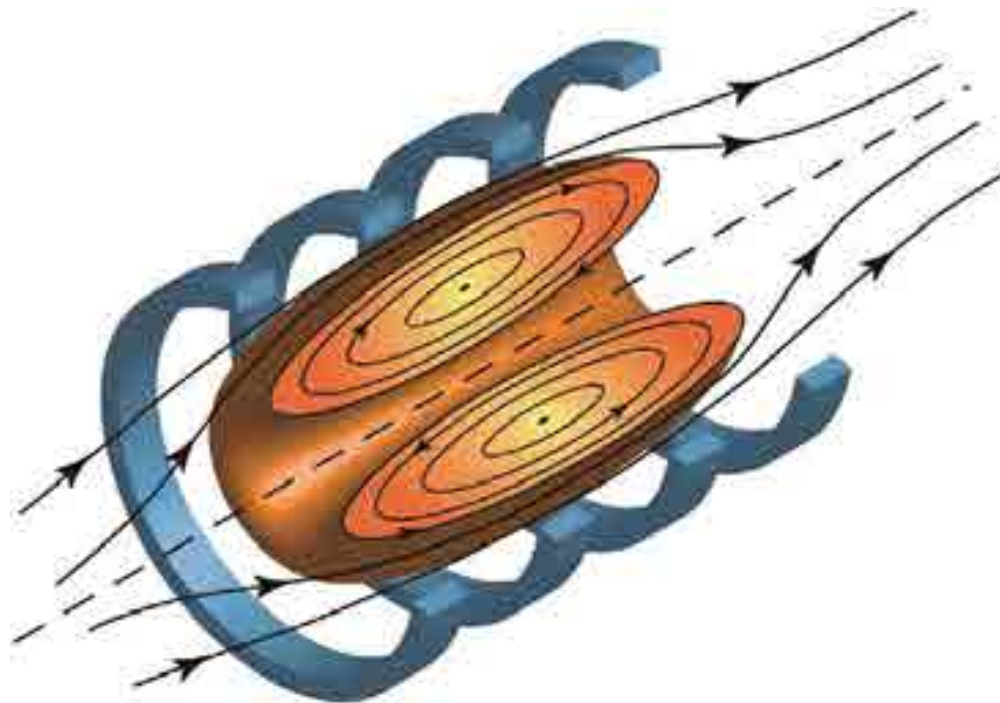
Figure 1.1: Depiction of a field-reversed configuration (FRC) inside external hoop coils. Reproduced from U.S. FESAC report [19].

apparatus outside the tube. The gas is pre-ionized (by various methods to be discussed in Chapter 3), which "freezes in" the applied bias field. Finally, a fast-rising, reversed axial field is applied by the coil apparatus outside the tube. An azimuthal plasma current is induced comparable to the external coil current, acting to maintain the bias flux trapped inside the plasma. Reconnection/tearing events initiated near the ends of the discharge tube produce and heat the closed-field line FRC, which contains some amount of the initial bias flux. Depending on the behavior of the applied external field, the FRC typically goes through some radial and axial contraction/oscillation phase, before relaxing to a pseudo-equilibrium.

If the applied reversal field contains a gradient in the axial direction, a net axial force can be imparted to the FRC during formation. This force can be tuned to eject the FRC from the formation tube up to supersonic speeds. The FRC can then be merged with other CTs for heating and/or captured in an adjacent section for sustainment or compression, as depicted in Figs. 1.3 and 1.4. The ability to robustly translate and merge CTs has proven to be another advantage for MTF. Modern FRC experiments [21] [22] [23] almost always use translated, dual-merging FRCs, since this "collisional formation" (see Fig. 1.4) cancels momentum for easy capture, and adds a heat/flux boost to the resulting FRC target.

Once in pseudo-equilibrium, the FRC is subject to two global magnetohydrodynamic (MHD) instabilities of concern, which are illustrated in Fig. 1.5. The rotational instability is thought to be
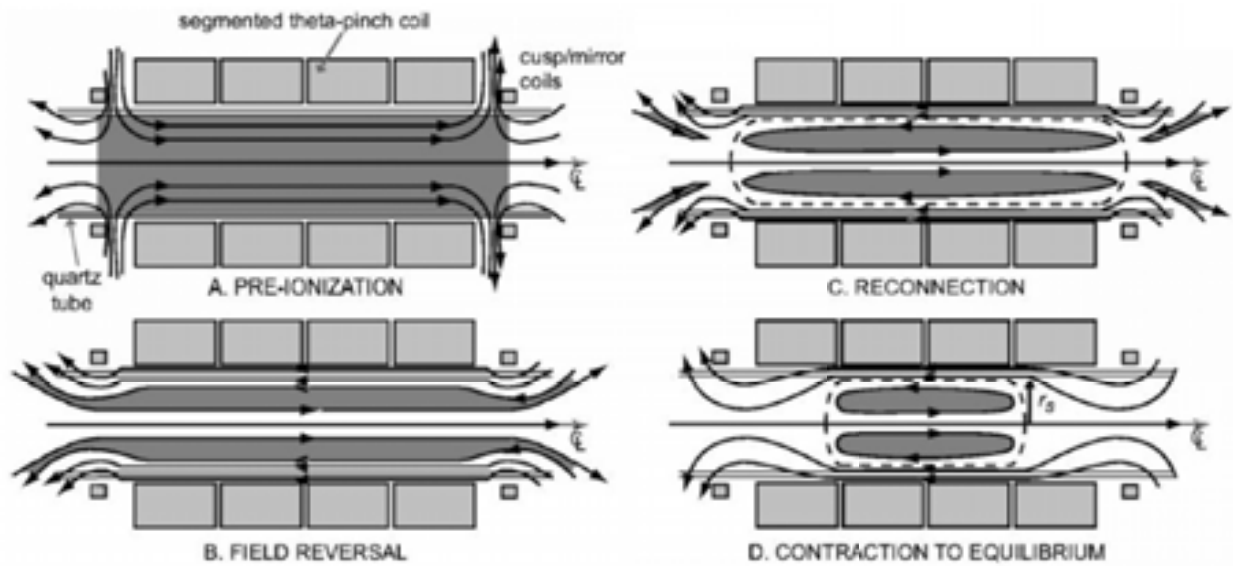
Figure 1.2: Stages of the reversed θ-pinch method to produce a field-reversed configuration (FRC). Reproduced from Grabowski et al. [20]. © 2007 IEEE.
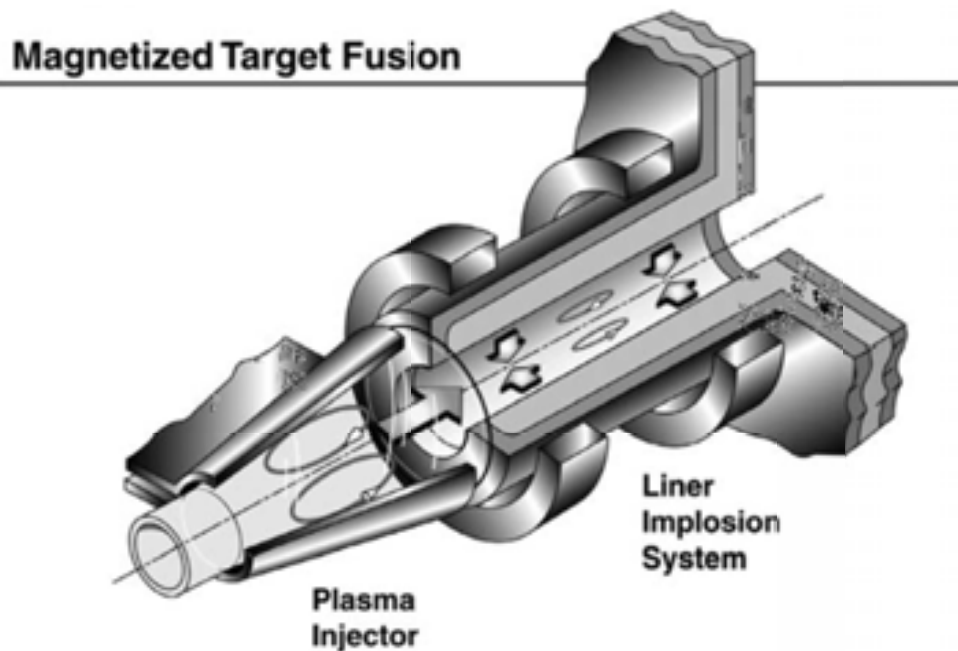
Figure 1.3: Conical reversed θ-pinch formation and translation of an FRC into a Z-pinch liner-based compression section. Reproduced from Intrator et al. [24] © 2004 IEEE.
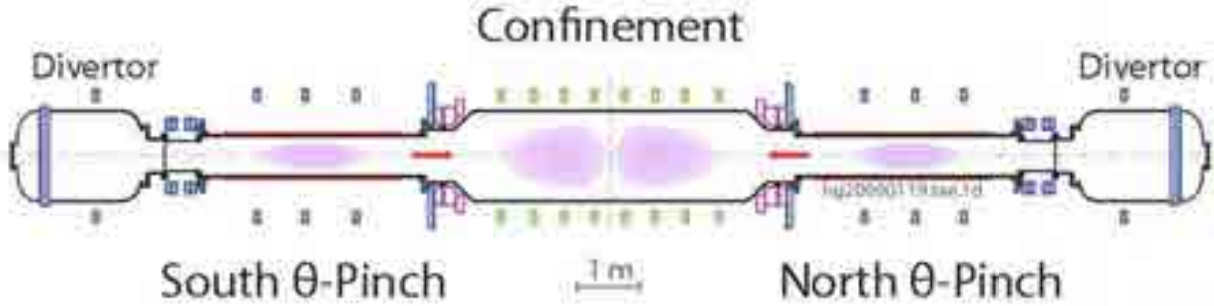
Figure 1.4: Modern collisional formation technique for an FRC: two CTs are produced by reversed θ-pinches and merged in a central chamber. The resulting CT can be sustained and heated to MCF conditions or compressed for MTF yield. This schematic of the C-2 device is reproduced from Binderbauer et al. [25].

driven by ion diamagnetic viscosity effects and is not immediately fatal, while the tilt instability represents complete disruption of the magnetic structure and is always terminal (analogous to a tokamak disruption). Rotational instability can be tolerated in some instances or stabilized by high-voltage biasing of open-field lines and other rotation control techniques [26] [22] [27]. The FRC tilt instability is predicted to occur very fast, on the order of the Alfvén time, but it can be stabilized indefinitely by ion gyroviscous effects. As such, susceptibility to tilt is often assessed by the s-parameter [28], or ratio of FRC separatrix radius to ion gyroradius: $s = \frac{r_s}{\rho_i}$. FRCs with large s-parameter have weaker kinetic effects, making them more susceptible to tilt. A more accurate stability parameter [26] is S^*/E, where $S^* = \frac{r_s \, \omega_{pi}}{c}$ is the ratio of FRC radius to ion plasma skin depth, and $E = \frac{L_x}{2 \, r_s}$ is the elongation of the FRC (which has a tilt stabilizing effect). FRCs with $S^*/E > 3$ are predicted to be tilt unstable. However, the tilt instability is rarely seen in merging FRC experiments due to the difficulty in cleanly producing final target FRCs of such high density. Furthermore, experiments are reported to have vastly exceeded the S^*/E stability parameter in a transient fashion during FRC translation and merging, with no evidence of tilt instability. High-density and larger s/S^*-parameter FRCs are desired to maximize fusion power, so pushing the limits of large-s FRC target production represents an area of active research by some programs. Density and s limits for FRCs will be discussed more in Chapters 3 and 5.

1.3 FRC Compression

Once formed, an FRC can be sustained in an MCF approach [29], or compressed for fusion yield in an MTF approach. Compression of the FRC can be achieved via continued external application of the reversed axial field [21], or by the implosion of a flux-conserving cylindrical liner containing the FRC [30] [24] [31]. As an FRC is compressed by one of these methods in the radial direction, it
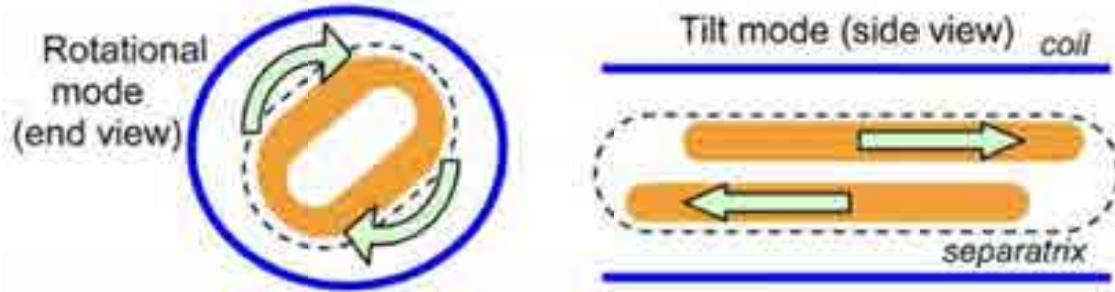
Figure 1.5: Two global instabilities of concern with the field-reversed configuration. Reproduced with edits from Steinhauer [26].

will also tend to contract in the axial direction. This phenomenon is driven by magnetic tension effects, as detailed in Ref. [31]. A radially compressed FRC's plasma volume scales as $V \propto r^{2.4}$, which is more favorable than the $V \propto r^2$ scaling of a pure cylindrical implosion. This represents another advantage of FRCs for MTF.

1.4   The Fast Z-pinch

Compression of a plasma target can be performed within an imploding, flux-conserving (e.g., metal) liner. Unless a closed-field target can be made with an extraordinary long lifetime to allow for pneumatic drive timescales [32] [30] [13], the liner must be driven electromagnetically. One such electromagnetic drive is known as the fast Z-pinch.

In a fast Z-pinch, a pulsed electrical current is driven through a cylindrical conductor, as shown in Fig. 1.6. The current produces an azimuthal magnetic field surrounding the conductor and an intense, inward-directed Lorentz $\mathbf{J} \times \mathbf{B}$ force, which accelerates the conducting material toward the axis. The speed and energy of the implosion are only limited by the voltage, current, and risetime of the pulsed-power machine driving the Z-pinch. Various pulsed-power architectures are discussed in Section 1.5.

The Shiva Star capacitor bank at the Air Force Research Laboratory was used to drive Z-pinches of solid liners for FRC compression [34]. Such implosions occurred with large (∼10 cm inner diameter, ID) liners over a timescale of ∼10 μs. The Z-machine at Sandia National Labs is also used to implode solid liners on a much smaller and faster hydrodynamic scale (∼0.5 cm ID, ∼0.1 μs). Liner implosions on the Z-machine are carried out in support of another MTF program called MagLIF [35], to be discussed in Chapter 2. Slutz [31] has suggested that metal liners on the Z facility could be imploded to compress high-energy-density (HED) FRCs for thermonuclear yield, inspiring this dissertation work.
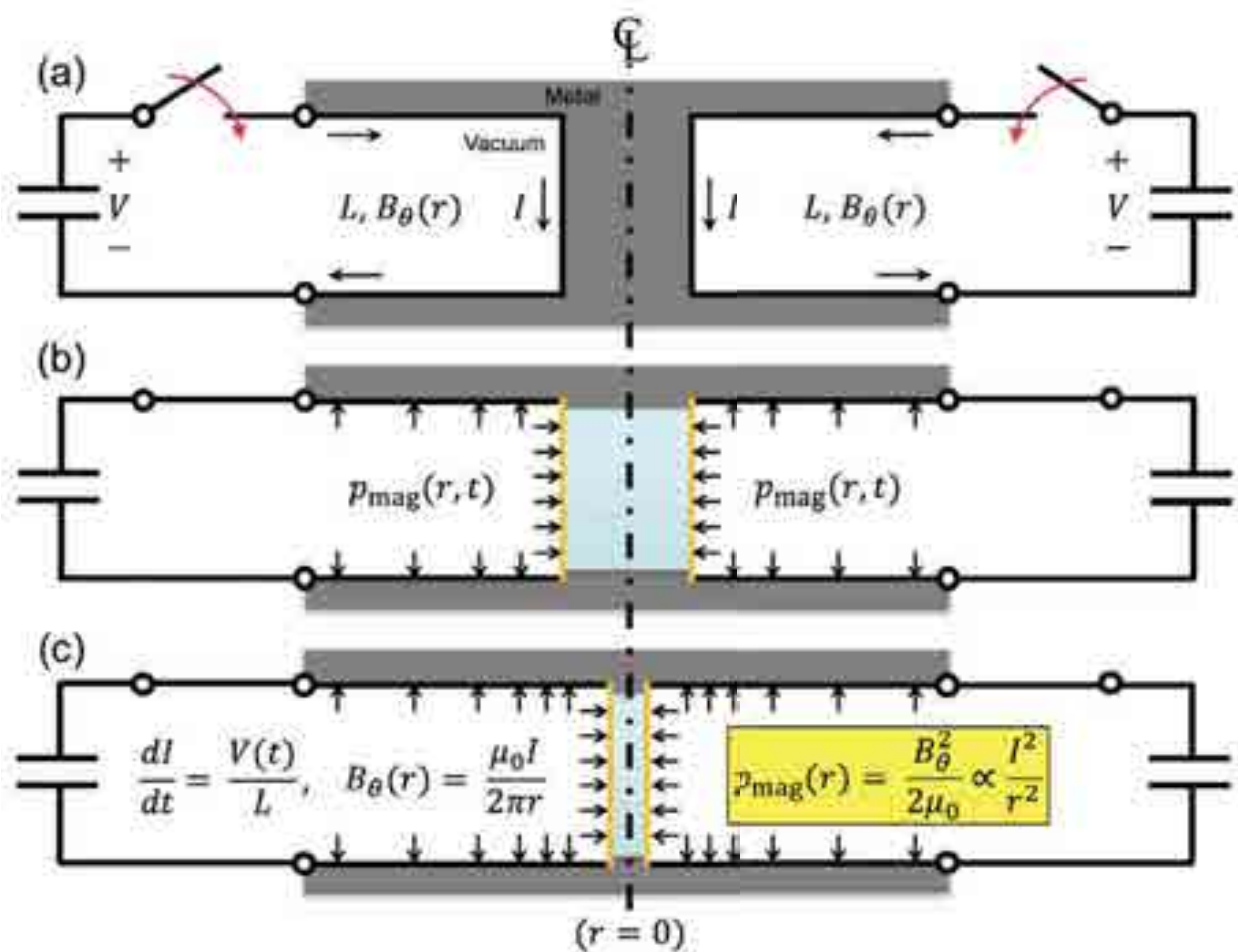
Figure 1.6: Depiction of a fast Z-pinch, where intense electrical current is driven through a conductor to implode it via the inward-directed $\mathbf{J} \times \mathbf{B}$ force. Material inside the imploding conductor (e.g., an FRC in a liner) can be compressed to enormous pressures. Reproduced from McBride et al. [33] © 2018 IEEE.

1.5   Pulsed-Power and Linear Transformer Drivers

Fast Z-pinches reside in the rather broad field of electromagnetic drive via pulsed-power, which requires pulsed-power machines usually comprised of fast, high-voltage capacitors and switches. Electrical energy is stored in the capacitors over many seconds of charge time, then discharged via the switches into a transmission line(s) that converges to a final load region. The machine has thus compressed electromagnetic energy in space and time, and delivered it to a target. Various "architectures" of pulsed-power exist, representing unique methods for amplifying voltage and current and delivering electrical power to a load.

A common architecture for pulsed-power devices of relevance to Z-pinches is the bipolar Marx generator. The standard circuit of a bipolar Marx generator is shown in Fig. 1.7. The Z-machine at SNL utilizes 36 coupled pulsed-power sources of similar bipolar Marx design [9]. Marx banks such as those in Z (to be discussed more in Chap. 2) are typically comprised of capacitors with a large capacitance-to-voltage ratio, making them physically large and energetic. However, the inductance-to-voltage ratio can also be large, producing a naturally longer risetime ($\sim \mu$s) of the discharge current pulse. To shorten the risetime ($\sim$100 ns) and apply higher peak current and electrical power to low-inductance loads, ultra-powerful machines like Z use pulse-compression stages (see Fig. 2.1). Such stages utilize intermediate capacitive storage in a liquid dielectric (e.g., water), and precise triggering of very high-voltage switches. While achieving large power amplification, these pulse-compression stages are also prone to energy loss via mechanical shock and dielectric flashovers, especially in the final self-breaking water switches.

A more ideal and efficient architecture for high-power electrical pulse delivery is comprised of capacitors with a small capacitance/inductance-to-voltage ratio, such that the natural risetime is short and pulse-compression is not required. Unfortunately, this requires physically small capacitors with low energy storage. A very large number of these capacitors (and accompanying switches) is required to produce an overall energetic facility, greatly complicating the engineering and reliable operation of such a facility.

Linear transformer drivers (LTDs) represent a novel architecture geared towards naturally fast pulsed-power. As shown in Fig. 1.8, an LTD is based on a fundamental pulsed-power unit: the "brick". A bipolar LTD brick (Fig. 1.8) is comprised of two capacitors and a bipolar switch. When the switch is closed, a bipolar voltage pulse is applied to the common output transmission line, where the current from many bricks in the cavity is added together and delivered to the load. Multiple LTD cavities can be stacked in series to increase the voltage, impedance, and stored energy of the machine, while keeping the maximum current and risetime constant. Multiple LTD cavity stacks can be added in parallel to increase the current while decreasing the overall driver impedance and preserving the stacked voltage and risetime.
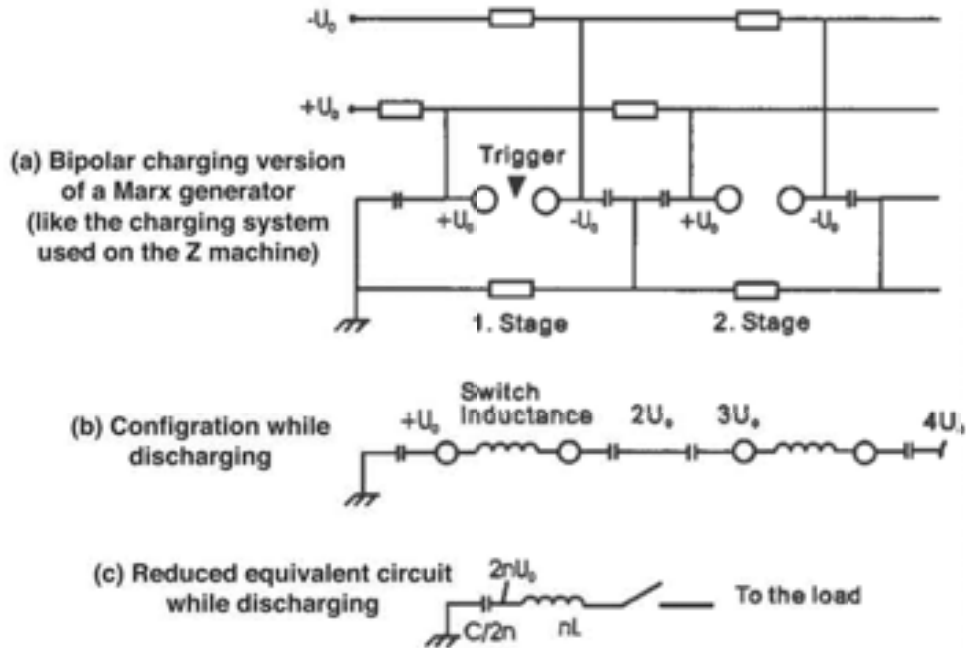
Figure 1.7: Circuit of a bipolar Marx generator, as found in the Z-machine. Reproduced from McBride et al. [33] © 2018 IEEE.

The distinguishing feature of an LTD cavity is complete enclosure of the bricks in metal, which can alleviate high-voltage breakdown and EMP issues. However, it also introduces a parasitic current path in parallel with the load (see Fig.1.8). To prevent the LTD discharge current from taking this parasitic path and force it through the load as intended, LTDs contain one or more ferromagnetic "cores". These toroidal-shaped cores work on similar principle to ferromagnetic chokes on surge protection or high-frequency diagnostic equipment, increasing the effective inductance of the parasitic path to limit current. To maximize the effectiveness of the cores, they can be "pre magnetized" before the LTD shot by a separate current pulse source. This maximizes the required travel distance in hysteresis-space of the core material before saturation, maximizing the effective impedance [36].

The Pulsed-Power and Microwave Laboratory (PPML) at the University of Michigan is home to two LTD systems: MAIZE and BLUE. MAIZE (to be described in Chapter 3) is a single-cavity, 40-brick system, while BLUE is a four-cavity, 10-brick-per-cavity system. This author spent the first few years of his PhD constructing the BLUE LTD system, as detailed in Appendix C and Ref. [37].

Linear transformer drivers are being considered [38] as a base architecture for the next DoE flagship pulsed-power facility, referred to as Next Generation Pulsed-Power (NGPP) or, colloquially, "Z-next". NGPP will be capable of delivering 50 to 100 MA of current with a 100 ns risetime [38] to an imploding load (e.g., a MagLIF liner), exceeding the power and energy delivery capabilities

9
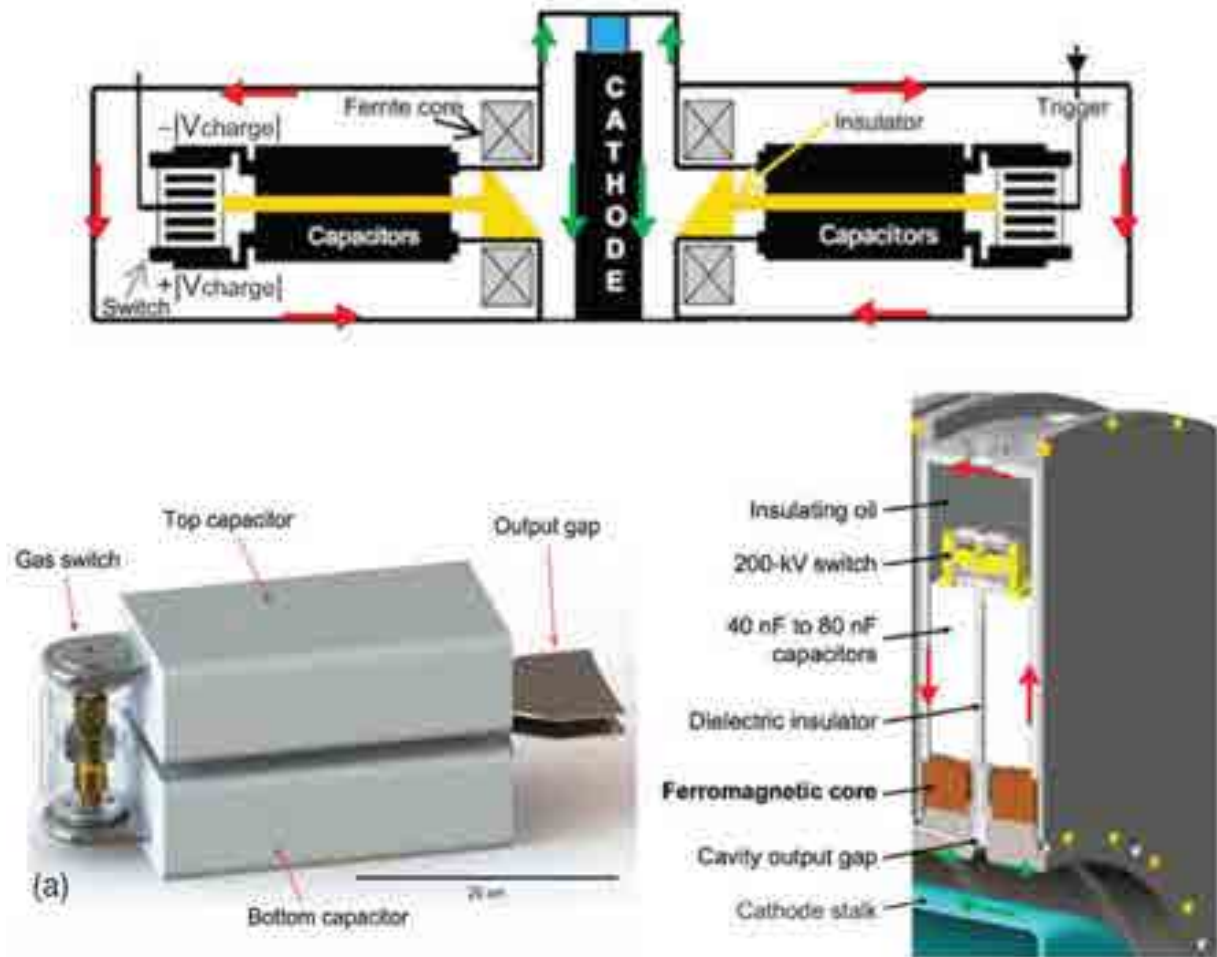
Figure 1.8: Depiction of a bipolar linear transformer driver (LTD) cavity. The fundamental unit of an LTD cavity is the "brick" (bottom left), composed of two high-voltage capacitors and a bipolar spark-gap switch. Many bricks are added in parallel to deliver high current to the load. Multiple LTD cavities can be stacked to increase voltage to the load. Ferromagnetic cores discourage the discharge current from taking the parasitic current path (indicated by the red arrows in the top and bottom-right images) around the all metal cavity's casing. Reproduced from McBride et al. [33] © 2018 IEEE.

of the NIF. NGPP is expected to replace the existing Z-machine in the 2030s to 2040s timeframe, and is believed to be capable of fusion ignition with the MagLIF concept [39].

1.6   Organization of this Dissertation

The purpose of the research documented in this dissertation was to explore the nascent idea of producing and compressing high-energy-density, centimeter-scale FRCs on the Z-machine at Sandia National Laboratories. Future experimental goals for an FRC program on the Z facility could include large fusion yield, magnetic reconnection studies, and improved simulation capabilities. The experiments would be done utilizing bias coils and liner-based compression hardware similar to that already developed for the MagLIF program. This dissertation is organized as follows:

Chapter 2 gives a detailed introduction to the Z-machine and the MagLIF concept, as well as the AutoMag liner concept that is key to the *in-situ* FRC formation concept presented in this dissertation. AutoMag experiments performed by the author on the Mykonos pulsed-power driver at SNL are presented. Finally, FRC production and compression in an AutoMag liner will be discussed conceptually.

Chapter 3 details the experimental platform developed on the MAIZE pulsed-power driver at the University of Michigan to produce and diagnose FRCs that are hydrodynamically similar to those desired for compression on the Z-facility. Justification for FRC production is presented and results are compared with simulations and the existing FRC literature.

Chapter 4 presents 2D axisymmetric simulation results from the resistive MHD code Kraken of high-density FRC equilibrium, decay, and formation. A background description of the code will be given, along with modifications made by the author for high-density FRC initialization/formation and anomalous resistivity. FRC resistive decay results are benchmarked against the literature. MAIZE-like FRC formation simulations are presented and compared with experimental results using synthetic imaging techniques.

Chapter 5 concludes with an overview of the FRC work presented, and suggestions for future work to be performed in consideration of the first Z shot proposal.

Appendix A is a reproduction of Ref. [6], a publication by this author that analyzes the implications of modern HTS technology on an MCF concept known as magnetic electrostatic plasma confinement (MEPC) in the pseudo-classical limit.

Appendix B summarizes the results from thin-foil implosions carried out by this author on the Mykonos pulsed-power driver. Implosion stabilization by dynamic screw pinch [40] is explored, as well as AutoMag-like axial field production preceding an implosion using laser-etched foils.

Appendix C is a reproduction of Ref. [37], a publication by this author that discusses construction and initial testing of the BLUE linear transformer driver (LTD) system at the University of Michigan.

When all four cavities become operational, BLUE will be an 800 kV, 250 kA, 100 ns, 1-Hz, four-cavity LTD system capable of driving various Z-pinch and high-power microwave (HPM) experiments.

CHAPTER 2

MagLIF and AutoMag

2.1 Overview of the Z-machine and MagLIF

The flagship facility for fast pulsed-power in the USA is the Z-machine (or "Z") at Sandia National Laboratories in Albuquerque, NM. A cutaway of the Z-machine facility is shown in Fig. 2.1. Z's prime pulsed-power architecture uses 36 modules of the bipolar Marx design (see Fig. 1.7), which deliver a 5–6 MV, multi-microsecond current pulse to the pulse-forming section. In the pulse-forming section, energy is stored in 36 intermediate storage "capacitors" using deionized water dielectric, before being discharged into another transmission section via 36 laser-triggered gas switches [41]. Finally, 36 self-breaking water switches at the output of the final transmission line further sharpen the pulse, and deliver it through the vacuum insulator stack to four levels of magnetically-insulated transmission lines (MITLs) in the central vacuum chamber. Current on the four MITL levels is combined via the "post-hole convolute" and delivered to the load, which can be less than a centimeter in size.

The resulting electromagnetic pulse has the following approximate properties at the load: 5 MV, 20 MA, 100 ns risetime, 80 TW peak power. Such a powerful pulse can be used to explore a plethora of scientific questions asked in the fields of high-energy-density-physics (HEDP), astrophysics, planetary science, material science, radiation science, nuclear weapons physics, fusion science, and many more [9]. Furthermore, precise shaping of Z's final output pulse can be realized via staggered triggering of the laser-triggered switches in the pulse-forming section, allowing for even more flexibility in the magnetic pressure profile delivered to the experiment [42] [43].

The Z-machine was originally built for physics experiments that support the DoE mission of stockpile stewardship, and many of the exotic experiments performed currently were never imagined during its design. An example is the magnetized liner inertial fusion (MagLIF) program [35]. Conceived of by Slutz [44] circa 2010, MagLIF represents a form of magnetized target fusion, and is one of the few unclassified fusion programs on Z.

The three stages of MagLIF are depicted in Fig. 2.2. First, a centimeter-sized, metallic (typically beryllium), thick-walled tube known as a "liner" is filled with deuterium gas at several atmospheres

13
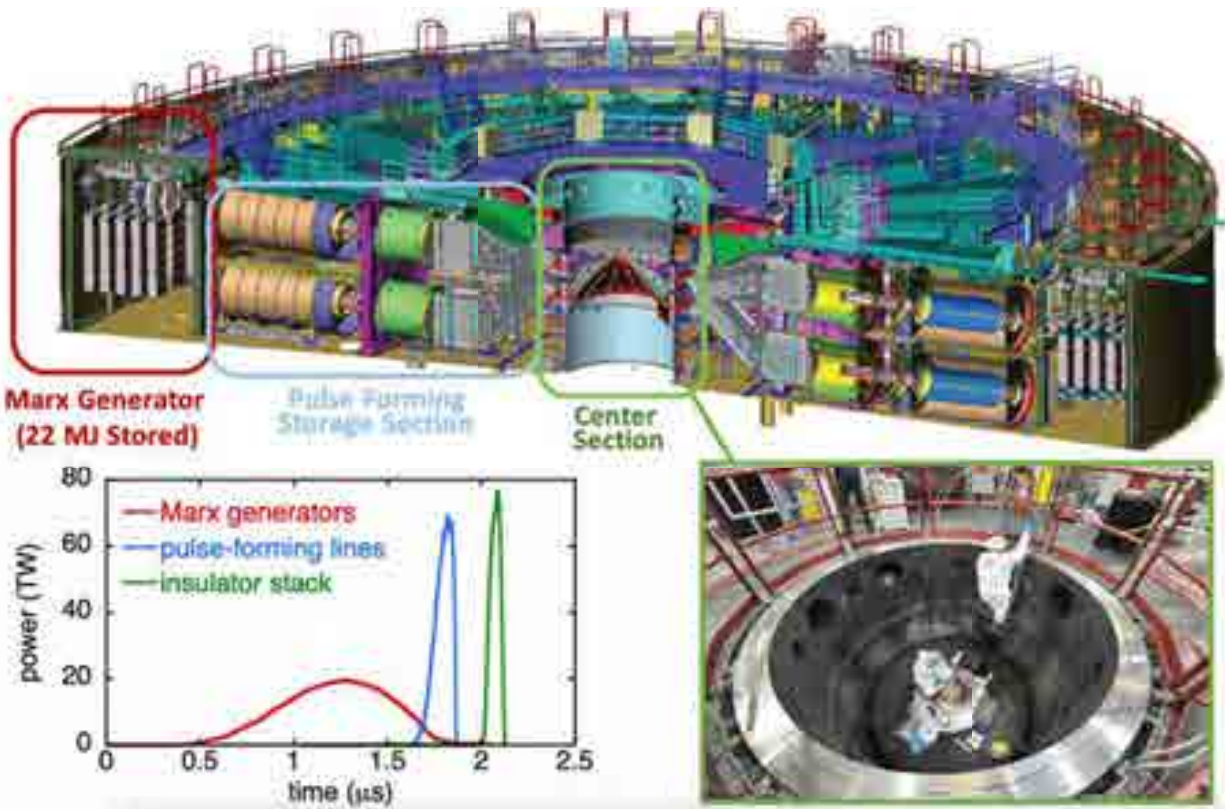
Figure 2.1: Cutaway of the Z-machine at SNL showing the bipolar Marx generators, interme-
diate storage capacitors, laser-triggered gas switches, self-breaking water switches, MITLs, and
load/target region. Reproduced from Sinars [9].
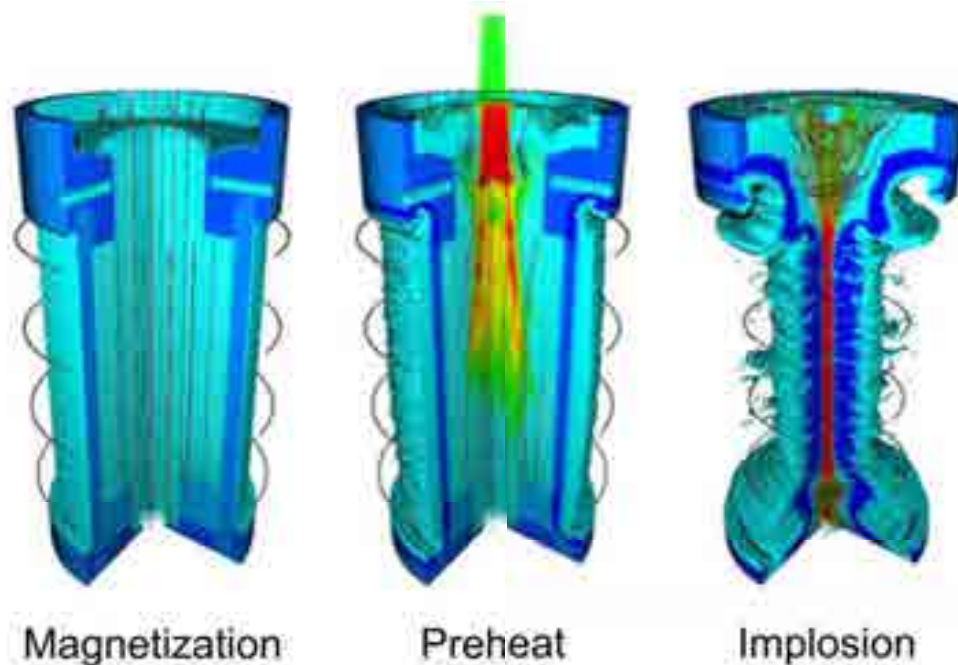
Figure 2.2: The three stages of magnetized liner inertial fusion (MagLIF), a unique MTF/ICF fusion concept explored on the Z-machine. Reproduced from Yager-Elorriaga et al. [35].

of pressure and axially magnetized by an external coil assembly. Second, the deuterium gas is ionized and pre-heated to several hundred eV by a kJ-class, NIF-like laser pulse, which enters through a thin plastic window at the top of the liner. The kJ-class laser used at the Z-facility, known as Z-beamlet [45], is from the original prototype NIF quad, and it was typically only used for X-ray diagnostic purposes before the advent of MagLIF. Third, the Z-machine pulse arrives, driving up to 20 MA of current along the outer surface of the liner. The intense magnetic pressure Z-pinches the liner in less than 100 ns, compressing the magnetized deuterium fusion fuel inside. Upon stagnation, having been insulated by the magnetic field throughout the implosion, the fuel reaches thermonuclear conditions.

Compression and burn on Z is so fast (and cylindrical) that the fuel is pseudo-confined inertially in the axial direction, requiring only radial insulation by an axial magnetic field component. Thus, as stated, MagLIF represents a unique form of MTF – and the simplest form in the sense that no closed-field-line plasmas need be created or stabilized. In fact, MagLIF does not require magnetic "confinement" at all in the sense of $\beta \leqslant 1$; it only requires a large Hall parameter for effective thermal insulation. Thus, optimum MagLIF plasmas are actually wall-confined [46] with $\beta \gg 1$, and subject to unique drift instabilities [47]. The "Nernst" effect is well-known [48] in MagLIF to advect magnetic field out of the hot plasma core. The Nernst effect can be thought of as the dynamic, transport-limited development of the high-β plasma's diamagnetism.

15

In addition to improving physics understanding and simulation capabilities, current MagLIF experimental efforts are directed towards increasing the strength of the bias field produced by external coils, the laser energy coupled to the gas, and the peak current delivered to the MagLIF target by the Z-machine. Increase in all of these parameters simultaneously is required for large increases in fusion yield. With the near-term realistic goals of 30 T applied bias field, 2 kJ of laser energy coupled, and 20 MA of Z current, it is expected that DT-equivalent yields with MagLIF on Z could exceed 100 kJ [39]. Note this is comparable to the yields achieved on the purpose-built NIF until August 8, 2021 [7]. On an NGPP facility delivering 50 to 70 MA, fusion ignition with MagLIF is believed to be possible [39]. Furthermore, it is shown in Ref. [39] that, at the energy density associated with 70 MA current levels, a burn wave can be propagated from the hot-spot MagLIF fuel to a cryogenic DT ice layer deposited on the liner's inner surface, producing multi-GJ yield and resolving earlier conjectures [49] [50] [51]. Indeed, a long-held criticism of MTF is the weak scaling of gain with increased drive energy [14] [15] [31].

2.2   The AutoMag Liner Concept

Large fusion yield with MagLIF on Z requires large applied bias fields, optimized in the range 40–60 T on Z (but, interestingly, closer to only 10–20 T for NGPP) [39]. Such fields are not trivial to apply with external coil hardware; in fact, fields much exceeding 30 T are impractical. This is due to the fact that the external bias field must be applied over milliseconds to effectively magnetize the MagLIF liner and surrounding hardware, and is thus limited by the material strength of the coil. Furthermore, fully-encapsulating (bulk) coils are undesirable as they restrict diagnostic access to the target. Modern MagLIF experiments at Sandia use steel-reinforced coils and sometimes fringe fields from bulk coils, since the axial non-uniformity has proven more acceptable than a lack of diagnostic access [35].

To magnetize the liner more effectively, the "AutoMag" concept was proposed [52], and has been explored on smaller pulsed-power drivers [53] and even Z [54]. As shown in Fig. 2.3, an AutoMag liner has helical cuts in it filled with dielectric, encouraging the Z-pinch current from the Z-machine to flow helically. The helical current flow produces the desired axial field inside the liner, without the need for external coils. Furthermore, the bias field strength is no longer limited by material or skin depth considerations, since it is applied locally and dynamically on the timescale of the implosion. Fields in excess of 150 T have been produced in AutoMag experiments on the Z-machine [54] [35]. More recent AutoMag work [55] has focused on controlled initiation of the breakdown process in AutoMag, to more precisely control the strength and timing of the produced field.

The stages of MagLIF with an AutoMag liner (which has not yet actually happened experimen-
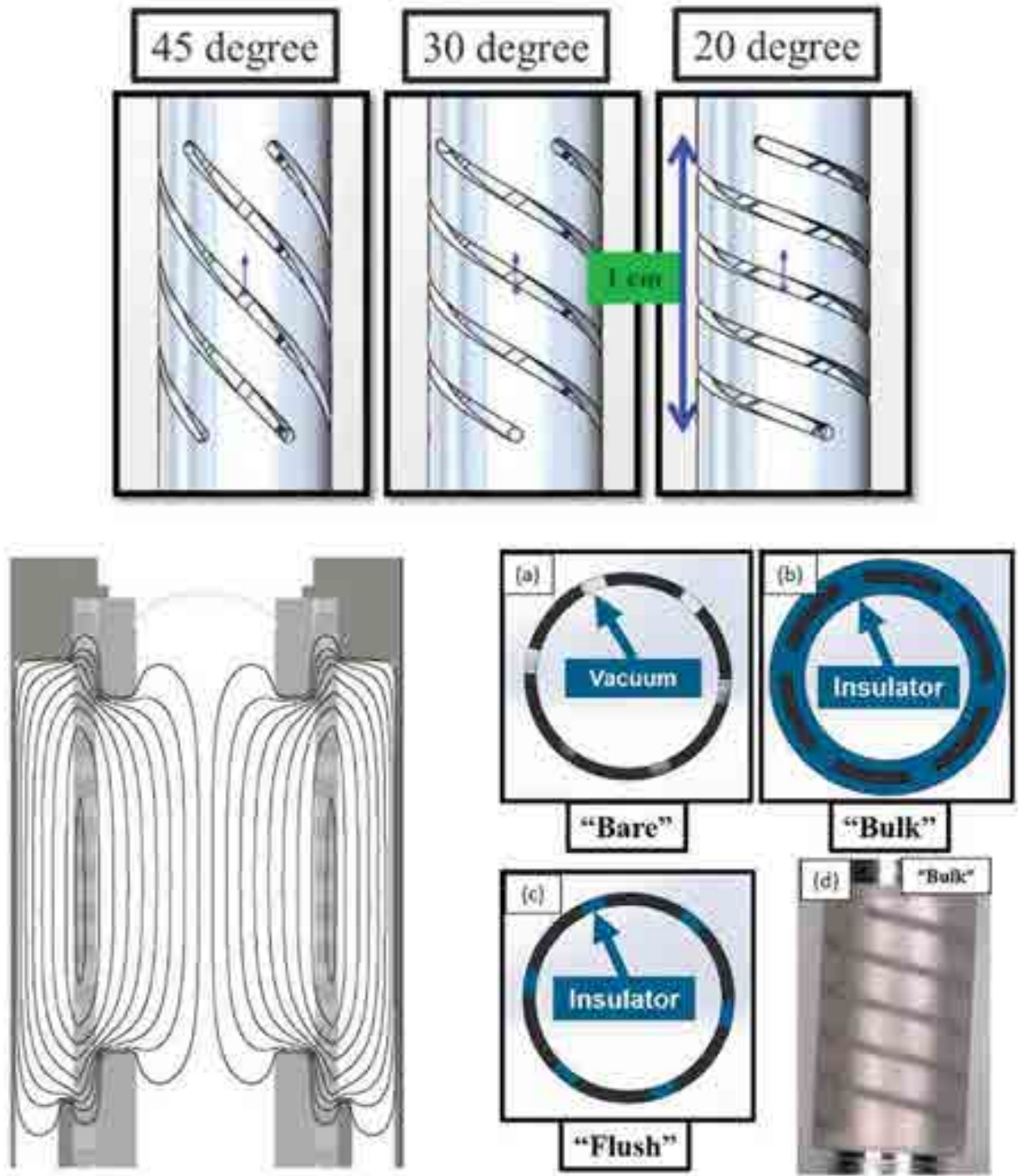
Figure 2.3: The AutoMag liner concept developed for MagLIF. Helical cuts in the liner produce an axial field from the foot of the Z-pinch drive pulse, eliminating the need for external field coils. The dielectric then flashes over, and the Z-pinch of the liner proceeds as normal. Frames (a)-(c) show different methods of potting and post-finishing the AutoMag liners; the "bulk" preparation (b and d) will likely be required for FRC studies to prevent Z current from leaking through the plasma in the liner. Reproduced from Shipley and Slutz et al. [53] [52].

tally) are as follows: the Z-machine is discharged, producing the Z-pinch current. The first few mega-amps of the Z current flow helically through the AutoMag liner, producing a strong axial magnetic field in the neutral gas. The neutral deuterium is at several atmospheres of pressure, so is not expected to break-down inductively. As the current and voltage of Z continue to ramp up, the inductive load voltage across the AutoMag liner becomes large enough to result in surface flashover of the dielectric-filled helical gaps on the outside of the liner. Additional current delivered by Z now flows purely axially, and the implosion of the liner proceeds as in a standard Z-pinch. Sometime after the magnetization – but before the liner implodes – the 2 ns Z-beamlet pulse arrives to pre-heat the magnetized gas inside the AutoMag liner to a higher adiabat (as with standard MagLIF).

In Ref. [52], it is suggested that an AutoMag liner could be used *in combination* with external bias coils to produce the reversing field behavior required for FRC production. The liner would then implode as a flux conserver, and the high-energy-density FRC produced *in-situ* could be compressed to thermonuclear conditions. This concept is explored further in Ref. [31], which inspired this dissertation.

2.3   AutoMag Experiments on the Mykonos LTD

As part of the author's fellowship residency experience at Sandia National Labs, experiments related to the AutoMag concept were carried out on the Mykonos pulsed-power system. Mykonos is a five-cavity LTD system, with each cavity identical to the (sole) MAIZE LTD cavity (see Chap. 3). Thus, Mykonos has five times the voltage and impedance of MAIZE, but the same nominal current (∼1 MA).

The Mykonos experiments reported herein do not represent work directed towards FRCs *per se*, and are an extension of the work done in Ref. [55], using the same machine hardware and 20-degree pitch angle AutoMag liners. The return current hardware used for experiments in Ref. [55] was modified to include a helical return current can surrounding the AutoMag liner known as a dynamic screw pinch (DSP), as shown in Figs. 2.4 and 2.5. The DSP concept was proposed to slow the growth rate of the MRT instability by dynamically rotating the drive field angle during the liner implosion [40]. In practice, this is simply done with a helical return current can that produces an axial component to the drive field that has weak dependence on liner radius, as shown in Fig. 2.4. These contours were generated in CST Studio Suite simulating an 800 kA peak current pulse at 2.5 MHz (100 ns risetime) through the liner and return structure. In the designs of Fig. 2.4, the peak axial field from the DSP return structures is approximately 18 T throughout the liner imploding region (if it were to implode on Z). The peak azimuthal field at the liner surfaces is approximately 50 T, consistent with the 800 kA surface current on the 6 mm OD liner. Theory suggests this initial drive field ratio $\Xi \equiv \frac{B_{axial}}{B_{azi,0}} \approx 0.35$ should have a noticeable stabilization effect [56]. Fig. 2.4 also
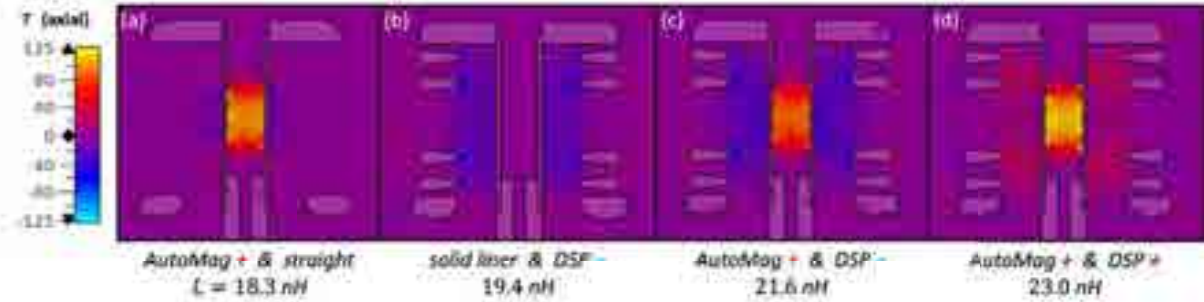
Figure 2.4: CST Studio Suite [57] simulations showing contours of *positive axial* magnetic field strength at 800 kA load current for Mykonos experiments with (a) 20-deg AutoMag with straight return can (b) solid liner with DSP return can (c) 20-deg AutoMag with DSP (axial fields destruct inside) (d) 20-deg AutoMag with DSP (axial fields construct inside).

lists the inductances of the load hardware, showing how DSP adds several nH which depends on the presence/orientation of an AutoMag liner.

With an AutoMag liner, the axial field produced by the DSP can penetrate into the the liner and be comparable in magnitude to the axial field produced by the AutoMag liner itself. The DSP axial field may interfere constructively or destructively with the AutoMag field and/or the bias field, as shown in Fig. 2.4. Thus, the DSP represents an additional source for producing axial field inside the liner and may have implications for the FRC concept. For instance, the surface flashover phenomenon might be exploited *twice* in a potted DSP with potted AutoMag to produce field-reversing behavior not limited in strength by slow bias coils.

The purpose of the reported DSP/AutoMag hybrid experiments was to determine if the DSP axial field penetrates the AutoMag liner as expected from simulation, both before and after breakdown of the liner. Micro B-dot probes as shown in the left inset of Fig. 2.6 were used to measure the axial field behavior inside and outside the liner, as in Ref. [55]. Micro B-dot fabrication is described in more detail in Section 3.9. Broadband photodiodes of the avalanche and silicon type were fiber coupled with collimators and used to observe the liner surface for breakdown, with field-of-view depicted by the red spot in Fig. 2.5. Two fibers were used looking at opposite sides of the liner, and an avalanche and silicon diode were coupled to each fiber.

While the full result and analysis of the experiments are left for later publication, three representative experimental results are presented herein. The B-dot field measurement results of the experiments corresponding to Fig. 2.4(a), (c), and (d) are shown in Fig. 2.6. Also shown are calibrated load current measurements depicting the expected field with pure vacuum conduction (i.e. no breakdown/surface flashover). Diode signals and independent visible imaging with UHSi and iStar 334T cameras reveal breakdown is quite a dynamic and non-uniform process that occurs over several tens of nanoseconds, with ever-increasing light emission.
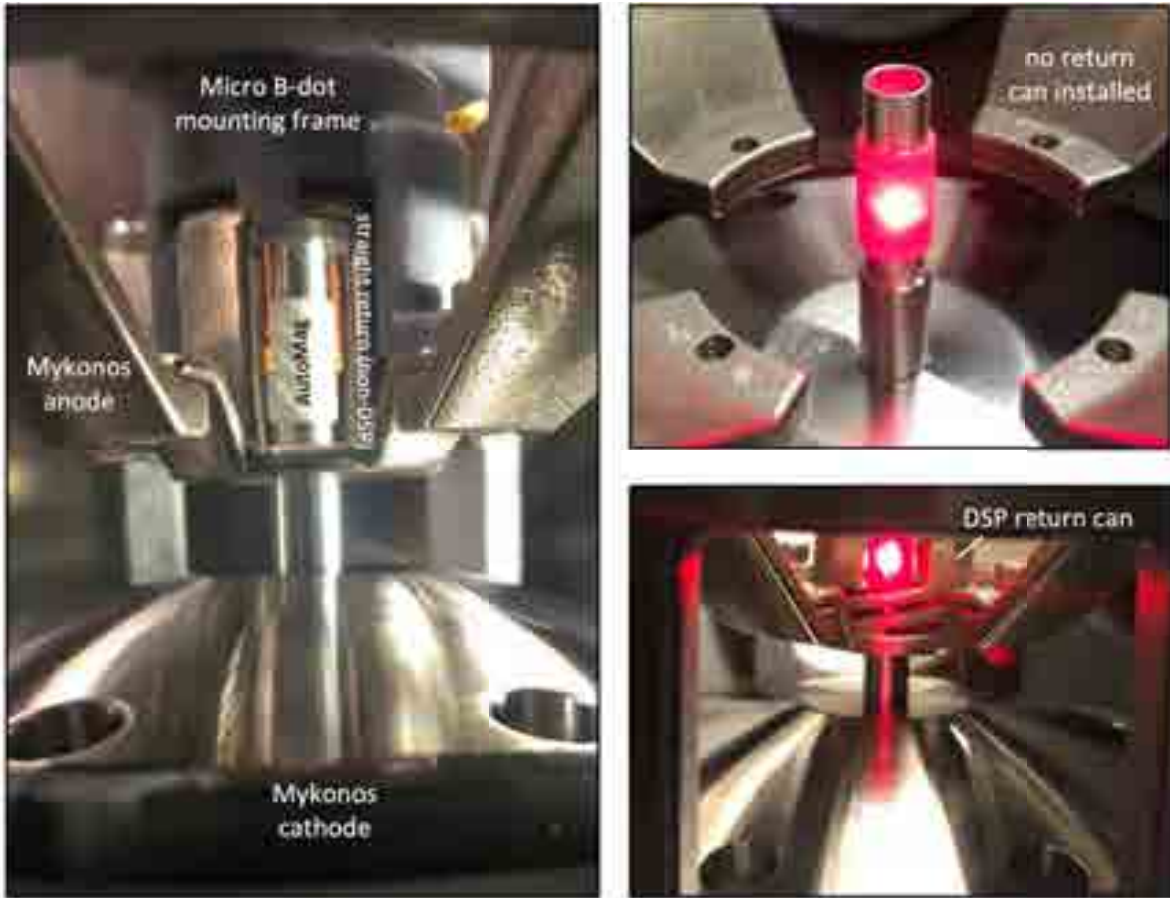
Figure 2.5: Images of actual Mykonos load hardware showing straight and DSP return cans around an AutoMag liner. The red laser spot indicates the field-of-view of the photodiodes (see text).
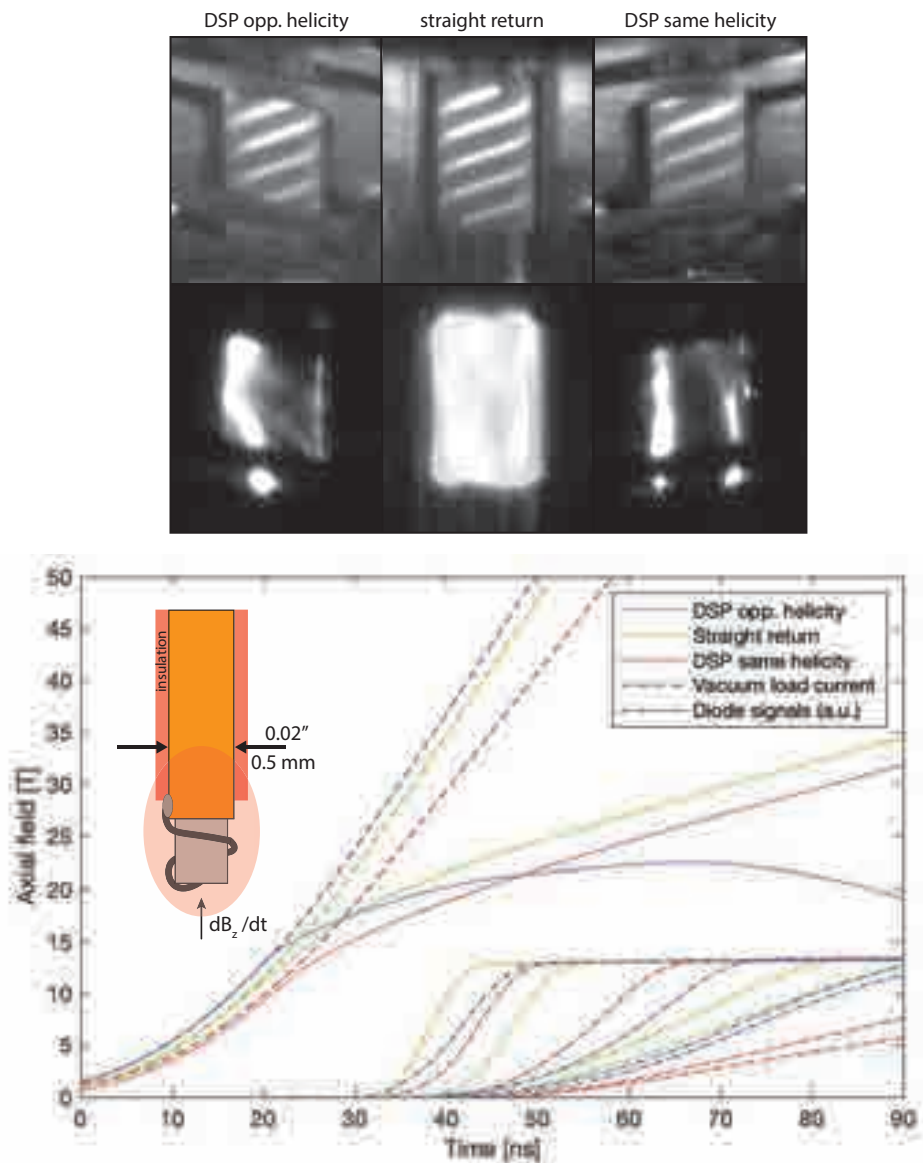
Figure 2.6: Axial magnetic field as measured by micro B-dot probes (plot inset) inside the 20-deg AutoMag liners for a straight return can and DSP return cans of the same and opposite helicity, corresponding to the cases of Fig. 2.4(a), (c), and (d). Also plotted are the axial field for each experiment inferred from the load current traces and simulation with vacuum currents (i.e. no surface flashover). Normalized photodiode signals observing the AutoMag surface reveal flashover is a dynamic process lasting several tens of nanoseconds. This was independently confirmed by images taken with a UHSi camera and 10 ns exposure images taken with an iStar 334T (top).

The presence of the DSP return cans does not significantly affect the breakdown timing, as can be seen by the similar timing of the first "knees" in the B-dot traces and the random rise of the diode signals. At the first sign of breakdown (the knees), the DSP can with opposite helicity has successfully injected more axial flux into the liner than the liner alone. However, during and after the breakdown process, it is clear the AutoMag liner continues to produce axial flux – eventually a greater amount than initially injected before the first signs of breakdown, if the B-dots are to be believed at this point (it is possible a DC offset of some sort causes an artificial near-linear rise to the signal). The disparate behavior of the B-dot after breakdown in the case of DSP with opposite helicity is not yet understood at this time. The preceding analysis also assumes there is no current shunting from turn-to-turn in the DSP can (which is a strong possibility).

In addition to the AutoMag experiments, thin-foil implosion experiments were carried out on Mykonos to demonstrate the stabilization effectiveness of the DSP return can that was designed. These experiments followed the methods of Yager-Elorriaga [58] and Campbell [59] [60] using 800-nm aluminum foils which can be imploded with sub-MA drivers. The results of these experiments are detailed in Appendix B.

2.4   Hydrodynamic Prospects of HED FRC MTF on Z

In Ref. [31], Slutz et al. develop an analytic model of FRC adiabatic compression by a liner, showing that interesting yields approaching $Q_{sci} \sim 1$ may be possible on the hydrodynamic scale of the Z-machine. His reasoning is based on the following assumptions as inputs to the analytic model:

- A bias field from external coils of -30 T is currently feasible on Z (with severe diagnostic restrictions). Fast-reversal fields greater than $+150$ T have already been demonstrated on Z [54] with the AutoMag concept, ensuring robust reversal (and even pre-compression of the FRC).

- In liner implosion experiments (i.e. MagLIF), Z routinely couples nearly 500 kJ of kinetic energy to solid liners (corresponding to implosion speeds of >100 km/s) [61].

- Experiments have shown beryllium liners with aspect ratio ($AR = \frac{r_o}{r_o - r_i}$) less than 6 have inner surface that is robustly stable through stagnation to the helical magneto-Rayleigh-Taylor (MRT) instability [62], which is the prime symmetry disruptor in fast, magnetized Z-pinch implosions.

- Integrated MagLIF experiments on Z have been radiographed as hot, stable columns at convergence ratios ($CR = r_{\text{in},0}/r_{\text{in,f}}$) of approximately 40, and there is further evidence to support this degree of fuel compression [63] [61].

With the parameters stated above, the Slutz analytic model predicts optimum gain (fusion yield / liner kinetic energy) greater than unity with an initial liner radius of 6.1 mm and implosion time of 270 ns.

Also in Ref. [31], this prediction is used as input to a 2D LASNEX simulation. LASNEX is a radiative hydrodynamic code originally developed at Lawrence Livermore National Laboratory [64]. The simulation in Ref. [31] is summarized as follows: FRC formation in a 6.1 mm initial outer radius beryllium liner is modeled by direct control of the flux or "stream" function at the boundary with the liner conductivity turned off, from a value corresponding to $B_{bias} = -30$ T to $B_{fast} = +30$ T. The simulated applied field change is a linear ramp from negative to positive value in 100 ns. Anomalous resistivity based on the often-cited Chodura model [65] [66] is used to model reconnection heating in the low-temperature, fully-ionized DT fill. The liner is then prescribed an instantaneous implosion velocity corresponding to its mass (with $AR = 6$) and energy (E_k =500 kJ). The resulting compression of the FRC to $CR \sim 20$ produces a DT yield of 538 kJ, which is greater than the liner kinetic energy and in agreement with the analytic model.

The Slutz LASNEX simulation is extremely encouraging and demonstrates that HED FRCs can be compressed nearly adiabatically on this timescale, even with anomalous resistivity and magnetic diffusion into the beryllium liner material. Furthermore, the assumptions of Slutz are viewed as conservative for the following reasons:

- Pulse shaping and self-crowbar effects on the Z-machine may allow greater energy coupling to liners of larger size and longer implosion time than those optimized for MagLIF. Very long implosion times could allow liners to maintain some material strength during the first stages of implosion, adding MRT robustness. Given the extreme non-linear complexities of optimizing liner energy coupling on Z specifically as a machine, perhaps it is advisable to first determine that optimal liner size. Then the ideal FRC can be designed for compression in such a liner.

- Large AR implosions can have more energy coupled to them in a Z-pinch; for example, wire array and gas puff experiments on Z couple over 2 MJ [67] [68]. Max AR for liners is limited by acceptable robustness to MRT, which again becomes a highly non-linear analysis. Liners with $AR = 9$ have performed well in MagLIF experiments [35], and methods to stabilize MRT have been developed such as dielectric coatings [69] and the dynamic screw pinch [40] (see Sec. 2.3).

- A convergence ratio of 20 is self-imposed on the LASNEX simulation (assuming near-adiabaticity), which is conservative. There is evidence for MagLIF compression ratios exceeding 40, which would nearly double the achievable gain according to the Slutz analytic model, and reduce FRC initial adiabat requirements.

- Since the FRC contracts axially during compression, the length of the imploding region of the AutoMag liner need not be as long as the initial FRC that is produced. Limiting the height of imploding region of the liner reduces the inductance of the target and allows better current/energy coupling from Z to the liner region containing the FRC.

- While likely not effective on Z, on a future 70 MA NGPP, it is unclear if a burn wave could be propagated into a cryogenic DT ice layer on the inner surface of the liner for FRC implosions, as in MagLIF [39]. Ice burn could greatly amplify the gain.

In summary, FRC liner compression on the hydrodynamic scale of the Z-machine could be very interesting from a fusion gain perspective, at least in the pseudo-classical limit. However, there are a number of concerns with the concept to be addressed before the first Z experiment could be confidently designed. Excluding the entire issue of optimizing the energy coupling of Z, a select few are:

- Can FRCs be reliably produced via the method conceptualized, i.e. with a slow external bias field and AutoMag-like fast reversal field?

- What methods of pre-ionization can be used to trap the bias flux? What degree of pre-ionization is required? What phenomenon limits formation at arbitrarily high density?

- Are the FRCs that Slutz proposes expected to be stable from an S^*/E perspective throughout the compression? Does the classical and anomalous resistive decay match existing theory for low-density FRCs and exceed the intended compression time?

This thesis attempts to address some of these questions via a two-pronged approach, with formation experiments on the MAIZE LTD and 2D decay simulations in the resistive MHD code Kraken.

2.5 FRC Equilibrium in an AutoMag Liner

As detailed in the previous section, the proposition of an FRC formed in an AutoMag liner is superficially straightforward – but there are many subtleties that make it quite novel. Namely, to the author's knowledge, all FRC experiments to date have taken place in a single-turn, flux-conserving coil(s). This coil(s) is driven by one or more capacitor banks to produce *both* the bias and fast reversing field from the same conductor. The inductive "loop voltage" generated in the FRC discharge tube is equal to the voltage driving the coil (or some multiple thereof if sectioned coils are used).

In the case of AutoMag, the bias and fast fields are produced by two different sources: the external coils and AutoMag liner. The loop voltage is smaller than the voltage driving current rise in

the helical (solenoidal) section of the AutoMag liner. The AutoMag liner itself (before breakdown) is not a perfect flux conserver, as flux can distort into the dielectric gaps. Furthermore, there is a 3D asymmetry and azimuthal component to the fast drive field near the surface of the AutoMag liner. Some of this azimuthal field could become trapped in the FRC, potentially forming a more spheromak-like compact toroid. The breaking of azimuthal symmetry and presence of an azimuthal field component near the flux conserver is reminiscent of adding multipole fields to a single-turn FRC experiment, which is known to help stabilize the rotational instability [26].

In summary, FRC formation and equilibrium in a solenoidal fast coil may have unique properties, perhaps some beneficial and some not beneficial. The 3D asymmetry and thus the formation/equilibrium effects are expected to have strong dependence on the helical pitch, spacing, liner thickness, and AutoMag coating thickness. An experiment to demonstrate formation of an FRC in such a geometry is warranted.

CHAPTER 3

FRC Formation Platform on the MAIZE LTD

As noted in the final paragraph of Ref. [31], an AutoMag FRC with parameters at-scale for Z compression could be produced on a machine delivering about 1 MA of current. An experimental campaign for such FRCs is warranted, given the tendency for FRCs to defy theoretical and computational predictions, and the uniqueness associated with formation from two solenoidal field sources.

The MAIZE LTD system at the University of Michigan, to be described in Sec. 3.1, was used to explore high-density, high-field FRC formation and stability. This chapter describes each aspect of the experimental setup in turn, then discusses the results. High-density FRC production on MAIZE will be justified by dynamics seen in axial fast-framing images and field measurements made by micro B-dot probes. Furthermore, Chap. 4 will present the results of *a posteriori* simulations and post-processing synthetic images qualitatively consistent with experimental imaging results on MAIZE.

3.1   Description of the MAIZE LTD System

MAIZE is a single-cavity, 40-brick, bipolar LTD system in the PPML lab at the University of Michigan [70]. For an introduction to LTD technology, see Chap. 1. MAIZE is nominally a MA-class, 100 ns machine, thus competing in capability to Marx-based fast, MA-class machines that are much larger and less efficient. However, MAIZE has a low driver impedance of 0.1 Ω, so only loads of the lowest inductance can receive MA-class fast discharges. The experiments reported herein typically received only 300–400 kA of current with >200 ns risetime. A cross-sectional rendering and two photographs of the MAIZE LTD cavity are shown in Fig. 3.1.

Each brick of MAIZE consists of two 40 nF, 100 kV capacitors and a bipolar field-distortion spark-gap switch from L3 Harris. The forty switches are connected to a common trigger bus suspended in the oil section of the cavity via forty $\sim$3 μH trigger inductors which help to isolate the switches from each other. A trigger pulse is produced from the low-side spark-gap switching of a 20 nF capacitor charged to $\sim$90 kV and fed to the trigger bus line in the cavity via four
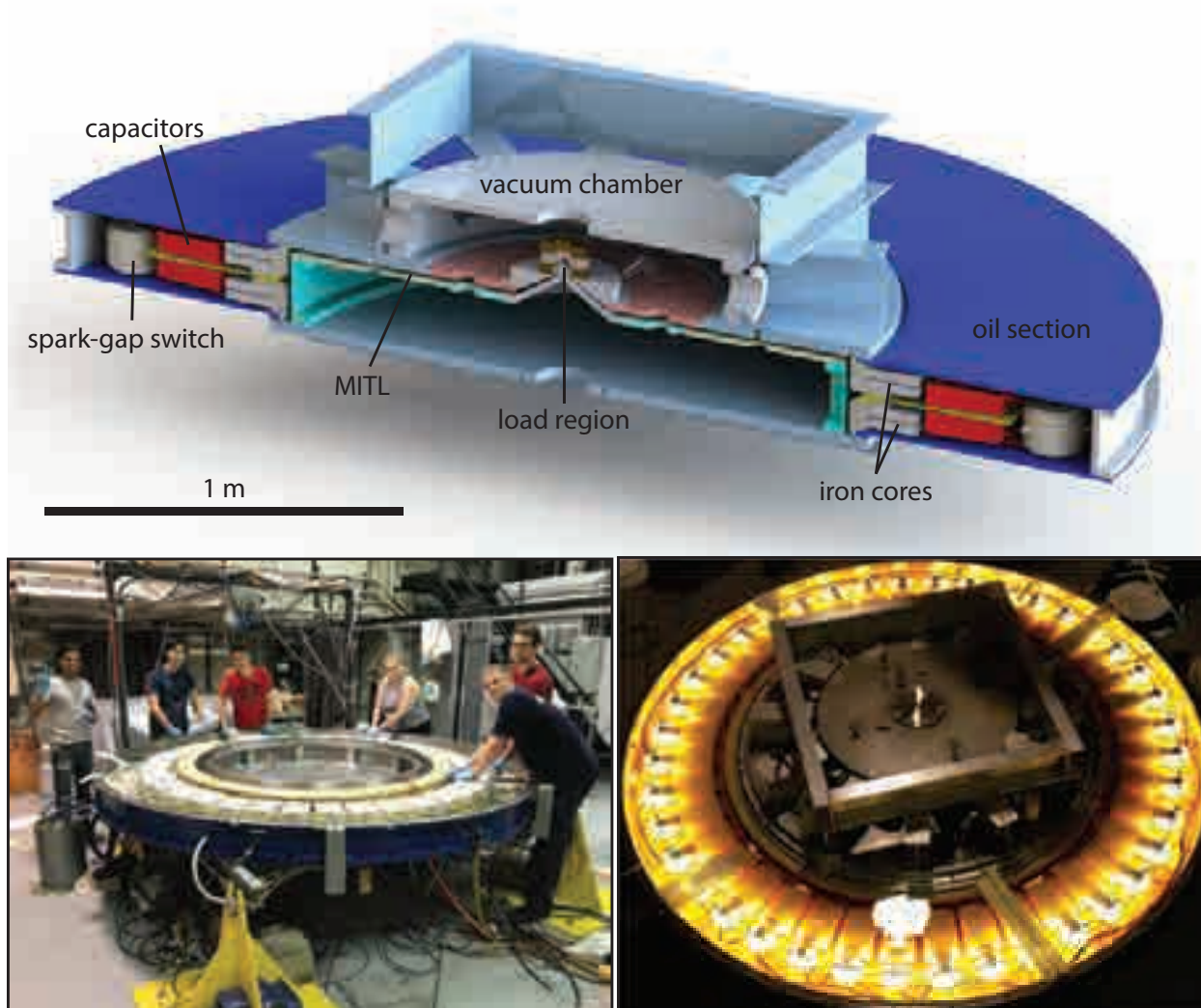
Figure 3.1: Cross-sectional rendering (top) and photographs (bottom) of the MAIZE LTD cavity. The left picture shows the cavity with experimental vacuum chamber and spark-gap switches removed, while being refurbished by students (including the author!). The right image shows a test shot of the cavity with the metal lid removed, revealing the bright flashes from the forty spark-gap switches. The flashes appear yellow because the switches are submerged in insulating transformer oil, which is transparent amber in color.

Figure 3.2: Various helical load hardware designs for MAIZE, showing the flexibility afforded by 3D-printing. Printing methods include binder-jet (steel 316/bronze alloy), DMLS (steel 316), and lost-wax casting (bronze or brass). Red parts are coated in a dielectric paint called Glyptal.

cables and feedthroughs of equidistant length. The switching of the "RPG" trigger module is via a Russian-made multi-gap switch triggered by a PT55.

Data acquisition is performed with a number of TDS oscilloscopes in a screenroom (i.e. Faraday cage) next to the MAIZE charge and control system. A Labview program reads data from the scopes after each experiment and records the data to a server for future analysis.

3.2   3D-Printing Methods for Helical Hardware

Metallic 3D-printing has emerged in recent years as a fast and inexpensive method to produce parts with complex geometry, such as AutoMag and DSP hardware. Metal 3D-printing was used heavily for the helical load hardware detailed in this thesis.

Fig. 3.2 shows a number of helical load hardware pieces used in MAIZE experiments. The dull gray parts were produced in a micro-structured steel 316/bronze alloy by the binder-jet method [71], an economical option. Light gray parts were produced in pure steel 316 by direct metal laser sintering or DMLS [72], a more expensive option with smoother surface finish. Gold-colored parts are pure brass or bronze, created by the lost-wax casting method [73], with the smoothest surface finish but weakest material options.

The parts in Fig. 3.2 deviate from the shape and thickness of a standard AutoMag liner because

28

they are designed to be re-usable and inhibit arcing. Any amount of arcing on the helical pieces, even during late time current ringing, was found to be unacceptable as it destroyed the quartz discharge tube (to be described in Section 3.4). Given the rough surface finish of 3D-printed parts, various helix coatings were tested to discourage arcing – including Glyptal, Epon, and urethane – with mixed success.

Design of the helices in simulation followed the same principle to be discussed in Section 3.10 for the "final" hardware design.

3.3 Quartz Discharge Tube and ZPI

In typical FRC experiments, the FRC is produced inside a dielectric (usually quartz) discharge tube concentric within the drive coil(s). A dielectric barrier is necessary because if the gas were in direct contact with the metal coil, drive current would be shunted. Furthermore, it is desirable to locate diagnostic probes in a small gap between the drive coil and the outer surface of the discharge tube (see Section 3.13).

In an AutoMag liner, the FRC "discharge tube" would be the dielectrically insulated inner surface of the liner. A dielectric barrier is again necessary because if the gas were in direct contact with the metal AutoMag liner, drive current would be shunted axially. Note, this is not a concern in MagLIF, because the thick solid liner isolates the gas from the drive fields via skin depth considerations. Replicating this condition in MAIZE would undoubtedly result in destructive hardware and contamination of the gas/plasma every shot, so small quartz discharge tubes were used.

An early example of a discharge tube is shown in Fig. 3.3. Quartz tubes were purchased from McMaster-Carr with 1 mm wall thickness and outer diameter ranging from 10–14 mm. Lengths of quartz tube were diamond cut and attached with Torr-Seal to 3D-printed manifolds produced with a Formlabs Form 2 SLA printer using Tough 2000 resin [74]. The manifold adapts the discharge tube to the 1/4" PTFE or polypropylene gas fill line and quartz axial viewing window.

As discussed in Chap. 1, pre-ionization of the gas is required to efficiently trap bias flux in FRC experiments. Various methods of pre-ionization exist [26] such as ringing θ-pinch, ringing multipole, and Z-discharge. Z-discharge pre-ionization (ZPI) is the most feasible to implement on MAIZE, and requires electrodes to be in contact with the gas fill at the top and bottom of the discharge tube. As shown in Figs. 3.3 and 3.4, the bottom ZPI electrode is also the bottom plug of the discharge tube, and the top ZPI electrode is a ring to allow axial visual access. The electrodes are made of aluminum for its ease of machining and low-Z. Methods for energizing the ZPI electrodes and coupling energy to the gas fill prior to field reversal on MAIZE will be discussed in Sections 3.7 and 3.9.
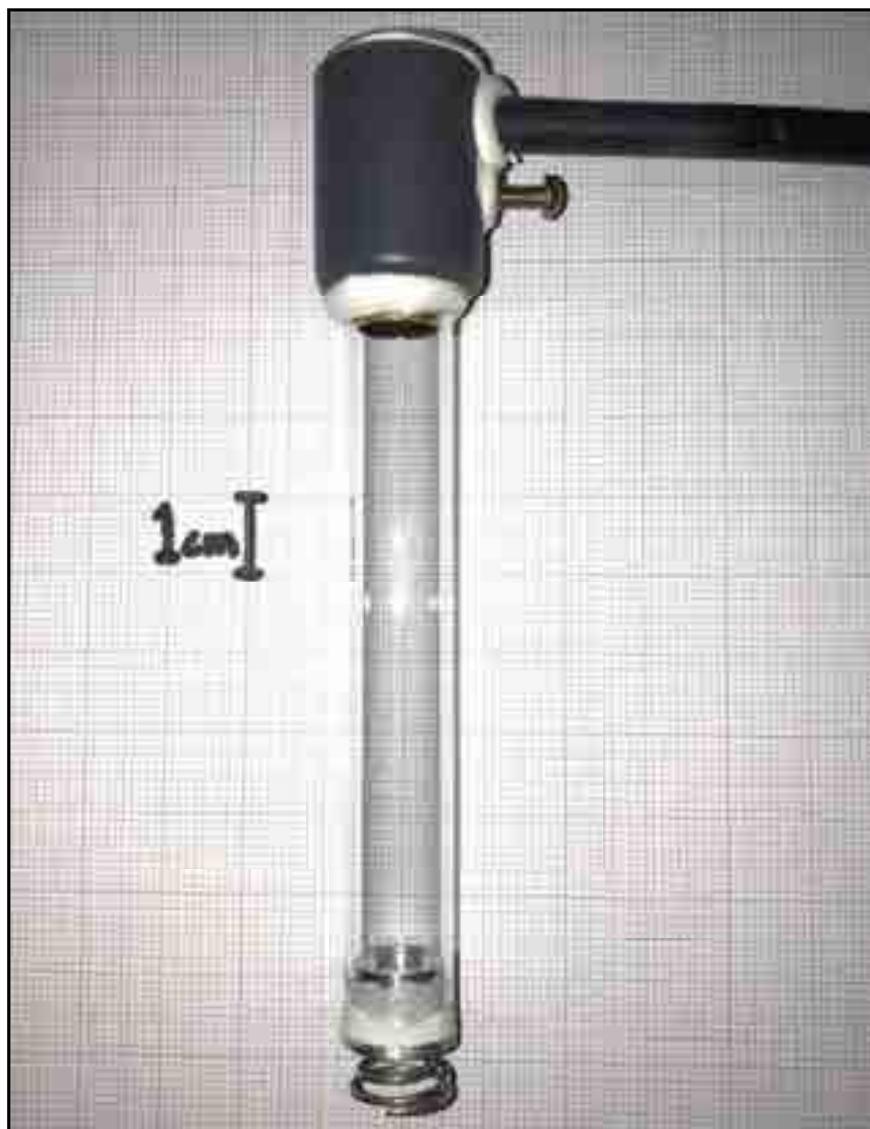
Figure 3.3: Early prototype of quartz discharge tube with PTFE fill tube and aluminum and brass ZPI electrodes. The discharge tube is inserted axially into the helical load hardware of Fig. 3.2, which is installed as part of MAIZE's final transmission line.

Figure 3.4: A later generation of discharge tube used in the "final" hardware of Section 3.10. Top ZPI ring is not visible. Hexagonal holes in the top (plastic) manifold are for SMA connectors of micro B-dots, which are not installed on this tube (see Section 3.13).
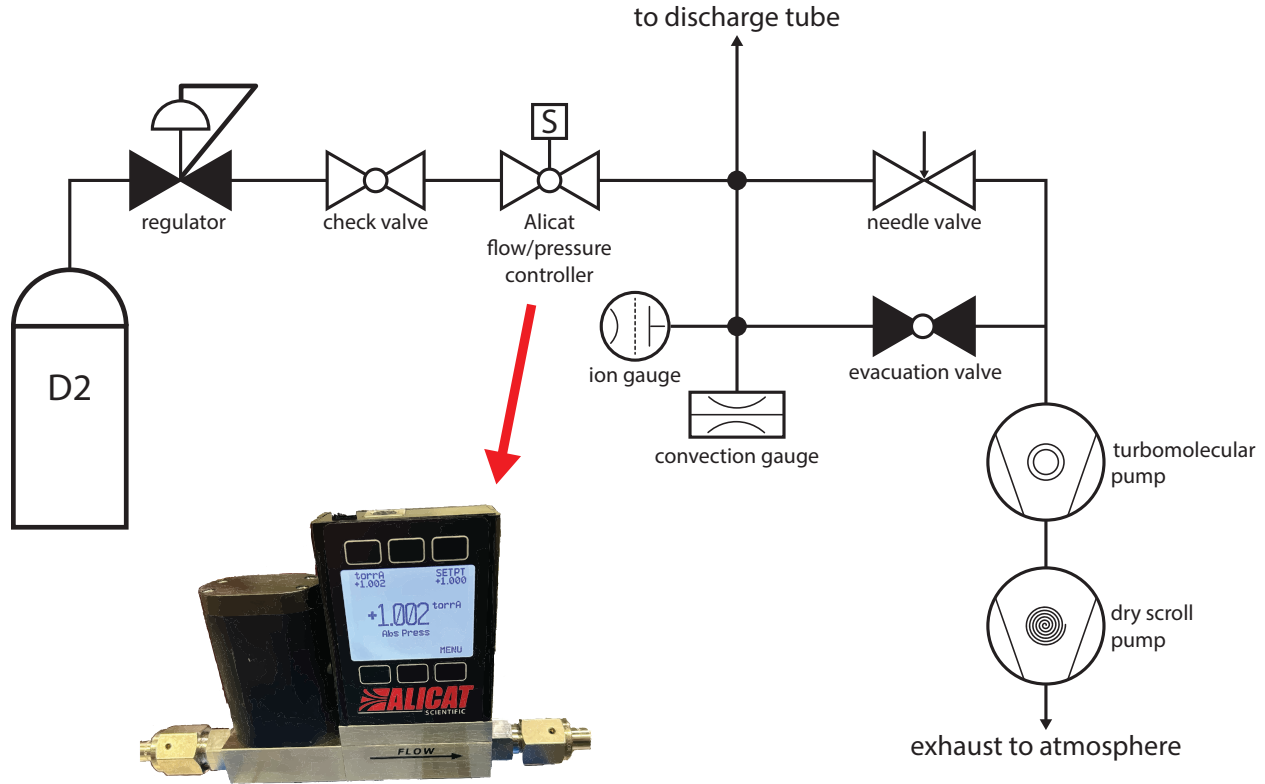
Figure 3.5: Schematic of the deuterium gas fill system for FRC discharge tubes on MAIZE, also showing an image of the Alicat pressure/flow controller.

3.4 Deuterium Fill System

Deuterium was used as the fill gas for all experiments reported in this thesis. Hydrodynamic scaling based on previous FRC experiments with deuterium [28] suggests gas fill pressures on the order of 1 Torr are desired for θ-pinch and FRC experiments on MAIZE. A gas handling system was designed to evacuate and pressurize the discharge tube assemblies discussed in Section 3.3.

A schematic of the gas fill system is presented in Fig. 3.5. Deuterium from a high-pressure bottle is regulated and supplied to an Alicat single-valve pressure controller tuned for operation at 0.1–10 Torr, measured via gas-independent pressure transducer. Low-pressure gas from the Alicat is bled to a reservoir line connected to the discharge tube and vacuum gauges. The reservoir bleeds through a needle valve to the high-vacuum frontend of a turbomolecular pump, which can also be grossly connected to the reservoir line to evacuate the discharge tube. Such a setup is required for a small amount of flow in the Alicat controller, which enables precise gas fills accurate to within ± 0.01 Torr to be stabilized in a few minutes and in some conditions even ± 0.001 Torr. The small amount of flow may also help impurities be continuously flushed out of the gas fill.

The first implementation of the fill system is shown on the left side of Fig. 3.6. A $\sim$6 m,
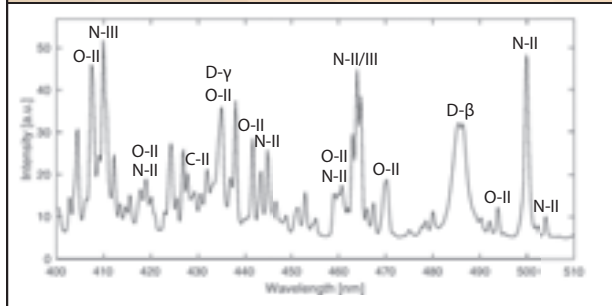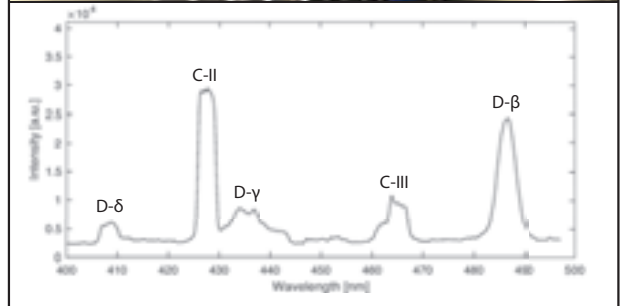
Figure 3.6: Two implementations of the deuterium gas fill system on MAIZE. An earlier implementation (left) used a long fill line and resulted in impure gas fills as evidenced in spectra taken during ZPI (bottom). The new system based on mostly QF40 ducting adjacent to the MAIZE chamber (right) produces much cleaner gas fills (bottom right). A QF40 ceramic break between the gas system and the MAIZE chamber isolates the gas system electronics from electrical noise during the LTD discharge.

3/8" OD copper pipe was used to connect the discharge tube feedthrough on the MAIZE vacuum chamber to the reservoir line at the Alicat controller near the MAIZE control room. Such a long connection was found to result in very impure plasmas, as evidenced in spectra taken during ZPI (see Sections 3.6 and 3.8). The right side of Fig. 3.6 shows the more recent implementation of the gas system, located adjacent to the MAIZE chamber and using large diameter ducting for the low-pressure reservoir. This fill system was able to achieve much higher deuterium purity levels as measured spectroscopically (Fig. 3.6 bottom). The reason for this improvement is obviously the much greater vacuum conductance of the QF40 system as compared to the long copper pipe system. Improved vacuum conductance allows a lower base vacuum pressure to be reached in the discharge tube through gross pumping, which more thoroughly de-gasses the walls of the discharge tube and vacuum system such that fewer adsorbed impurities are available to contaminate the gas fill.

The procedure for conditioning of discharge tubes for the experiments reported in this thesis is as follows: First, the entire gas system including the regulator is grossly evacuated to high-vacuum

33

($< 10^{-5}$ Torr) for at least 12 hours (sometimes several days). The tube is then filled with deuterium at 1–10 Torr and the ZPI system is discharged several times in an attempt to clean the discharge tube and ZPI electrodes of impurities. The tube is again evacuated for several hours before being filled for experiments. Every few shots, the system is grossly flushed to high-vacuum and re-filled in a bid to maintain consistent purity. It is found that when the discharge tube is isolated from the pumps and D2 fill system, the pressure rises over several minutes to no higher than 5×10^{-3} Torr, suggesting impurity levels even for the lowest D2 fill pressure of 0.5 Torr should be less than 1%.

3.5 Bias Coil Development

FRC experiments on MAIZE require the helical hardware and return current structure (i.e., the final load region of MAIZE) to be encased in a large coil that produces the bias field. The bias coils contain many turns of thick copper wire or strip and are driven by a high-capacitance, medium-voltage bank with the intent of long risetimes to the field pulse. Multiple milliseconds of risetime is usually required so that the bias field can effectively penetrate the load and surrounding machine hardware.

Initial experiments on MAIZE used bias coils made in-house, which allowed flexibility in size and field shaping. An assortment of custom made bias coils at various stages of development is shown in Fig. 3.7. Most of these coils were made by manually winding several hundred turns of enameled wire or Kapton-insulated copper strip onto resin 3D-printed frames using a lathe. The winding pack was then fitted in a 3D-printed casing and potted with flexibilized Epon 8131 epoxy, using rough vacuum to assist with epoxy penetration. Some coils featured a split Helmholtz-like design to allow radial viewing of the load helix. Some coils featured flaring of the field lines near the ends in a bid to control the reconnection region, referred to as "cusp coils".

Later experiments with larger applied fields (i.e. Section 3.10 onward) used a pair of bias coils manufactured at Sandia for the MagLIF program [75], and gifted to PPML. An image of this coil pair is shown in Fig. 3.8. Bias field strength and shape will be discussed further in Section 3.10. The bias field strengths quoted in tesla (T) throughout this thesis are the peak on-axis field at the centroid of the winding pack(s).

The bias coils on MAIZE are driven by a 1.4 mF, <5 kV capacitor bank switched by an NL7171 ignitron. It was found that to avoid destruction with homemade coils, the ignitron sometimes needed to operate at voltages <2 kV – at which it did not reliably trigger (perhaps due to age). A new floating ignitor circuit was designed and built to exceed the (contradicting) specifications of the NL7171. The circuit, shown in Fig. 3.9, is based on a N0530YN250 phase control thyristor and 1:1 cable transformer. It allows reliable operation of the aging ignitron at charge voltage as low as 500 V.

Figure 3.7: An assortment of bias coils made in-house for FRC experiments on MAIZE. Coils were made by manual winding of enameled wire or copper strip on 3D printed resin frames and potted in flexibilized Epon 8131. Peak (non-destructive) fields reached with later coils were around 3–4T.

Figure 3.8: A pair of 2" (5 cm) ID coils made at SNL for applied bias fields on the Z-machine. With the limits of the capacitor bank at PPML, the pictured coils can produce a peak on-axis field of 5–6 T depending on their spacing. These coils were used in FRC experiments on MAIZE, as shown in Fig. 3.22.
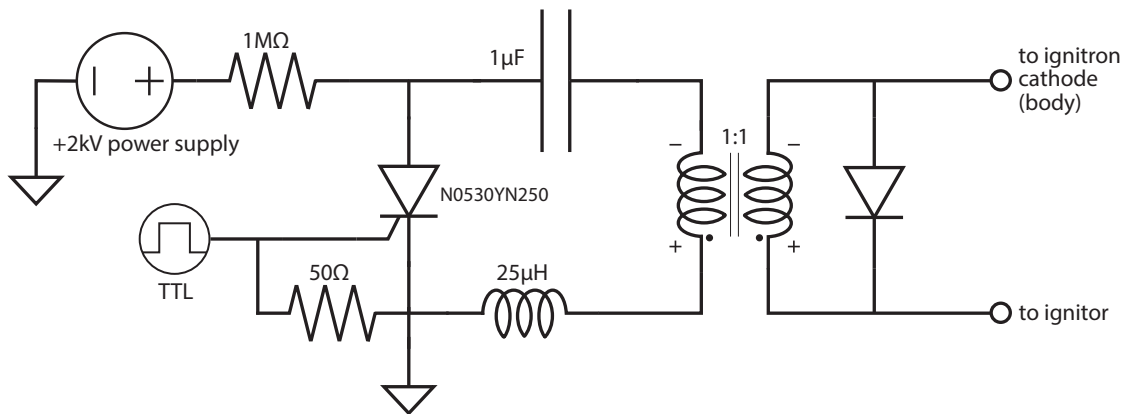
Figure 3.9: A new ignitor circuit constructed for the NL7171 ignitron that switches the bias coil capacitor bank. The large black coil is a 1:1 cable transformer which allows the ignitor circuit on the ignitron to float to >5 kV.

3.6 Imaging and Spectroscopy Setup

A primary diagnostic in MAIZE experiments was visible 12-frame imaging performed with an IVV UHSi camera with Nikon lens apparatus for zoom and focus, as shown in Fig. 3.10. Imaging was performed primarily axially, through the 1/16" quartz window on the top of the discharge tube and a 3/4" borosilicate window on top of the MAIZE vacuum chamber (not visible in Fig. 3.10, under the breadboard). Oblique axial and radial imaging was also performed, as shown in Figs. 3.11 and 3.12. Radial imaging was severely limited in most later experiments by the helical hardware or bias coils, but is also shown for demonstration purposes in Fig. 3.12.

Focusing of the camera was done by placing small fiducial inserts into the load helix where the discharge tube was to be inserted. These inserts typically consisted of 8-point font black text on white paper fastened to a plastic spacer. The spacers positioned the text at the axial center of the helix, where it was resolved in the UHSi viewport as shown in Fig. 3.11. 8-point font text has stroke thickness of approximately 200 micron, so this can be estimated as the upper size limit of resolution for the presented images. The plasma is distributed along the entire length of the discharge tube, so only the plasma at the very center of the tube is in focus with this resolution.

Another diagnostic used for MAIZE experiments was spectroscopy. Light emanating from the discharge tube was collected via bare fiber optic or collimator, and coupled via patch cable and additional collimator to the slit of a SpectraPro-750i spectrometer in the MAIZE screenroom. The CCD camera on the spectrometer allows for gating as fast as 20 ns.

Spectroscopy was used to assess purity as well as temperature of the plasma during ZPI-only discharges and full FRC shots. Most of the spectroscopy was done axially with a collimator that captured light from a similar view as the UHSi camera using a partial mirror, as shown in Fig. 3.13. Spectroscopic analysis will be discussed more in Sections 3.8 and 3.11.

3.7 ZPI Pulser Design and Construction

An independent pulser was desired for more powerful and energetic ZPI in the MAIZE FRC experiments. Furthermore, the PPML benefits from having a general purpose, easy-to-use, portable pulse module handy in the lab for probe calibrations and pre-ionization of experiments. To satisfy both of these needs, a new pulser was designed and constructed. The completed pulser and circuit are shown in Fig. 3.14.

The pulser stores ~75 J in three 80-nF, 100 kV NWL capacitors charged to 25 kV by an onboard HV supply. An atmospheric spark-gap (field-distortion) switch with UV-pin is triggered by the 28 kV, 750 ns rise output pulse of a TR-1700 trigger transformer. The trigger transformer is driven from TTL logic level using a MOSFET as shown in the circuit diagram in Fig. 3.14. The outputs of the pulser are floated such that either polarity pulse can be chosen by grounding the other. In other
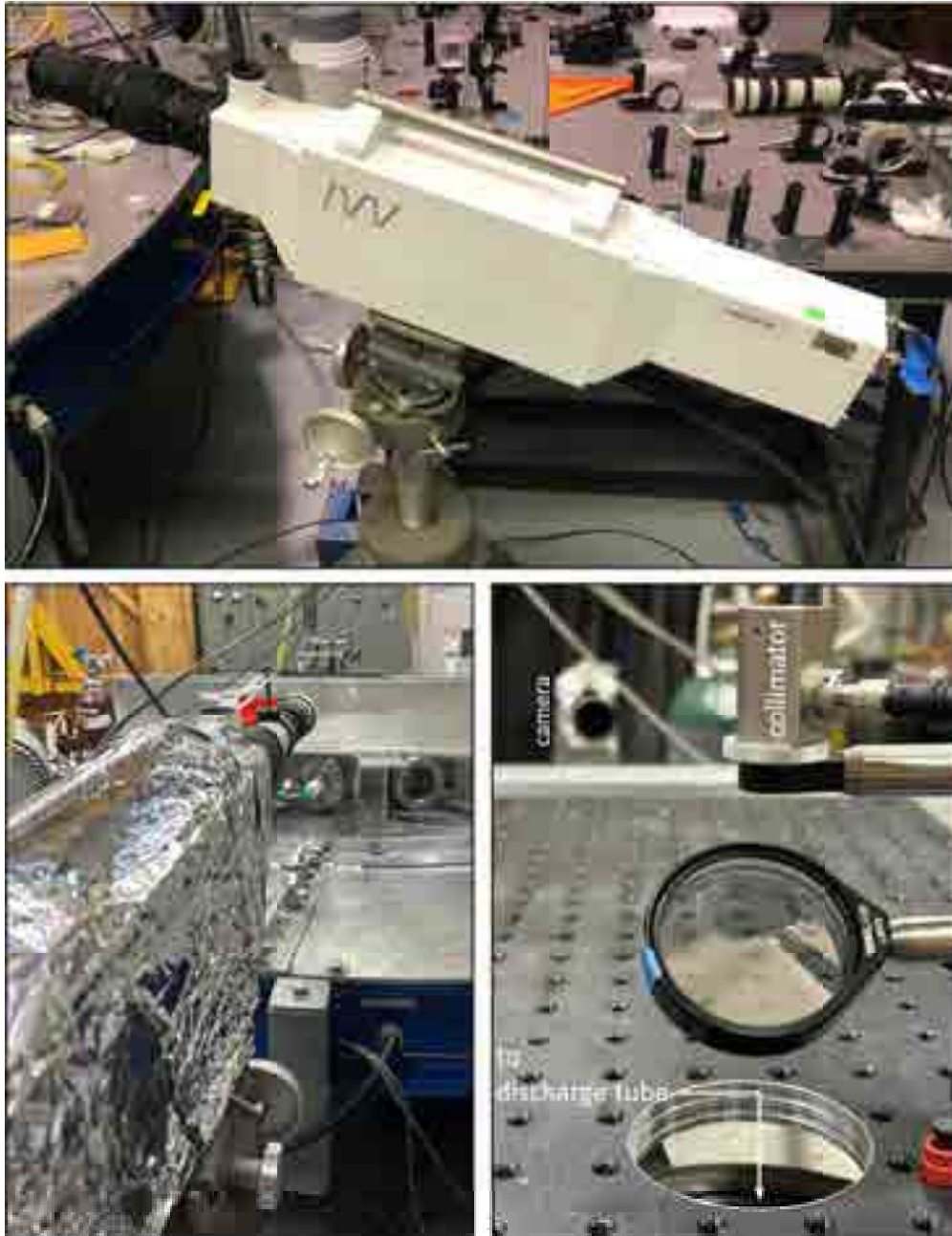
Figure 3.10: An IVV UHSi visible fast-framing camera with lens apparatus for zoom and focus was used to image plasmas in the discharge tube in MAIZE experiments. The camera is capable of taking 12 frames as fast as 5 ns exposure, 200 Mfps. Additional photographs show the camera as set up to image MAIZE experiments via a 50:50 mirror positioned above the top port chamber window. The collimator is for coupling light to a spectrometer. In the bottom photos, the camera is covered with thick aluminum foil to minimize electrical interference from nearby pulsed-power components.
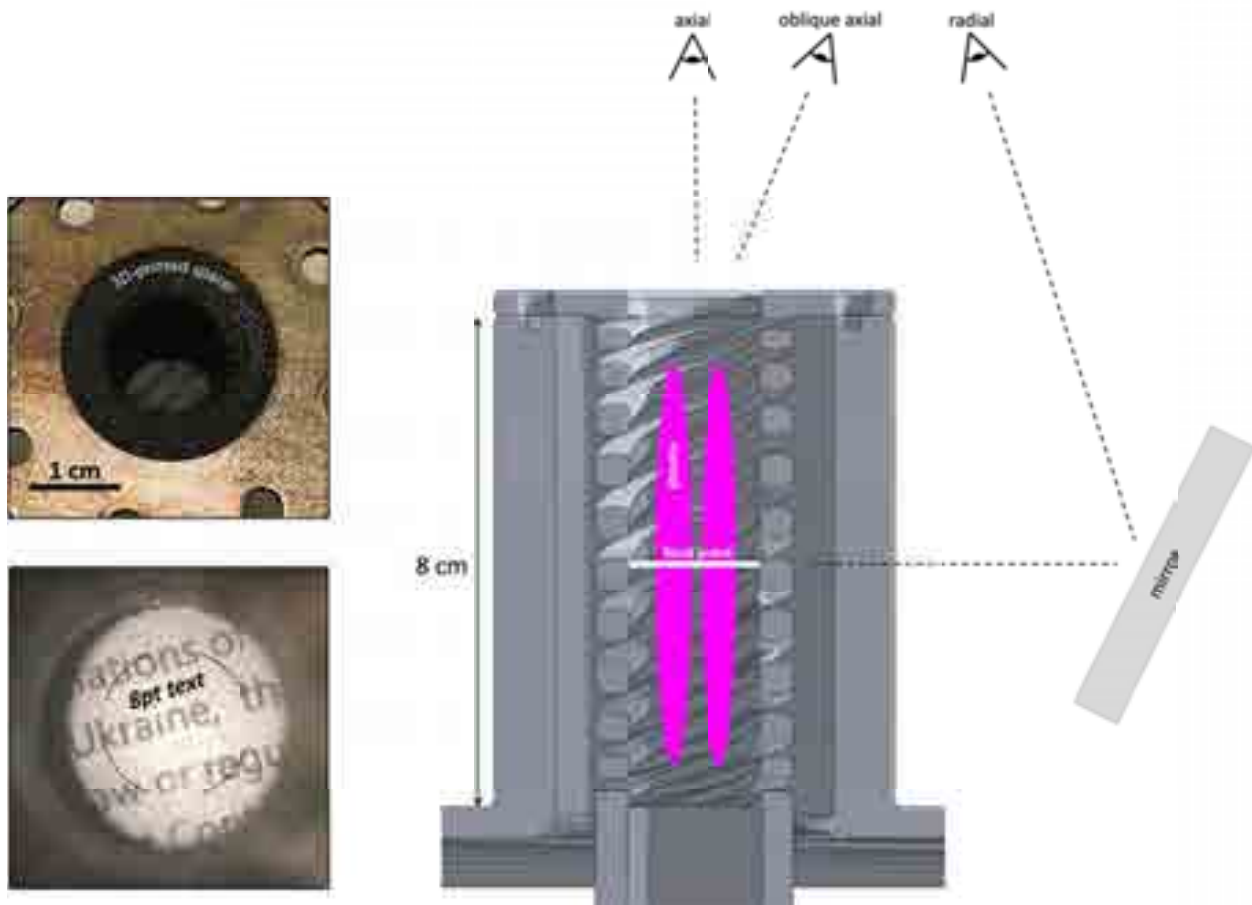
Figure 3.11: Setup for focusing UHSi camera, including image taken through the viewport of the UHSi camera for a typical axial focusing. Fiducial text is 8-point font ($\sim$200 micron stroke) on white paper positioned at the center of the helical load hardware, as illustrated on the right. The right image also depicts how radial imaging was performed in early experiments.
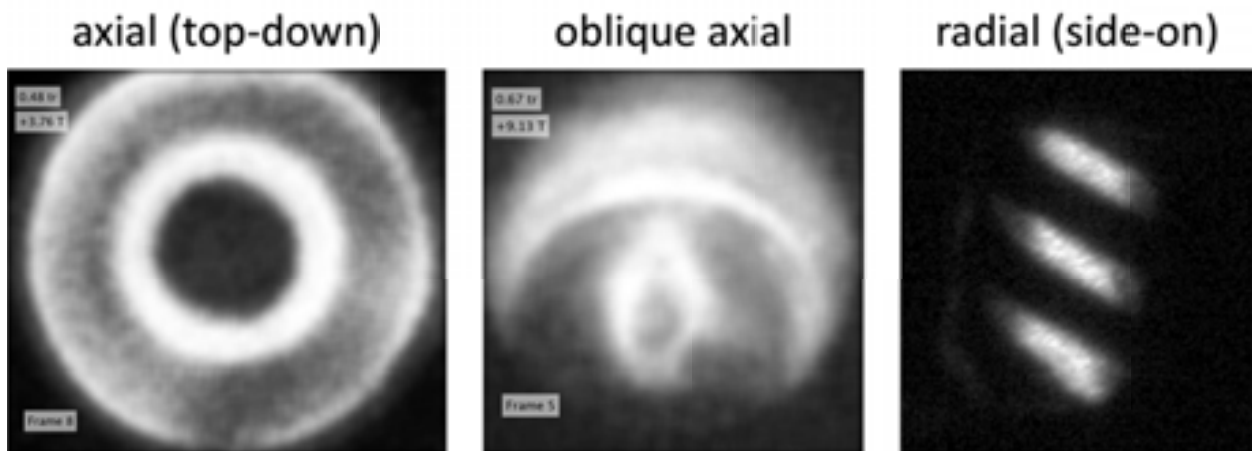
Figure 3.12: Example images taken with the UHSi axially, oblique axially, and radially. Images are a random selection across various hardware and campaigns with exposure 5–20 ns.
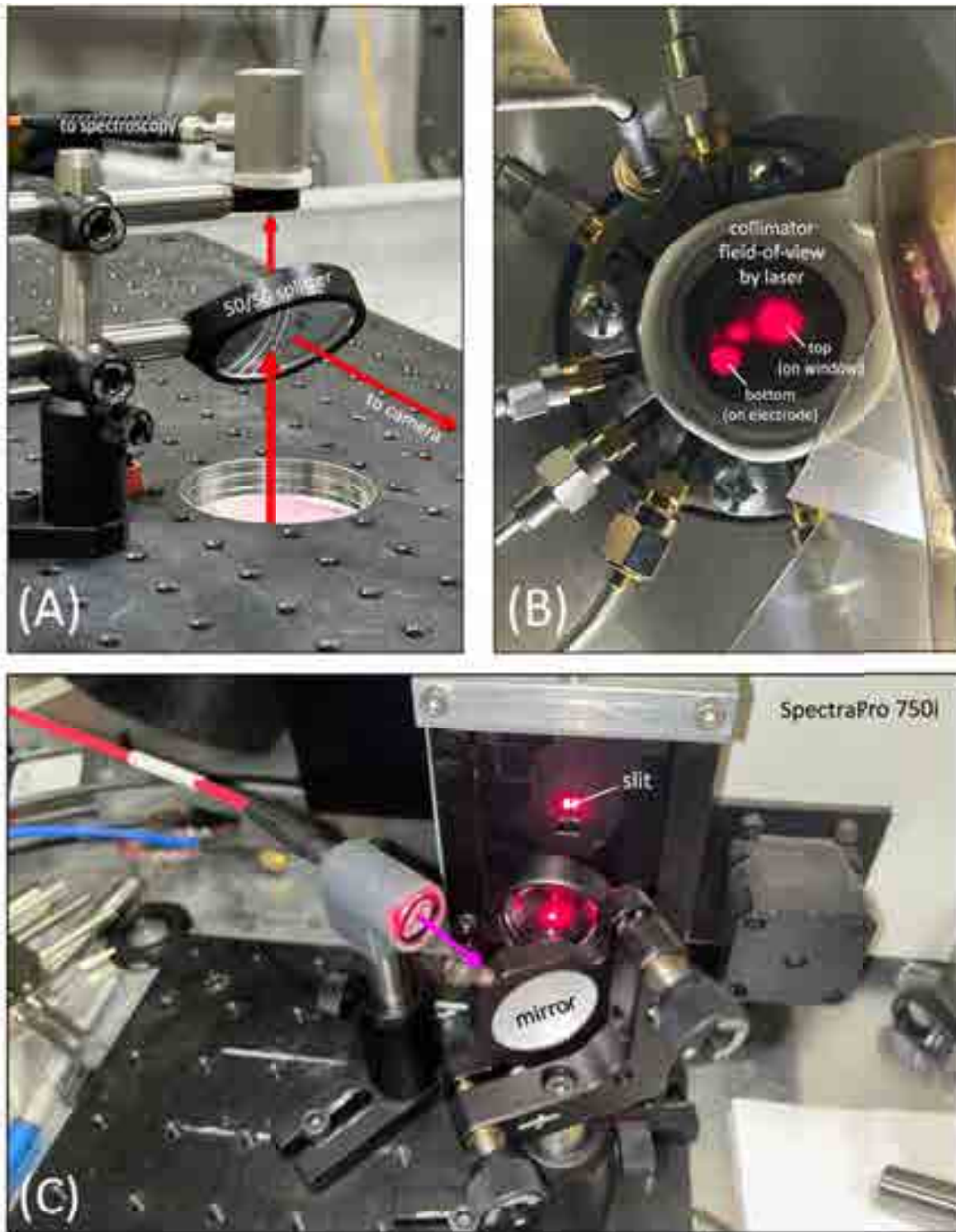
Figure 3.13: Typical axial spectroscopy setup at the MAIZE chamber (A and B) and coupling of the fiber optic to the spectrometer slit (C) in the MAIZE screen room. A 50:50 partial mirror is used so axial imaging and spectroscopy can be performed at the same time (A). Collimators are used so the spectrometer only views the central plasma column ($r < 2.5mm$), not the quartz walls or ZPI connections, as shown by the red laser spot reflecting on the top window and bottom ZPI electrode surface.
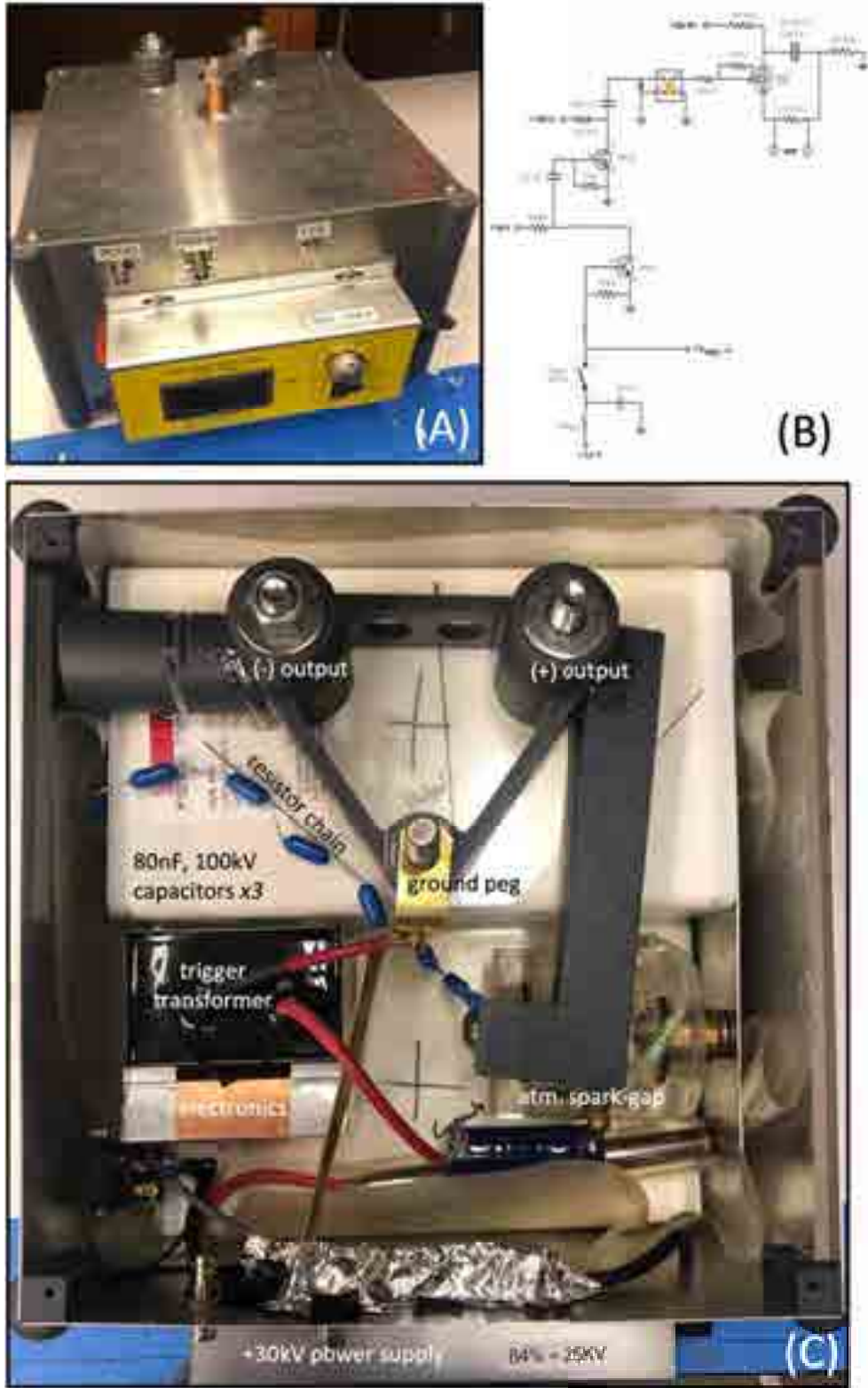
Figure 3.14: (A) The compact, portable pulser constructed and used for ZPI in MAIZE experiments. (B) Circuit diagram of the pulser. (C) The inside of the pulser with some components labeled.
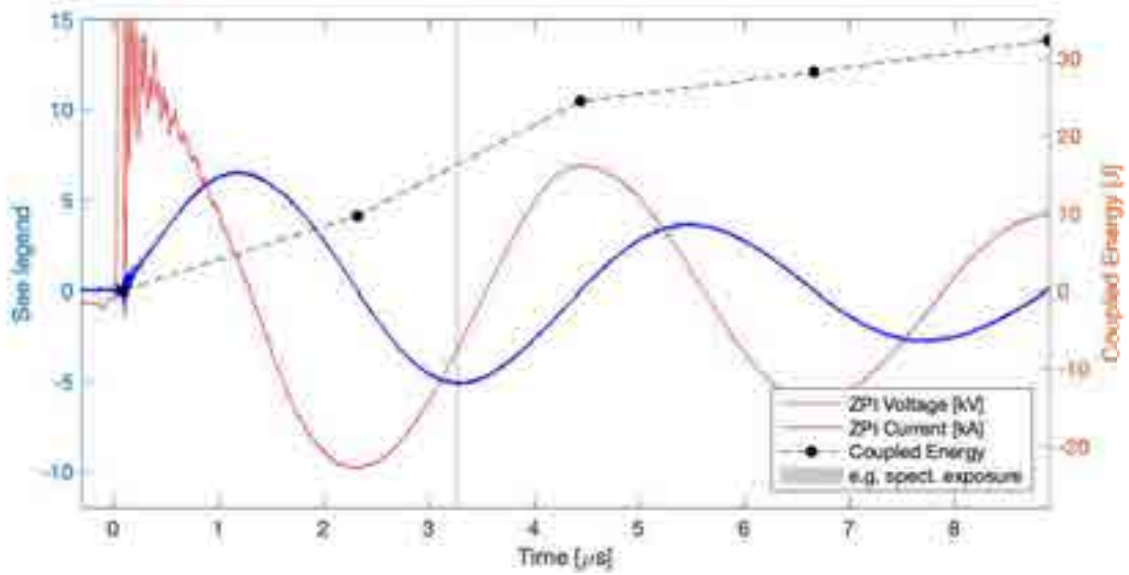
Figure 3.15: Example voltage, current, and coupled energy trace for ZPI discharge in 1 Torr deuterium fill.

words, the spark-gap can act as a low-side or high-side switch.

The resulting output pulse into a short-circuit has ~1 μs risetime to ~9 kA, and is significantly under-damped. The relatively long risetime is due to the high inductance of the switch, which was designed to be atmospheric for portability. The resultant high impedance means the ZPI circuit through the deuterium does not affect the current pulse much, as shown in Section 3.8.

3.8 ZPI Discharge Characterization

ZPI was performed in MAIZE by attaching the top and bottom ZPI electrodes of the discharge tube to the output of the ZPI pulser via HV feedthrough on the MAIZE chamber. An example voltage and current waveform measured at the feedthrough for ZPI of 1 Torr deuterium (D2) is shown in Fig. 3.15. By integrating the product of voltage and current into the discharge tube, it can be seen that several joules of energy is resistively coupled to the gas in the first full period of the discharge. Since the discharge is fairly low-impedance compared to the pulser's switch, the current trace is not significantly different across the fill pressures of interest (0.5–10 Torr) or the size of the discharge tube.

As the D2 pressure is increased, only slightly more energy is coupled to the gas, and thus significantly less energy per molecule of D2. The expected result is lower temperature at higher fill pressures, which is confirmed via spectroscopic measurements. Short-exposure (50–100 ns) spectra were taken at different times throughout many ZPI discharges at different fill pressures. During the repeated shots, all attempts were made to keep the D2 consistently pure with constant flushing

43

and tube conditioning. Spectra were compared to synthetic spectra generated by the NIST LIBS database [76] to determine plasma electron temperature, assuming an electron number density equal to the deuterium atomic density at the fill pressure (fitting is not sensitive to the number density in this range). The results of the spectral temperature analysis in the discharge tube of Fig. 3.4 are plotted in Fig. 3.16. Also shown is an example fitting for a spectrum taken at 2.0 Torr using data from the LIBS database for hydrogen. A carbon component is also detected in many spectra at disparate (higher) temperature; this is thought to be related to arcing where the ZPI connections are made in the gas/window manifold at the top of the discharge tube. This manifold is 3D-printed in a photopolymer resin, which is the likely source of the carbon. It is possible some hot carbon from arcing makes its way into the view of the collimator, but likely does not mix with the deuterium in the discharge region since it appears to have random temperature across all conditions.

As shown in Fig. 3.16, the deuterium plasma temperature oscillates with the current at low pressures, suggesting it is strongly radiating. To achieve the maximum plasma conductivity (temperature) during field-reversal, it becomes desirable to fire MAIZE during the first period of the ZPI discharge at this pressure. This is in stark contrast to ZPI in low-density FRC experiments [28], where the field-reversal occurs many dozens of periods into ZPI, when the oscillations have fully died down. This issue persists despite the much faster period of ZPI on MAIZE than in Ref. [28] It is proposed this scaling discrepancy is due to the n^3 nature of the radiative recombination rate.

The skin-depth of the ZPI plasma for the MAIZE-driven field-reversal can be estimated using the cross-field classical electron conductivity and is interestingly only dependent on ZPI electron temperature. There is only weak dependence (maximum factor of $\sqrt{2}$) on bias field if the Hall parameter is near unity, and very weak dependence on density through the Coulomb logarithm:

$$\delta_{\text{skin}} = \sqrt{\frac{2\,\eta_\perp}{f_{\text{maize}}\,\mu_0}} \tag{3.1}$$

$$\eta_\perp = 1.03 \times 10^{-4}\,Z\,\ln(\Lambda)\,T_e^{-1.5} \tag{3.2}$$

In Eqs. 3.1–3.2, δ_{skin} is the skin-depth in meters, $T = T_e \approx T_i$ is the plasma temperature in eV, and $f_{\text{maize}} = (4\,t_{\text{rise}})^{-1} \sim 1$ MHz is the frequency of the MAIZE discharge. For the hottest temperature shown in Fig. 3.16 (0.33 eV), the plasma skin-depth is 10 cm, which is much larger than the radius of the discharge tube. This apparent shortcoming for effective flux-trapping is rebutted by the fact that field-reversal will immediately begin driving current in the plasma, which quickly increases its temperature and reduces the skin-depth throughout the reversal risetime. As will be shown in the remainder of this thesis, ZPI clearly has an effect on the plasma dynamics during the MAIZE discharge.

The uniformity of the ZPI discharge plasma was characterized via UHSi imaging. Fig. 3.17
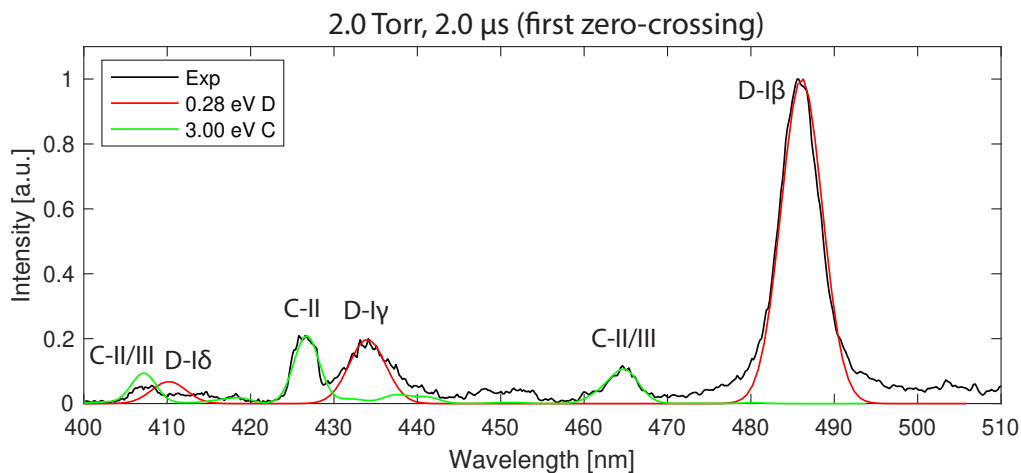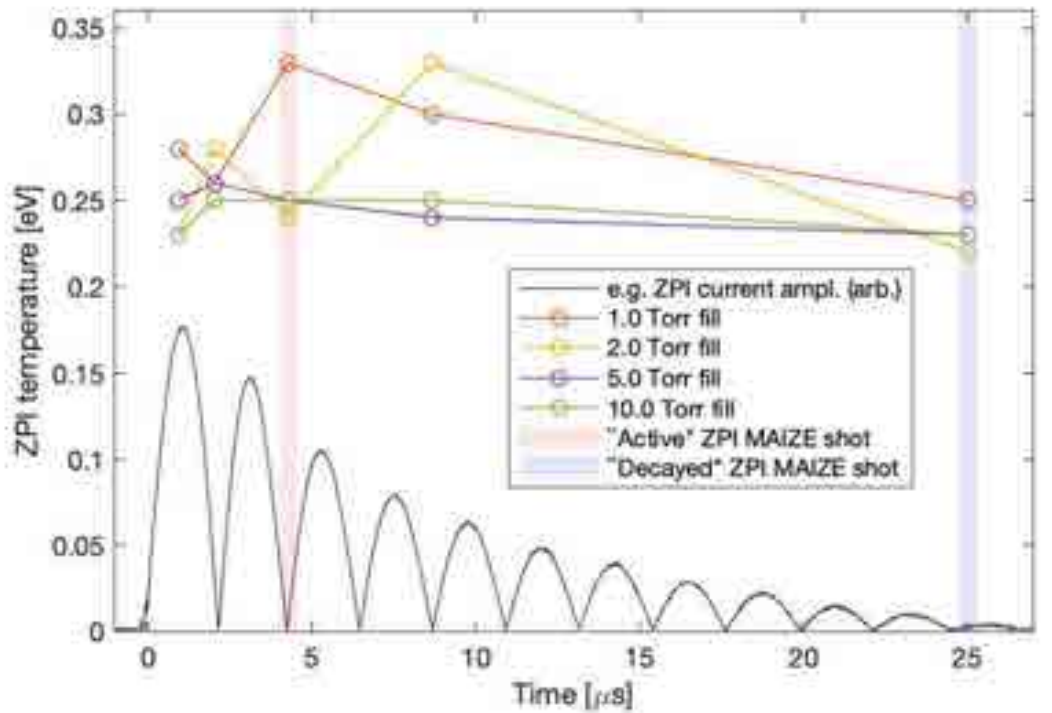
Figure 3.16: Top: Electron plasma temperature during Z-discharge pre-ionization as determined by spectral analysis for various fill pressures as a function of time. A typical ZPI current trace (of arbitrary amplitude) is also plotted for timing reference. The MAIZE discharge experiment occurs in a few hundred nanoseconds (color shaded) – very fast compared to the ZPI period. Spectra for temperature analysis were taken with 100-ns exposure, and the error in timing and temperature fit is approximately the size of the hollow markers. Bottom: An example spectra fitting with the NIST LIBS database for hydrogen. A carbon component at disparate temperature is thought to be from a separate plasma component produced by arcing of the ZPI connections in the tube manifold.

shows image sequences taken with identical exposure and frame rate for four ZPI discharges at 1, 2, 5, and 10 Torr fill pressure. As the fill pressure is increased, the ZPI plasma clearly becomes non-uniform throughout the discharge, driven by dense plasma instabilities within the ZPI current column. It should be noted that the bias field was not used for these tests; however, given the low temperature and relatively high density, the plasma is not expected to have a large Hall parameter. Thus the bias field should have negligible (if not stabilizing) effect. The worst non-uniformities seen in the high-pressure ZPI discharges of Fig. 3.17 can be taken as representative of the possible plasma state preceding integrated MAIZE shots at these D2 fill pressures.

The plasma one period into the ZPI discharge (fourth frame from left in Fig. 3.17) is seen to be fairly quiescent and bright, especially for lower pressures. The brightness of the plasma gauged from raw imaging data correlates with spectroscopic measurements of higher temperature, as presented in Fig. 3.16. This represents further justification to using the one-period, second zero-crossing of the ZPI current as the starting plasma state for field-reversal experiments around 1 Torr.

3.9 Flux-Trapping Experiments

Initial experiments on MAIZE sought to characterize the flux-trapping behavior of the gas fill with and without ZPI. Effective flux-trapping of the bias field is a pre-requisite for FRC formation and usually requires the gas to be sufficiently conductive (i.e. "pre-ionized") before the start of the field-reversal process. Behavior of the axial field at the centroid of the load/helix/discharge tube was probed intrusively with "micro B-dot" probes, as depicted in Fig. 3.18.

The micro B-dots for flux-trapping experiments were produced out of .020–.047" OD copper rigid coax by stripping the end and curling the inner conductor around the insulator to be soldered to the outer conductor, as shown in Fig. 3.18. The B-dots were then coated in a Glyptal, Epon, heat-shrink insulating layer to minimize their electrical disturbance on the ZPI. It is expected that the B-dots are quite perturbative. B-dot data during a MAIZE shot is not taken as meaningful after plasma first impacts the B-dot tip (as determined by fast-framing images and characteristic transients on the signal) and FRCs are not expected to form.

The described B-dot design is very similar if not identical to that used in many experiments on the 100 ns COBRA machine at Cornell [77] [78] and even the Z-machine [79] [80], so frequency response is not expected to be an issue. To confirm this assumption, a few MAIZE B-dots' S_{11} response was tested on a freshly calibrated HP spectrum analyzer from 50 MHz to 40 GHz. The response plot was indistinguishable from that of a short-circuit calibration load, indicating the maximum frequency response of the B-dot is limited by the 50-Ω coaxial connections (i.e. several GHz) and not the the probe tip. Furthermore, the resonant frequency of the B-dot tip in Hz can be estimated as:
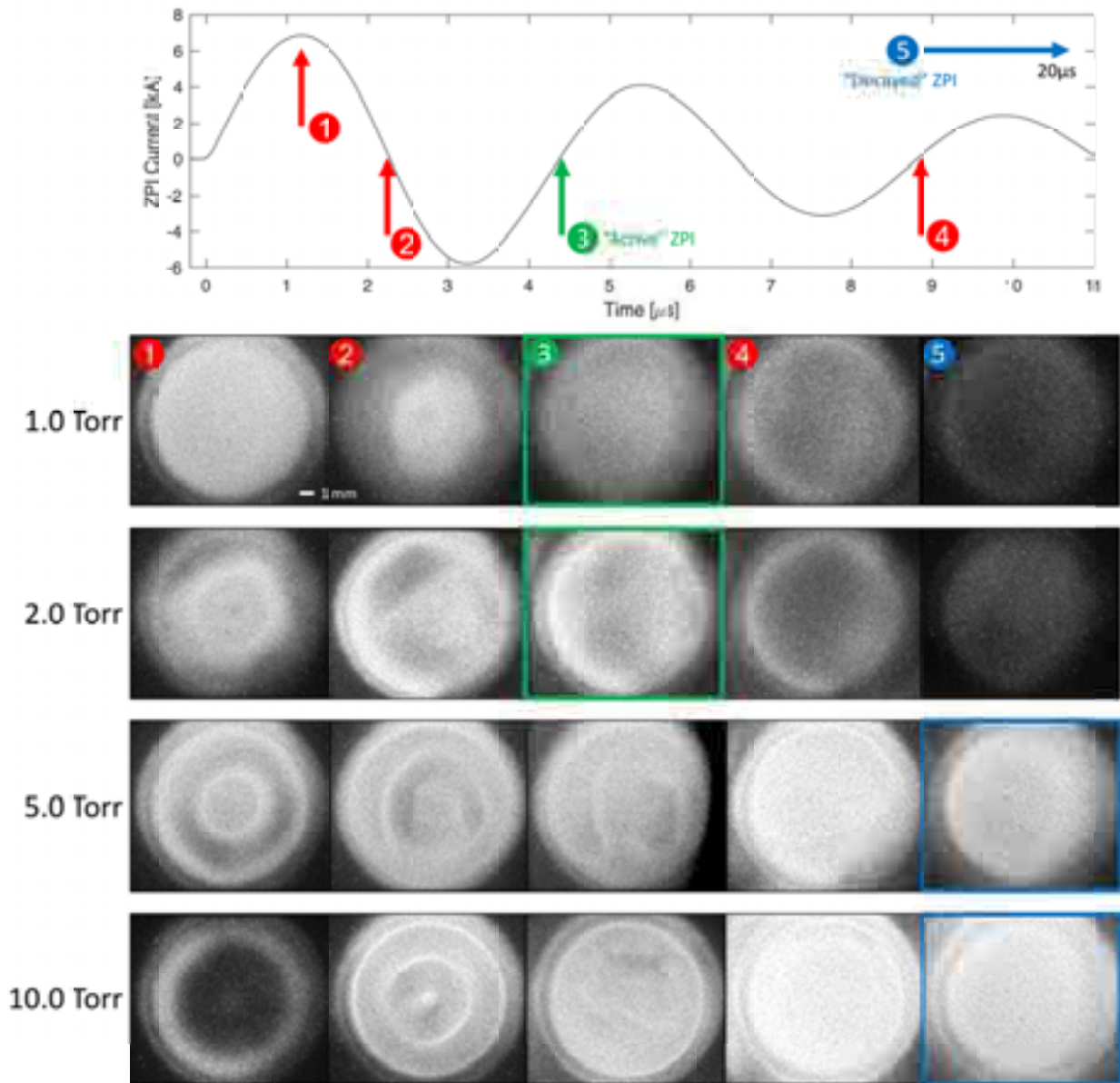
Figure 3.17: UHSi image sequences with 50 ns exposure at 1 Mfps showing evolution of the ZPI discharge plasma at four different D2 fill pressures. Arrows show the timing of each image column, sequentially. The last column was taken at $t = 20\mu$s, which is much later than the other frames when current oscillations have nearly died out. The green arrow indicates the second zero-crossing, one period into the discharge, where MAIZE was typically fired. To show relative brightness, images have not been contrast enhanced or otherwise edited. Pinch-like non-uniformities in the plasma can be seen to worsen at higher pressures. Plasma at higher pressures seems to persist for longer.

.020 -.047"

dB$_z$/dt

.020"   .034"   .047"

1 cm
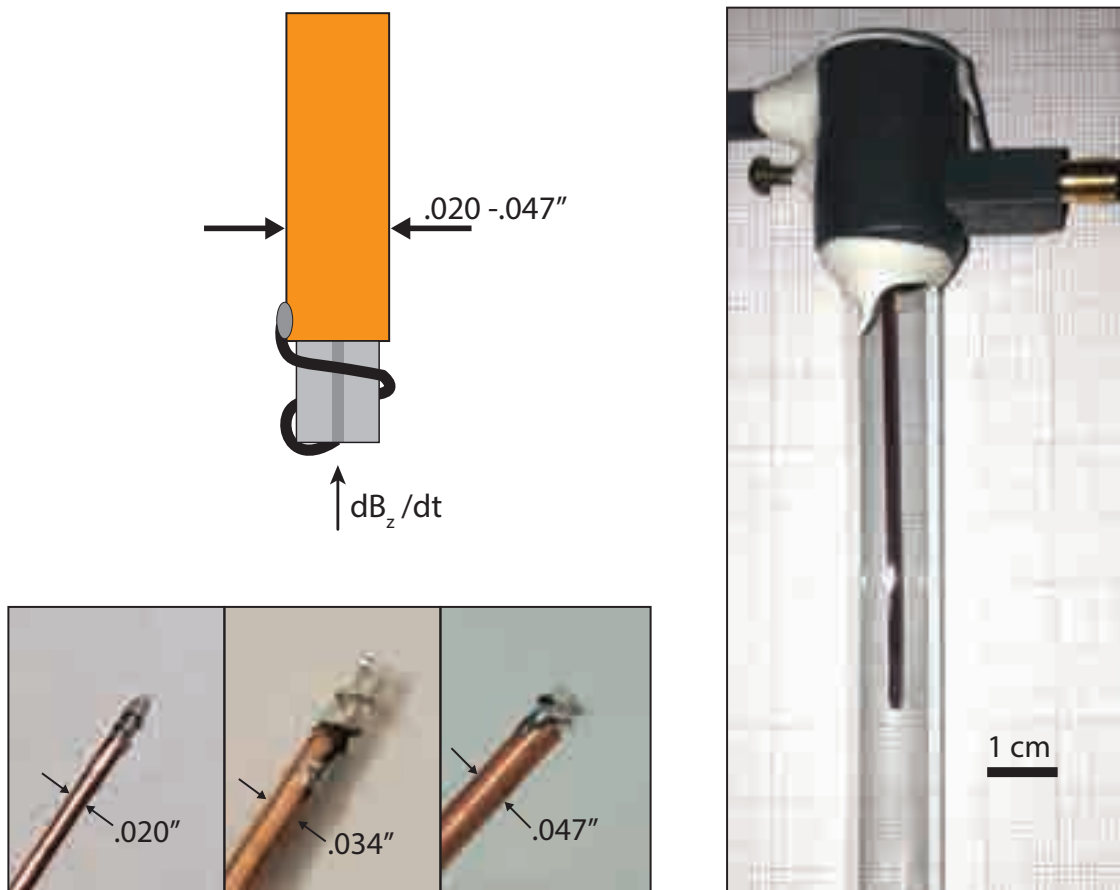
Figure 3.18: Small B-dot (flux loop) probes were created for flux-trapping experiments. Point-like B-dots were produced by stripping .020–.047" rigid coax and curling the center conductor around a small section of insulator before soldering it to the outer conductor. A B-dot coated in Glyptal dielectric is shown on the right installed in the center of a discharge tube with ZPI electrodes (not visible).

$$\omega_{\text{r,tip}} \ [\text{Hz}] = \frac{1}{2\pi\sqrt{L_{\text{tip}}C_{\text{tip}}}} \tag{3.3}$$

where the inductance of the tip can be estimated as a small number N of solenoidal loops [81]:

$$L_{\text{tip}} = \mu_0 \, N^2 \, \frac{\tilde{D}}{2} \left(\ln \frac{8\tilde{D}}{d} - 2 \right) \tag{3.4}$$

and the upper-limit of the capacitance estimated by that of a coaxial section representing the tip:

$$C_{\text{tip}} = \frac{2\pi\epsilon_0}{\ln \frac{D}{d}} \, l \tag{3.5}$$

In these equations, $\tilde{D} \sim 0.5$ mm is the average diameter of the conductor looping around the insulator, $d \sim 0.1$ mm is the diameter of the inner conductor, $l \sim 1$ mm is the length of the tip, and $D \sim 0.4$ mm is the diameter of the insulator. With this formula, the resonant frequency for .020" B-dot tips with $N \sim 2$ is estimated as $\sim$15-GHz, which is much larger than the cutoff frequency of the connecting cables or any signals measured in MAIZE experiments. The resonant frequency scales only as the inverse square root of B-dot diameter and length, so the largest B-dots (e.g. .047" coax) should still have low attenuation at the GHz level (a small fraction of their resonant frequency).

The B-dots were calibrated for axial field using a calibration coil built to fit to the ZPI pulser, as shown in Fig. 3.19. The axial field of the coil per kA of pulser current is determined from CST simulation, also shown in Fig. 3.19. The axial field measured in MAIZE experiments by the B-dots with this calibration constant is consistent with that expected from CST simulation of field produced by the helix per kA of MAIZE current as measured by Rogowski coil. This can be seen by the agreement between black and green curves in the vacuum shot of Fig. 3.20.

B-dot flux-trapping results from three experiments are shown in Fig. 3.20. In the top of Fig. 3.20, an image in MAIZE's open chamber shows the discharge tube with B-dot probe and bias coils installed around the helical load. In the bottom of Fig. 3.20, traces are presented for three shots on MAIZE. The black traces show an axial field proportional to the MAIZE current pulses of the three experiments as measured by Rogowski coil, which are all similar. The currents have an amplitude of several hundred kiloamps to produce a vacuum axial field of several tesla at the B-dot location (as calculated by CST simulation). No arcing or current losses upstream of the Rogowski coil are detected on these shots that would indicate MAIZE current not traveling through the load helices.

The colored traces show integrated and calibrated signals from the center B-dot probe, which is (primarily) sensitive to axial field. The green trace is a vacuum shot with no plasma detected by the UHSi camera, such that the green trace should closely follow a black trace. The blue trace shows
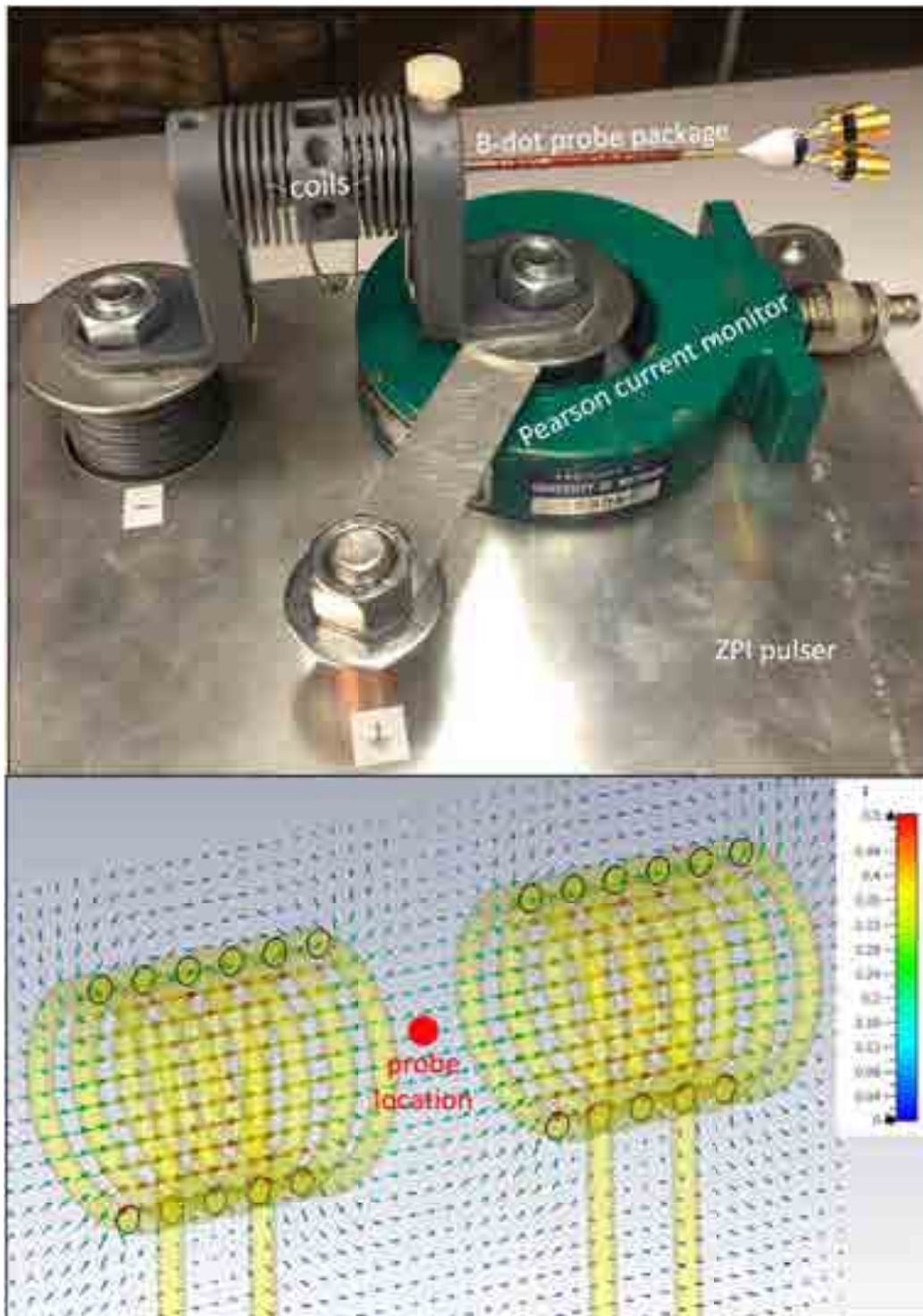
Figure 3.19: B-dot calibration coil designed to mount on the ZPI pulser in image and simulation. The coil material is resistive nichrome to dampen the pulse. B-dots can be pinned at the position of known axial field production in any orientation with plastic set screws.

the B-dot signal with 0.5 Torr of deuterium in the tube *without* ZPI pulse applied, while the red trace represents 0.5 Torr *with* ZPI applied. For the case with ZPI, MAIZE was fired approximately one period into the ZPI pulse, near the second zero crossing of the ZPI current. The delay seen in the B-dot signals with gas is interpreted as plasma (diamagnetic) shielding of the applied axial field, which becomes much more effective with ZPI (red trace). The sudden signal changes after the delays is interpreted as a strong electromagnetic response due to plasma impact on the thinly-insulated B-dot, as confirmed by fast-framing images.

Fig. 3.21 shows the center B-dot signal behavior when a bias field is added with ZPI. When the MAIZE current starts to rise, the B-dot signal at first shows an increase from the initial bias (negative) field value, interpreted as bias flux loss due to incomplete plasma breakdown. During this time, the pre-ionized plasma is seen pinned to the inner quartz wall by the out-flowing bias flux, as shown in the insets of Fig. 3.21. When the plasma ring is imaged as lifting off the wall, the B-dot signal's time derivative ($\frac{dB}{dt}$) changes sign. This *increase* in magnitude of the negative field at the center is interpreted as compression of the bias field, which is known to occur during FRC formation and axial contraction. When the imploding plasma ring nears the B-dot on axis, the signal $\frac{dB}{dt}$ again changes sign and the value quickly swings positive, interpreted as strong electromagnetic response from plasma impact and loss of plasma shielding effects. Note that, despite the application of a bias field and ZPI, an FRC is not expected to form in these experiments because the B-dot is so perturbative. However, the apparent bias flux conservation and even compression behavior before plasma impact is encouraging as enabling to FRC formation when the B-dot is not present.

Finally, it should be noted that the data to be presented after this section was taken with different hardware than that shown in Figs. 3.18 and 3.20, and with improvements to MAIZE current reliability.

3.10   Final Hardware Design

The final hardware design for data reported in the remainder of this thesis is shown in Fig. 3.22. The bias coils used are the Sandia made coils of Fig. 3.8, capable of peak bias fields exceeding 5 T. The 12 mm ID, 14 mm OD quartz discharge tube with aluminum ZPI electrodes is most visible in the cross-sectional rendering of Fig. 3.22. The ID of the load helix is 16.5 mm, giving some space between the quartz and the helix metal for B-dot probes and to discourage arcing/shock transfer.

The load helix was designed for survivability using intuition gained over many MAIZE experimental campaigns with various helical hardware, and by rapid iterative use of CST to optimize the vacuum fields produced by a MAIZE-frequency discharge through the helix and return current structure. The quadruple helix (four-fold azimuthal symmetry) has varying helical pitch to flatten the axial field profile as much as practically possible, as shown in Fig. 3.23. The flattening of the
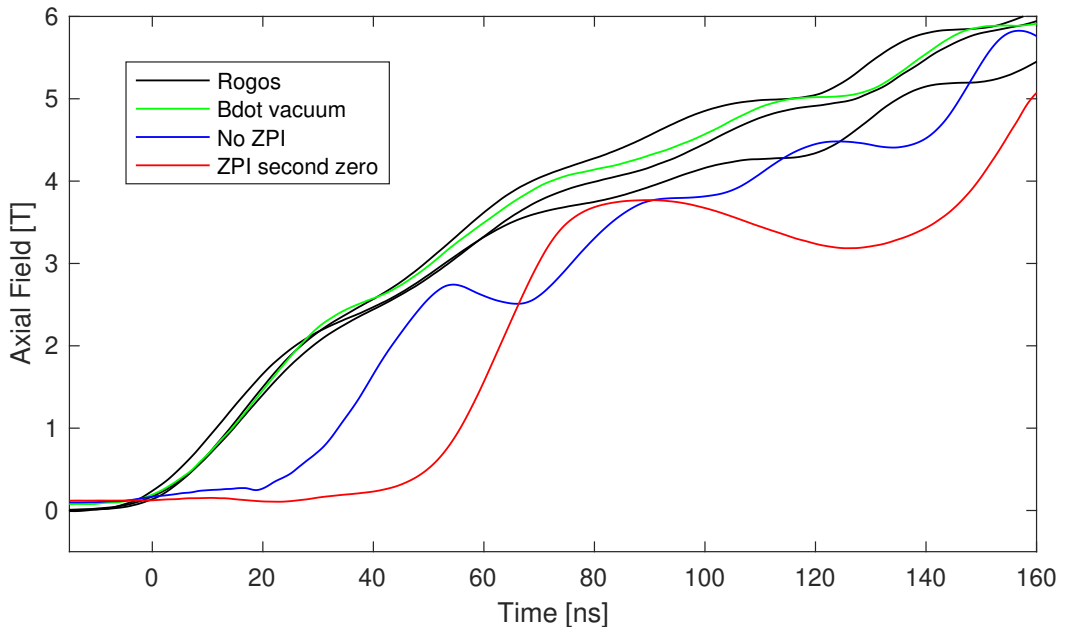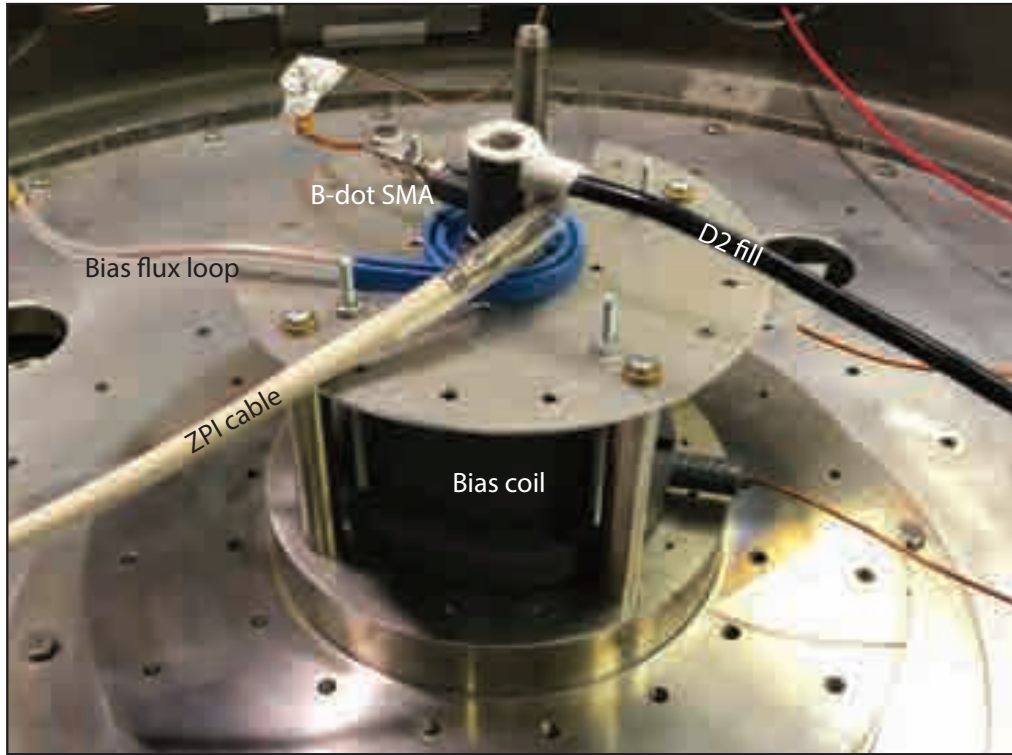
Figure 3.20: Top: installed hardware for early flux-trapping experiments on MAIZE. Bottom: Integrated and calibrated B-dot and MAIZE current signals showing the effect of ZPI on plasma shielding of the applied axial field with (red) and without (blue) ZPI at 0.5 Torr D2 fill. Also shown is a vacuum shot (green), where the B-dot signal should agree with the Rogowski signal.
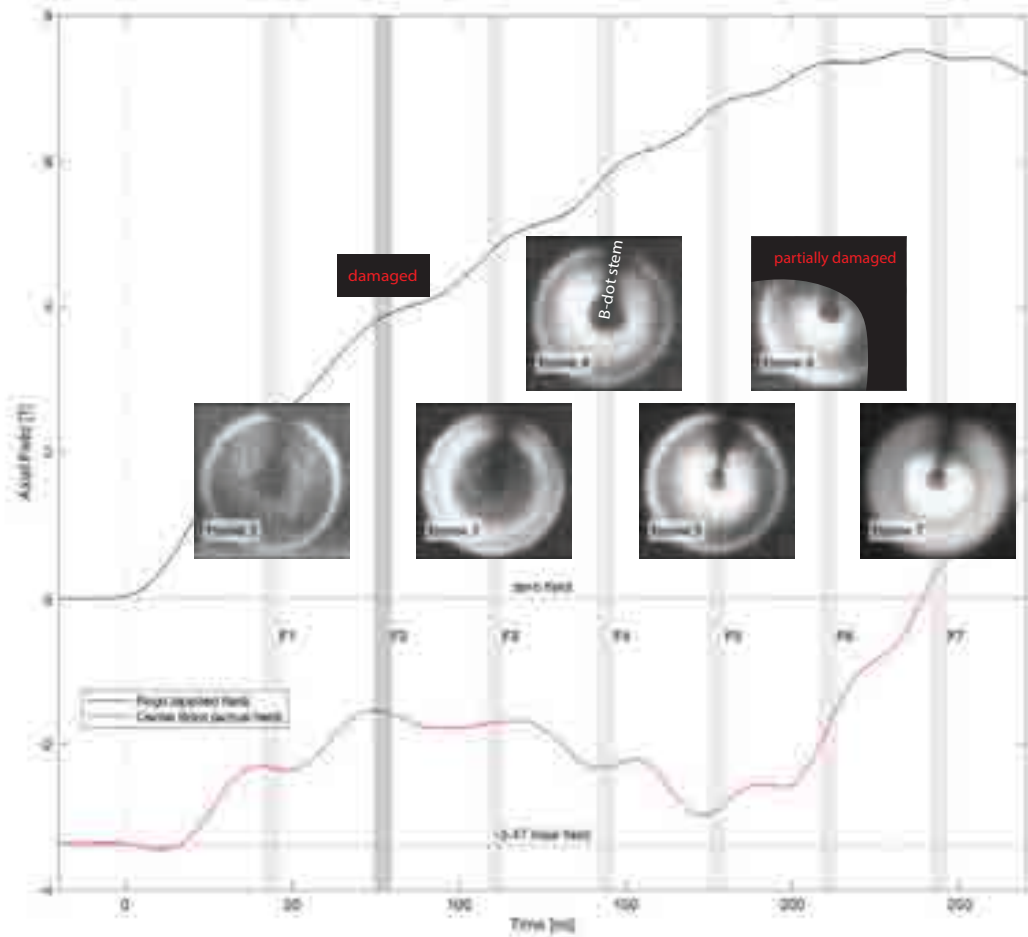
Figure 3.21: Integrated and calibrated B-dot signal for axial field at the center of the discharge tube for a flux-trapping experiment with 3.4 T bias field at the B-dot location. A negative field value and negative $\frac{dB}{dt}$ correlated with the plasma ring implosion is interpreted as bias flux compression before plasma impact with the B-dot stem. Gray shading indicates the frame exposures; frames #2 and #6 of the UHSi's CCD were damaged during this shot campaign. Insets show contrast-enhanced and filtered images.
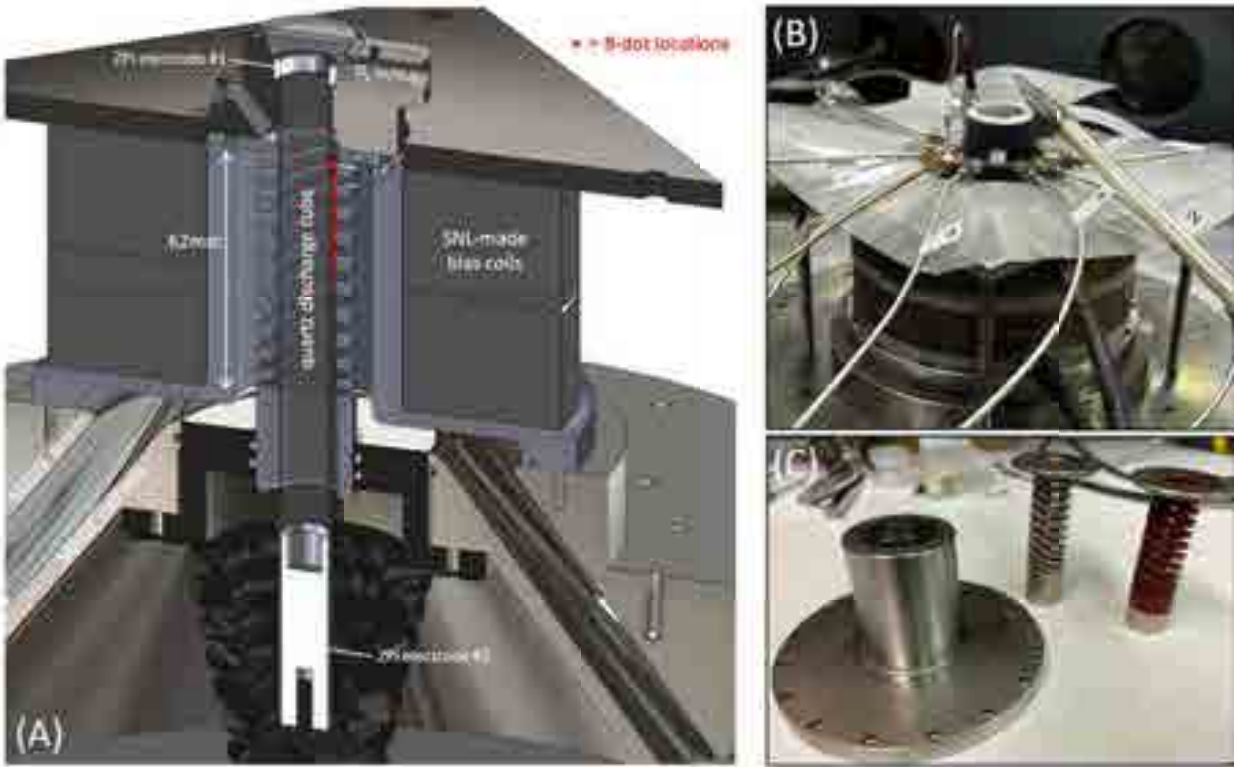
Figure 3.22: "Final" MAIZE FRC hardware used for most of the experiments presented herein, shown in CAD cross-section (A) and photographs while installed in MAIZE with B-dots (B) and disassembled (C). The axial positions of excluded flux B-dots are marked with red dots in the CAD image (see Section 3.13).

field profile is limited by inductance considerations and the minimum thickness/spacing of the helices near the ends. The radial thickness of each helix is 4.25 mm for durability and the spacing between helices is approximately 1.3–2.3 mm, depending on the local pitch. Note, an AutoMag liner would have thickness and helix spacing of only a few hundred microns (at least for the imploding region); however, MAIZE experiments were designed for discharge tube survivability rather than replication of AutoMag geometry – prioritizing shot rate and data acquisition.

The actual helical load inserts of Fig. 3.22 simulated in Fig. 3.23 were 3D-printed using the binder-jet method in Steel 316i alloy (60% steel 316, 40% bronze), and ceramic bead-blasted for polishing. The external dimensional accuracy of the part is within 0.5 mm axially and 0.2 mm radially. Two parts were ordered and one coated in a thick layer of dielectric Glyptal paint to test arc prevention at higher MAIZE charge voltages. Interestingly, in contrast to earlier experiments, it was found that the non-coated helix tended to preserve the discharge tube at larger MAIZE charge voltages.

Fig. 3.24 shows several panels illustrating the *vacuum* field-reversal process in the final load hardware of Figs. 3.22 and 3.23. The initial bias field from the Sandia made coils has peak on-axis
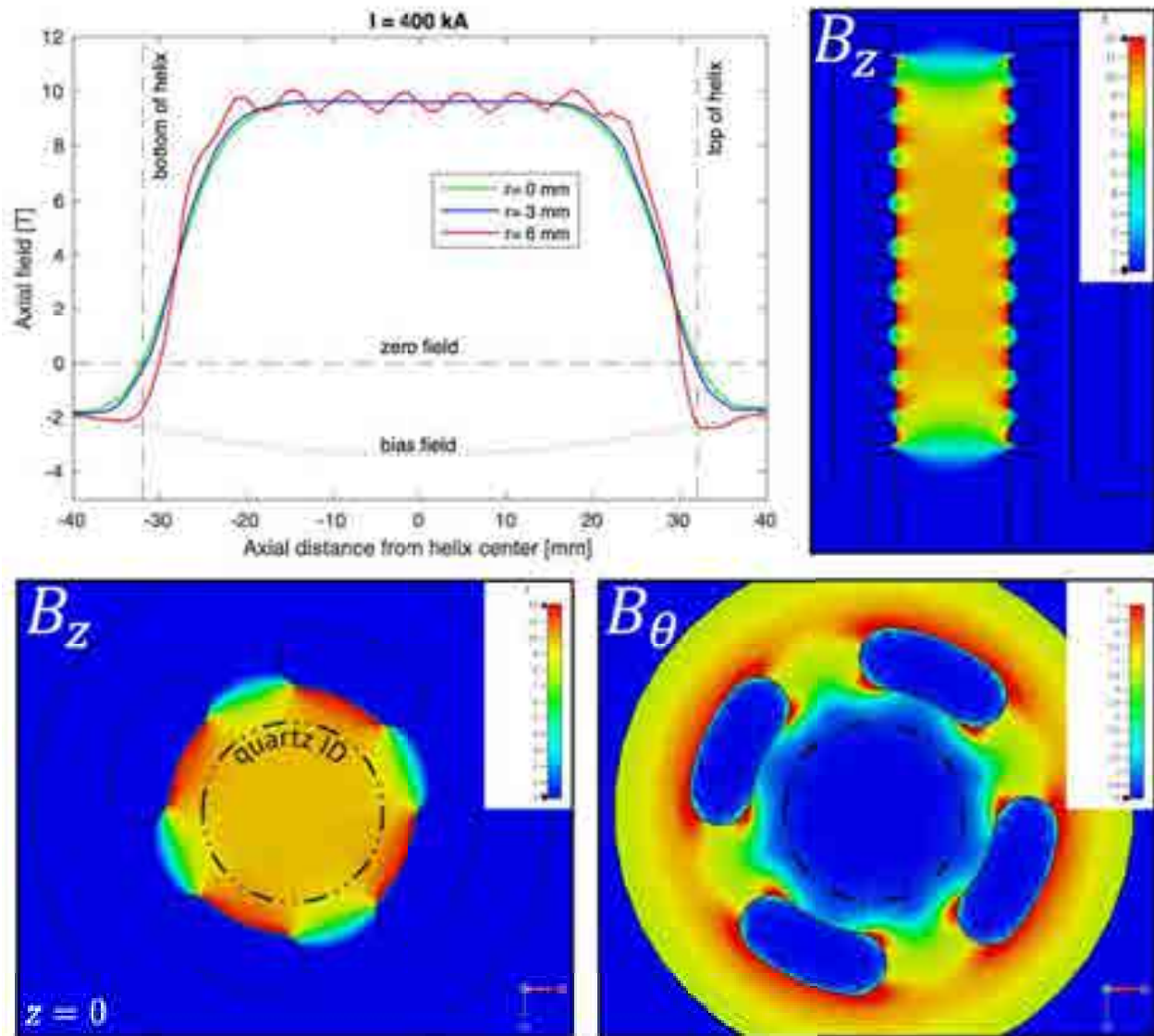
Figure 3.23: Results of CST simulations showing the magnetic field produced by the load helix of Fig. 3.22. The field becomes three-dimensionally non-uniform near the inner surface of the helix, with a finite azimuthal field component, which could have implications for FRC experiments.

strength -3.4 T. The reversal field rises to peak on-axis strength of approximately $+13$ T (400 kA load current) in 250 ns, resulting in a final reversed field strength of $+9.6$ T. Note that Fig. 3.24 is for elucidation purposes only – with plasma present, the reversal process would look much different as plasma eddy currents are generated to trap flux.

The inductance of the load hardware above the MAIZE conical feed in Fig. 3.22 is approximately 25-nH according to CST, which is quite high for MAIZE (0.1Ω). While reducing peak power and current and increasing the risetime of MAIZE's output, the high inductance load is found to have the beneficial effect of causing self-crowbar (i.e. plasma shunting) in the MAIZE transmission line shortly after peak current. Crowbar of the current in the load helix is actually desirable to prevent the machine from pulling flux out of the discharge tube while the FRC decays, and in fact is used in nearly all pulsed-power FRC experiments [82] [26].

The accuracy of the simulated field from the Sandia-made bias coils was compared to measurements taken with a LakeShore Gaussmeter probe (Hall sensor) within the fully installed bias and helical hardware of MAIZE, as shown in the image of Fig. 3.25. The bias coils capacitor bank was discharged many times while the probe was scanned through the height of the region where the discharge tube would be installed. The results show excellent fit to the simulation, as shown in Fig. 3.25. The slight reduction in measured field at large negative and positive z values is likely due to some persistent eddy currents in the large mass of steel hardware beneath the load helix, despite the 2 millisecond risetime of the field.

3.11   Imaging Results and Discussion

Since physical probes could be used minimally in the discharge tube region (see Section 3.13), optical self-emission was found to be the most useful diagnostic for experiments on MAIZE. This included visible imaging by the UHSi camera and spectroscopy, as described in Section 3.6. Visible imaging was used to track the plasma dynamics, while spectroscopy was useful to estimate the plasma temperature and purity, as discussed in Section 3.8. All imaging to be discussed in this section was performed axially or obliquely axial, due to the blocking of radial access by the bias coils in the final hardware design of Section 3.10.

Many sequences of axial images from the UHSi camera are presented in Fig. 3.26. All sequences presented in this figure used an exposure time of 10 ns at constant frame rate and have been contrast-enhanced and filtered to improve visibility of the central plasma dynamics. The five sequences present characteristic dynamics for five types of shots on MAIZE, representing θ-pinch and FRC shots (i.e. shots without bias field and with bias field, respectively) with varying levels of ZPI (see labels in Fig. 3.26). Comparison of the sequences reveals the expected dynamics for the two types of shots, as well as characteristic instabilities. For instance, the second sequence (a θ-pinch)
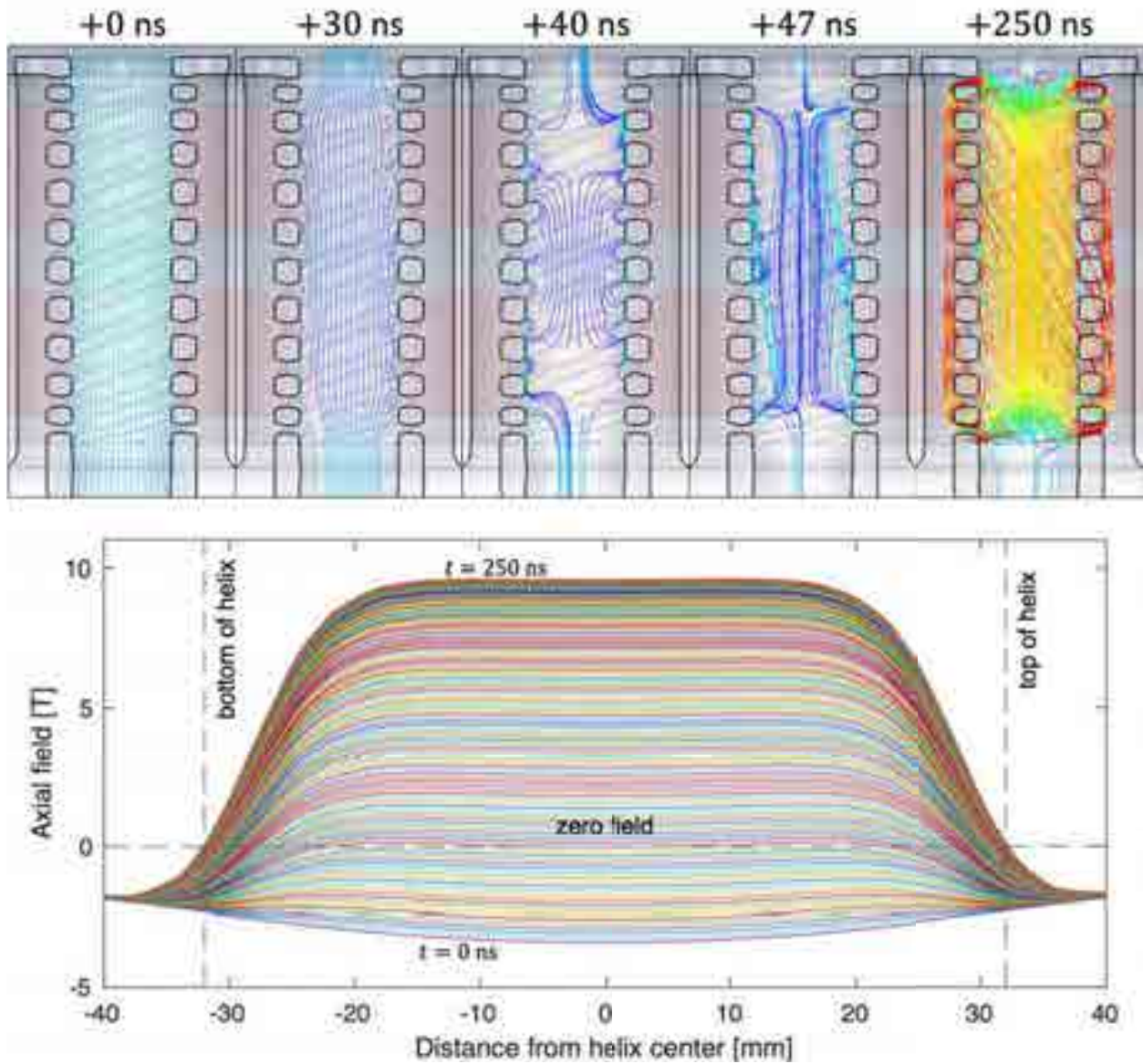
Figure 3.24: Top: Simulation frames sequential in time showing the evolution of field lines around the helix during field reversal *with no plasma present*. Peak on-axis bias field is −3.4 T; fast-field raises peak on-axis field to 9.6 T (400 kA load current) in 250 ns.
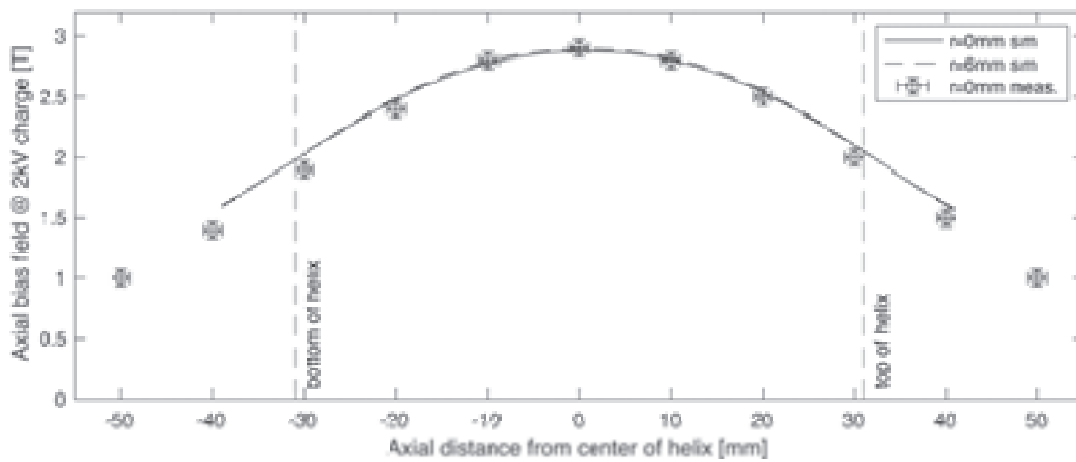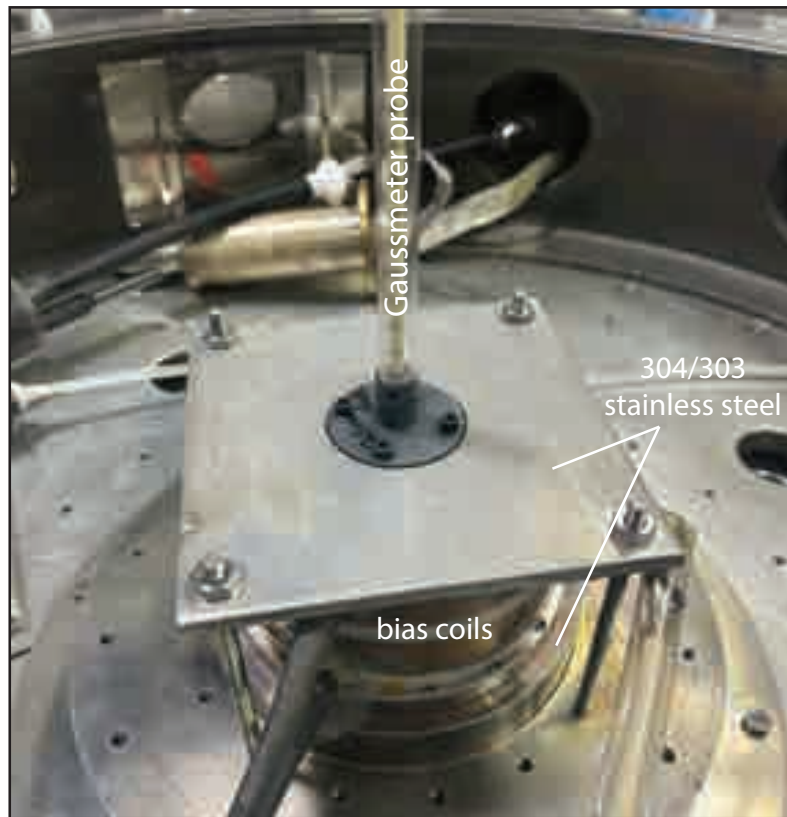
Figure 3.25: Simulated bias field shape was confirmed via gaussmeter measurements. Slight deviation is likely due to partial eddy currents in steel hardware above and below the bias coils, which is necessary to secure them.
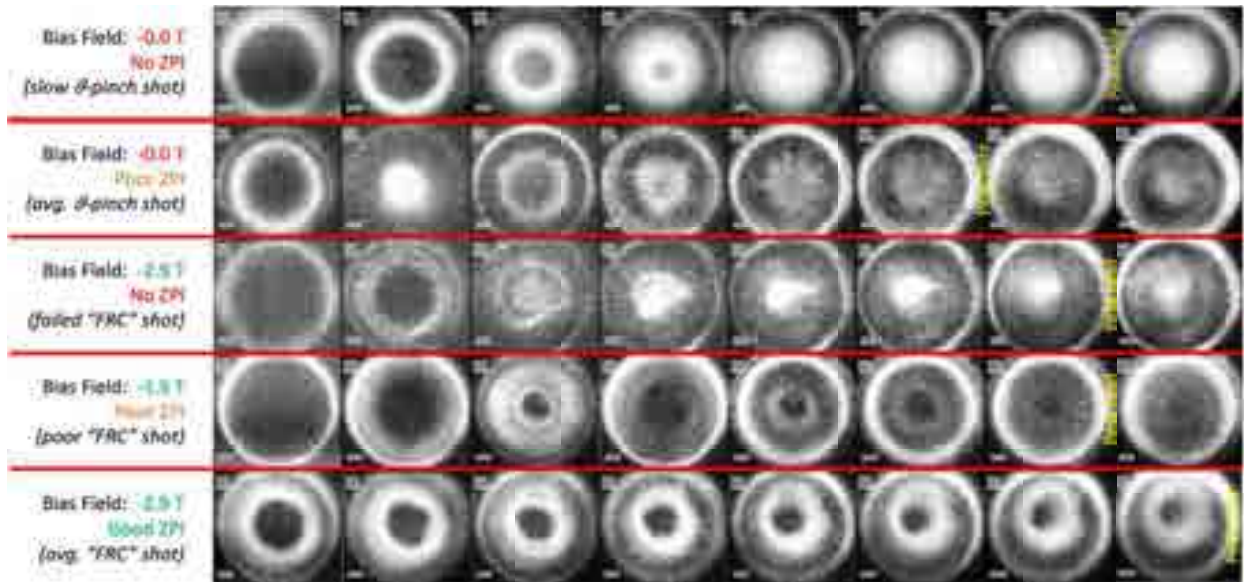
Figure 3.26: Image sequences from the UHSi camera with 10 ns exposures at 25–50 Mfps constant frame rate showing the characteristic behavior observed in different MAIZE experiments. Expected θ-pinch and FRC dynamics are seen in the images, as explained in the text. Images are independently contrast enhanced and filtered to bring out central plasma dynamics. The approximate position of the peak of the MAIZE current pulse is labelled in yellow in the sequences. Future image sequences include more detailed timing information; this figure serves to demonstrate the overall plasma dynamics.

stagnates quickly on axis, bounces, and then seems to show a high azimuthal mode number (n) fluting structure develop – an expected instability for fast θ-pinches [83]. The first sequence (also a θ-pinch) does not show the fluting instability since the plasma experiences much slower acceleration and stagnation. The fifth sequence (an FRC shot) shows a persistent ring of plasma, which then gradually moves off-axis in the northern direction of the frames. Such dynamics might be interpreted as the $n = 1$ "wobble" mode in FRCs, where the entire FRC moves off-axis. Since all "wobble" FRC shots seemed to move in the northerly direction, it could be an asymmetry in the drive field that was causing the plasma displacement from the axis.

Fig. 3.27 illustrates the criticality of ZPI for good flux trapping. Three image sequences with identical bias field (-2.9 T) and fill pressure (1 Torr) but different levels of pre-ionization are shown. The frames of each sequence have identical frame rate and similar timing relative to the current pulse of MAIZE. The first sequence has no ZPI: the ZPI pulser was not powered on for the shot. The second sequence has decayed ZPI: MAIZE was triggered 20 μs after the start of the current pulse, when the ZPI oscillations have fully decayed (see Section 3.8). The third sequence has active ZPI: MAIZE was fired exactly one period into the ZPI pulser discharge, when the ZPI current is crossing zero, and the plasma is found to be hot and relatively uniform (at this fill pressure). Active ZPI, which is better in this pressure case, results in a brighter (hotter) and larger (more trapped flux)

59
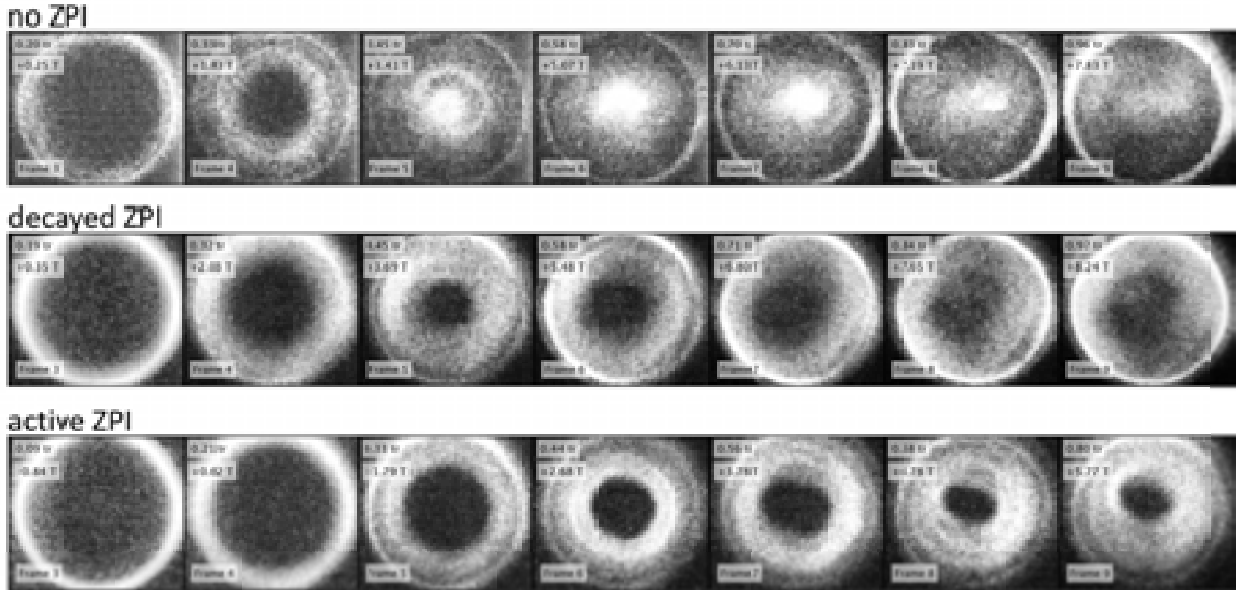
Figure 3.27: Partial image sequences from the UHSi camera with 5 ns exposures at 25 Mfps showing the effects of ZPI on FRC shots with identical mid-plane bias field (–2.9 T) and D2 fill pressure (1 Torr). Decayed ZPI is defined as firing the shot many microseconds after the ZPI current oscillations have died down, when the plasma is cooler. For active ZPI, the shot is fired one period into the ZPI pulse, when ZPI current is near zero but PI plasma is seen to be hot and somewhat uniform at this pressure. Upper-left insets in each frame show the time relative to MAIZE current peak (normalized by current risetime t_r) and the applied external field at the mid-plane B_0 as inferred by the measured MAIZE current. Images are independently contrast enhanced and filtered to bring out central plasma dynamics.

plasma ring – consistent with expectations for FRC formation.

To illustrate the effects of density on the plasma dynamics, Fig. 3.28 shows four sequences of FRC shots with active ZPI and initial D2 fill pressure at 1, 2, 5, and 10 Torr. Increasing the initial gas fill pressure is an easy way to increase the mass swept up into the FRC during formation and thus increase the final density and s-parameter. However, formation is known to become more difficult as density is increased for two reasons: (1) pre-ionization non-uniformities are generally worse at higher fill pressure (see Section 3.8) and (2) decreased viscosity and increased inertia means more violence to the formation event, amplifying any initial perturbations and disrupting the plasma before it can relax from compression. Both of these effects can be seen in Fig. 3.28, where the plasma columns/annuli do not form cleanly at the higher fill pressures.

Optimization of FRC formation and lifetime on any given machine is usually a strongly empirical process requiring many hundreds of shots turning many dozens of knobs. Since MAIZE experiments were limited to a dozen or so shots per discharge tube before quartz cracking or window blackening, such detailed optimization is not feasible. Nevertheless, an example of empirical improvement can
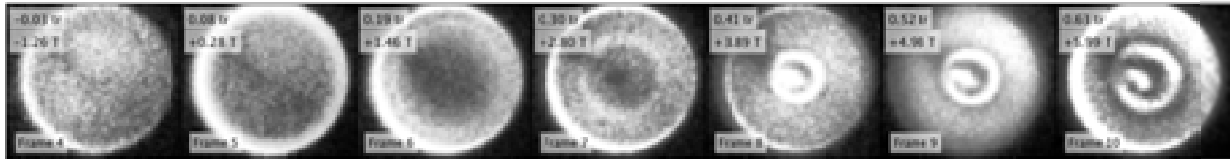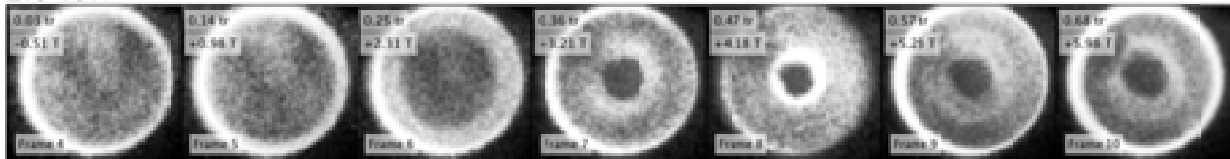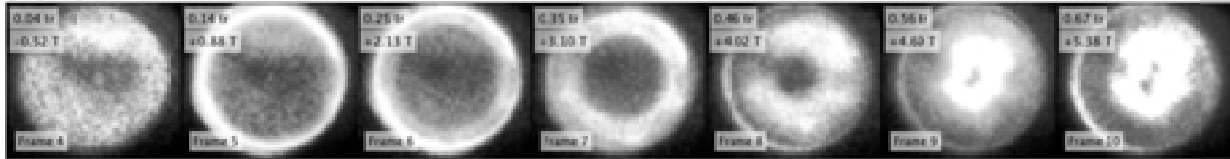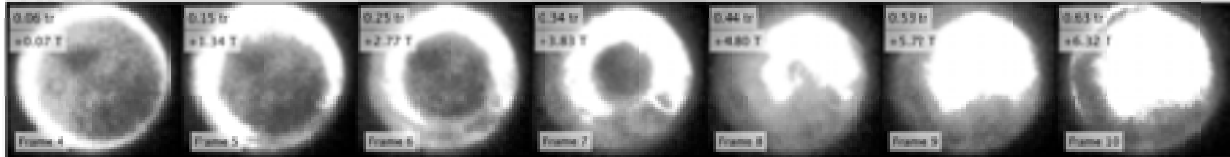
Figure 3.28: Partial image sequences from the UHSi camera with 10 ns exposures at 50 Mfps showing the effects of D2 fill pressure on FRC shots with identical bias field (–1.5 T) and active ZPI. Higher fill pressure results in more non-uniform active ZPI, which has a strong effect on plasma ring formation. Images are independently contrast enhanced and filtered to bring out central plasma dynamics.

be presented. As shown in Fig. 3.28, plasma ring "FRC" formation is limited at higher fill pressure by non-uniformities in the ZPI plasma. From Fig. 3.17, it can be seen that at high pressure (e.g. 10 Torr) the ZPI plasma remains hot/bright and actually becomes more quiescent very late into the ZPI pulse. This is in contrast to lower pressures, where the plasma is seen to be very dim late in time.

To explore the effect of ZPI uniformity on improving formation at high pressure, identical shots at 10 Torr D2 fill were taken with active ZPI (one period into ZPI pulse) and decayed ZPI (20 μs late into the ZPI pulse). As can be seen in Fig. 3.29, plasma ring formation is actually better with decayed ZPI, despite the presumed lower temperature of the ZPI plasma. It is assumed that this improvement comes from better uniformity of the plasma late in time when the ZPI current oscillations have decayed and density gradients have had time to smooth out.

The pressure effects and ZPI effects summarized by Figs. 3.28 and 3.29 were reproduced in 2, 5, and 10 Torr fill pressures with oblique axial imaging, as depicted in Fig. 3.30. The oblique images give a clearer picture of the plasma structure in the axial dimension, showing non-uniformities and instability structures that become more severe at higher fill pressures. At lower pressures, the plasma is seen to take on a football shape (with a wider waist at the center) due to the trapping of more bias flux in this region.

Finally, a few interesting instability sequences noticed in visible imaging are displayed in Fig. 3.31. As discussed, θ-pinch shots occasionally showed very high mode fluting structures develop, whereas FRC shots showed $n = 1 - 4$ rotational modes. Rotational modes are expected in MAIZE FRCs due to the lack of rotation control via end-biasing, as discussed in Chap. 1. It is believed that these instability identifications further bolster the claim of FRC formation in these experiments on MAIZE.

Visible spectra from the SpectraPro 750i were of limited use to determine temperature during FRC experiments due to the swamping of any spectral lines with continuum emission. The high deuterium purity achieved in the gas fill also meant no characteristic impurity lines were observed. Doping for spectroscopic purposes is recommended for exploration in future experimental campaigns. Furthermore, in order to determine plasma temperature by blackbody estimates, the wavelength peak of the blackbody emission would need to be of similar magnitude to the spectral range of the spectrometer (visible 400–900nm). The blackbody emission peak wavelength can be calculated [] as:

$$\lambda_{\text{peak}} = 1.47 \times 10^{-6} \, \frac{c}{T} \tag{3.6}$$

where λ_{peak} is in nm and T is in eV. Therefore, only plasmas with <10s of eV temperature would be expected to show a noticeable slope to the emission spectrum in the visible range, and the plasmas produced on MAIZE are expected to have temperature much higher than that (50–500eV).
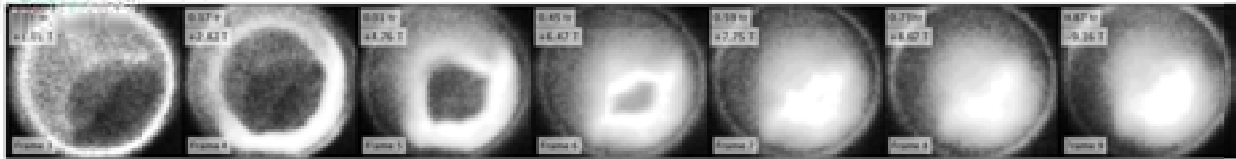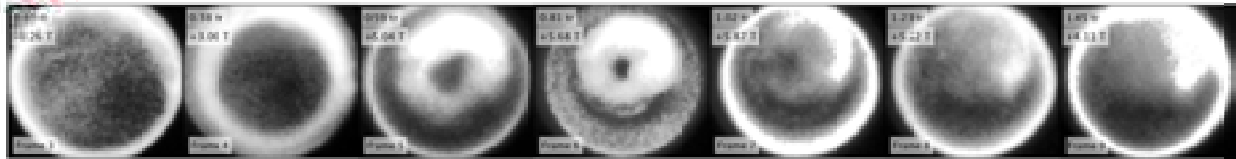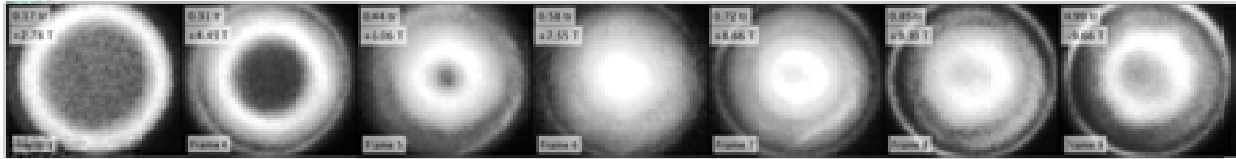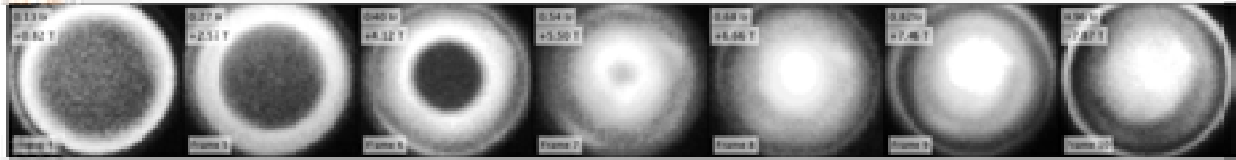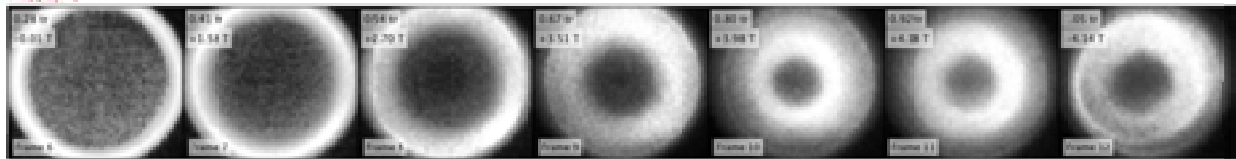
Figure 3.29: Partial image sequences from the UHSi camera with 5 ns exposures at 40–50 Mfps showing the difference between active and decayed ZPI on shots with various bias fields. All shots are at the maximum D2 fill pressure of 10 Torr. Decayed ZPI is defined as firing the shot many microseconds after the ZPI current oscillations have died down, when the plasma is cooler but more uniform. For active ZPI, the shot is fired one period into the ZPI pulse, when ZPI current is near zero but PI plasma is seen to be hot (but not very uniform at this pressure). Frames are similarly timed across shots where possible. Images are independently contrast enhanced and filtered to bring out central plasma dynamics.
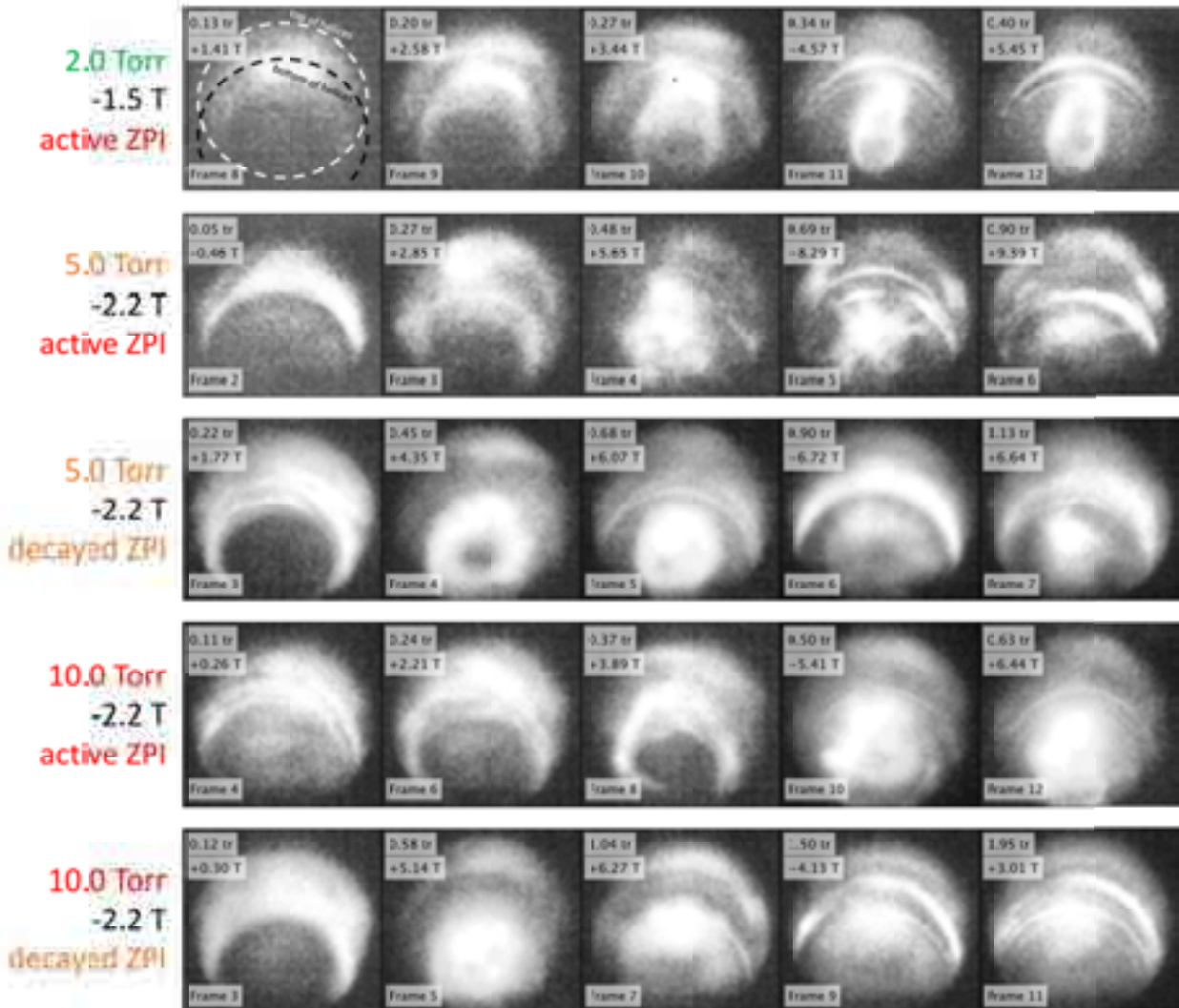
Figure 3.30: Partial image sequences from the UHSi camera with oblique axial imaging (10 ns exposures at 50 Mfps) showing the effects of D2 fill pressure and ZPI timing on FRC shots. Higher fill pressure results in more non-uniform active ZPI, which has a strong effect on plasma ring formation. Images are independently contrast enhanced and filtered to bring out central plasma dynamics.

θ-pinch (flute)

0.59 tr	0.75 tr	0.91 tr
+6.91 T	+7.85 T	+8.76 T
Frame 6	Frame 7	Frame 8

FRC (rotate)

0.67 tr	0.82 tr	0.97 tr
+4.29 T	+5.23 T	+5.85 T
Frame 6	Frame 7	Frame 8

FRC (wobble)

0.48 tr	0.89 tr	2.34 tr
+6.66 T	+9.59 T	+3.98 T
Frame 3	Frame 5	Frame 12
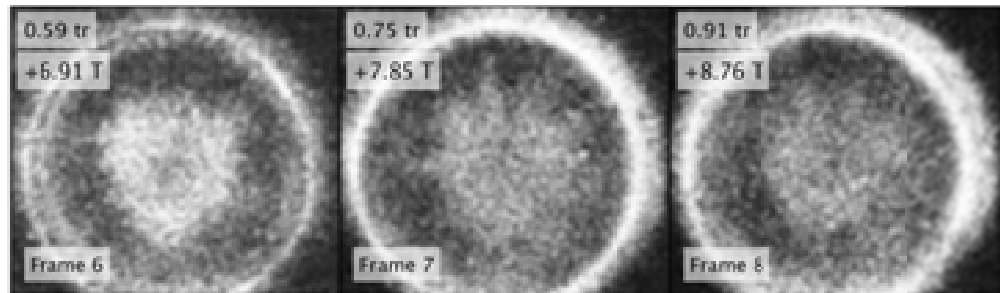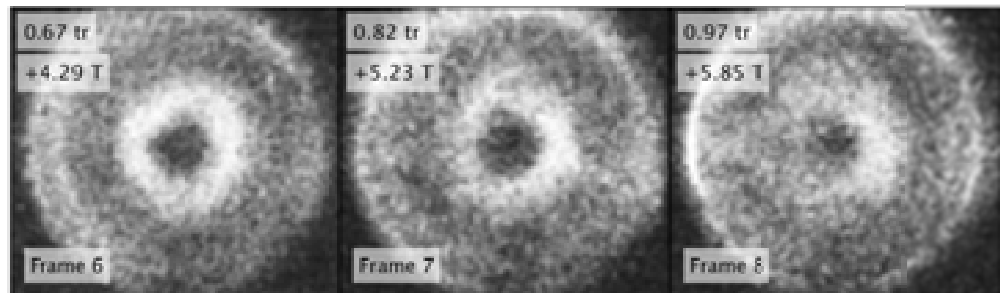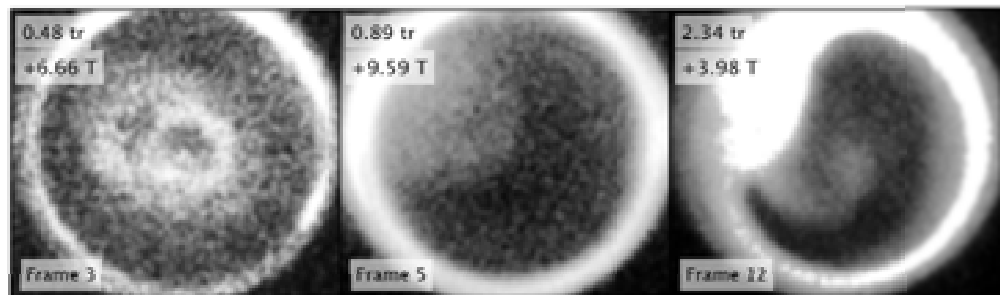
Figure 3.31: Images from the UHSi camera with 5 ns exposures for three MAIZE experiments showing instability structures produced in the plasma columns. High-n fluting instability (top) is associated with θ-pinches, while low-n wobble and rotational modes (bottom) are expected in FRCs. Images are independently contrast enhanced and filtered to bring out central plasma dynamics.

From the lack of features in spectra taken during full-scale MAIZE experiments, it can only be concluded from the spectral data that the plasmas produced during MAIZE shots had temperature above several eV.

3.12 Re-strike Phenomenon

Historically, in low-density FRC experiments, the induced loop voltage around the inner surface of the quartz tube driving field reversal (and FRC formation) is similar to the capacitor discharge voltage – several tens of kilovolts. For discharge tubes of 0.2–1 m diameter, the corresponding electric field along the quartz surface is on the order of 0.1–1 kV/cm. For MAIZE experiments, although the loop voltage is smaller (only $\sim$10 kV), the much smaller discharge tube means a loop electric field of 3 kV/cm or higher. For Z experiments, this figure could be many times higher than that.

It is believed the relatively high loop electric fields are at least partially responsible for a phenomenon seen in many MAIZE experiments termed re-strike, which has not been discussed in historical experiments to the author's knowledge. As seen in many figures throughout this thesis, axial UHSi imaging often captured a second (and even third) annulus of bright plasma current produced on the quartz inner surface, which sometimes lifted off the quartz surface. Oblique axial imaging revealed this to perhaps be a helical phenomenon in some circumstances, with proximity to the load helices outside the quartz, as shown in Fig. 3.32.

A helical re-strike suggests (induced) re-strike current is flowing along but opposite to the helical load current. Since no net current can enter or exit the discharge tube (except through the ZPI circuit, which is a high-impedance path never seen to carry more than a few kA of current), a helical re-strike suggests a poloidal current component fully contained within the discharge tube. This induced poloidal current serves to conserve the small amount of toroidal flux being injected into and removed from the discharge tube by the load helices. The in-board axial part of this poloidal re-strike current must be flowing along the plasma column; it is unclear how much current flows along the surface of the plasma annulus vs. the bulk – i.e. how much toroidal field is entrained in the plasma annulus.

Re-strike was identified to occur most often under two circumstances: on current rise, if the original plasma current annulus (either θ-pinch or FRC) imploded very quickly to the axis of the discharge tube; or, on current fall, as MAIZE voltage reversal begins to pull applied flux out of the discharge tube. The latter is unavoidable due to the inability to trigger a crowbar event on MAIZE. However, in addition to MAIZE's unpredictable self-crowbar (insulator flashover), the re-strike serves as a pseudo-crowbar of the flux in the discharge tube. Thus, the effect is somewhat advantageous as it allows temporal study of the produced plasmas in excess of MAIZE's natural fall

66

axial

oblique axial

2.47 tr +3.15 T Frame 12	1.75 tr +4.69 T Frame 10	0.40 tr +5.45 T Frame 12
0.63 tr +7.42 T Frame 3	2.17 tr +4.48 T Frame 12	0.70 tr +8.69 T Frame 4
1.06 tr +6.87 T Frame 5	2.07 tr +3.51 T Frame 12	0.84 tr +6.20 T Frame 6
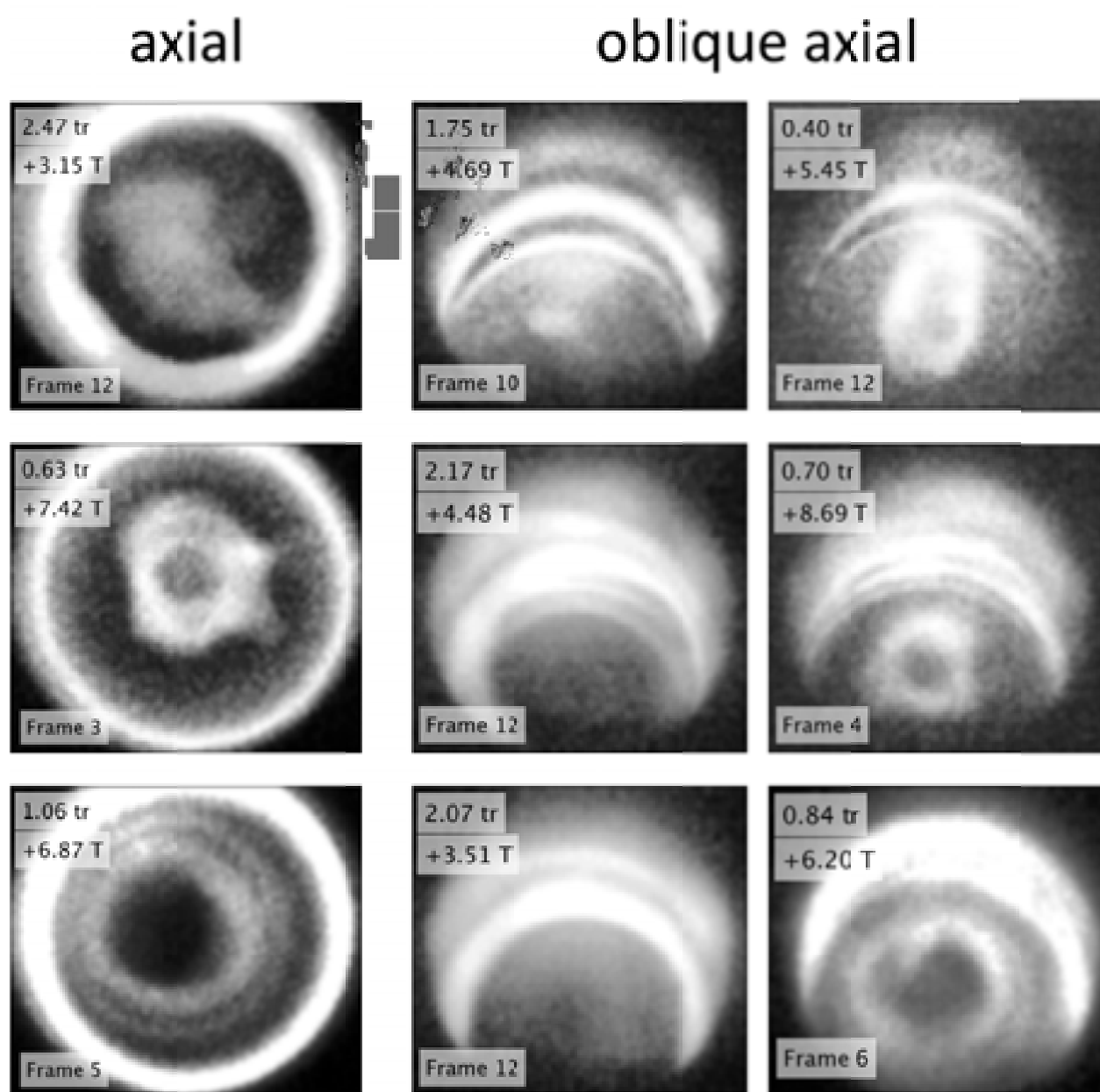
Figure 3.32: UHSi images with 5-10 ns exposure showing the re-strike phenomenon: a second current sheath produced on and sometimes lifted off of the quartz discharge tube inner surface. Oblique axial imaging revealed some re-strikes appear helical.

67

time.

3.13 "Excluded Flux B-dot" Design

A commonly used diagnostic in FRC experiments is the "excluded flux loop" [84]. While there are many embodiments of this apparatus of flux loops to measure the shape of the FRC, they are all based on the same phenomenon: the FRC trapped flux volume bulges and pins the applied fast-field against the flux conserver to a degree proportional to the FRC radius (see Fig. 1.1). If the fast coil is a perfect flux conserver, then the flux normally produced by the external coil (without the FRC present) must now occupy the annular volume not containing the FRC of excluded flux radius $r_{\Delta\phi}$:

$$B_0 \cdot \pi r_c^2 = B_e \cdot \pi \left(r_c^2 - r_{\Delta\phi}^2 \right) \tag{3.7}$$

and therefore the the excluded flux radius (which has been shown [26] to be essentially the same as the separatrix radius) at a given axial position is:

$$r_s \approx r_{\Delta\phi} = r_c \sqrt{1 - \frac{B_0}{B_e}} \tag{3.8}$$

In these equations, B_0 is the applied fast-field that would result with no plasma present, and B_e is the amplified external field outside the FRC (in pressure balance with the plasma). Therefore, a measurement of B_0 and B_e via flux loop probes at multiple axial positions can yield an axially resolved radius of the FRC. From the FRC radius, one can back out many other useful FRC parameters [26]. The excluded flux measurement is thus remarkably useful for such an unobtrusive and inexpensive diagnostic.

In most FRC experiments, B_e at many axial locations is time-resolved with small integrating flux loops (i.e. B-dots) or even fast Hall sensors in a small gap between the discharge tube and the fast coil or even within the discharge tube [22]. This gap can be many millimeters or centimeters in large devices. B_0 can be measured throughout the experiment by placing a flux-integrating loop around the entire discharge tube. For a single-turn coil, the loop voltage V_l is equal to the coil discharge voltage (typically 10's of kV). This voltage is insulated by a few millimeters of dielectric in a cable or strip and resistively divided to logic level to be measured by a data aquisition system.

In scaling FRC dynamics to MAIZE experiments, unfortunately high-voltage insulation does not scale well. The maximum single-loop voltage for MAIZE experiments can be approximated as:

$$V_{l,max} \sim \pi \, r_{qo}^2 \, b_c \, \left. \frac{dI}{dt} \right|_{max} \tag{3.9}$$

where r_{qo} is the outer radius of the quartz discharge tube, I is the MAIZE current, and b_c is the

peak axial field produced in the helix center, per ampere of MAIZE current. For typical MAIZE experiments, $V_{l,max}$ is of the order 10 kV. Since any gap between the discharge tube and the inner surface of the helix adds unacceptable inductance and a limit on x_s, it is not practical to have a 10 kV rated diagnostic cable nor a resistive voltage divider in this gap. Furthermore, it is not just the loop diagnostic signal that is high-voltage, but also the helix itself, which is thinly insulated at best and carries some fraction of the MAIZE discharge voltage (>100 kV). The helix gaps are too small to feed any high-voltage cabling through.

An alternative method to measure B_0 in MAIZE experiments is through CST simulation of a known load helix current. Since the magnetic field produced in vacuum by the load helix is linearly proportional to the current therein (in the surface current limit), a measurement of the load helix current (i.e. MAIZE current) equates to a known B_0 at all axial locations. Thus, only B_e need be measured at a known axial location to determine r_s. This is essentially the method illustrated in Fig. 1 of Green [84], where the "outer loop" signal is a measurement proportional to the MAIZE current in the helical load.

However, the situation is complicated on MAIZE in many ways. First, the helix is not a perfect flux conserver, so this slightly reduces B_e for a given r_s in some hard-to-predict manner, leading to an underestimate of r_s. Second, the strong 3D asymmetries of the field near the inner surface of the liner where B_e is to be measured will introduce strong uncertainties into the measurement, since azimuthal flux is compressed as well as axial flux and the B-dot locations are not precisely known within hundreds of microns. Third, MITL current losses anywhere in the MAIZE feed upstream of the Rogowski coil will introduce error to the B_0 calculation. The latter issue was addressed by a "calibration" B-dot: a large flux loop inserted *outside* of the load helix in the return feed, sensitive to azimuthal flux. Essentially, the calibration B-dot measures the load current in the helix right at the top of the helix, and is not affected by plasma in the discharge tube.

Despite the aforementioned uncertainties, the flux exclusion effect should be qualitatively seen if B_e can be successfully measured on the outer surface of the quartz tube within the bore of the load helix. To this end, the micro B-dot design described in Section 3.9 was used with the smallest rigid coax available (.02"), and the B-dot stems were fed axially along the discharge tube from SMA connectors at the top, as pictured in Fig. 3.33. The outer diameter of the quartz discharge tubes was 14 mm and the helix bore was 16.5 mm, leaving ~ 0.75 mm of radial room for B-dot-insulation and a vacuum gap to prevent tracking between helices. Targets were designed with seven (or four) external B-dots distributed along the upper half of the discharge tube, with axial positions indicated in Fig. 3.22. The lower half of the tube was avoided due to issues with B-dot proximity to the high-voltage cathode of MAIZE (i.e. the bottom of the helix). If one is expecting some degree of axial mirror symmetry about the mid-plane, then clustering of B-dots on one half also provides higher axial resolution.

Figure 3.33: Early "B-dot discharge tube" with four external micro B-dots for measuring B_e at various axial heights on the top half the discharge tube. The B-dots on this tube were insulated with clear, high dielectric strength heat-shrink tubing approximately 0.5 mm in thickness.

The excluded flux micro B-dots were calibrated *in-situ*, with all hardware installed, via calibration shots with a fully evacuated ($< 10^{-5}$ Torr) discharge tube. Lack of plasma breakdown in the tube during the calibration shots was confirmed with long-exposure UHSi imaging, and the B-dot signals in the vacuum shots were (within error) directly proportional to the Rogowski signal as expected – at least for some time beyond the current risetime. Late in time, the B-dot signals are not expected to be accurate due to current shunting and numerical integration drift effects.

With the factor of proportionality for each B-dot determined by best visual fit to the calibration shot current trace (up to peak current), the excluded flux radius indicated by a B-dot in a plasma shot (assuming perfect flux conservation by the helix) is:

$$r_{s,i}(t) \approx r_c \sqrt{1 - \frac{C_{0,i}I(t) - B_{bias,i}}{C_{e,i}S_i(t) - B_{bias,i}}} \tag{3.10}$$

where $C_{0,i}$ in T/kA is the average vacuum fast-field per kA in the load helix (according to vacuum CST simulation) at B-dot i location, $C_{e,i}$ is the vacuum axial fast-field per kA obtained for each B-dot i through the *in-situ* calibration shot, $I(t)$ is the MAIZE current obtained through calibrated and integrated Rogowski coil signal, $S_i(t)$ is the integrated signal from B-dot i, and $B_{bias,i}$ is the bias field at the axial location of each B-dot i, as determined by the methods of Fig. 3.25. r_c is taken to be the helix inner radius of 8.25 mm, though Eqn. 3.10 is just an estimate because the helix is does not perfectly conserve flux at that radius.

The results of three characteristic experiments with a discharge tube with seven external micro B-dots are shown in Figs. 3.34 – 3.36. The first experiment (Fig. 3.34) represents a θ-pinch shot, with no bias field applied. The second and third experiments (Figs. 3.35 and 3.36) represent FRC shots. The surface plots in each figure illustrate the normalized excluded flux radius $x_s = \frac{r_s}{r_c}$ as a function of the seven (thirteen when reflected) axial positions and time in the experiment. The black bars on the surface plots highlight the exposure time of the UHSi image frames for the two experiments, which are also depicted in the figures.

The average excluded flux radius determined by the B-dots is consistent with the plasma radius estimated from UHSi images, for both θ-pinch and FRC experiments. θ-pinch experiments show a small value of excluded flux radius (due to the diamagnetic stagnation column), whereas FRC experiments show a much larger excluded flux persisting in time, which is encouraging. Furthermore, some FRC experiments such as that in Fig. 3.35 show a temporal collapse in excluded flux radius near the top of the discharge tube (but not in the center), coincident with some sort of lift-off dynamics of the plasma ring. This possibly demonstrates some form of axial contraction or bulk axial movement of the plasma, expected only if reconnection has occurred at the top of the ring.

Finally, Fig. 3.36 shows the results of a failed FRC experiment using active ZPI at high pressure (10 Torr), which was shown to produce asymmetries (see Section 3.11). The excluded flux indicated

71

5.0 Torr
0.0 T bias (θ-pinch)
active ZPI
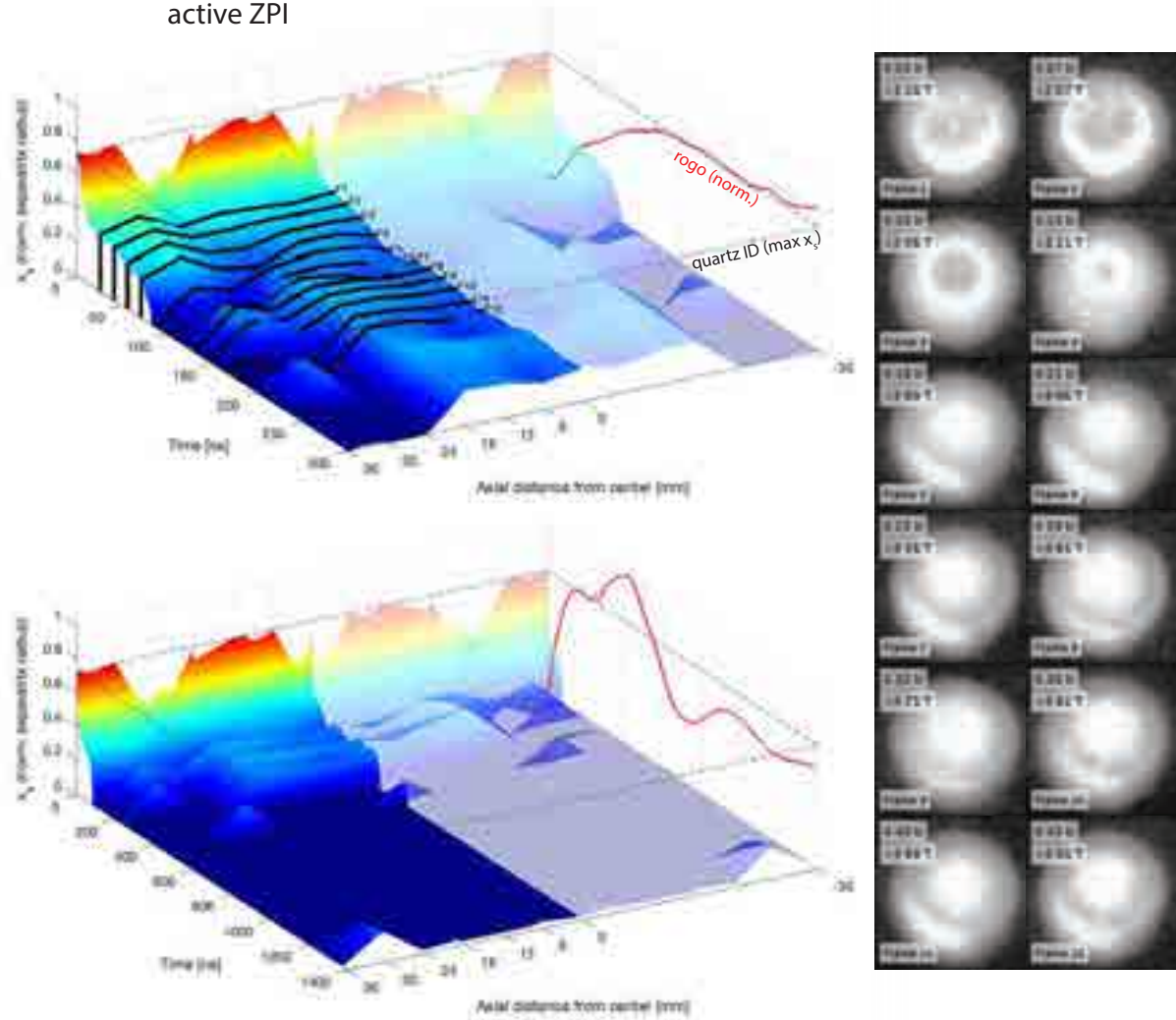
Figure 3.34: Results of a θ-pinch experiment with seven excluded flux micro B-dots. Right: full UHSi image sequence with 5 ns exposure. Left: surface plots show spatial and temporal behavior of the normalized excluded flux radius x_s as calculated from the B-dot signals. The seven B-dots are distributed on the top half of the discharge tube, so their positions are reflected in the plots, assuming axial mid-plane mirror symmetry (this is likely NOT a good assumption so the reflection is faded). Plots for short (upper left) and long (lower left) time scales are shown. Black bars indicate exposure time of frames in top of figure. The trace on the x_s-t plane shows the normalized MAIZE current for the shot. A dashed line indicates the maximum possible x_s of the plasma (the quartz ID).

2.0 Torr
-2.8 T bias (FRC)
active ZPI

rogo (norm.)

quartz ID (max x_s)
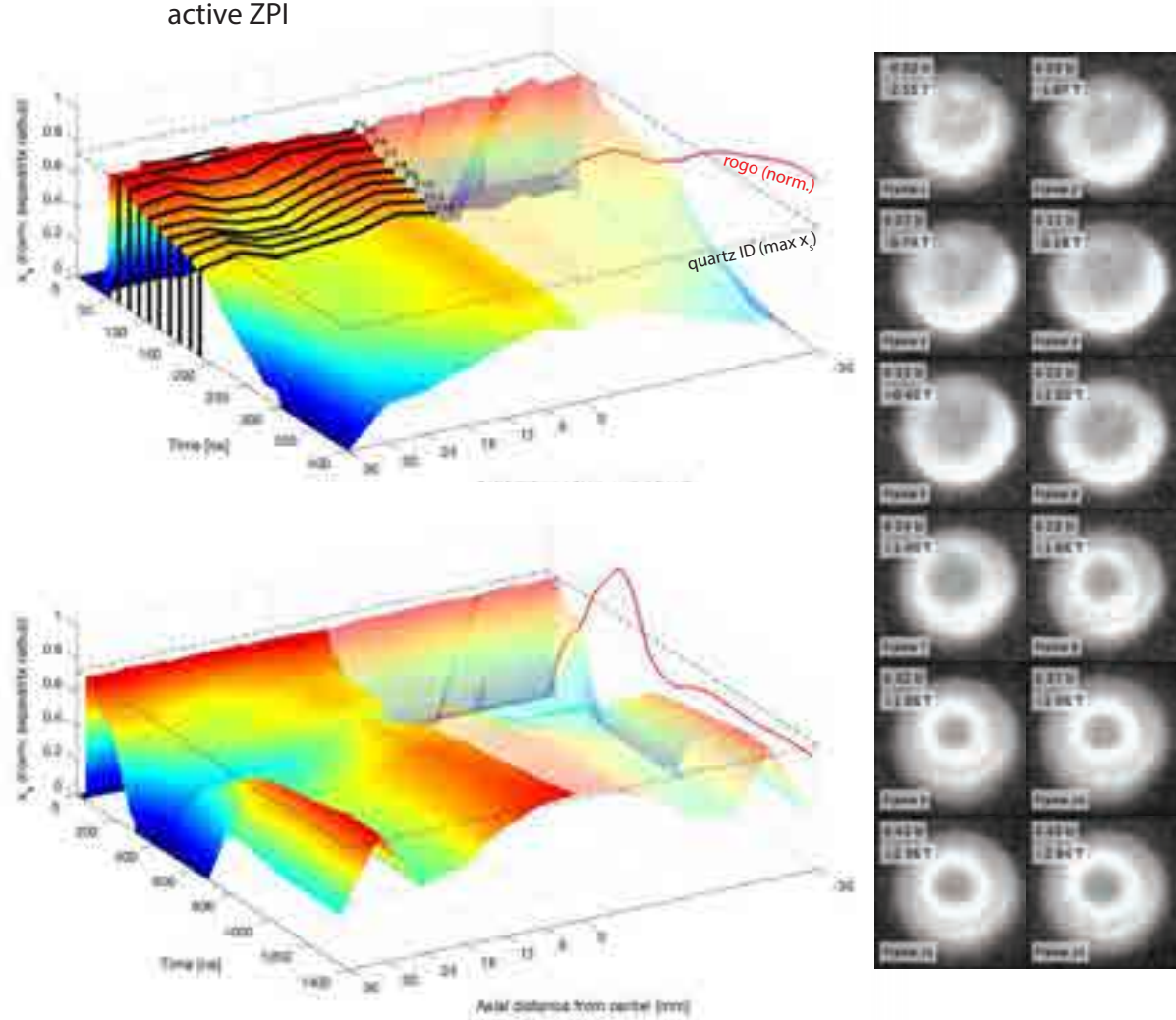
Figure 3.35: Results of an FRC experiment with seven excluded flux micro B-dots. Right: full UHSi image sequence with 5 ns exposure. Left: surface plots show spatial and temporal behavior of the normalized excluded flux radius x_s as calculated from the B-dot signals. The seven B-dots are distributed on the top half of the discharge tube, so their positions are reflected in the plots, assuming axial mid-plane mirror symmetry (this is likely NOT a good assumption so the reflection is faded). Plots for short (upper left) and long (lower left) time scales are shown. Black bars indicate exposure time of frames in top of figure. The trace on the x_s-t plane shows the normalized MAIZE current for the shot. A dashed line indicates the maximum possible x_s of the plasma (the quartz ID).

10.0 Torr
-2.8 T bias (failed FRC)
active ZPI
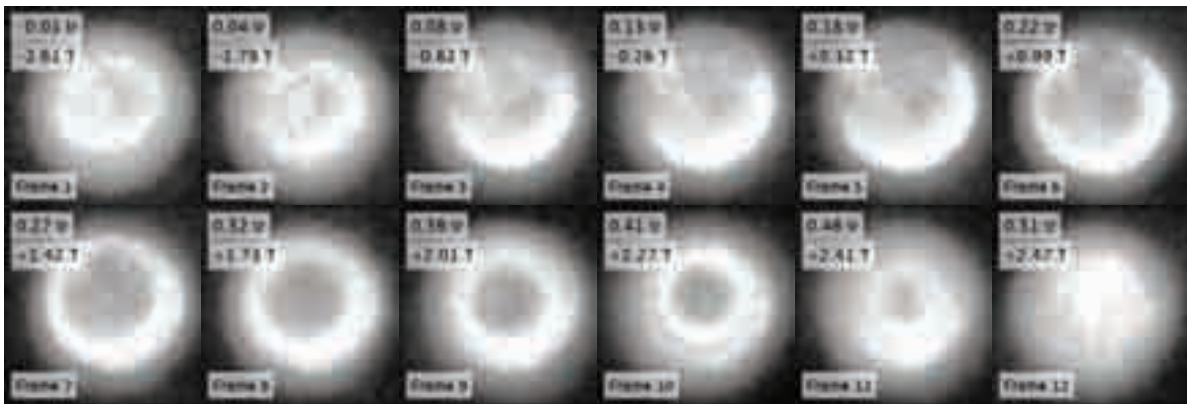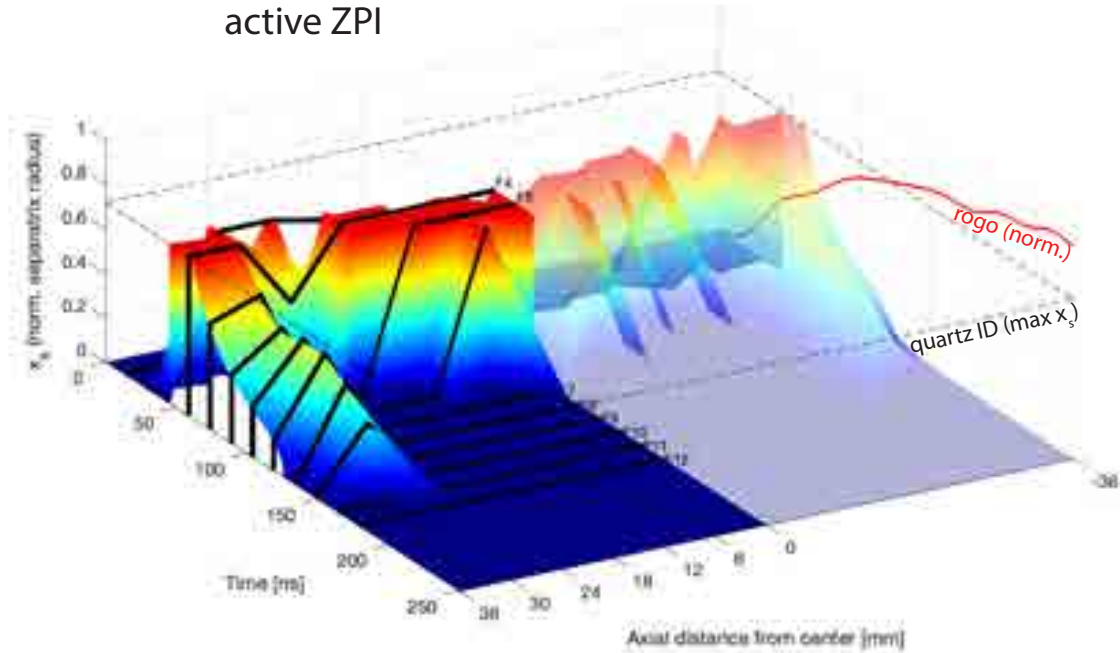
Figure 3.36: Results of a failed FRC experiment at high fill pressure (10 Torr, active ZPI) with seven excluded flux micro B-dots. Bottom: full UHSi image sequence with 5 ns exposure. Top: surface plot shows spatial and temporal behavior of the normalized excluded flux radius x_s as calculated from the B-dot signals. The seven B-dots are distributed on the top half of the discharge tube, so their positions are reflected in the plots, assuming some sort of axial mid-plane mirror symmetry (this is likely NOT a good assumption so the reflection is faded). A short- and long-timescale surface plot are shown. Black bars indicate exposure time of frames in top of figure. The trace on the x_s-t plane shows the normalized MAIZE current for the shot. A dashed line indicates the maximum possible x_s of the plasma (the quartz ID).

by B-dot probes collapses to zero at all axial positions temporally consistent with the collapse of the central plasma ring in imaging. Again, the B-dot signals seem to indicate plasma radii and dynamics consistent with those observed in visible imaging.

As stated, the B-dot signals are not expected to be accurate long after peak current due to current shunting and integration error. Furthermore, in this series of experiments, fast-framing images were never taken late in time to observe the dynamics of the plasma very long after peak current. Nevertheless, the long-time B-dot behavior is depicted the extended bottom plots of Figs. 3.34 and 3.35 because it was found to show results consistent with the expected degree of trapped flux.

While Figs. 3.34 – 3.36 show promising results representative of a trend in the data, in practice, B-dot response was found to be a bit erratic and concerns were raised regarding the azimuthal sensitivity of the micro B-dot design and positional uncertainty in the point-like measurement. To address these issues, a new flux loop was designed. The newer design used a thin crescent-shaped conductor loop made of 3 mm wide, 70 μm thick copper strip insulated by 12 μm polyester film, as depicted in Fig. 3.37. The crescent does not enclose the entire discharge tube, because the loop voltage $V_{l,max}$ caused the ends of the crescent to arc to each other along the surface of the quartz, despite many layers of Kapton insulation. Later crescents were designed to extend only 1/4 the circumference of the tube, which matches the azimuthal symmetry pattern of the helical load. The maximum voltage generated by the quarter-turn crescent loop is approximately:

$$V_{cl,max} \sim 0.5\,\pi\,r_{qo}\,\delta\,b_c\,\left.\frac{dI}{dt}\right|_{max} \tag{3.11}$$

where $\delta \sim 12$ μm is the thickness of the insulator in the crescent loop. $V_{cl,max}$ is on the order of hundreds of volts, which can be carried by .02" rigid coax to the SMA connection at the top of the discharge tube. This minimizes probe/insulation thickness so the discharge tube can fill the most of the helix active volume.

Four of these targets were made with various insulation design, but unfortunately none survived the vacuum calibration shots. The large surface area of the crescents was found to persistently arc to the helices. Fig. 3.38 shows B-dot discharge tubes destroyed by arcing related to the B-dots. Red arrows show evidence of arcing between the helix and the B-dots or between B-dots themselves, despite several layers of insulation. Also shown are quartz burn patterns on a heavily used (non-B-dot) discharge tube consistent with the magnetic field structure, which is overlaid in white dashed lines.
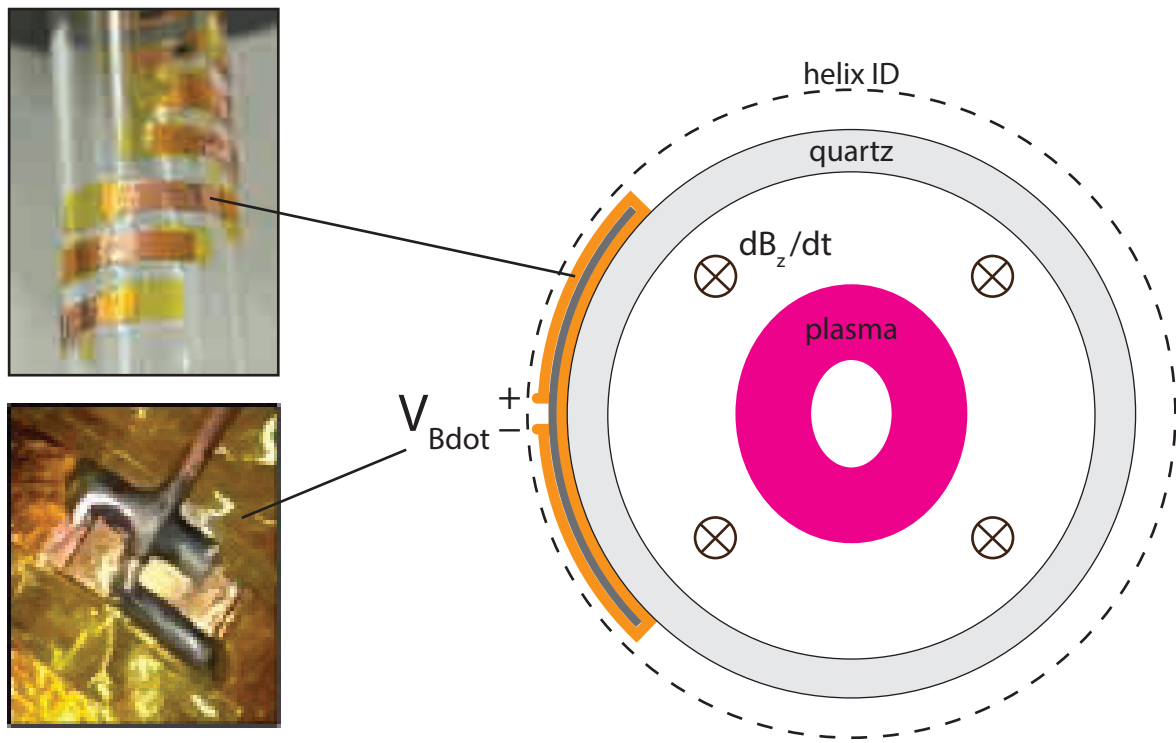
Figure 3.37: Newer excluded flux B-dot probe design using crescent-shaped loops covering 1/4 the circumference of the discharge tube. Photographs on the bottom show eight of the flux loops installed on a discharge tube, as well as the calibration B-dot that is sensitive to azimuthal flux in the return current structure outside the helix (essentially measuring current in the helix).
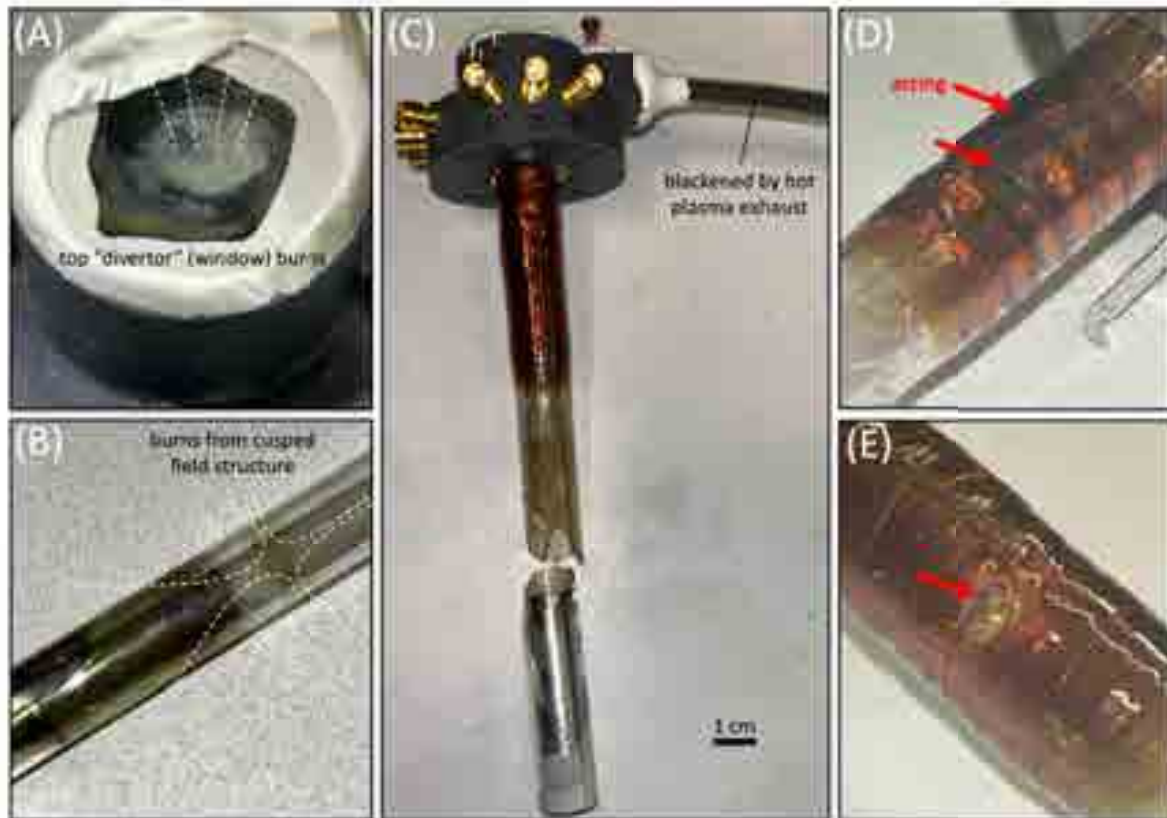
Figure 3.38: B-dot discharge tubes destroyed by arcing related to the presence of the B-dots (C-E). Red arrows show evidence of arcing to or between B-dots. The plastic fill tubes are blackened by hot plasma exhaust. For non-Bdot tubes that survived many shots, the burn marks on the top quartz window (A) and the bottom of the tube quartz (B) show patterns consistent with the magnetic field structure during FRC shots (white dashed field lines overlaid).

CHAPTER 4

2D Resistive MHD Simulations of High-Density FRCs

4.1 Description of the Kraken Code

Simulations discussed in this chapter were performed using an early 2D version (c. July 2022) of the resistive MHD code Kraken, courtesy of Chris Jennings at Sandia. Kraken has been under development at Sandia originally from a version of the GORGON code [85] from Imperial College London.

Kraken is a finite volume multi-material hydrodynamics code that implements the GORGON system of resistive MHD equations [85] [86] coupled to detailed transmission line circuit models, utilizing tabulated equation of state and transport parameters [87] [88], and implementing single group radiation diffusion [89] and anisotropic thermal conduction. Kraken is capable of tracking separate ion and electron temperatures, but not separate densities (no charge separation or two-fluid physics).

After most of the simulations reported in this dissertation were performed, it was found that the intended bremsstrahlung radiation loss model was not actually included by the solver. Therefore, no radiative loss physics were included in the simulations reported herein. However, radiation is not expected to play a significant role in HED FRC decay. This can be illustrated by the ratio of classical (i.e., maximum) resistive FRC decay time (see Section 4.7) to characteristic bremsstrahlung decay time:

$$\frac{\tau_{\phi \text{clas.}}}{\tau_{\text{brems}}} = \frac{\frac{\mu_0 \, r_s^2}{16 \, \eta_\perp}}{\frac{2 \, n \, k_B T}{A_{\text{brems}} \, n^2 \, \sqrt{k_B T}}} \tag{4.1}$$

where $A_{\text{brems}} = 1.6 \times 10^{-38} \, \frac{\text{W m}^3}{\sqrt{\text{eV}}}$, and $\eta_\perp = 1.03 \times 10^{-4} \cdot \ln \Lambda \cdot T^{-\frac{3}{2}}$ with T in eV is the classical cross-field Spitzer resistivity from the NRL Plasma Formulary [90]. This ratio is much smaller than unity for all FRC parameters reported herein, and thus radiation is not expected to be an important loss mechanism.

4.2 Comments on HED FRC Simulation

FRCs represent a formidable simulation task due to the kinetic and two-fluid physics simultaneously critical to their observed behavior. Furthermore, formation of FRCs involves magnetic reconnection, itself an active area of research in simulation. Reconnection-based formation and non-classical FRC decay has been successfully modeled by adding an anomalous resistivity component based on electron drift turbulence [47] expected to be present due to the diamagnetic, cross-field current. Specific anomalous resistivity treatments will be addressed further in Section 4.6.

While Kraken is capable of 3D simulation, it is not expected to model 3D instabilities such as rotation and tilt correctly due to the lack of kinetic and two-fluid physics. Therefore, the goal of the 2D simulations reported in this thesis was to determine the equilibrium properties and resistive lifetime of FRCs suitable for compression on Z and/or produced on MAIZE; i.e. the ideal lifetime as limited by anomalous resistivity rather than macro-instability. For a discussion of HED FRC macro-stability, see Chap. 1.

The first batch of simulations presented in this chapter had no time-changing inputs, FRC formation, or FRC compression phase: they simply represent relaxation from the analytic approximation to pseudo-equilibrium, and anomalous resistive decay of the initialized FRC plasma state in a uniform flux-conserver. 2D initialized simulations were also used to evaluate the effect of field-flare (Section 4.5) and axial non-uniformity (Section 4.8) effects that may be present in real AutoMag liners. However, it is important to note that the Kraken simulations were performed with a flux-conserving boundary that does not properly model the 3D asymmetries near the inner surface of an AutoMag liner/helical load hardware.

The second batch of simulations presented used time-changing input in the form of modifying the flux function near the boundary (as will be described in Section 4.10) to actually form FRCs in the applied field geometry of experiments.

4.3 Analytic FRC Initialization

To study the quiescent (ideal) lifetime, FRCs with the desired parameters for compression on Z were initialized analytically based on the solutions of Steinhauer [91]. The solutions represent an improvement over the common Hill's vortex, being applicable to a race-track like separatrix (high elongation). However, they are split into two solutions, inside and outside the separatrix, which are approximately matched at the separatrix by solving a system of equations.

The simplified relevant equation copied from Ref. [91] for the flux (or stream) function ψ_o outside the separatrix is:

$$\psi_o \approx \frac{B_e a^2}{2} \left(E_0 \frac{r2}{a^2} + E_1 \frac{r2}{a^2} \left(\frac{r^2}{a^2} - 4\frac{z^2}{a^2} \right) + E_2 \left(\frac{\alpha b + z}{\sqrt{r^2 + (\alpha b + z)^2}} + \frac{\alpha b - z}{\sqrt{r^2 + (\alpha b - z)^2}} \right) \right)$$

(4.2)

Inside the separatrix, the equations for flux function ψ_c and the plasma pressure p are:

$$\psi_c \approx \sqrt{\frac{3}{2}} \frac{x_s B_e r^2}{2} \left(1 - \frac{r^2}{a^2} - \frac{z^4}{b^4} + f\epsilon^2 \right)$$

(4.3)

$$p \approx \frac{B_e^2}{2\mu_0} \left(1 - \frac{3}{2}x_s^2 + \sqrt{\frac{3}{2}} x_s \frac{8\psi_c}{B_e a^2} + f\epsilon^2 \right)$$

(4.4)

In Eqns. 4.2–4.4, $a \equiv r_s$ is the FRC separatrix radius, $x_s \equiv \frac{a}{r_c}$ is the separatrix radius normalized to the coil radius, $b \equiv \frac{L_x}{2}$ is the FRC half length, $\epsilon \equiv \frac{1}{E} = \frac{a}{b}$ is the inverse elongation, and E_0, E_1, E_2, and α are separatrix matching factors obtained by solving a system of equations involving x_s, ϵ, and σ. The factor f is of order unity which helps smooth the separatrix region (1.5 was used for most simulations reported herein), and $\sigma \equiv \sigma_{\text{flare}} \geq 1$ is a parameter which can be chosen to control the external field profile far from the FRC.

These solutions are found to be accurate enough to limit initial oscillation energy of the simulated FRCs, and have the added benefit of a parameter ("σ" in Ref. [91], hereafter referred to as σ_{flare}) that controls the axial distance at which the applied field flares out of the discharge tube. Essentially, this parameter represents the ratio of the AutoMag liner length to the FRC length, which has an effect on the dynamics to be described in Section 4.5.

For flux conservation, all cells in the simulation at radius greater than the coil radius r_c are initialized with a very low resistivity ($\mathcal{O}(10^{-10})$ Ω·m). Plasma incident on the boundary at $r = r_c$ in the positive r direction is reflected back in the negative r direction. Again, it is important to note that this represents a perfectly uniform flux conserving boundary, which is not the case for an AutoMag liner before breakdown (see Chap. 2 Section 2.5). However, the flux conserving boundary is expected to be appropriate after AutoMag breakdown, during the liner implosion. The selection of the boundary resistivity is somewhat arbitrary. Without any hydrodynamics to the flux conserver, the flux is almost perfectly conserved for any realistic metal resistivity at these timescales.

4.4   Resolution Tests

An FRC with parameters of relevance to an AutoMag experiment was chosen for resolution tests, as shown in Fig.4.1. The applied field was chosen to be 30 T, a reasonable limit at the current Z-facility. The value of x_s for θ-pinch FRCs is typically 0.4–0.8, so 0.6 was chosen. An initial

temperature of 50 eV was used, as this is a reasonable estimate for a dense FRC for MTF. Identical code initializations were run with five different square-cell sizes: 10, 25, 50, 200, and 500 μm. Note that the 10 μm case has nominally $2500\times$ the CPU time of the 500 μm case and did not finish in the allotted 2400 node-hour cluster time. A MATLAB script was written to analyze the Kraken results for trapped flux and other FRC parameters as a function of output timestep. Several hundred timesteps (many GB of data) were output for each simulation. The Kraken simulated flux decay times, "τ_ϕ sim fit", are determined by using MATLAB to fit an exponential decay to the flux data points of the form:

$$\phi = \phi_0 \; e^{\frac{-t}{\tau_\phi}}$$

It is found that the 10, 25, and 50 μm results are essentially indiscernible from each other when parameters are plotted, while the 200 and 500 μm tests show some deviation. Therefore, it is assumed that 50 μm cell size is a suitable resolution and was used for the results presented in subsequent Sections 4.5, 4.7, and 4.10. Simulations with special resolution changes will be noted and cell size was generally scaled with flux-conserver radius.

4.5   Field-Flare Effects

Historically, most FRC experiments have taken place in a single-turn coil(s), so the flux (or stream or B_0) function is held constant at the coil inner radius along the axial length of the discharge tube. Furthermore, external applied field gradients are usually engineered so as to slightly increase the axial field strength beyond the formation region of the FRC, i.e. to trap the FRC in the well of a magnetic mirror. This ensures the FRC plasma is stabilized axially in the center of the discharge tube, were it to gain any small axial momentum during formation.

Neither of these facts is the case for the proposed AutoMag-formed FRCs. To minimize the inductance of the AutoMag liner on a fast pulsed-power machine like Z, it is desired to make the helical section of the liner (or at least the imploding helical section) as short as possible. In this case, the field gradient is strongly opposite the desired mirror configuration: the field lines flare out of the discharge tube just above and below the FRC, as shown in Fig. 4.2, eventually reversing direction on the other side of magnetic nulls. Therefore, there are actually four magnetic nulls along the axis of the proposed FRC experiment: two at the ends of the helical region of the AutoMag liner, where the AutoMag field meets the opposing bias field, and two at the X-points of the FRC. This arises from the fact there are three concentric dipole sources of different heights: the bias coils, the helical liner, and the plasma current!

The axial distance between the FRC and the field line flare/exit can be increased in the Steinhauer model by increasing the parameter σ_{flare}. Fig. 4.2 shows the decay of two identical FRC
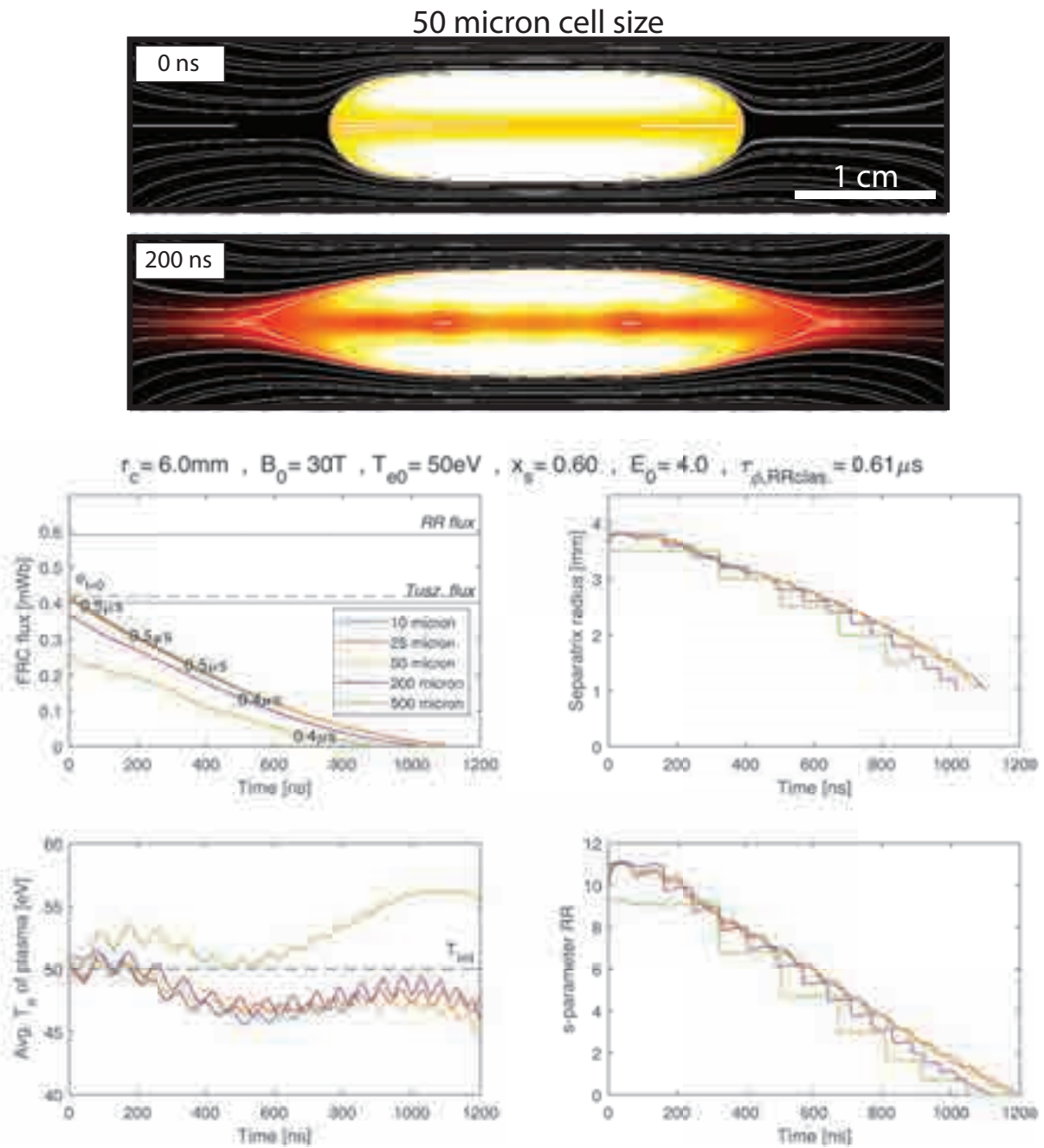
Figure 4.1: Decay of parameters for the same high-density FRC initialized in Kraken with five different levels of square-cell resolution. Initial values and decay behavior become different when the resolution is too coarse. 50 μm was used for most simulations reported in this thesis.
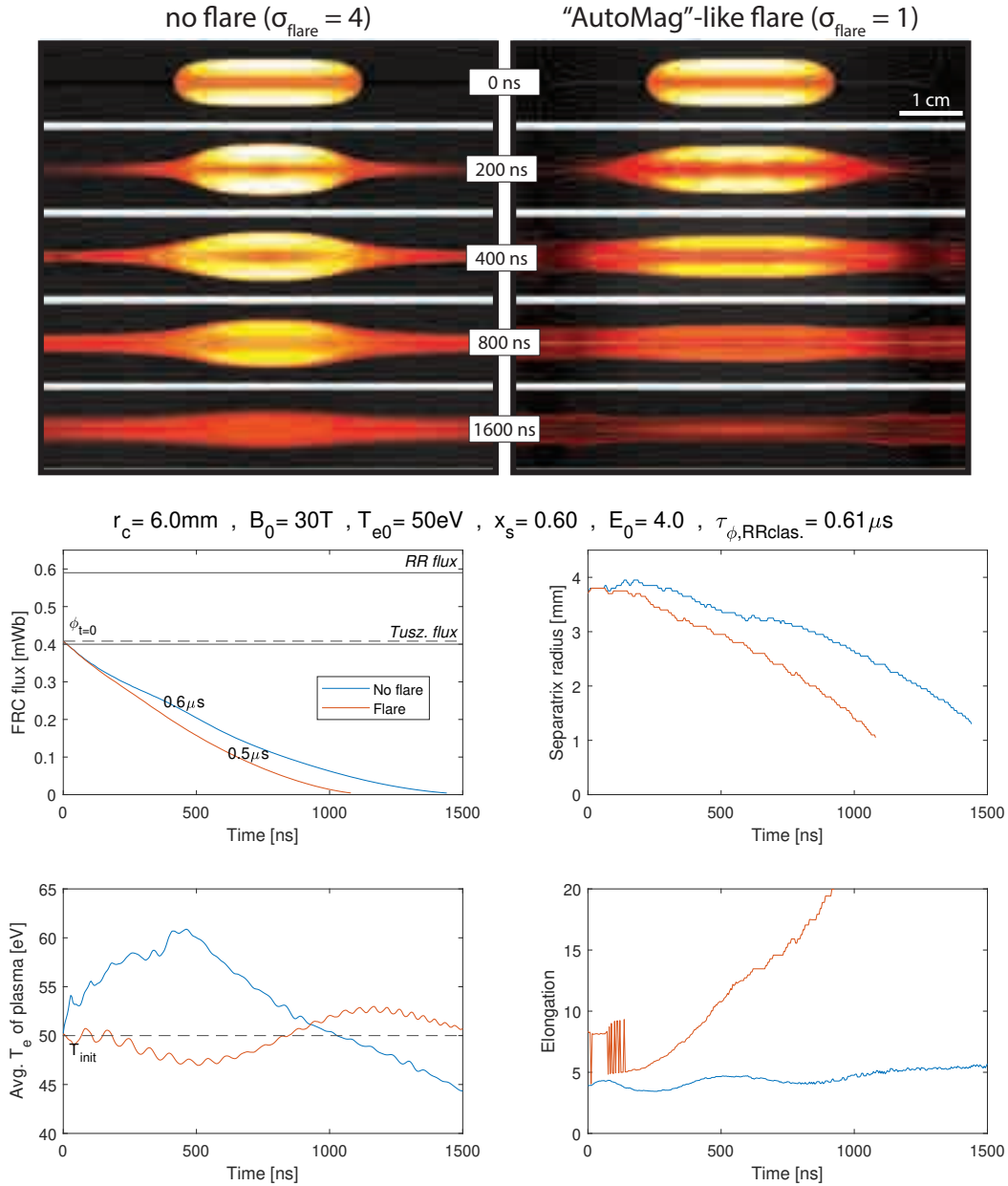
Figure 4.2: Initialization and classical decay of two high-density FRCs in a 12mm-ID flux-conserver. The initialization with $\sigma_{\mathrm{flare}} = 4$ is representative of historical FRC experiments and has minor field-flare effects, while the $\sigma_{\mathrm{flare}} = 1$ has strong field-flare effects representative of an AutoMag liner. This can be visualized by the magnetic field streamlines in the density contours (top).

initializations with $\sigma_{\text{flare}} = 1$ and $\sigma_{\text{flare}} = 4$. The flux, separatrix radius, and elongation of the FRCs are plotted as well, as calculated by the MATLAB script. Curiously, the strong field-flare ($\sigma_{\text{flare}} = 1$) only slightly reduces the (classical) flux decay time of the FRC, but has a much clearer effect on the shape and dynamics of the FRC. This is reminiscent of the results of Ref. [92], where axial field gradients are applied dynamically during long-lived (low-density) FRC experiments to optimize the elongation or separatrix shape of the FRC, sometimes improving the lifetime.

The dynamic elongation of the decaying FRC in the $\sigma_{\text{flare}} = 1$ case (i.e., the AutoMag-like case) of Fig. 4.2 may prove favorable for AutoMag FRC compressions on Z. The first reason is the same as in low-density FRC experiments, where an increase in elongation represents a more favorable value of S^*/E. The second is related to energy efficiency during Z-pinch compression: the self-axial contraction of an FRC (see Chap. 1) would mean that axial regions at the ends of the liner would stagnate while containing no fusion fuel, just axial magnetic field – essentially wasting the implosion energy coupled to those sections of the liner. Thus, the dynamic elongation of the decaying FRC observed for the $\sigma_{flare} = 1$ case in Fig. 4.2 may counteract the self-axial contraction effect and keep the imploding region filled with FRC plasma. Additionally, the dynamic elongation effect may allow the imploding region of the liner to be made shorter than the initial FRC length, which may help lower the dynamic load inductance as the liner implodes.

4.6 Anomalous Resistivity

Accurate modeling of FRC decay has long been known to require anomalous resistivity treatments. The equations of Chodura [31] and Davidson and Krall [66] were used to increase the resistivity above the classical Spitzer value $\eta_{\text{clas.}}$ as:

$$\eta = \eta_{clas} + \eta_{anom} \tag{4.5}$$

where

$$\eta_{anom} = C_{lh} \, \omega_{pi} \, \left(1 - e^{-\frac{v_e}{f c_s}} \right) \quad \text{(Chodura)} \tag{4.6}$$

or

$$\eta_{anom} = 7.2 \times 10^6 \, C_{lh} \, \frac{|B|}{n_e} \, \left(\frac{v_e}{f v_i} \right)^2 \quad \text{(D and K)} \tag{4.7}$$

and $\omega_{pi} = \sqrt{\frac{n_i Z^2 e^2}{\epsilon_0 m_i}}$ is the ion plasma frequency, $v_e = \frac{j_e}{n_e e}$ is the electron current drift speed, $c_s = \sqrt{\frac{Z k_B T_e + 3 k_B T_i}{m_i}}$ is the ion sound speed, $v_i = \sqrt{\frac{k_B T_i}{m_i}}$ is the ion thermal velocity, and $C_{lh} \sim 1$ and $f \sim 1$ are empirical fitting factors. All units are in SI. These equations both have strong
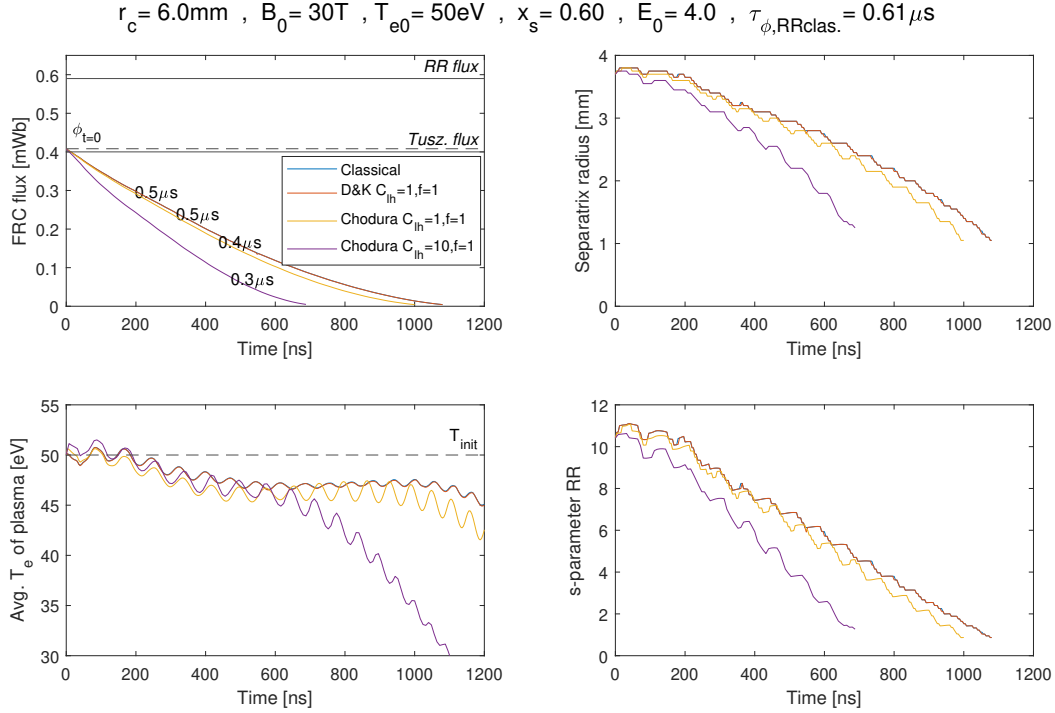
Figure 4.3: Classical and anomalous resistive decay of the baseline FRC used in previous sections. Anomalous effects do not strongly affect the decay time since the electron drift velocity is relatively low (cold, low-flux).

dependence on the electron drift velocity, which can carry most of the FRC plasma current. Electron cross-field drift much faster than the ion characteristic speed is known to excite drift instabilities, the micro-turbulent result of which is theorized to be responsible for the anomalous increase in plasma collisionality above the classical value. It has been found [66] that the Davidson and Krall treatment works well for the FRC formation/reconnection phase, while the Chodura treatment is appropriate for the resistive decay phase.

Both anomalous resistivity treatments were tested for the baseline FRC case of the previous sections 4.4 and 4.5. The results are shown in Fig. 4.3. Though there are interesting effects on the plasma electron heating, neither treatment significantly shortens the flux lifetime of the FRC. This may be expected since the chosen baseline FRC is fairly cold and dense. A hotter FRC with more trapped flux (higher electron current, higher drift velocity) will show stronger anomalous effects, as shown in the next Section 4.7.

4.7   Simulation of Slutz 2021 LASNEX FRCs

As discussed in Section 2.4, Slutz [31] has simulated HED FRC compression using the classified LASNEX code. In Figs. 11–16 of Ref. [31], Slutz presents figures for three stages of the FRC

Table 4.1: Estimated and simulated parameters for the HED FRC simulated in Ref. [31].

	as formed	start of burn	peak of burn
CR	1	10	20
r_c [mm]	6.1	0.61	0.305
x_s	0.89	0.89	0.89
E	2.9	15	25
B_0 [T]	30	1200	3000
$T_e \approx T_i$ [keV]	0.46	18	55
σ_{flare}	1.5	4	4
$\phi_{0,\text{RR}}$ [mWb]	4.13	1.65	1.03
$\phi_{0,\text{Tusz.}}$ [93] [mWb]	4.20	1.68	1.05
s (rigid rotor)	7.3	4.6	3.3
S^* [94]	20.5	13.0	9.34
S^*/E	7.1	0.9	0.4
$\tau_{Alf/tilt}$ [ns]	53	4.4	2.1
$\tau_{\phi\text{clas.}}$ theory [94] [μs]	23.9	49.3	61.5
$\tau_{\phi\text{LSX}}$ theory [94] [μs]	16.1	0.84	0.28
$\tau_{\phi\text{clas.}}$ sim fit [μs]	27.4	–	–
$\tau_{\phi\text{Chod.}}$ sim fit [μs]	15.1	–	–

compression: initial equilibrium ($CR = 1$), start of fusion burn ($CR = 10$), and peak of fusion burn ($CR = 20$). Based on rough estimates from these figures and values stated in the text, the parameters in Table 4.1 were estimated for the LASNEX FRC at these three stages.

The values from the top of Table 4.1 were used as inputs to the Kraken code to study the predicted lifetime at these three HED FRC conditions. The cell sized was scaled proportionally with the r_c value to be 5 μm and 2.5 μm for the start and peak of burn simulations, respectively. The results for classical and anomalous decay of the "as formed" FRC stage are presented in Fig. 4.4. The characteristic flux decay time results of the computations are also displayed in the "τ_ϕ sim fit" rows of Table 4.1. As seen in Fig. 4.4 and Table 4.1, the classical and Chodura ($C_{lh} = 1$, $f = 1$) anomalous decay times of the initial (as formed) LASNEX FRC is in excellent agreement with those predicted by classical and LSX theory [94], reproduced as:

$$\tau_{\phi\text{clas.}} \text{ theory} = \frac{1}{16} \frac{\mu_0 r_s^2}{\eta_\perp} \tag{4.8}$$

$$\tau_{\phi\text{LSX}} \text{ theory} = 9\, x_s^{0.5} \left(\frac{r_s}{\rho_{i0}^{0.5}} \right)^{2.14} \tag{4.9}$$

where $\rho_{i0} = 0.46 \cdot \frac{T^{0.5}}{B_e}$ is the external ion gyroradius. All units in the preceding equations are SI MKS except for ρ_{i0} in centimeters and $T \approx T_i \approx T_e$ in keV.

The burning FRCs from Ref. [31] Fig. 11 had dimensions very roughly estimated since they can
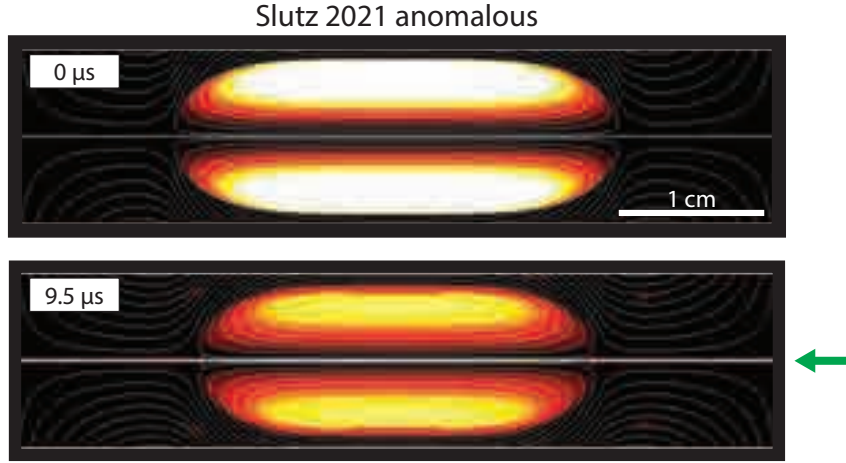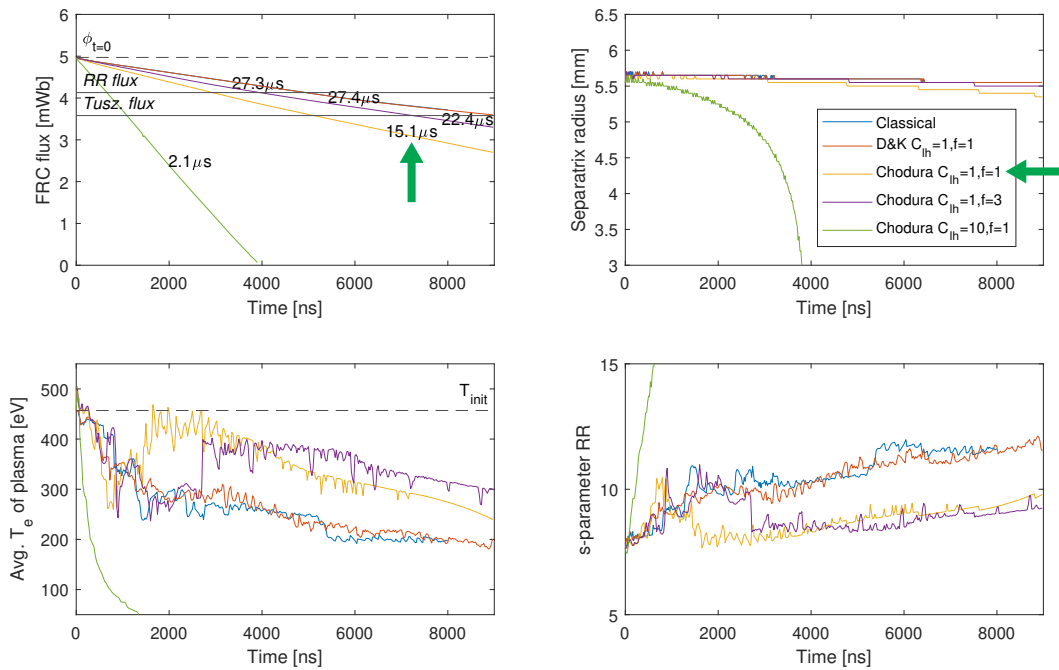
Figure 4.4: Classical and anomalous resistive decay of the "as formed" FRC stage from Slutz [31] with initial parameters listed in Table 4.1. Anomalous effects more strongly affect the decay time since the electron drift velocity is relatively high (high, high-flux). Chodura anomalous treatment with $C_{lh} = 1$, $f = 1$ is shown to agree very well with LSX theory [94].

be seen actively tearing apart in the LASNEX simulations. It can be assumed that the racetrack-like FRC equilibrium is not stable at the extreme elongations (10–30) experienced during dynamic compression to large CR. Extreme elongations are driven for compressed FRCs because the elongation scales as $E \propto CR^{0.6}$.

Similar rapid tearing behavior on order of a few Alfvén times (i.e., the ideal MHD predicted tilt time) was observed for the burning FRCs of Table 4.1 when initialized in Kraken. Interestingly, simulations with Chodura ($C_{lh} = 1$, $f = 1$) anomalous resistivity showed more resilience to tearing than those with classical resistivity, as shown in Fig. 4.5. This is unexpected since tearing is known to be driven by resistive effects. Tearing for the "peak of burn" FRC (Fig. 4.5) with anomalous resistivity is found to be a few nanoseconds, which is comparable to the desired burn time. LASNEX results suggested this was just long enough to achieve high fusion gain, but this remains a concern. It is also not clear if kinetic effects (not captured in LASNEX or Kraken) would stabilize the tearing modes for any time, or perhaps lead to intense particle heating during the tearing event not captured by the code. The latter effect could generate a high-energy ion population throughout the thermonuclear population, blurring the line between beam-target and thermonuclear plasma yield in the turbulent FRC daughter plasmoids.

The contours of Fig.4.5 are shown with expanded aspect ratio to elucidate the structure of the FRC at large elongation. Fig. 4.6 shows select contours for the three initialized stages of the implosion at scale for a more realistic visualization.

For all simulations reported, deuteron and electron temperatures were initialized to the same value. Kraken is capable of tracking separate ion and electron temperatures, and small but insignificant differences (<10 eV) between the two were observed throughout the simulation space during the burn simulations. The electron-ion energy equilibration time τ_{ei}^E at the start of burn parameters ($n \sim 10^{27} m^{-3}$ and $T \sim 18$ keV) can be expressed from Stacey [95] as:

$$\tau_{ei}^E \approx 2.77 \times 10^{19} \; \frac{T^{-\frac{3}{2}}}{n \; \ln \Lambda} \sim \; 100 \text{ ns} \tag{4.10}$$

which is significantly larger than the compression or burn time of tens of nanoseconds. Therefore, it appears that the tearing events affect ions and electrons equally to the resolution of the code. However, the tearing events are seen to initiate a new, more favorable phase of plasma thermal energy decay, as shown in the bottom right panel of Fig. 4.5. Plasma energy is shared equally between ions and electrons.

4.8   Field Gradient Effects

As mentioned in Section 4.5, the axial field gradients introduced by the AutoMag liner may have an important effect on FRC equilibrium and decay, even when symmetric about the FRC

classical   anomalous (Chodura)
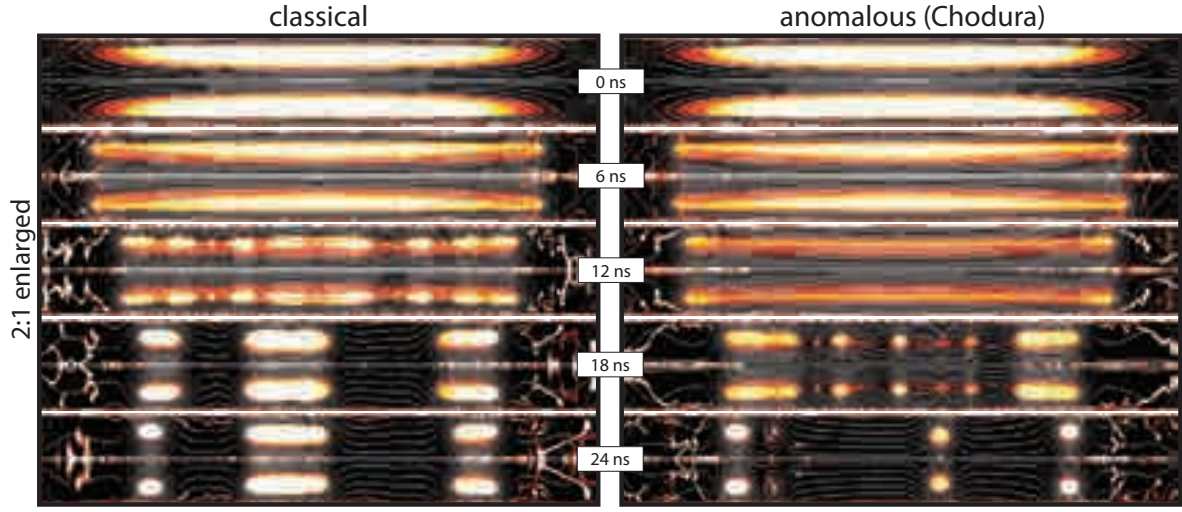
$r_c = 0.61$ mm , $B_0 = 1200$ T , $T_{e0} = 18$ keV , $x_s = 0.89$, $E_0 = 15$, $\tau_{\phi\,RRclas.} = 49\mu$s , $\tau_{\phi\,LSXtheo} = 0.8\mu$s
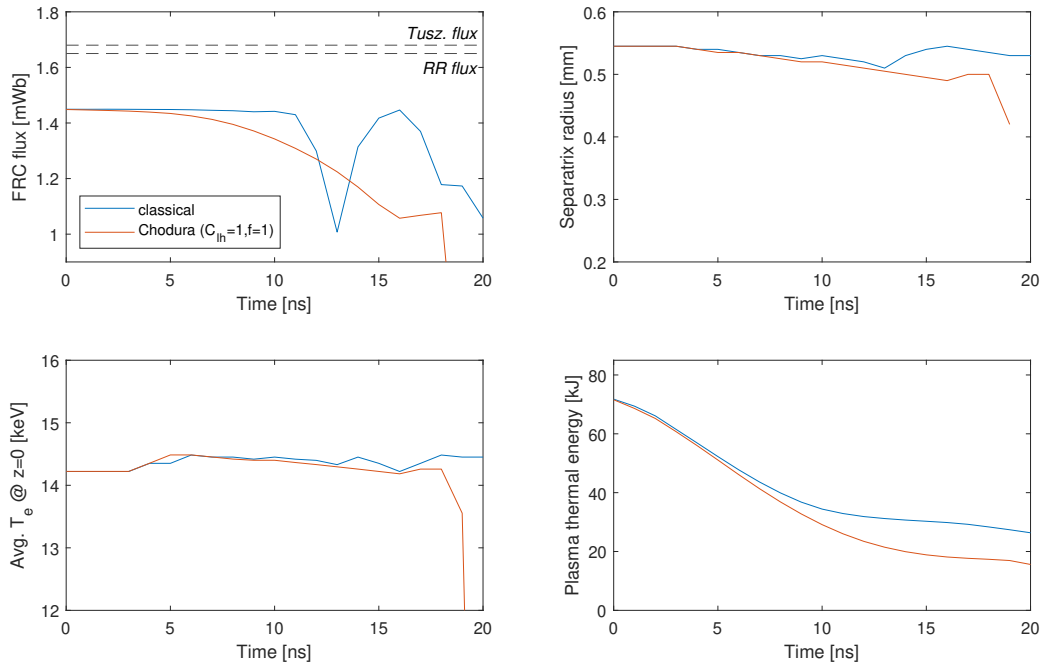
Figure 4.5: Immediate ($\sim$10 ns) tearing of a burning, extremely elongated FRC initialized in Kraken. This is the "start of burn" FRC stage from Slutz [31] with initial parameters listed in Table 4.1, for both classical and Chodura ($C_{lh} = 1$, $f = 1$) anomalous resistivity treatment. In the images, the FRCs are even more elongated than they appear since the aspect ratio has been adjusted to enhance detail. The disagreement of initial parameters in the plot from the analytic input shown in Table 4.1 is due to the inaccuracy of the analytic solution at extreme elongations and the rapid relaxation to more realistic equilibrium from the estimated parameters.
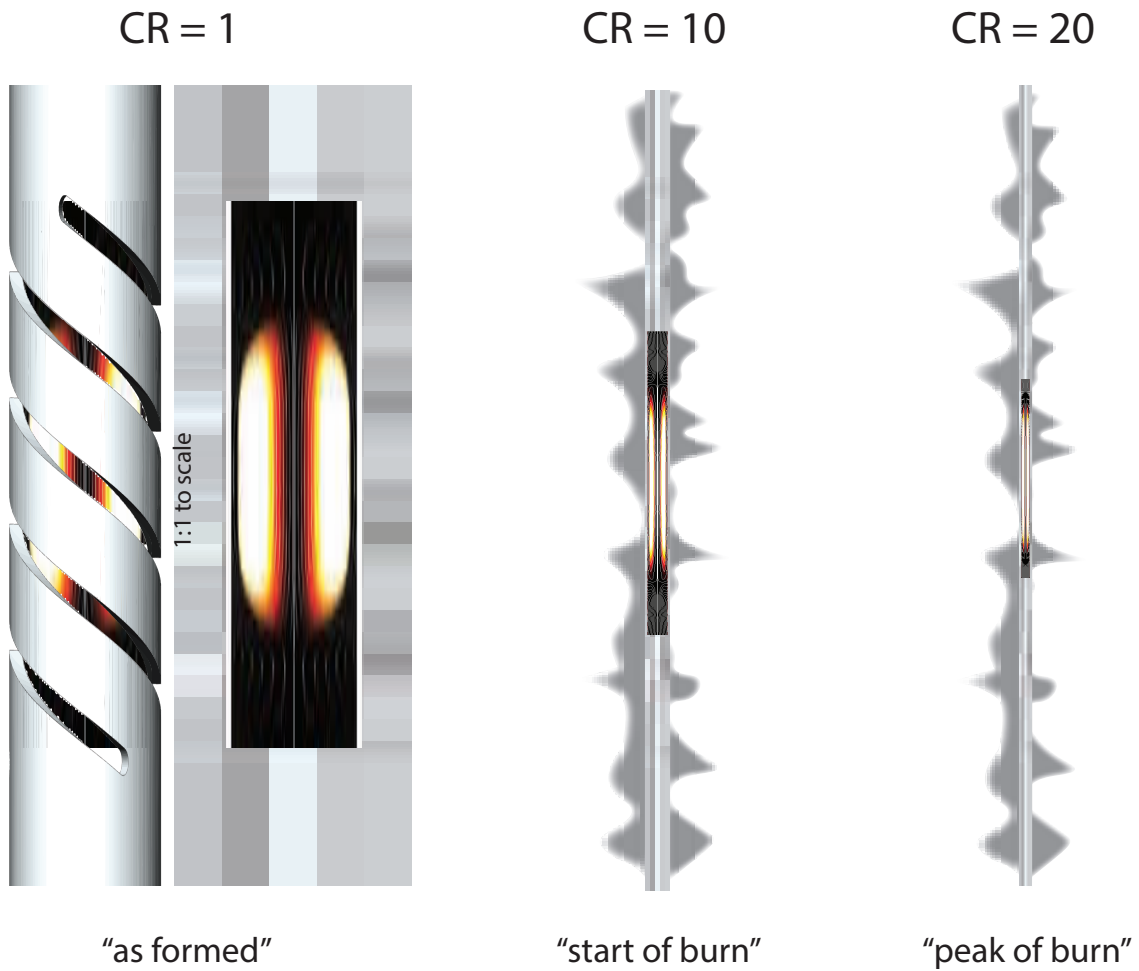
Figure 4.6: Three stages of the Slutz LASNEX implosion [31] as initialized in Kraken, shown vertically (as would be installed on the Z-machine) and to-scale in a fictionalized AutoMag liner for visualization purposes. Grey wisps depict MRT instability structures that would develop in a real Z-pinch and limit the effective convergence ratio to 20–30. Parameters of these three FRC states are summarized in Table 4.1.

.

mid-plane ($z = 0$). If the gradients are not symmetric about the mid-plane, the FRC experiences a net force axially. This effect is taken advantage of in translation experiments [24] to eject FRCs from their formation tube up to supersonic speeds. In AutoMag experiments, if breakdown of the AutoMag dielectric does not occur symmetrically, it is possible that undesirable field gradients could be produced and locked into the imploding liner. Such gradients could eject the FRC before complete burn.

The timescale for ejection of an FRC in a field gradient can be estimated as:

$$\tau_{eject} \sim \sqrt{\frac{2L_x}{a}} \tag{4.11}$$

where the X-point length L_x is used as an axial length-scale and a is the acceleration of the FRC. The acceleration a can be expressed from the net B_e force as:

$$a \approx \frac{\tilde{B}_e^2}{2\mu_0} \frac{\pi r_s^2}{M} (f^2 + 2f) \tag{4.12}$$

where $\tilde{B}_e$ is the average external field, M is the mass of the FRC plasma, and $f \ll 1$ is the fractional field gradient across the FRC; for example, $f = 0.1$ if B_e is 10% greater at one X-point of the FRC than at the other. The mass of the FRC can be estimated from its simpler parameters as:

$$M \sim \pi \, r_s^2 \, L_x \, m_i \, n_m \tag{4.13}$$

where $n_m = \frac{\tilde{B}_e^2}{4\mu_0 k_B T}$ is the maximum ($\beta = 1$) deuterium ion density in the FRC. With these approximations, the ejection time can be succinctly expressed as:

$$\tau_{eject} \sim \sqrt{\frac{L_x^2 m_i}{k_B \, T(f^2 + 2f)}} \tag{4.14}$$

which is only dependent on the FRC length scale, temperature, and the applied field gradient.

The accuracy of Eqn. 4.14 was tested in simulation for the baseline FRC of Sections 4.4 – 4.6 and the hotter "as formed" FRC of Section 4.7. The "start of burn" FRC was simulated as well to test the validity of Eqn. 4.14 at thermonuclear conditions, but with an E of 5 and x_s of 0.6 to prevent the tearing phenomenon. For a field gradient of 25% ($f = 0.25$), τ_{eject} is predicted to be about 800 ns and 320 ns for the two non-thermonuclear FRCs, respectively. With a field gradient of 15%, $\tau_{eject} \sim 9$ ns for the burning FRC. $\sigma_{\text{flare}} = 1$ was used as a worst case scenario for ejection (weaker field downstream). The unidirectional field gradients were added to the initialization section by multiplying the flux function *outside* the separatrix by a factor dependent on axial position offset from the mid-plane (defined as $z = 0$), such that the field at the mid-plane and the average applied field was unchanged.
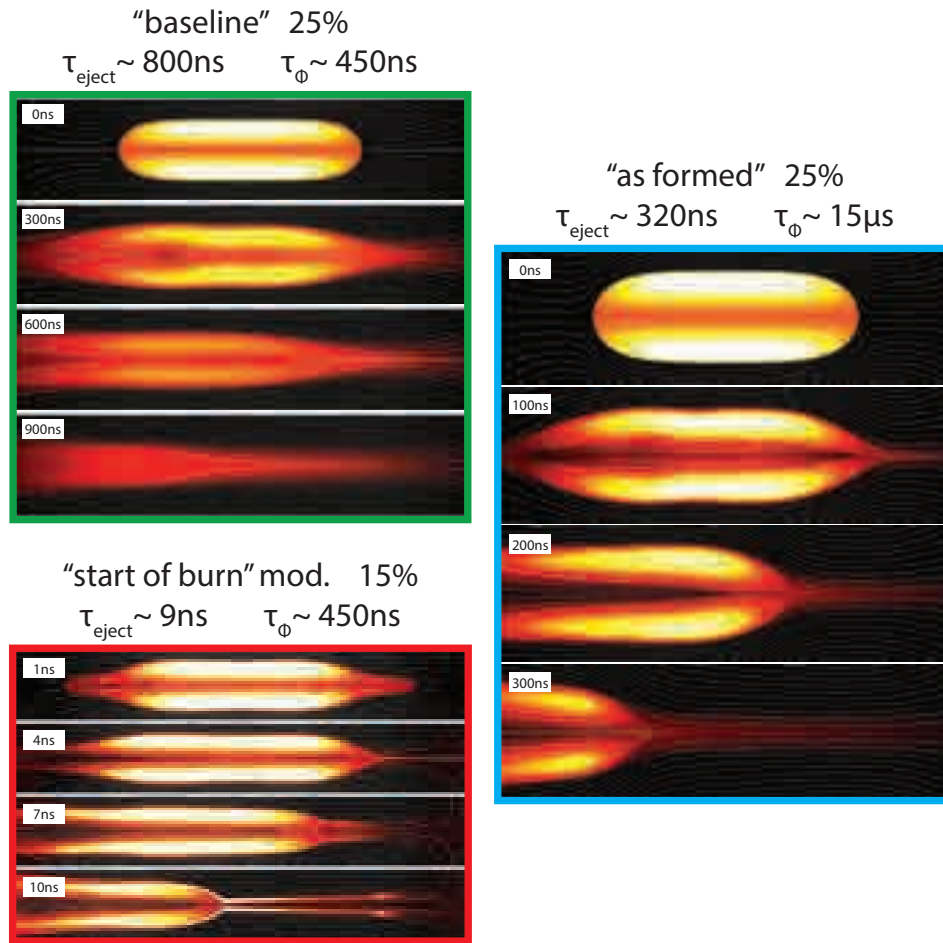
Figure 4.7: Simulation of the baseline (top left), "as formed" (right), and "start of burn" modified (bottom left) FRCs with external field gradients of 25%, 25%, and 15% respectively. The gradient results in a net force axially that accelerates the FRC to the left out of the reversed field region on a timescale remarkably consistent with that predicted by Eqn. 4.14. For the baseline (top) FRC, the ejection time is longer than the anomalous decay time constant τ_ϕ.

Fig. 4.7 shows the results of the gradient simulations which are remarkably accurate to the estimate of Eqn. 4.14. Since the baseline FRC has predicted ejection time longer than its (Chodura) anomalous decay time, it is expected to be almost fully decayed as it is ejected – confirmed in the left sequence of Fig. 4.7. The "as formed" FRC, in contrast, being hotter and less massive, is ejected in a few hundred nanoseconds, long before decaying. Similarly, the "start of burn" FRC is ejected in the predicted time of about 9 ns.

A compressed FRC is most vulnerable to ejection at peak convergence, when the asymmetric force on the FRC's mass is at a maximum. This dependence is captured in Eqn. 4.14 by the dependence on temperature, which will maximize at peak compression. Fig. 4.8 plots ejection time from Eqn. 4.14 as a function of burn temperature for various f values, assuming a characteristic
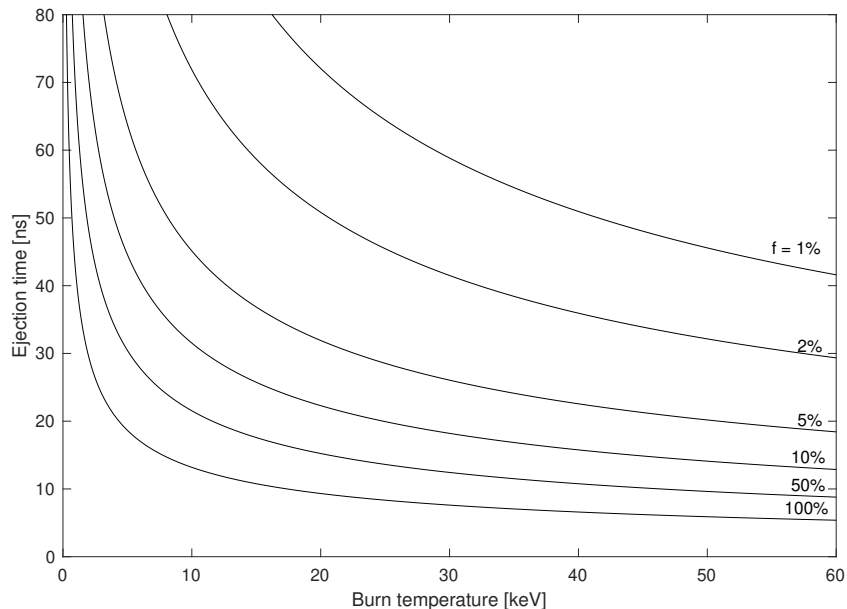
Figure 4.8: FRC ejection time predicted by Eqn. 4.14 for characteristic length $L_x = 1$ cm as a function of burn temperature and fractional field gradient f along the separatrix.

length-scale $L_x = 1$ cm.

The burn time of the FRC that was proposed for compression on Z in Ref. [31] is approximately 10–20 ns, with a burn temperature of around 50 keV. According to Fig. 4.8, extreme axial field gradients approaching 50% might be tolerated before such an FRC would risk ejection. Despite this apparent gross safety margin, uniformity of AutoMag-produced fields after the breakdown process should be thoroughly investigated on MA-class pulsed-power drivers to ensure limits do not risk being exceeded.

Now, rather than a unidirectional field gradient, we briefly explore a bidirectional field gradient effect – a magnetic mirror. As shown in Table 4.1, the burn simulations reported were performed with a large σ_{flare} value, since the applied field lines will be fairly straight near peak compression since the FRC has axially contracted during the implosion (see Fig. 4.6). Another effect that may occur in real FRC liner implosions is an axially asymmetric stagnation.

Above and below the FRC, the back-pressure on the imploding liner is smaller than in the region containing the FRC. Therefore, the top and bottom regions of the liner would stagnate first, amplifying the field there and effectively creating a magnetic mirror around the FRC. This mirror effect was simulated for the "start of burn" case by linearly ramping the conserved flux to 4x its initial value beyond the X-points of the FRC. While the initial equilibrium was seen to change, the stronger mirror fields did not seem to significantly affect the decay or tearing of the burning FRC, as shown in Fig. 4.9. It can be concluded that any mirror effects which might occur near stagnation

are minor and not necessarily beneficial or detrimental to the FRC burn.

4.9   Synthetic Imaging

The simulated FRCs presented so far in this chapter have shown fairly hollow *density* profiles – consistent with the hollow *visible emission profiles* seen in experimental imaging on MAIZE (see Chap. 3) – which were assumed to be FRCs given that this unique profile is obtained only under the correct conditions.

To confirm the apparent correlation between the ring-like plasma density profile in an FRC and the ring-like axial emission in the visible range at this density, synthetic visible axial images were generated for the baseline FRC of the previous sections, as well as an FRC with parameters more likely found on MAIZE ($r_c = 8.25$ mm, $B_0 = 10$ T, $x_s = 0.5$, $T_0 = 50$ eV, and $E = 5$). The synthetic analysis was performed for a purely axial view ($\phi = \theta = 0$) using the SpK code [96] developed specifically for GORGON, from which the Kraken code evolved. All synthetic images presented in this chapter included opacity calculations and impurities of 1% silicon, 1% oxygen, and 1% nitrogen to match the maximum expected quantities (though it was found that the visible emission changed negligibly with these opacity/impurity toggles across a realistic range of densities and temperatures). The emission profile determined by the code included a "filter" for only the visible light that would be seen by a UHSi-like camera, with spectral response data provided by the manufacturer of the PPML camera used for MAIZE experiments.

Since the simulations were 2D in r-z space, the post-processed "image" from the SpK code is a radial vector of intensity values, which was 'spun' around the axis as a contour plot to produce the actual circular synthetic image (i.e. the synthetic images are always axisymmetric, like the simulations). Synthetic images for the aforementioned FRCs after 100 ns of evolution are presented in Fig 4.10, to the right of their respective simulation density contour images. Also shown are plots with the normalized emission profiles and normalized density at the mid-plane and axially integrated.

To the author's surprise, the synthetic images do not show nearly as hollow of an emission profile as expected given the density profiles of the simulated FRCs. It was thought that since the temperature is relatively uniform throughout the FRC, the emission profile should follow the axially integrated density profile. The reason for this discrepancy lies in the details of the SpK spectral calculations and is not fully understood at this time. The issue persists throughout the FRC decay and across a broad range of initialized FRC parameters, firmly disagreeing with MAIZE experimental results.

Fortunately, the particularly hollow emission profile of the MAIZE FRCs is explained by the specific dynamics and shape of the applied field on MAIZE, as will be shown in the next section,
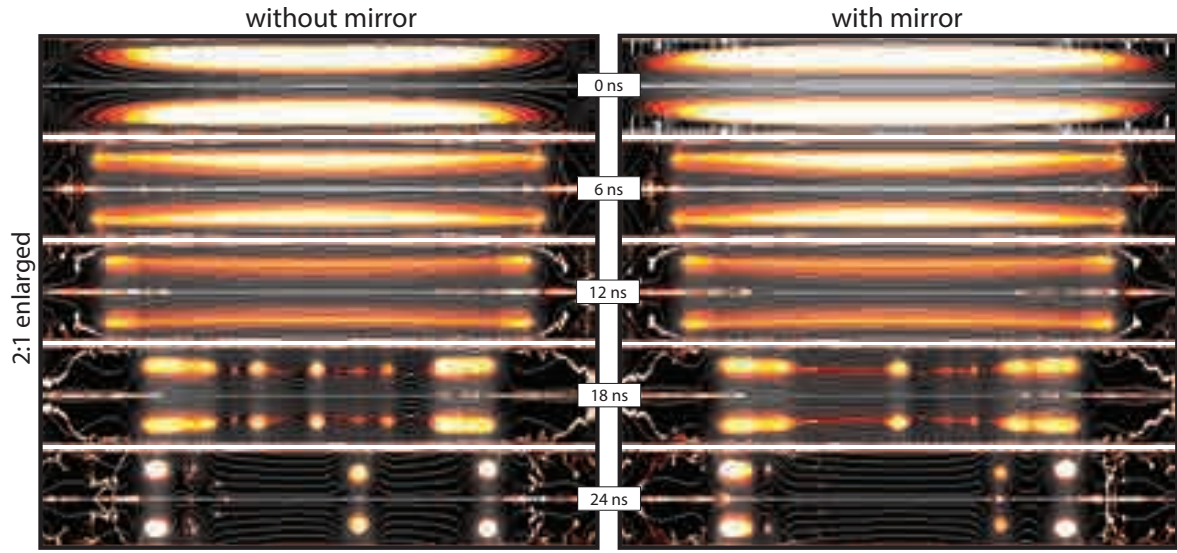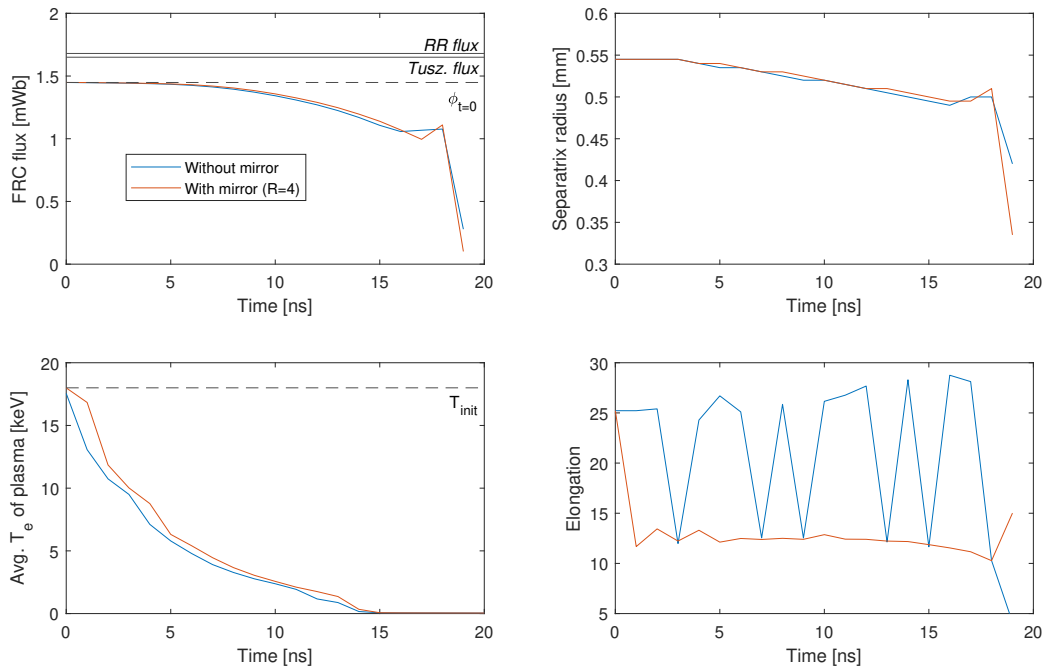
Figure 4.9: The "start of burn" FRC stage from Slutz and Gomez [31] with initial parameters listed in Table 4.1 and the Chodura ($C_{lh} = 1$, $f = 1$) anomalous resistivity treatment. One initialization amplified the applied external field by 4x beyond the ends of the FRC, creating a magnetic mirror effect which might occur in asymmetric stagnations. The mirror did not significantly effect the decay or rapid tearing behavior of the FRC. Jagged effects in the elongation traces are thought to be a numerical issue with the analysis code, not a result of plasma behavior.
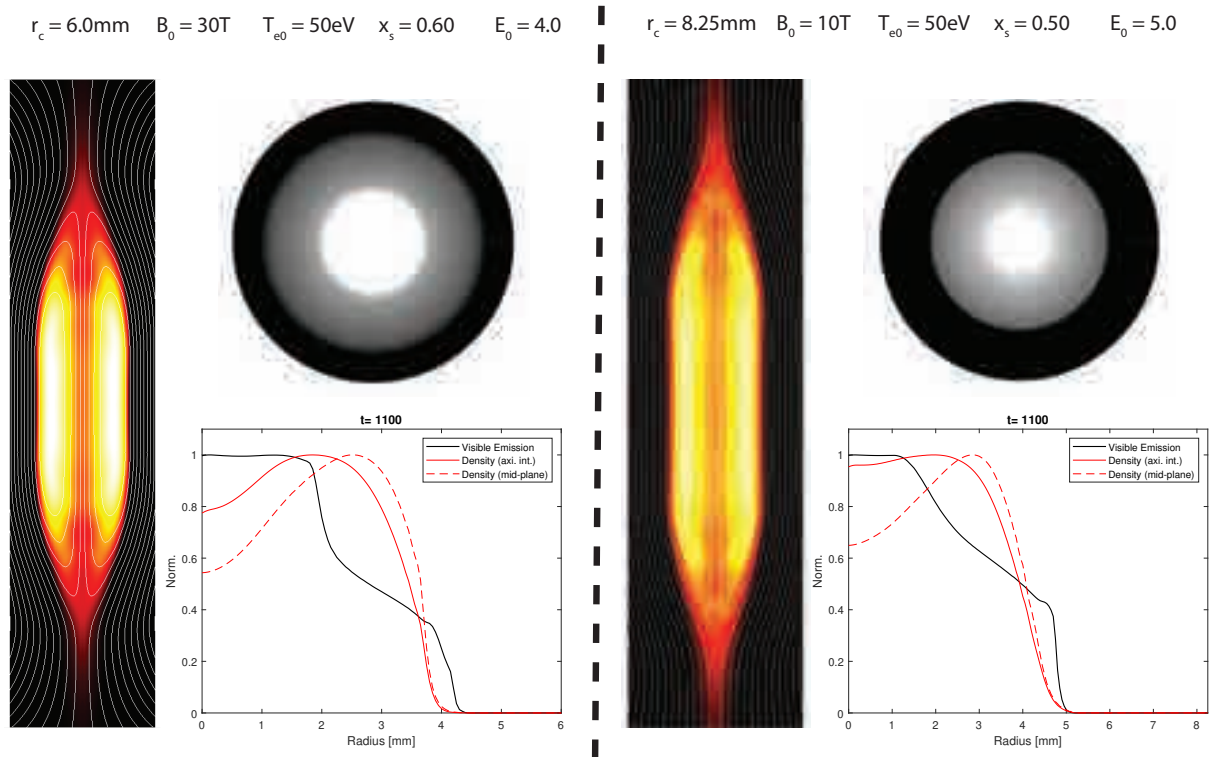
Figure 4.10: Synthetic visible images generated from the SpK code [96] operating on Kraken output data for the "baseline" FRC of previous sections as well as a more MAIZE-like FRC after 100 ns of evolution. Also shown are plots with the normalized synthetic emission profiles and normalized density, both at the mid-plane and axially integrated. Unexpectedly, the synthetic images do not show nearly as hollow of an emission profile as expected from the integrated density profile.

4.10 MAIZE-like FRC Formation Simulations

As mentioned in the previous section, synthetic visible images of high-density FRC initialization and decay simulated in Kraken did not show the expected hollow profiles seen in MAIZE experimental images. This was suspected to be at least in part due to the particular applied field shape of the MAIZE hardware, as well as the dynamic nature of formation effects (as opposed to starting with pressure-balanced equilibrium).

To simulate plasma dynamic behavior in the unique hardware of MAIZE *a posteriori*, a Kraken scheme was devised in which pure, cold deuterium plasma was initialized in a column the size of the quartz inner radius (6 mm) at an initial temperature of 0.3 eV (typical of the ZPI temperatures measured spectroscopically on MAIZE). A uniform bias field was also embedded throughout the initialized volume, including in the plasma. However, in the vacuum region just beyond the initial plasma radius, the flux function was continuously updated each time step to a trapezoidal function representing the MAIZE field profile including bias field, as plotted in Fig. 4.11. The shape of the simulated profile can be compared with the actual MAIZE profile of Fig. 3.23. The trapezoidal section of the profile was temporally amplified as a sinusoidal function with 200 ns risetime (1.25 MHz), similar to most of the experimental current traces on MAIZE.

The simulated FRC formation process in Kraken is depicted in Fig. 4.12, which was initialized with 0.3 eV deuterium plasma at 1.1×10^{-4} kg/m^3 (0.5 Torr fill density at room temperature). Synthetic images are also shown corresponding to the times depicted in the density contour/field line plots. Anomalous resistivity of both Chodura and D and K formulations (see Section 4.6) was successfully used to model FRC formation, and it was found that classical resistivity allowed formation in most circumstances as well (likely due to anomalous numerical diffusion).

D and K anomalous resistivity has been found in the literature [66] to be the more appropriate treatment for the reconnection/formation phase; indeed it was found that the Chodura treatment caused very rapid heating and decay (10s of ns) after formation, inconsistent with experiments. Other than this phenomenon with Chodura, the simulations did not qualitatively change much with the choice of anomalous resistivity parameters (as judged by the contour plot, synthetic image videos, and resultant FRC parameters). Furthermore, the simulations seemed insensitive to the initialized plasma temperature in the range 0.2–1.5 eV. The simulations depicted in Fig. 4.12 and throughout the rest of this section used D and K with $C_{lh} = 1$ and $f = 1$ and initial plasma temperature of 0.3 eV.

SpK synthetic images of the formation process, at the conditions of Fig. 4.12, clearly depict a more hollow profile to the FRC than the static decay simulations of previous sections. This is an
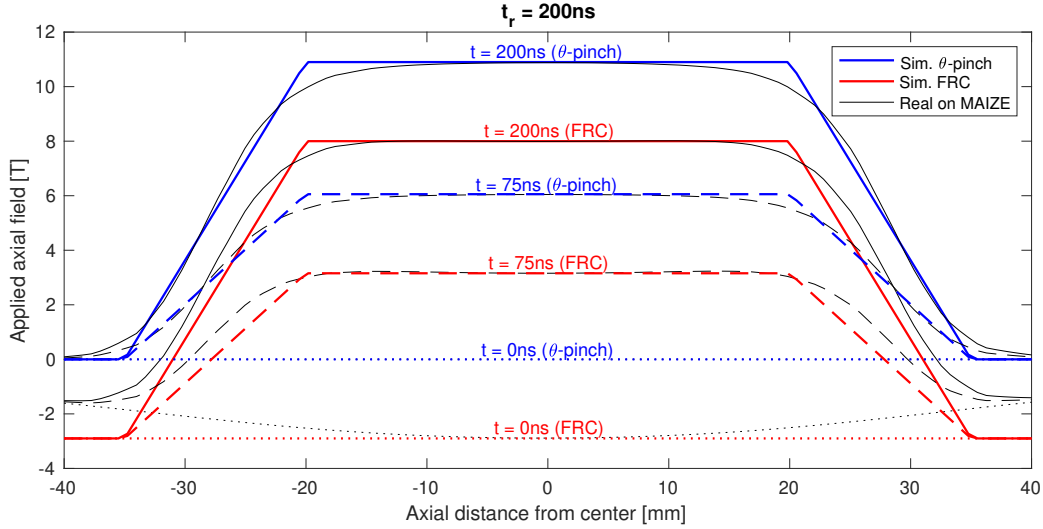
Figure 4.11: Trapezoidal field profile applied from the boundary in Kraken formation simulations, representing the approximate shape of applied fields on MAIZE (as simulated in CST). The field strength in the trapezoidal region is amplified in a sinusoidal fashion by altering the flux function at the boundary. $B_0 > 0$ is the flat-top (final) applied field near the center and $B_b \leq 0$ is the uniform bias field. In this case, $B_0 = 10.9$ T and $B_b = 0$ T for the θ-pinch; $B_0 = 8$ T and $B_b = -2.9$ T for the FRC. The sinusoidal risetime to peak field in both cases is $t_r = 200$ ns (1.25 MHz).

exciting result that more closely matches the unique experimental results. However, it was found that only simulations started with plasma density on the lower end ($< 2 \times 10^{-4}$ kg/m$^3 \sim 1$ Torr fill) resulted in the unique hollow visible emission rings. Higher-density simulations still formed FRCs under a wide range of parameters, but the emission profiles were not as hollow as at lower densities.

To further demonstrate the aforementioned density effects on FRC synthetic emission, two partial experimental sequences and four simulation sequences are presented in Fig. 4.13. The experimental results were performed at 1 and 2 Torr fill pressure with active ZPI, but the hollow imaging results clearly match better to simulations with initial density corresponding to fill pressures 3–10 times lower. Another comparison between experiment and simulation is shown in Fig. 4.14 at different bias field and for a longer timescale (500+ ns) – beyond current reversal in simulation (MAIZE current likely does not reverse due to self-crowbar effects). In this comparison, the terminus of the experimental FRC is drift/wobble into the wall, while the simulated FRC terminates at $t \sim 400$ ns when the applied sinusoidal field reverses. The simulation does not appear to fully capture the re-strike (or self-crowbar) phenomena which allow the MAIZE FRC to live longer. Interestingly, concentric striations can also be seen in the experimental images, consistent with the striated rings seen in synthetic images.

In FRC MAIZE experiments, plasma emission without the characteristic hollow structure was assumed to have failed in producing an FRC, since the non-hollow emission was more suggestive
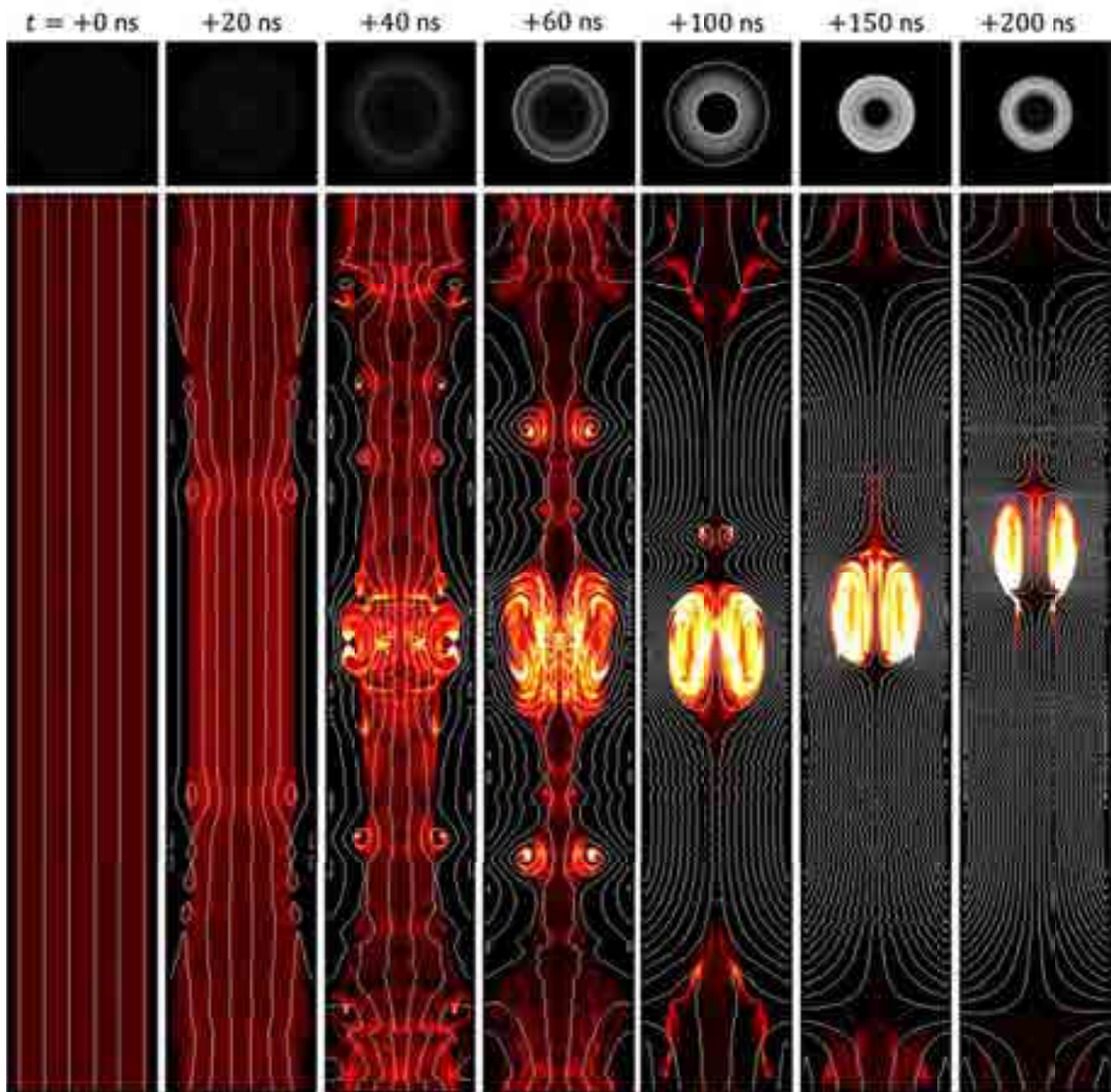
Figure 4.12: An FRC formed in Kraken using sinusoidal modification of the flux function just inside the flux-conserving boundary of the simulation. The flux function at the boundary is modified to approximate that of MAIZE experiments, with plateaued reverse applied field within and bias field beyond the load helix region (see Fig. 4.11). This particular simulation used a 6 mm radius deuterium plasma column initialized at 0.11 g/m^3 (0.5 Torr fill at room temperature) and $T_e = T_i = 0.3$ eV initial temperature, a bias field of -1.5 T, and an applied final field of 8 T with 200 ns risetime. Anomalous resistivity of the D and K formulation is used with $C_{lh} = 1$ and $f = 1$. Synthetic images normalized to each other are also shown – note the hollow emission profile that develops reminiscent of real MAIZE experimental images.
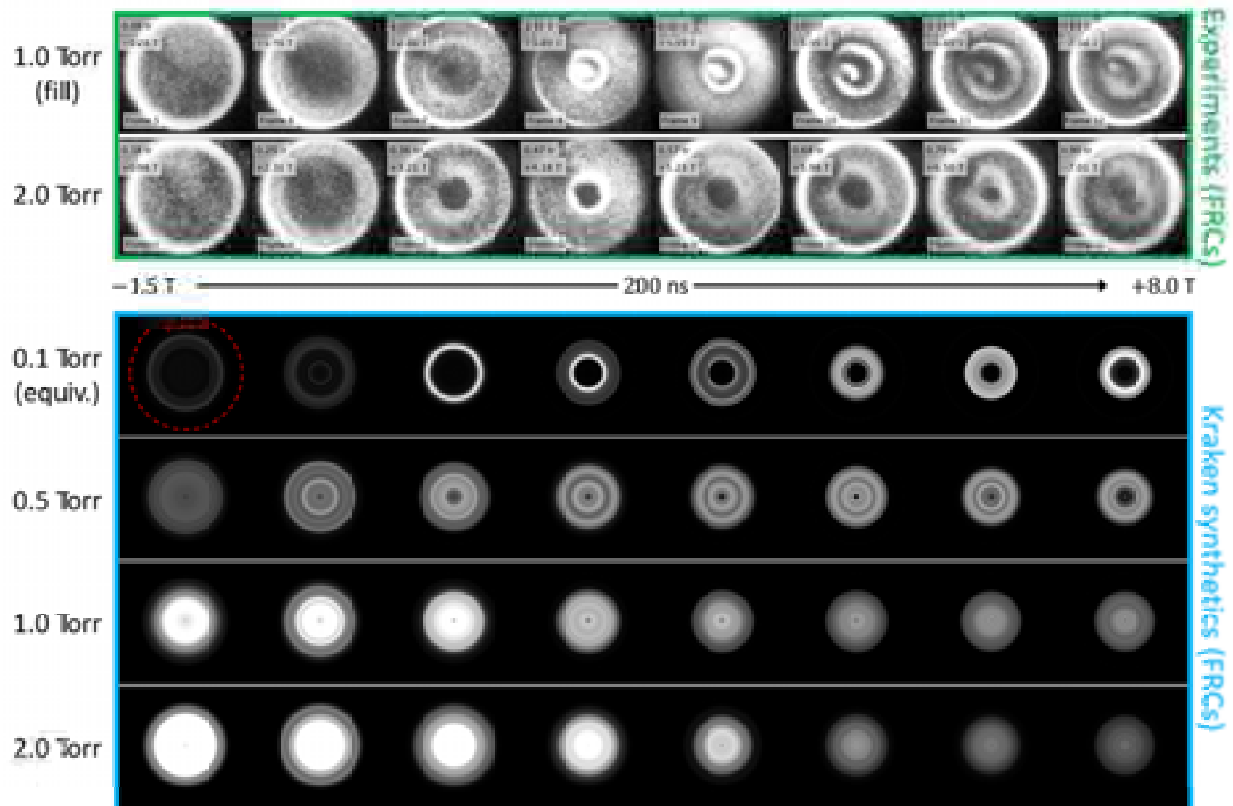
Figure 4.13: Comparison of *a posteriori* Kraken simulation synthetic images to partial experimental image sequences for two similar MAIZE FRC shots at -1.5 T bias field. The hollow profile of the experimental profiles better matches lower initial pressure simulations, suggesting a significant fraction of gas is lost from the discharge tube during ZPI, despite the relatively low thermal velocity.
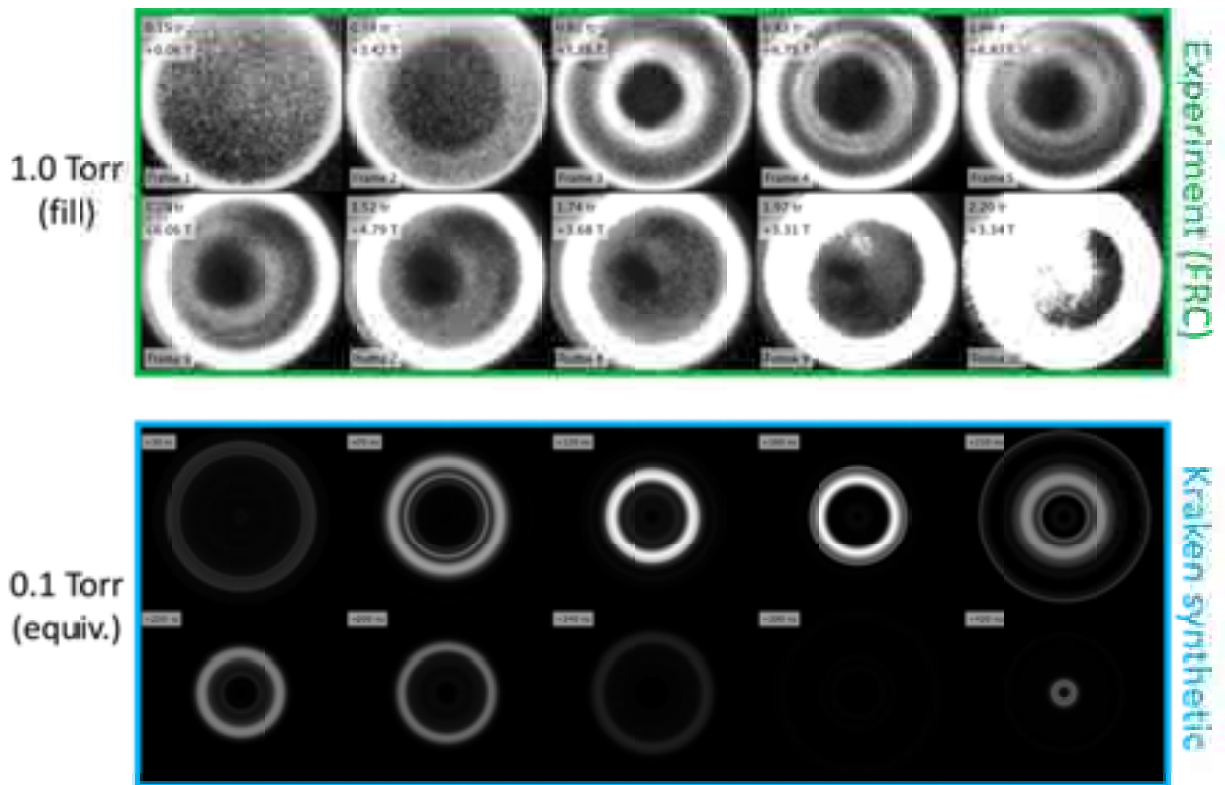
Figure 4.14: Comparison of *a posteriori* Kraken simulation synthetic images to the full experimental image sequence of a MAIZE FRC shot at -2.9 T bias. Again, the hollow profile of the experimental profile best matches a lower initial pressure simulation, suggesting a significant fraction of gas was lost from the discharge tube during the ZPI, despite the relatively low thermal velocity.

of a θ-pinch shot. The inability to produce ring-like structures at higher fill pressure (e.g. 10 Torr) was assumed to be failure, though now it is apparent from simulation synthetic imaging that some of the imaged plasma structures may indeed have been FRCs.

For example, Figs. 4.15 – 4.17 present three experimental sequences for θ-pinch shots at 2 and 10 Torr fill and an FRC shot at 10 Torr, with their corresponding simulations. The experimental images might match better with simulations at lower initial pressure, as in previous figures of this section. Nevertheless, the point is illustrated that it becomes difficult to distinguish between successful FRCs and failed FRCs (i.e. θ-pinch shots) at higher densities based solely on visible imaging profile. Note that the lower-pressure θ-pinch shot of Fig. 4.15 shows a clear high-mode 3D instability (fluting?), which cannot be captured in the 2D axisymmetric simulations.

The simulations that were compared to experiments in Figs. 4.13 – 4.17 also generated extremely high (many keV) temperatures during both θ-pinch and FRC shots, with the latter predicted to give relatively large thermonuclear DD neutron yields on the order of $10^8 - 10^{10}$. During MAIZE experiments, neutron diagnostics were never fielded because it was not expected that keV temperatures could be reached.

An abbreviated campaign was undertaken in which a dozen or so θ-pinch and FRC shots were successfully executed as determined by imaging. Four bubble detectors were placed on the MAIZE steel chamber lid approximately 20 cm from the center of the discharge tube. Two each of the detectors had sensitivity of 15 and 33 bubbles/mrem, corresponding to a single bubble yield for the most sensitive detector of approximately 10^8 neutrons. No bubbles were logged for the duration of the abbreviated campaign. A beryllium detector was also fielded on the chamber lid with floor/noise sensitivity of approximately 5–15 counts or 10^7 neutron yield. Counts of 9–14 were registered each shot, suggesting yield below the floor of the detector.

Based on the lack of neutrons produced in experiments and the realization that radiation losses were not included in the simulations, it can be assumed that the extreme temperatures during formation simulations are artificial. This may explain the observed pressure discrepancy between simulation and experiment: if the simulation were to regulate to a more realistic temperature via radiation, then the same pressure distributions and plasma emission behavior might be achieved with higher density. It is hoped that by including radiation losses (and perhaps other numerical boundary control methods) to control the super-heating phenomenon, a better match to experiment (in terms of initial gas density) can be achieved. This results of this effort are left for later publication.

2.0 Torr θ-pinch
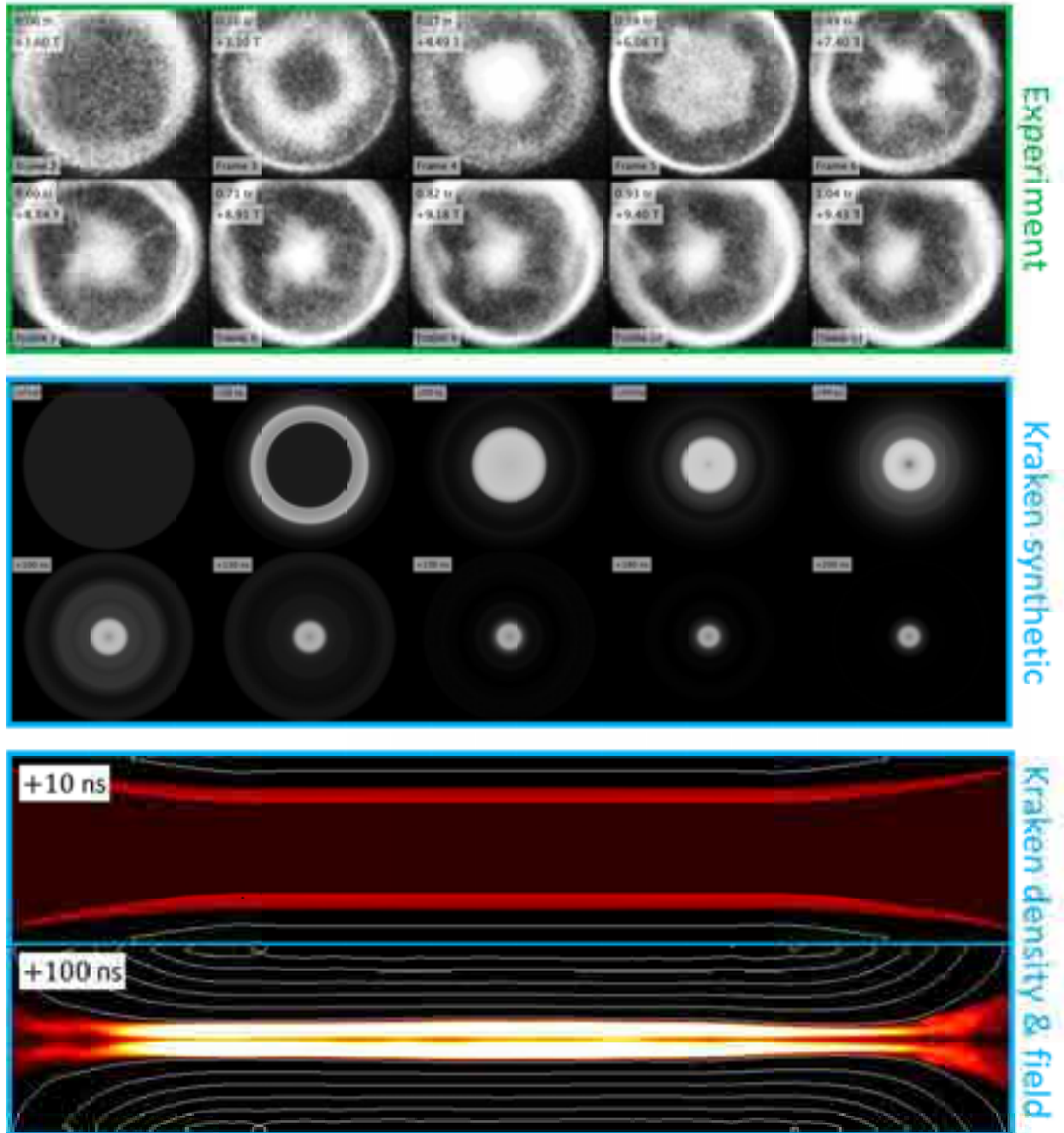
Figure 4.15: Comparison of *a posteriori* Kraken simulation synthetic images to the full experimental image sequence of a MAIZE θ-pinch shot at 2.0 Torr fill. Also shown are two simulation density and flux contours at arbitrary times from the Kraken simulation illustrating the plasma dynamics.

103
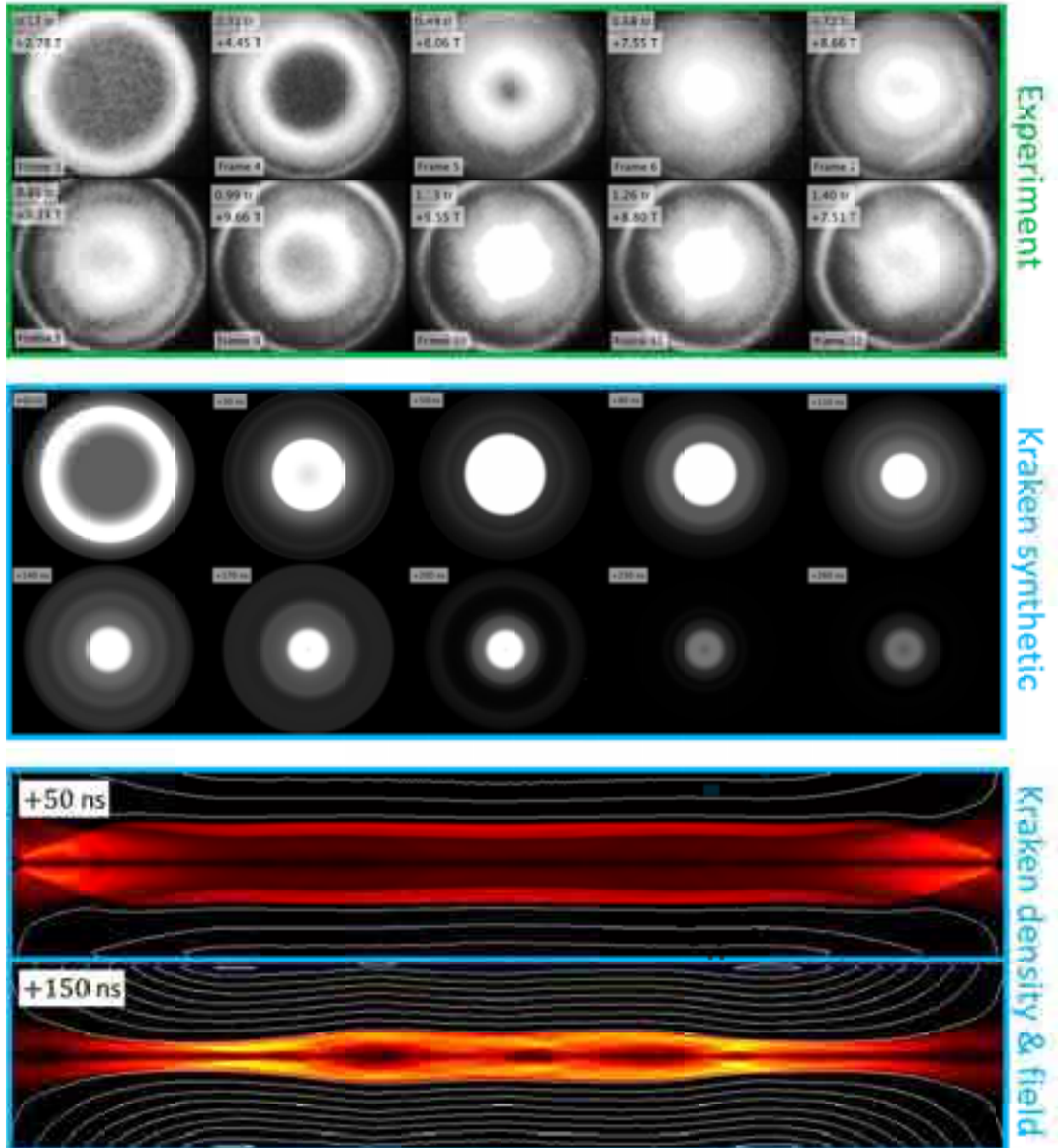
10.0 Torr θ-pinch

Figure 4.16: Comparison of *a posteriori* Kraken simulation synthetic images to the full experimental image sequence of a MAIZE θ-pinch shot at 10.0 Torr fill. Also shown are two simulation density and flux contours at arbitrary times from the Kraken simulation illustrating the plasma dynamics.
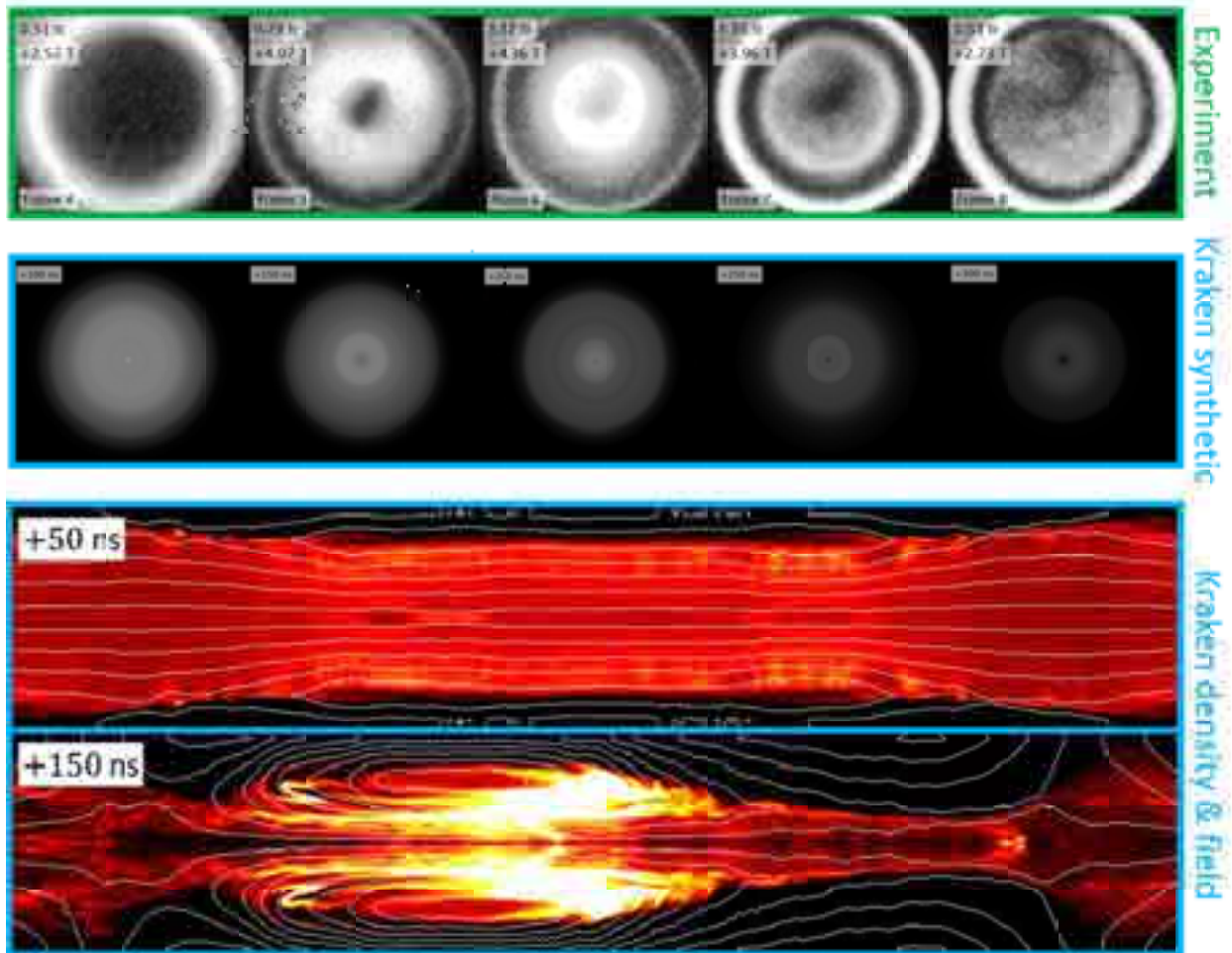
Figure 4.17: Comparison of *a posteriori* Kraken simulation synthetic images to the partial experimental image sequence of a MAIZE FRC shot at 10.0 Torr fill, −3.6 T bias. Also shown are two simulation density and flux contours at arbitrary times from the Kraken simulation illustrating the plasma dynamics.

CHAPTER 5

Conclusions and Suggestions for Future Work

Field-reversed configurations (FRCs) are an attractive closed-field line plasma target for magnetized target fusion (MTF) efforts, which may produce very interesting fusion yields on existing and future energetic pulsed-power facilities around the world. Slutz [31] has suggested creation and solid liner compression of high-energy-density (HED), centimeter-scale FRCs on the Z-machine (20+ MA, 100 ns) at Sandia National Labs. This would be done using hardware already developed for the MagLIF platform, specifically the applied bias field (ABZ) capability and AutoMag concept for fast-reversal field. Once formed, the FRC would be compressed for thermonuclear yield as the liner is imploded in less than a microsecond. Such FRC compressions to modest convergence ratio (20–30) are predicted by theory and simple 2D simulation to produce $Q_{DTsci} \sim 1$ relevant gains.

The proposal for HED FRCs in large AutoMag liners on Z begets many physics questions to be explored before a shot proposal, notably: What are the energy-coupling implications for large, shaped-pulse liner implosions on Z? Can FRCs be reliably formed in the proposed method with two separate applied field sources? What pre-ionization methods are effective and uniform, and what PI temperature is required? Are the desired FRCs predicted to have sufficient anomalous lifetime and stability to adiabatically survive the proposed compression?

This thesis attempts to shed light on some of these uncertainties with an experimental formation effort on the MAIZE LTD at the University of Michigan and a computational effort with a 2D version of the Kraken resistive MHD code provided by Chris Jennings at Sandia.

Experimental efforts on MAIZE prioritized FRC physics over AutoMag physics, and so they used thick, widely-spaced steel helices to allow multi-shot survival of the load hardware. 3D-printing in both steel and plastic was found to be invaluable for hardware. A quartz discharge tube was used as in traditional FRC experiments, rather than direct use of the dielectric-coated liner as would be needed for an integrated implosion experiment on Z. With the impedance limits of MAIZE, it was possible to produce fast axial fields on the order of 10–15 T within the volume of the load helix. It was found that *if and only if* Z-discharge pre-ionization (ZPI) was used to pre-ionize the deuterium gas fill with proper timing, and a bias field of 1–5 T was applied before the experiment, ring-like plasma formations could be seen in axial visible fast-framing images. These plasma annuli

and columns are seen to have temporal dynamics and instability structures consistent with θ-pinches when no bias field is applied, and FRCs when bias field is applied. Effective ZPI is shown to be critical to the FRC formation process. While difficult to implement and not recommended for future experiments, magnetic field measurements taken on the outside of the discharge tube with small flux loops known as "micro B-dots" indicate the presence of excluded flux to radii consistent with the imaged plasma rings/columns, consistent with (but not definitively proving) the presence of an FRC.

Formation under certain conditions is shown to be consistent, and consistency is ultimately limited by non-uniform ZPI at high fill pressure (and high s-parameter), as expected from historical experiments. No evidence of tilting instability is yet observed in experiments on MAIZE, and many of the MAIZE plasma rings appear to have lifetimes longer than the proposed compression timescale (fractions of a microsecond). Wobble and/or decompression into the wall is a common terminus for MAIZE plasma rings; higher-quality target fabrication in the future should limit magnetic pressure asymmetries which are hypothesized to exacerbate the wobble effect in MAIZE experiments.

2D axisymmetric simulations were performed in the resistive MHD code Kraken to explore the resistive decay of FRCs at the proposed energy density and applied fields for Z implosions. Analytic FRC profiles with field-flare effects (finite AutoMag length) were initialized in a flux-conserving boundary, and their decay observed with both classical and anomalous resistivity treatments. Decay times were found to match well with those predicted by classical and/or anomalous theory of historical FRC experiments. The effect of realistic field-flare and gradient effects in an AutoMag liner and their potential effects on an FRC are discussed and simulated. Highly-elongated, burning FRCs initialized in the code were found to tear apart into smaller plasmoids in less than 10 ns, consistent with the LASNEX results of Slutz [39]. The tearing occurs on the order of the desired burn time, suggesting that this is a critical effect to model correctly. Given the highly kinetic nature of the FRC at thermonuclear burn parameters, a hybrid fluid-kinetic code is desired to study this phase.

Curiously, SpK [96] synthetic visible images (axially integrated) of the FRCs simulated in Kraken *did not* indicate the expected hollow emission profiles seen in MAIZE FRC experiments and expected from the density and temperature profiles – across a wide range of parameters. To resolve this issue, Kraken simulations were prepared in an *a posteriori* sense to model the specific dynamics of formation on MAIZE by initializing a cold plasma and temporally modifying the flux function at the boundary of the simulation to approximate the MAIZE applied fields. FRCs were successfully produced using all resistivity models, and the formed FRC parameters were not especially sensitive to the resistivity model or initial plasma temperature. At initial plasma densities corresponding to lower fill pressures ($<$1 Torr), formation simulations give synthetic visible image profiles with especially hollow rings closely matching those seen in MAIZE experiments. The

hollow emission profiles achieved in low-density simulations appear to further strengthen the claim of FRC production on MAIZE. However, ring-like emission is *not* predicted for higher-density FRCs; in fact, visible emission in this case may appear as a failed FRC experiment (or θ-pinch). Therefore, in future experiments, non-hollow visible emission profiles should not be perceived as unsuccessful, as often assumed in MAIZE experiments. The lack of radiation loss in the simulations likely explains the artificially high temperatures that are produced. It is suspected that by including radiation, hollow synthetic emission profiles could be achieved at higher densities, thus yielding a better match to experiments.

In conclusion, the path to FRC compression experiments on the Z-machine is bright, and there do not seem to be any physics showstoppers so far differentiating the proposed effort from historical FRC liner compression efforts. In fact, the novel in-situ formation concept with inherent multipole stabilization may provide critical advantages to succeed in obtaining high yield, whereas previous efforts have been unable to do so [34]. There remains much work to be done before the first Z experiment can be confidently designed. This author recommends the following research paths be considered:

- **Theory**: With the closed-field line FRC, implosion/burn time is not limited by axial conduction as in MagLIF. Solid liner extended implosion times up to or beyond a microsecond could be imagined using the pulse-shaping capabilities of the Z-machine. Such implosions would not be subject to the same MRT instability growth and energy coupling considerations as MagLIF. Optimizing FRC MTF fusion gain on Z as a facility could very well be strongly dependent on optimizing the energy coupling to the solid liner implosion over a huge parameter space of pulse shapes, with full consideration of Z's specific circuit behavior, self-crowbar effects, and the achievable convergence ratio (i.e. MRT stability) of the implosion. Optimum liner dimensions and highest stable convergence obtained from this parameter scan might inform the desired FRC parameters.

- **Experiment**: A true MA-class driver of higher impedance than MAIZE (e.g. Mykonos) should be used to form FRCs with fast reversal fields closer to those of the LASNEX simulation or higher (>50 T). Such field strength will likely be destructive for the load hardware and thus might as well be done with a true AutoMag-like liner. Hardware should be conceptually designed to pressurize a dielectric-coated AutoMag liner with size and thickness suitable for implosion on the Z-machine – these will eventually need to be produced in large numbers and easily interchangeable for Mykonos and Z experiments. Bias field capability (at least up to 15 T) should be developed for Mykonos. As shown in MAIZE experiments, ZPI with a $\sim$100 J pulser is a simple but effective pre-ionization method, and axial visible imaging is a simple but effective diagnostic for FRC gross dynamics. Additional laser-based

diagnostics such as interferometry and Faraday rotation are recommended for exploration, as micro B-dot probes are likely too perturbative in an implosion-ready AutoMag design. Spectroscopic and imaging methods might be developed in the UV and X-ray range; this affects hardware design since any such diagnostics would need to be vacuum coupled to the inside of the AutoMag target.

- **Experiment and Computation (pre-ionization)**: ZPI is a fairly crude and inexpensive method of pre-ionizing the gas that has been shown to work sufficiently on MAIZE and in historical experiments, and could probably work for additional experimental campaigns. However, MAIZE experiments have also shown the non-uniformities and impurities associated with ZPI-produced plasmas, and the need to incorporate HV electrodes and cabling is a challenge for Z hardware design. Thus, the exploration of other pre-ionization methods is warranted. Laser-induced ionization and heating by Z-beamlet is used at the kilojoule energy level in MagLIF experiments, while only a few dozen joules would be needed for pre-ionization for FRCs. Given the vast differences in laser energy, liner size, and gas fill pressure needed for standard MagLIF vs. FRC MagLIF, initial exploration of laser heating via computational and experimental methods is warranted.

- **Computation (FRC)**: FRCs represent a unique computational challenge due to their hybrid kinetic and fluid-like nature. The additional 3D challenge introduced by helical formation (i.e. AutoMag) makes integrated simulations quite ambitious. First, in a 3D fluid code such as Kraken, it is recommended to study the formation stage using dynamic applied field input with anomalous resistivity. This is suspected to point to maximum limits on density for successful and/or repeatable FRC formation (as limited by the viscosity/violence of the formation event). Second, a hybrid fluid-kinetic code such as Chicago could be used to study the tearing phenomenon at high compression, which may limit the achievable burn time. It is hoped that such tearing might be limited in growth rate by the gyroviscous effects captured in the hybrid code. A hybrid code might also be used to study tilt and rotational stability of the desired FRCs throughout the stages of compression.

Given the favorable results presented in this dissertation, this author believes that the inertial confinement fusion program at Sandia should pursue solid liner FRC compression experiments on the Z-facility, beginning with the aforementioned suggestions for research. ☢

APPENDIX A

Analysis of Two Fusion Reactor Designs Based on Magnetic Electrostatic Plasma Confinement (MEPC)

A.1   Introduction

Superior magnetohydrodynamic stability can be obtained in a magnetic confinement system with open field lines, though loss of plasma along these open field lines must be greatly inhibited somehow for a realistic net-gain reactor. As demonstrated in the tandem mirror concept [97], direct control of ambipolar electric fields can be used to reduce end losses in a magnetic mirror system.

The same control can be applied to magnetic cusp arrangements (see Figs. A.1 and A.2), which have further stability advantages: global favorable curvature (discouraging interchange/ballooning modes) and a magnetic null region to randomize magnetic moments (discouraging loss-cone and other kinetic instabilities). With sufficient heating power, magnetic cusp-confined plasmas can remain quiescent at $\beta \to 1$ and beyond; i.e. the plasma pressure pushes out on the magnetic field and 'inflates' the cusp, forming a bulk, field-free plasma volume surrounded by a thin, magnetized sheath [98] [99] [100]. Experiments in a quasi-spherical cusp confinement device known as the "Polywell" [101] (see Fig. A.2) have shown enhanced electron confinement in the high-β 'inflated' state [102]. A disadvantage of global favorable curvature is that it requires at least one ring/line cusp, through which leakage can be excessive.

Simple tandem mirrors use separately heated plasma in two end-cells to create a potential barrier for particles leaking from the main mirror region. Alternatively, voltage can be applied directly via electrodes in contact with the leaking plasma, as shown in Fig. A.3. Typically, the anode electrodes, magnet coils, and vacuum chamber are at ground potential, while cathode electrodes are positioned to reflect electrons emanating from point and ring cusps.This technique is known in the literature as electromagnetic or magnetic electrostatic plasma confinement (MEPC). MEPC has received the most attention in the Soviet Union by Oleg Lavrent'ev at the Kurchatov Institute [105], and in the United States by Thomas Dolan. In the 1990s, Dolan wrote an excellent summary and scaling analysis of MEPC [106] [103], inspiring this work.

Lavrent'ev, whose fusion proposals inspired Andrei Sakharov, continued to advocate for an
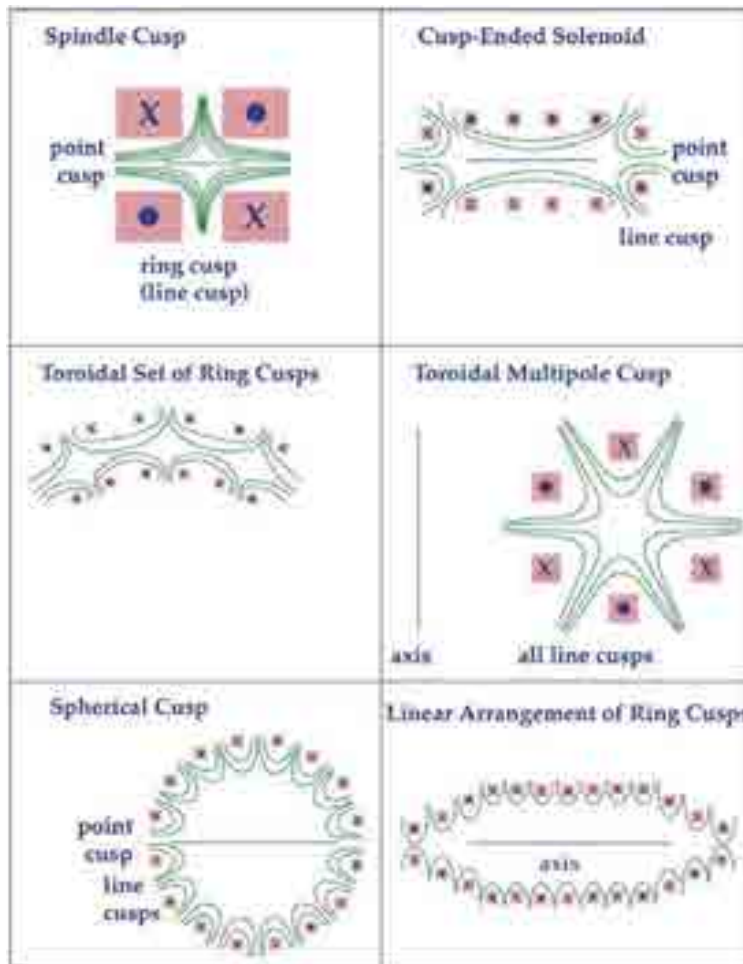
Figure A.1: Various magnetic cusp arrangements for plasma confinement. Figure reproduced from Dolan [103].
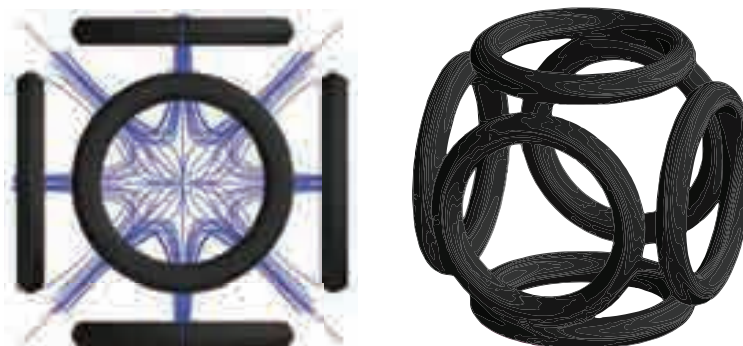
Figure A.2: The "Polywell" is another quasi-spherical cusp confinement arrangement. An embodiment of MEPC, the concept utilizes electron space charge to confine ions and has shown enhanced electron confinement at high-β. Figure reproduced from Park [104].
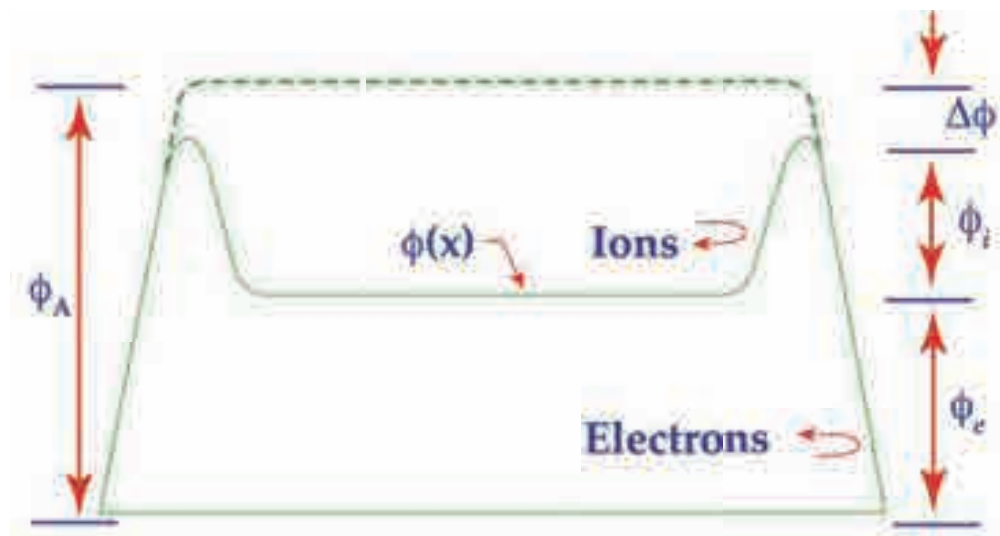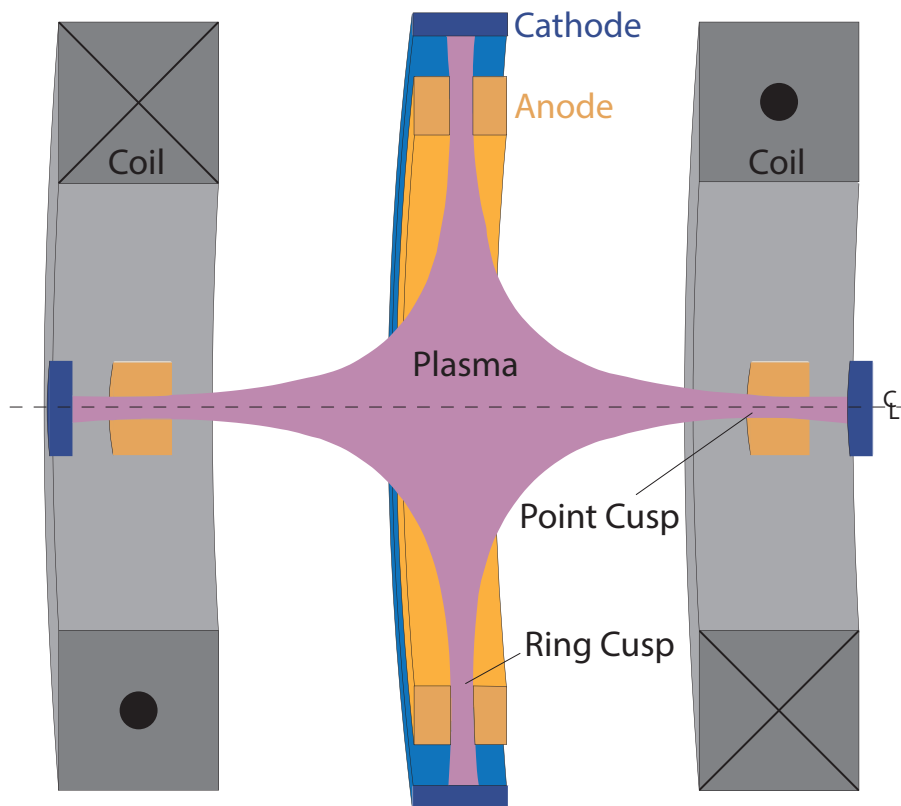
Figure A.3: Basic geometry and electric potential distribution of magnetic electrostatic plasma confinement in a spindle cusp. The dashed line is the vacuum potential with no plasma present. $\Delta\phi$ is the self-shielding potential due to space charge effects, ϕ_i is the potential barrier for ions, and ϕ_e is the potential barrier for electrons. The sum of these three potentials is equal to the applied voltage, ϕ_A. Figure reproduced from Dolan [103].

MEPC/electromagnetic thermonuclear reactor that he called "Elemag" [107] until his death in 2011. The Elemag reactor point design is very consistent with Dolan's scaling analysis.

This work will consider the thermonuclear and engineering implications of the MEPC reactor envisaged by Dolan [106], as well as a more compact reactor design which may be possible considering recent advances with high-temperature superconductor (HTS) technology.

A.2 Electric Pressure Requirements in MEPC Cusps

Before discussing the reactor designs, a common concern with electromagnetic confinement should be rebutted. Fusion reactor concepts proposing any sort of electrostatic confinement of the plasma can be suspicious, since the plasma pressure at usable fusion power density would far exceed conceivable electric pressure. For example, the electric field required to match the pressure of a plasma with $n_e = n_i = 10^{20}$ m^{-3} and T=10 keV would be 2.7 MV/cm, which is unrealistic to sustain in a reactor environment for a net-gain burn duration.

However, with careful consideration of the Maxwell stress tensor, it has been shown theoretically and computationally [108] that the magnitude of the electric field required for pressure balance is reduced when the plasma has dimensions smaller than the local Debye length. Such can often be the case in MEPC, where the electric field merely assists magnetic confinement, and where the reduced-density, anisotropic plasma streaming through the cusps may have a half-width comparable to the electron gyroradius.

The reduced electric pressure required for confinement in MEPC is:

$$p_E = \frac{\epsilon_0}{2} E_{\max}^2 = \frac{1}{4} \left(\frac{\delta}{\lambda_D} \right)^2 \cdot p_p, \tag{A.1}$$

where δ is the half-width of the plasma streaming through the cusps, λ_D is the local Debye length in the plasma stream, and $p_p = n_e k T_e + n_i k T_i$ is the local plasma pressure. With thermonuclear MEPC parameters, the required electric pressure may be reduced by a factor 4–20, bringing the corresponding applied voltages into the realm of feasibility.

Perhaps the greatest uncertainty in pursuing an MEPC reactor lies with the sustainable voltages and electric fields (and behavior of electrical insulators) in the high-radiation environment. Similar risks are encountered in supersonic rotating mirror and stabilized field-reversed fusion concepts [109] [110].

Though the plasma streaming through the cusps (mostly relativistic electrons) in MEPC is ostensibly non maxwellian and anisotropic, the dominant cusp-region instabilities encountered in MEPC experiments thus far are diocotron (Kelvin-Helmholtz) oscillations due to $\mathbf{E} \times \mathbf{B}$ shear. These, and other two-stream-type instabilities one might expect, may actually play a beneficial role by selectively removing lower-energy, trapped electrons from the cusp regions. These trapped electrons

do not contribute to bulk plasma density, but they do contribute to space charge in the gap and the self-shielding voltage drop $\Delta\phi$ (see Fig. A.3). Since the trapped electrons cannot energetically reach the bulk plasma, their active removal does not affect bulk plasma velocity-space.

While electric pressure balance is not imposed explicitly, the following reactor design analysis does account for the effect of electron space charge streaming through the cusps. This space charge effect sets the primary limitation on electron plasma density in MEPC.

A.3 Selection of HTS Reactor Parameters

For engineering simplicity, and to maximize the volume of field-free plasma per leaky cusp, a linear set of ring cusps is the preferred MEPC reactor geometry, as in Fig. A.4. Circa 1997, Dolan presented a reactor concept using low-temperature superconducting (LTS) magnets to produce a field of 6 T in the cusps (see Table A.1).

However, recent advancements with high-temperature superconductor (HTS) technology may allow a more compact, high-field MEPC reactor—analogous to the ARC/SPARC tokamak designs [111]. Furthermore, due to the simple axisymmetric geometry of a linear set of ring cusps, even higher in-plasma fields than expected in the SPARC tokamak ($\sim$12 T [3]) might be achievable.

A single, SPARC-scale HTS toroidal field coil was recently tested by Commonwealth Fusion Systems (CFS) in collaboration with the Plasma Science and Fusion Center at MIT, and demonstrated an on-coil magnetic field of 20 T [2] in nominal operation. The University of Wisconsin (in parternership with CFS/MIT) has received an ARPA-E grant to build an HTS magnetic mirror (WHAM) capable of 17 T across 5 cm bores, with a breakeven reactor design calling for 25 T across 30 cm bores [112]. In fact, HTS solenoids with fields $>$40 T have been designed [113], and 100 T HTS magnets shown to be technically feasible [114].

A cusp field strength of $B_a = 16$ T will be used as the basis for a second MEPC reactor design. Perhaps even higher fields are imaginable with HTS in the near future, but ultimately the limiting factor in HTS coil design is mechanical stress. Tolerable material stress, not HTS current density, limits the maximum field of a high-field reactor concept like SPARC [115]. Tolerable stress in the MEPC geometry is difficult to constrain without comprehensive coil engineering analysis.

The factor which limits MEPC plasma density is not the beta ratio as in tokamaks, but space charge limits in the anode/cusp gaps, where the applied electric fields must not be too distorted. Analyzing a variety of effects including acceleration and diocotron oscillations, Dolan estimates the electron density in the gaps will be approximately an order of magnitude lower than the bulk plasma density. He also conservatively assumes a Lorentzian-shaped electron density profile in the gap with half-width $w = 2\rho_e$, where ρ_e is the electron gyroradius in the anode/cusp field. Assuming these relations hold, the maximum bulk plasma electron density n_e while keeping the self-shielding

ITER
Tokamak

0   10 m

LTS Linear Set
of Ring Cusps
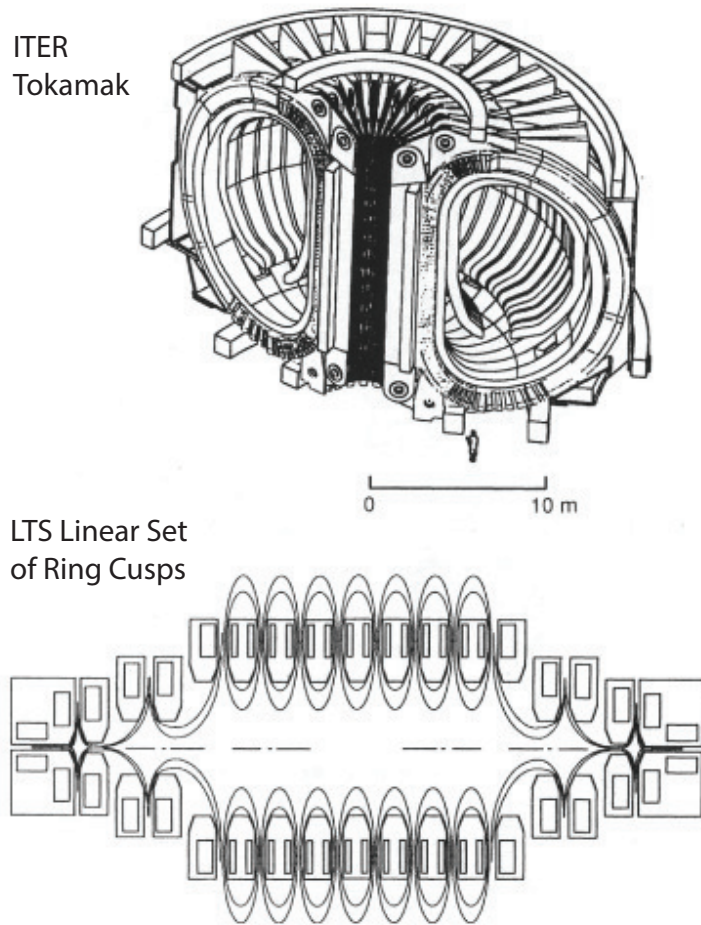
Figure A.4: A net-gain MEPC reactor (bottom) using a linear set of twelve ring cusps—at the scale envisioned by Dolan—in comparison with the ITER tokamak (top). Reflecting electrode structures for the MEPC reactor are not shown, but would be located in the cusp regions. Figure reproduced from Dolan [106].

voltage drop $\Delta\phi \leq 100$ kV is approximately:

$$n_e \leq 3.5 \times 10^{20} \; \frac{B_a}{d_{\mathrm{mm}}\sqrt{T_{e,\mathrm{keV}}}}, \tag{A.2}$$

where $T_{e,\mathrm{keV}}$ is the central plasma electron temperature in keV and d_{mm} is the anode gap in millimeters. For cusp field $B_a = 16$ T, plasma temperature $T_e = 25$ keV, and anode gap $d = 4$ mm, the maximum plasma electron density is $n_e = 2.9 \times 10^{20}$ m^{-3}. This electron density will be used for the high-field reactor design (see Table A.1).

As mentioned in the previous section, a significant area of concern in MEPC is maintenance of the applied voltage in proximity of dense, hot plasma and radiation. The larger the applied voltage ϕ_a, the greater the plasma temperature and the reactor gain Q. Dolan estimates the bulk plasma temperature as $T_e \approx T_i \approx 0.05\, e\phi_a$, using $\phi_a = 400$ kV for a plasma temperature of 20 keV in his LTS design.

There is precedent for maintenance of up to 500 kV applied voltage in the PSP-2 rotating mirror plasma experiment [110]. Lavrent'ev uses 600 kV in the latest Elemag design [107], and theoretically higher magnetic field strength with HTS might allow maintenance of higher voltages. With further consideration of advances in high-voltage and pulsed-power technology since 1997, use of 500 kV and 25 keV plasma temperature for the HTS design is motivated.

Finally, Dolan provides a simple scaling relation from Yushmanov [116] for the energy gain factor Q of an MEPC linear set of ring cusps reactor. This relation does not take into account alpha trapping and heating, which would increase the gain factor. Nor does it take into account energy losses due to neutral gas collisions or impurities, which would decrease the gain factor. Assuming a reasonable fraction of trapped electrons in the anode gaps, Dolan/Yushmanov's gain relation can be written simply as:

$$Q \approx 3 \times 10^{-6} \; B_a \; \phi_a^2 \; R, \tag{A.3}$$

with ϕ_a in kV, which gives $Q \approx 10$ for the LTS design with cusp/coil radius $R = 3.5$ meters. R is selected to be 0.83 meters for the HTS design to give $Q \approx 10$ as well. Note, using the other HTS parameters, a fairly small machine with radius only 0.17 meters is required for $Q \approx 2$, the minimum expected gain of the SPARC tokamak [111].

The parameters for Dolan's LTS reactor design ($B_a = 6$ T, $\phi_a = 400$ kV) and the new HTS design ($B_a = 16$ T, $\phi_a = 500$ kV) determined in this section are summarized in Table A.1.

Table A.1: Two sets of MEPC reactor parameters.

Parameter	Dolan LTS design [106]	New HTS design
B-field in ring cusps B_a [T]	6	16
Applied voltage ϕ_a [kV]	400	500
Anode gap spacing d [mm]	4	4
Plasma electron density n_e [m^{-3}]	1.1×10^{20}	2.9×10^{20}
Plasma temperature $T_e \sim T_i$ [keV]	20	25
Coil/cusp radius R [m]	3.5	0.83
Plasma length L [m]	36	10
Dolan scaling relation gain Q	10	10

A.4 Plasma Volume and Surface Area in a Linear Set of Ring Cusps

To further evaluate the reactor designs, the plasma volume and surface area of the designs will be needed. These can be calculated by assuming a given plasma profile in a linear set of ring cusps. The plasma in one-half of one cusp region might have a profile as shown in Fig. A.5. An exponential profile $r(z) = z^\gamma + r_p$ is assumed, where r_p is the radius of the bulk plasma.

Assuming a first-generation reactor design might have $R \sim 3r_p$ as shown in Fig. A.5, the volume V_s of the plasma section is:

$$V_s = \Gamma_v \cdot \pi R^2 l, \tag{A.4}$$

where

$$\Gamma_v = \frac{4}{9(2\gamma + 1)} + \frac{4}{9(\gamma + 1)} + \frac{1}{9} \tag{A.5}$$

The surface area S_s of the plasma section is:

$$S_s = \Gamma_s \cdot 2\pi R l, \tag{A.6}$$

where

$$\Gamma_s = \frac{2}{3(\gamma + 1)} + \frac{1}{3}. \tag{A.7}$$

Since the total plasma length $L = N_c \cdot l$ (from Table A.1) with number of ring cusps $N_c \gg 1$, the total plasma volume and surface area is approximately:

$$V = \Gamma_v \cdot \pi R^2 L \tag{A.8}$$
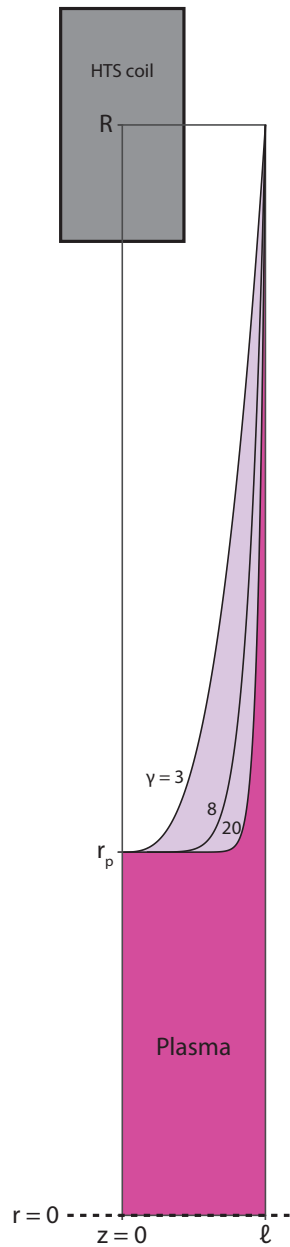
Figure A.5: Hypothetical plasma surface profile of one cusp half-region within a linear set of ring cusps. An exponential-shaped profile $r(z) = z^\gamma + r_p$ is assumed to calculate the plasma volume and surface area. This figure, with $R = 3r_p$ and $l = 0.2(R - r_p)$, may be approximately to scale for an HTS prototype reactor.

$$S = \Gamma_s \cdot 2\pi R L. \tag{A.9}$$

Note the plasma volume for the LTS design is 280 m^3, one-third that of the ITER tokamak [117]. Γ_v and Γ_s are weak functions of γ, taking values of Γ_v= 0.28–0.14 and Γ_s= 0.50–0.37 for γ= 3–20. For the remainder of this paper, $\Gamma_v = 0.2$ and $\Gamma_s = 0.4$ will be used.

A.5   Fusion Power and Radiation Losses

The DT fusion power of each design is:

$$P_{\text{fus}} = n_D \, n_T \, \langle \sigma v \rangle_{DT} \times \ 17.6 \text{ MeV} \times \Gamma_v \cdot \pi R^2 L. \tag{A.10}$$

The achievable DT fuel density in an MEPC reactor will be sensitive to the impurity level, because electrons have the density limit for effective electric confinement. So at this point, an assumption must be made on impurities in MEPC plasmas.

Unfortunately, high-Z ions will be well-confined electrostatically. Though some methods of impurity and ash removal have been proposed [103], impurity build-up remains a primary concern for an MEPC reactor. If no effective means of removal can be found, periodic shutdown and restart of the reactor may be required.

For 5% helium + 1% beryllium impurity ($Z_{\text{eff}} = 1.20$), the number densities are $n_D = n_T = 4.5 \times 10^{19}$ m^{-3} for the LTS reactor and 1.2×10^{20} m^{-3} for the HTS reactor. The total DT fusion powers are then 670 MW and 100 MW for LTS and HTS, respectively. Since the Dolan/Yushmanov energy gain Q and aspect ratio $\frac{L}{R}$ are approximately the same for both designs, one sees how the stronger fields enabled by HTS suggest medium-power, more compact reactors—a demand recognized already in the fission reactor industry.

Note that the real fusion power will be slightly less than the quoted values since the ion Maxwellian distribution is diminished for energies greater than $e\phi_i$ (see Sec. VI), reducing the normal reactivity parameter $\langle \sigma v \rangle$ for a given temperature. This weak effect has been quantified by Dolan [118], and should not affect the conclusions of this work.

An analysis of alpha particle trajectories in a high-β cusp reactor has not been performed to the author's knowledge. Partial alpha confinement would enhance the gain factor Q from the value listed in Table A.1. Assuming the first wall can be made more than one alpha particle gyroradius from the edge of the plasma, some significant alpha confinement and heating may occur. Though, many alphas directed along open field lines will impact the anode region before shedding much energy to the plasma. With total alpha confinement, the alpha heating powers are 130 MW and 20 MW for LTS and HTS, respectively. Interestingly, even with total alpha loss to the first wall,
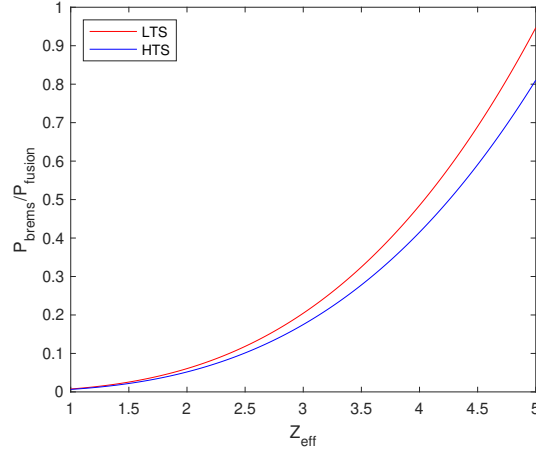
Figure A.6: Ratio of bremsstrahlung to fusion power as a function of Z_{eff} for each reactor design, with the approximation $n_D = n_T \approx \frac{n_e}{2\,Z_{\text{eff}}}$.

~5% of alpha energy will be recovered directly as electricity to the power source that is ultimately maintaining the negative potential of the bulk plasma.

Cyclotron radiation losses are assumed to be negligible since most of the plasma in cusp confinement is unmagnetized. Bremsstrahlung radiation loss is given by:

$$P_{\text{brems}} = A_{\text{brems}}\, n_e^2\, Z_{\text{eff}}\, \sqrt{k_B T_e} \times \Gamma_v \cdot \pi R^2 L, \tag{A.11}$$

where $A_{\text{brems}} = 1.6 \times 10^{-38}\, \frac{\text{Wm}^3}{\sqrt{\text{eV}}}$. For $Z_{\text{eff}} = 1.20$, the bremsstrahlung power is 8.7 MW for the LTS reactor and 1.1 MW for the HTS reactor. With the approximation $n_D = n_T \approx \frac{n_e}{2Z_{\text{eff}}}$, the bremsstrahlung power as a fraction of fusion power is shown for each design in Fig. A.6. The HTS design is slightly more robust to bremsstrahlung losses at large Z_{eff} due to the higher operating temperature.

Because an MEPC reactor would operate at high temperature, bremsstrahlung radiation is not such a concern with impurities as is reduction of the DT fuel density (and therefore fusion power density). The fusion power would scale roughly as $\frac{1}{Z_{\text{eff}}^2}$ for a constant electron density.

A.6 Conduction and Diffusion Losses

Plasma energy is primarily lost through conduction and diffusion. Electrons and ions upscattered over their respective potential barriers will quickly leak through a cusp and be lost to the cathodes. Additionally, electrons trapped in the magnetized edge layer will diffuse across the magnetic field until they impact the anode region or first wall.

Cohen et al [119] derives an expression for open-field line particle loss rates over potential barri-

ers based on the analytic treatments of Pastukhov, Chernin, and Rosenbluth. In his analysis [103], Dolan uses these loss rates to define a characteristic conduction time, which he combines with the edge-trapping and diffusion times for an overall energy confinement time.

A different model of conduction and diffusion losses will be explored here for comparison. However, this model is not entirely self-consistent because it uses the plasma temperature and potential barrier heights estimated semi-empirically by Dolan et al [103]. Electron losses will be considered first, with the ion loss rate set to match the electron loss rate for charge conservation.

Since $e\phi_a \gg T_e$, the electron energy distribution is approximately Maxwellian, but diminished at energies greater than $e\phi_e$. Each electron energy collision time, τ_E^{ee}, one-tenth of the electrons which would fill the truncated region of the Maxwellian are assumed to be lost over the electron potential barrier ϕ_e to the cathode. The one-tenth factor arises from the assumption that bulk plasma electron density is an order of magnitude greater than the electron density penetrating the cusp/anode gaps.

Therefore, the electron conduction energy loss rate is:

$$P_{\text{cond},e} = 0.1 \cdot \frac{E_e^* - N_e^* e\phi_e}{\tau_E^{ee}}, \tag{A.12}$$

where

$$E_e^* = \frac{2 N_e k T_e}{\sqrt{\pi}} \cdot \Gamma\left(\frac{5}{2}, \frac{e\phi_e}{k_B T_e}\right) \tag{A.13}$$

is the electron thermal energy in the diminished region of the Maxwellian at temperature T_e with total plasma electron inventory $N_e = n_e \times \Gamma_v \pi R^2 L$. Not to be confused with the plasma profile factors Γ_v and Γ_s, $\Gamma(a, x)$ is the incomplete gamma function – a result of the Maxwellian integration. $\phi_e = \phi_a - \Delta\phi - \phi_i$ is the potential barrier for electrons (see Fig. A.3). It is assumed $\phi_e \approx 0.5\phi_a$ as in Dolan [103]. Additionally:

$$N_e^* = \frac{2 N_e}{\sqrt{\pi}} \cdot \Gamma\left(\frac{3}{2}, \frac{e\phi_e}{k_B T_e}\right) \tag{A.14}$$

is the number of electrons in the diminished region. The factor $N_e^* e\phi_e$ in the energy loss rate equation accounts for the fact that conduction losses are to the cathode, which is at a potential difference ϕ_e from the bulk plasma (shifting the particle energies just before loss).

The electron energy collision time from Stacey [95] with $\ln \Lambda = 17.5$ can be written as:

$$\tau_E^{ee} = 6.1 \times 10^{14} \frac{T_{e,\text{keV}}^{\frac{3}{2}}}{n_e}. \tag{A.15}$$

Assuming $T_e = 0.05 \, e\phi_a$ as in Dolan, the electron conduction energy loss rate is estimated

121

to be 3.3 MW and 340 kW for the LTS and HTS designs, respectively. The power is relatively low because electrons have little kinetic energy left upon cathode impact, having surmounted their potential barrier.

Ion confinement in MEPC is almost completely electrostatic, but electrons are lost by diffusion across the magnetic field. Assuming that a fraction $(1 - e^{-1}) = 0.63$ of the thermal electron energy is lost each diffusion time τ_{diff}, the electron diffusion energy loss rate is:

$$P_{\text{diff}} = 0.95 \cdot \frac{N_e k_B T_e}{\tau_{\text{diff}}}. \tag{A.16}$$

The great achievement of MEPC and cusps is near-classical confinement, ostensibly due to the global stability advantages mentioned in Sec. I. The Jupiter-2M linear set of seven ring cusps achieved diffusion time of approximately half the classical prediction [120]. Introducing this factor of one-half to the classical confinement time as estimated by Pastukhov [121] and assuming $T_e \sim T_i$ in the central plasma gives:

$$\tau_{\text{diff}} \sim 0.11 \cdot \frac{\tau_{ei} V d}{S \rho_{e,a} \; \rho_{e,p}}, \tag{A.17}$$

where $\tau_{ei} = 4.3 \times 10^{14} \frac{T_{e,\text{keV}}^{\frac{3}{2}}}{n_i Z_{\text{eff}}^2}$ is the electron-ion momentum collision time from Stacey [95] with $\ln \Lambda = 17.5$, V is the plasma volume, S is the plasma surface area, $\rho_{e,a} = \frac{\sqrt{2 m_e k_B T_e}}{e B_a}$ is the electron gyroradius in the anode gap, and $\rho_{e,p} = \sqrt{\frac{m_e}{2 \mu_0 e^2 n_e}}$ is the electron gyroradius at the bulk plasma boundary (where local $\beta = 1$).

The ratio $\frac{V}{SR}$ of the plasma is:

$$\frac{V}{SR} = \frac{\Gamma_v}{2 \, \Gamma_s}, \tag{A.18}$$

which is an even weaker function of γ than Γ_v or Γ_s individually, taking values of $\frac{V}{SR} = 0.3$–0.2 for $\gamma = 3$–20.

Using a value of $\frac{V}{SR} = 0.25$ reduces the diffusion time equation to:

$$\tau_{\text{diff}} \sim 2.7 \times 10^{-2} \frac{\tau_{ei} R d}{\rho_{e,a} \; \rho_{e,p}}. \tag{A.19}$$

Thus, for the LTS design, $\tau_{\text{diff}} = 3.8$ seconds. For the HTS design, $\tau_{\text{diff}} = 1.8$ seconds. Using these values, the electron diffusion energy loss rates are 24 MW and 2.6 MW for the LTS and HTS designs, respectively.

Ion conduction losses are estimated based on charge conservation. Ions lost to the cathode will have an average energy:

$$\overline{E}_{\text{cond},i} = \frac{E_i^*}{N_i^*} + e\phi_e, \tag{A.20}$$

where E_i^* and N_i^* take the form of the electron diminished Maxwellian region equations (Eqs. 13–14), but use the ion potential barrier $\phi_i \approx 0.3\,\phi_a$ (as in Dolan [103]) when evaluating the incomplete gamma functions. The factor $e\phi_e$ accounts for the fact that ion losses are to the cathode, and ions are accelerated before impact.

Assuming total alpha confinement, ion charge will be lost via conduction at the same rate electron charge is lost via conduction and diffusion:

$$\dot{N}_{\text{cond},i} = \frac{1}{Z_{\text{eff}}} \left[0.1\,\frac{N_e^*}{\tau_E^{ee}} + 0.63\,\frac{N_e}{\tau_{\text{diff}}} \right], \tag{A.21}$$

assuming a fraction $(1 - e^{-1}) = 0.63$ of plasma electrons are lost each diffusion time. The ion conduction energy loss rate is:

$$P_{\text{cond},i} = \overline{E}_{\text{cond},i} \cdot \dot{N}_{\text{cond},i}, \tag{A.22}$$

which gives 270 MW and 30 MW for the LTS and HTS designs, respectively.

The energetics of the two reactor designs as calculated in the last two sections (Secs. V and VI) are organized in Table A.2. The gains with no alpha confinement are a factor of 3–5 lower than predicted by Dolan/Yushmanov's relation. This is likely in part due to use of a smaller characteristic electron-ion collision time and consideration of impurities. Also, the electron conduction and diffusion losses are added linearly in this model, unlike in Dolan where the characteristic timescales are added reciprocally. Since the two electron loss processes act on the same population and are not independent of each other, the reciprocal method may be more appropriate.

In both designs, loss of electron charge is dominated by diffusion. Loss of energy is dominated by ion conduction, due to acceleration into the cathode. In an advanced design, perhaps the cathode could be made semi-transparent to lost ions, such that they impact a different surface near ground potential. In theory, this might recover a large fraction of the ion energy and increase the energy gain of the system by a substantial factor.

A.7 Plasma Startup, Auxiliary Heating, and Fueling

Another advantage of MEPC is that the plasma can be heated relatively simply and efficiently by electron beam injection from the cathodes. In the Jupiter-2M experiment, over 80% of electron beam energy appeared in the plasma [103]. Beam current could be controlled by modulation of cathode gun voltage or temperature in point or ring cusps. Ion losses tend to be minimal at the point cusps due to angular momentum from $\mathbf{E} \times \mathbf{B}$ rotation of the plasma [122].

Table A.2: Energetics of the two MEPC reactor designs with the new conduction and diffusion models and $Z_{\text{eff}} = 1.20$.

Parameter	Dolan LTS design [106]	New HTS design
Fusion Power [MW]	670	100
Max Alpha Heating [MW]	130	20
Bremsstrahlung Power Loss [MW]	8.7	1.1
Diffusion Power Loss [MW]	24	2.6
Conduction Power Loss (e$^-$) [MW]	3.3	0.34
Conduction Power Loss (i$^+$) [MW]	270	30
Gain (no α confinement)	2.2	3.0
Gain (total α confinement)	3.8	7.1

Since the majority of plasma is not magnetized, RF heating does not seem ideal, but may have limited use. Strong electron resonance heating in the anode gaps could possibly reduce the cold, trapped electron population, and therefore reduce the self-shielding voltage drop $\Delta\phi$, leading to better confinement scaling. Cyclotron heating in the gaps could also reduce general electron leakage by "spinning up" electrons as they approach the cusp hole (driving them out of the loss-cone by increasing $v_\perp$). Applied RF could also influence diocotron oscillations. The electron cyclotron fundamental frequency in the anode gaps would be around 170 GHz for 6 T LTS and 450 GHz for 16 T HTS, ignoring relativistic effects.

As with many magnetic confinement concepts, neutral beam heating could be a suitable option for heating and refueling an MEPC reactor. However, hot ion confinement would be similar to alpha confinement in that collisions must slow the ions to below the ion potential barrier ϕ_i in only a few radial transits, or else leakage out of a cusp is likely. Also, it could be difficult to engineer neutral beam input ports in the geometry of a linear set of ring cusps.

Initial particle inventory could be provided by burnout of neutral gas fill by electron beam, though gas puffs for refueling are not recommended since neutral collisions would increase the diffusion rate of electrons in the sheath. As with tokamaks, pellet injection could be a good refueling option.

With no alpha confinement, the required auxiliary heating power is 310 MW and 34 MW for the LTS and HTS designs, respectively. This could correspond to electron beam currents of 770 A and 67 A from the cathodes of each design. The electron injection currents would constitute a tiny fraction of the electron space charge passing through the anode gaps. Other methods of heating, as well as partial alpha confinement, could contribute to the input power requirement.

Dolan/Yushmanov's model predicts $Q \approx 10$ for both designs. Interestingly, with the new conduction and diffusion model presented here, the HTS design shows a larger gain than that of the LTS design. This could suggest it is easier to reach ignition in MEPC with a high-field, compact

design.

A.8 First Wall, Blanket, and Tritium Breeding

The first wall surface area can be conservatively estimated as the plasma surface area:

$$A_w = \Gamma_s \cdot 2\pi R L. \tag{A.23}$$

Therefore, the areal neutron power to the first wall would be approximately 1.7 MW/m^2 for the LTS design and 3.8 MW/m^2 for the HTS design. The 'enhanced', beryllium-armored copper/steel tiles in mind for the ITER first wall are capable of 4.7 MW/m^2 neutron power [123], and a similar technology could be used in an MEPC reactor. Unlike in tokamaks, there should be no edge-localized modes (ELMs) or disruption-like events in the cusp geometry that would deposit excessive or unpredictable amounts of energy directly to the first wall.

Liquid lithium, lead-lithium, or some molten salt formulation could flow through tubes in the wall as a primary coolant and blanket, extracting the neutron heat and breeding tritium at a minimum rate of 4.3 and 0.64 grams per hour to match the consumption of the LTS and HTS designs, respectively. Each breeding event with lithium-6 produces an additional 4.8 MeV, enhancing the neutron heating power in the blanket by 35%. Uranium or other actinides could be dissolved in the primary coolant (e.g., FLiBe with dissolved uranium tetrafluoride as in some molten salt reactor designs [124]) to further boost heat output in a fission-fusion hybrid or actinide-burner scheme.

Behind the blanket, a lower-temperature coolant and vacuum radiation shield region could separate the cryostat containing the magnet coils. Considering the high current density and on-coil fields desired with HTS, liquid helium would likely be needed for both designs. If the coils were made larger with reduced engineering current density, liquid hydrogen might be an option for HTS. There could also be increased temperature margin for quenching with the HTS design.

Active cooling would also be needed for the cathodes, which see a small amount of neutron power but a great deal of conduction heating—primarily via impact of high-energy ions. The cathodes could be cooled with the primary coolant as well, or a separate coolant loop, depending on the desired operating temperature. Cathode surface area may be somewhat arbitrary, since the diverging field beyond the cusp acts as a natural divertor (similar to magnetic mirrors). If the arc length of each cathode surface is 20 cm for both designs with twelve ring cusps, the total cathode surface area is:

$$A_c = 24\pi \cdot (R + \delta R) \cdot 20 \text{ cm}, \tag{A.24}$$

where $\delta R \sim 20$ cm represents the larger radius of the cathodes as compared with the coil radius, R.

Therefore, the areal conduction power to the cathodes is 5.0 MW/m^2 for the LTS design and 1.9 MW/m^2 for the HTS design. Sputtering is not as concerning at the cathode since any liberated ions would be immediately pulled back, so the cathode could possibly be a high-Z material like tungsten. Erosion and ion implantation will be a concern, and the cathodes would probably need frequent replacement.

The anode surfaces will see most of the diffusion loss thermal power. Assuming the height of the anode surface $h = 10\,d$ (the maximum recommended by Yushmanov), the total anode surface area is approximately:

$$A_a \approx 480\pi \cdot d \cdot R. \tag{A.25}$$

Therefore, the areal diffusion power to the anodes is is 1.1 MW/m^2 for the LTS design and 0.53 MW/m^2 for the HTS design. Anode sputtering could be a primary impurity source in MEPC; luckily, few plasma ions can energetically reach the anodes.

High-voltage grading between the anode and cathode should be used to reduce the chance of insulator flashover. The insulator would likely be made of a ceramic appropriate for the reactor environment such as alumina or a carbide.

A sketch of a possible hardware design suggesting $\sim$16 T cusp fields (assuming 1000 A/mm^2 engineering current density is possible with the HTS coils as in SPARC [111], but ignoring magnet structural considerations) is shown in Fig. A.7.

For an MEPC reactor, pushing to higher field strengths with HTS technology has another engineering advantage. While the magnetic pressure scales as B_a^2, the bulk plasma pressure can only scale as B_a due to space charge restrictions in the anode gaps. Thus, by increasing B_a, the bulk plasma surface is moved physically farther from the coils, while the cusp/anode gaps can remain a set distance. This essentially elongates the cusps when depicted to scale (see Fig. A.7), stretching them outward radially so as to allow a greater volume of first wall, blanket, coolant, and shielding between the coils and the plasma. The cusp/anode gaps can remain close to the coils ($<$35 cm for HTS), taking advantage of the high fields there, because few hot ions exist in this region to produce damaging neutrons.

A.9   Stored Plasma and Magnetic Energies

Ignoring the effects of impurities, the energy stored in the plasma of each design is:

$$E_p = \frac{3}{2}\,n_e\,k\,(T_e + T_i) \cdot \Gamma_v \cdot \pi R^2 L, \tag{A.26}$$

which gives 260 MJ for the LTS design and 14 MJ for the HTS design. For comparison, the energy
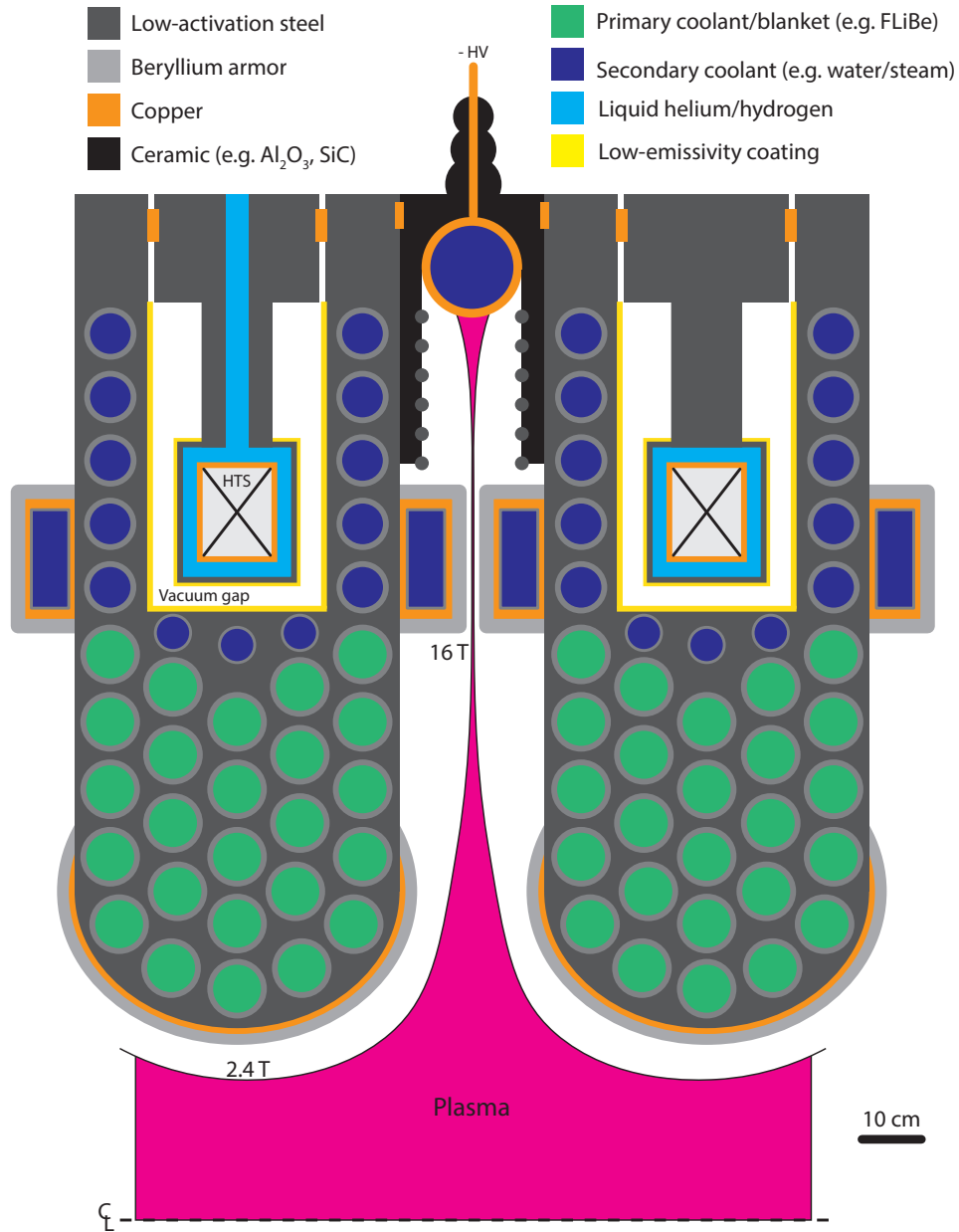
Figure A.7: Engineering design sketch of one ring cusp region for a high-field MEPC reactor utilizing HTS coils.

stored in the ITER plasma will be approximately 350 MJ.

The magnetic energy of a linear set of twelve ring cusps can be very roughly approximated as the energy of thirteen toroids carrying uniform current, with major radius R and minor radius $a = \sqrt{\frac{I_{\text{coil}}}{\pi J_e}}$. The engineering current density J_e is estimated as $100 \frac{\text{A}}{\text{mm}^2}$ for LTS [125] and $1000 \frac{\text{A}}{\text{mm}^2}$ for HTS. The total current in the coil cross-section is estimated as $I_{\text{coil}} = \frac{\pi L B_a}{24 \, \mu_0}$ to produce $\frac{B_a}{2}$ per coil in the cusps. Thus, the total magnetic energy is:

$$E_B = 13 \cdot \frac{1}{2} L_{\text{coil}} I_{\text{coil}}^2, \tag{A.27}$$

with each coil loop inductance given by:

$$L_{\text{coil}} \approx \mu_0 R \left(\ln \frac{8R}{a} - 2 \right), \tag{A.28}$$

which gives 38 GJ and 4.7 GJ for the LTS and HTS designs, respectively. The stored magnetic energy of the ITER tokamak will be around 50 GJ. The HTS coils would be at minimum 15 cm thick, producing 8 T *each* in the cusp about 35 cm from the surface of the coil (see Fig. A.7 for rough scale).

In a linear set of ring cusps (under normal operation), only the two coils on the ends of the reactor will see a large net force axially. The axial repulsive force on an end HTS coil in a thirteen coil system can be expressed as the summation of forces from the other twelve coils:

$$F = \frac{12 \mu_0 I_{\text{coil}}^2 R}{L} \cdot \sum_{n=1}^{12} \frac{(-1)^{n+1}}{n} \approx 230 \text{ MN} \tag{A.29}$$

Verifying the above estimate, a magnetostatic simulation in Computer Simulation Technology (CST) Studio Suite predicts a force of 200 MN between two toroidal coils with the HTS design parameters and maximum HTS engineering current density ($1000 \frac{\text{A}}{\text{mm}^2}$). A force of 200 MN may seem enormous, but the total centripetal force reacted by the ITER cylindrical vault from the 18 toroidal coils exceeds 400 MN [126]. Assuming a 400 MPa yield strength, ~ 0.5 m^2 of steel would be needed to restrain the HTS coils—e.g., seven solid bars with 30 cm diameter.

The ITER centripetal forces are partly managed with six fiberglass pre-compression rings, each 5 meters in diameter, because metal would not be magnetically or cryogenically compatible [127]. For the linear set of ring cusps design, coil support probably does not need to be cryogenically compatible. An external clamping frame made of many steel bars could hold the coil structure together. In the result of an uncontrollable coil quench, other coils could see strong net forces which must be managed by the external frame as well. Advanced quench detection and control on a reactor-scale HTS coil system would mitigate this risk. In conclusion, magnetic coil stresses in an HTS linear set of ring cusps would be an engineering challenge, but would not be too dissimilar to

those in other large magnetic confinement reactor concepts.

A.10 MEPC Reactor Concerns

There are several unresolved questions in MEPC which must be investigated before a reactor could be confidently designed. Primary concerns are listed below. Each of these issues has already been identified by Dolan [106].

- *Plasma Purity.* Perhaps the greatest issue facing an MEPC reactor is build-up of high-Z impurities, which would be well-confined electrostatically. Maintenance of clean plasma at fusion temperatures in MEPC must be assessed and methods of impurity and ash removal developed; otherwise, periodic shutdown and restart of the reactor may be required. Since MEPC reactors would operate at high temperature, bremsstrahlung radiation is not the primary concern with impurities. The major concern is reduction of DT fuel density, due to constraints on electron density in MEPC.

- *Voltage Holding.* Maintenance of large applied voltages (100–600 kV) must be demonstrated in the MEPC geometry, while in the presence of hot plasma and radiation. Sputtering control, voltage grading, and electrically insulating materials compatible with reactor engineering will need more investigation.

- *Electron Transport.* Encouragingly, diffusion at only twice the classical rate was observed in the Jupiter-2M experiment, but some other MEPC experiments (e.g., the toroidal ATOLL experiment) have shown anomalous transport—presumably due to ion acoustic and hybrid drift modes [103]. Good symmetry and a large volume of field-free plasma in the linear set of ring cusps geometry seems to be advantageous for micro-stability. Nonetheless, transport rates at reactor-relevant density and magnetic fields must be investigated.

- *Alpha Confinement.* If the first wall is located more than one alpha gyroradius (12 cm for the HTS design) away from the plasma surface, alpha particles should be partially confined. More assessment of alpha trajectories in the linear set of ring cusps geometry is needed. Partial alpha confinement would enhance the gain beyond the Q values of Table A.1.

- *Structure and Alignment.* Vacuum pump-out and the (quenching) magnet coils would apply large, transient forces to the reactor structure. These force changes must be managed simultaneously with precise alignment of electrodes and insulation of high-voltage. This represents a significant engineering and materials challenge, even in the relatively simple geometry of a linear set of ring cusps.

A.11 Conclusions and Suggestions for Future Work

Two MEPC fusion reactor designs using low-temperature and high-temperature superconducting technology have been investigated based on the summary works of Dolan and others. An alternate model of conduction and diffusion losses, including minor impurities, shows reduced gain, but reaches similar conclusions as Dolan. The LTS reactor design from Dolan is of similar magnitude to the ITER or DEMO tokamaks. In analogy to the ARC/SPARC tokamaks, HTS technology is shown to enable a more compact, medium-power reactor design with MEPC as well.

Engineering and material concerns of an MEPC reactor would be similar to other magnetic confinement concepts (e.g., tokamaks, mirrors), but could be simplified in some ways. A possible blanket and shielding concept is shown in Fig. A.7. More research is needed on insulation materials and high-voltage holding in the reactor environment, a concern not just in MEPC, but also in other fusion-directed concepts such as rotating mirrors.

As with many alternative concepts, MEPC experiments have suffered low budgets and limited attention. This has constrained experiment size to <1 meter, pulsed magnetic fields to <2 T, and applied voltages to <10 kV. A quasi-static, high-field, high-voltage experimental campaign is needed to confirm scaling theories and address unresolved questions in MEPC.

One such low-budget experiment could be a pulsed linear set of ring cusps with $B_a \sim 4$ tesla, applied $\phi_a \sim 100$ kV, and coil pulse time of at least one second. Key experimental studies to improve scaling predictions could investigate the fraction of electron density penetrating the cusps, the potential well depth and temperature at different applied voltages, diocotron (Kelvin-Helmholtz) oscillations in the anode gaps, and high-voltage maintenance in the radiation environment.

Another valuable MEPC experiment could be a spindle cusp (a single ring cusp) made of two superconducting coils and with large applied voltage. With a cusp field $B_a > 6$ T and an applied voltage $\phi_a \sim 100$ kV at sufficient power, the central plasma parameters could exceed 5 keV and 10^{20} m^{-3}, producing copious neutrons even with deuterium fuel. Insight gained on such a device could be sufficient to more confidently extrapolate to reactor parameters. Such a spindle cusp could be constructed using two HTS pancake coil assemblies, such as those supplied by Commonwealth Fusion Systems for the Wisconsin HTS Axisymmetric Mirror (WHAM). These coil assemblies are capable of producing 17 T across their 5 cm warm bores.

With imminent advancements in HTS coil technology, and if the scaling properties of Dolan and others can be verified at high-field, high-voltage parameters, then a fusion power reactor based on MEPC may be feasible.

APPENDIX B

Thin Foil Implosions on the Mykonos LTD

In addition to the AutoMag-DSP hybrid experiments discussed Section 2.3 of Chap. 2, thin-foil implosion experiments were carried out to test the stabilizing effect of the DSP return can hardware designed for Mykonos experiments.

Fast liner implosion at sub-MA current level requires sub-micron metal liner thicknesses. Fabrication of cylindrical liners with such thin foil thickness represents a challenge, but can be done in an academic lab with an acceptable level of uniformity to the surface as shown in Fig. B.1. The foil target shown in Fig. B.1 was made by rolling a rectangular piece of 800-nm aluminum foil around a dumbbell-shaped support structure, following the methods of Yager-Elorriaga [58] and Campbell [59] [60] The initial diameter of the foil is approximately 6 mm and the diameter of the thin part of the dumbbell support is 1.2 mm, meaning the foil can converge to a maximum convergence ratio of $CR \sim 5$.

While a more detailed analysis of DSP stabilization effects is saved for later publication, Fig. B.2 presents some initial results. The figure shows 10 ns exposure images by an Andor iStar 334T camera of four imploding liner experiments. The images are taken at similar times during the implosion relative to the current pulse, but the left images used a straight return can (non-DSP) while the right images used DSP return cans (of opposite helicity). Qualitatively, larger magneto-Rayleigh-Taylor (MRT) perturbations can be seen on the surface of the liner in the left image, suggesting the DSP is successfully providing a stabilization effect to the foil implosions. At least one DSP implosion appears to show helical MRT perturbations, as expected. Also, since the current profiles were similar on the relatively stiff Mykonos driver, it appears the DSP causes faster implosion of the foil, as predicted due to the additional axial field drive pressure.

Experiments were also performed with "AutoMag-like" thin-foil liners, i.e. foil liners with helical cuts in them. These delicate foil liners were fabricated by laser-etching, as shown in Fig. B.3, and also imploded on Mykonos with and without DSP return cans. The results of these implosions are also saved for later publication, but an example implosion image with DSP and AutoMag with the same helicity (axial fields destruct inside) is also shown in Fig. B.3.
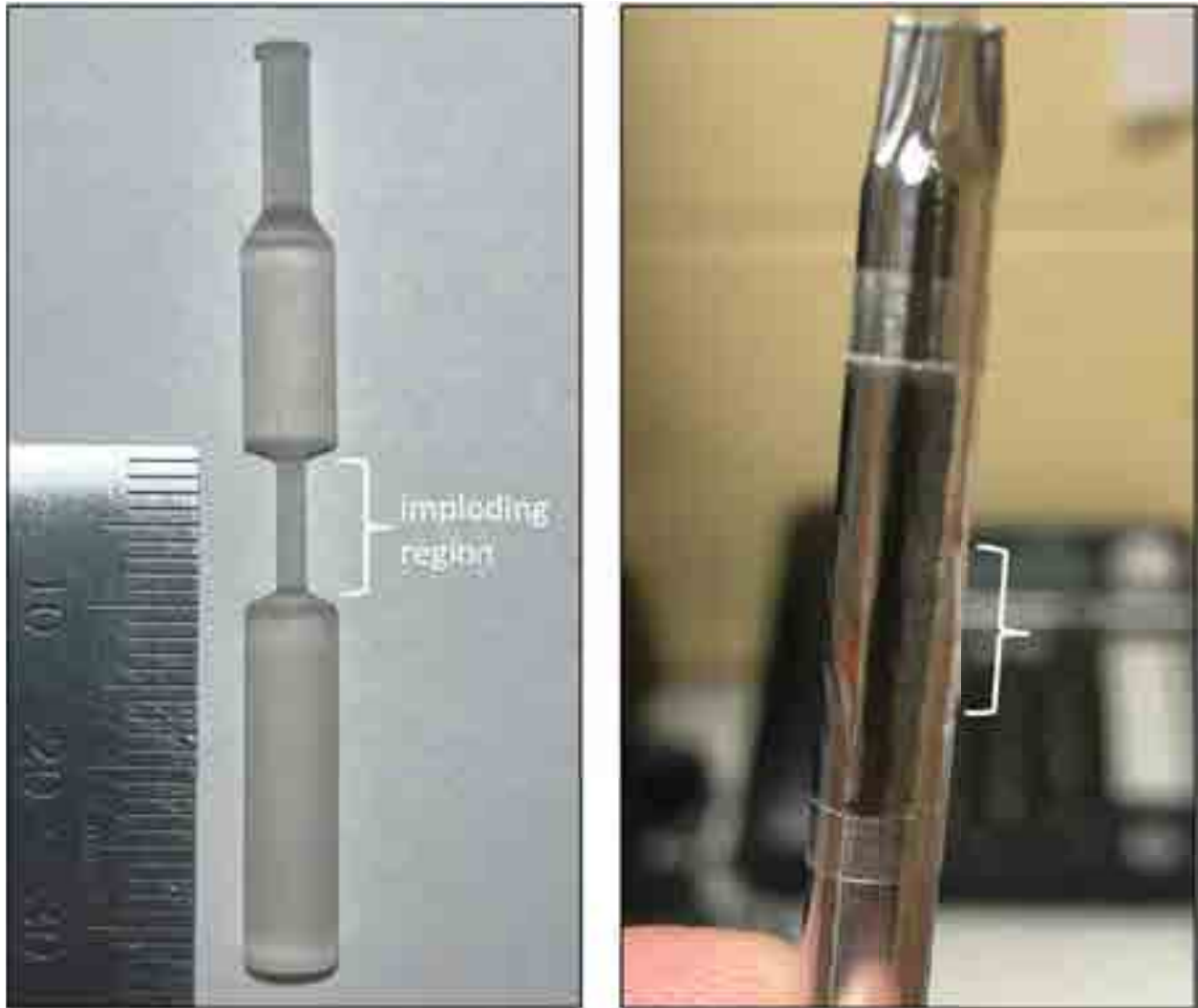
Figure B.1: Dumbbell-shaped plastic support structures were used to support the 800-nm aluminum liners for implosion on Mykonos, as shown on the right.
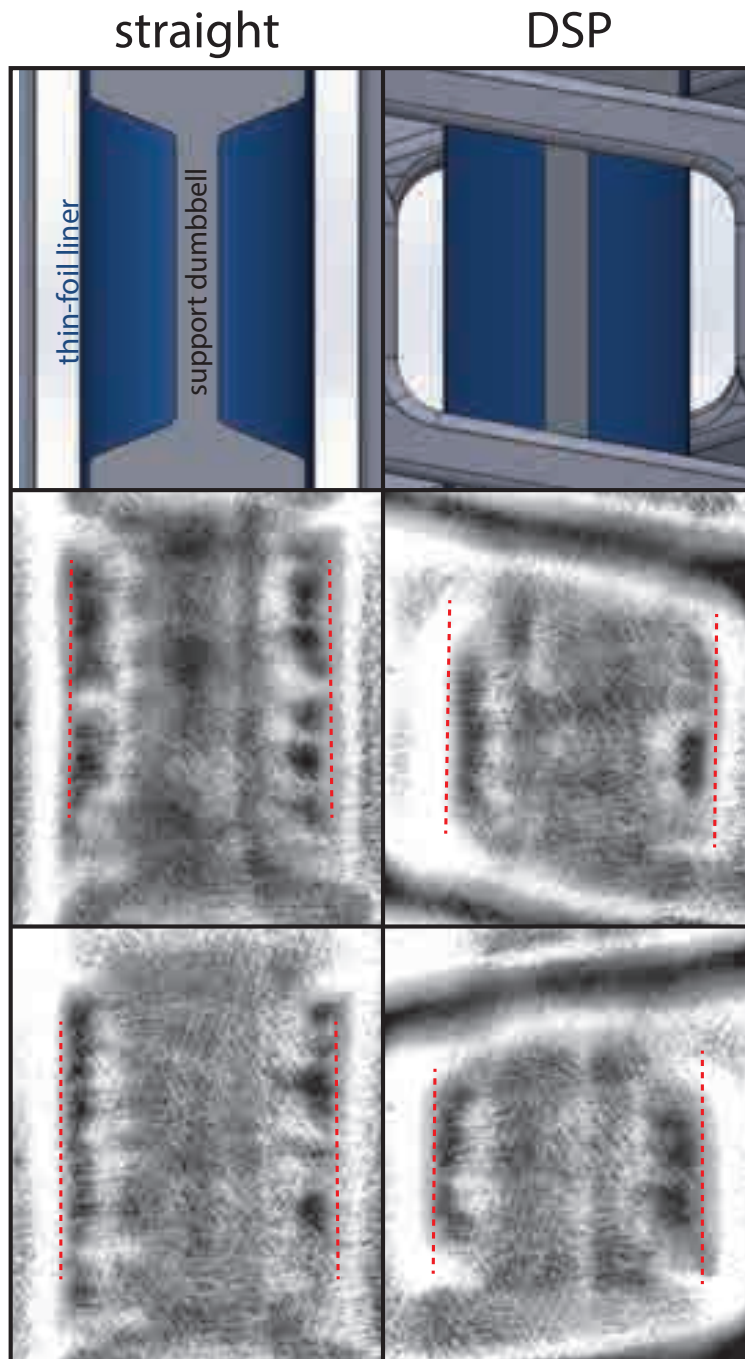
Figure B.2: Four 800-nm foil liner implosions imaged with an iStar 334T with 10 ns exposure at the same relative time on the Mykonos LTD. Images are contrast enhanced. The left implosions (straight) do not use DSP stabilization, while the right do. Mitigating effects on the MRT instability are up for debate, but given similar current profiles, it appears the DSP results in faster implosion as expected.
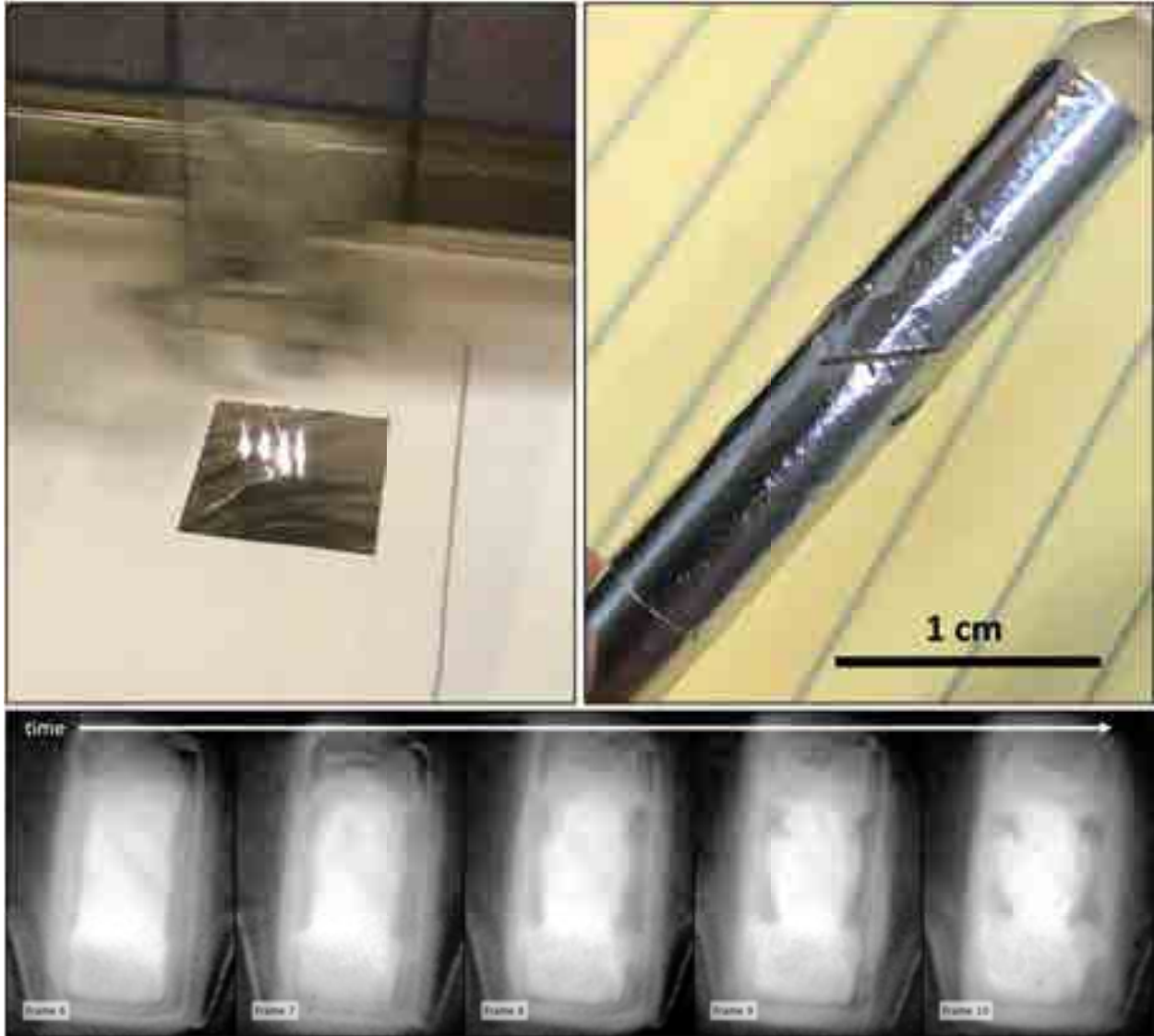
Figure B.3: A laser-etching process was used to produce "AutoMag-like" thin-foil liners for magnetized implosions on Mykonos. The bottom UHSi images show an AutoMag-like foil implosion with straight return can. A bulbous (perhaps helical) region can be seen after the implosion where the helical cuts were.

APPENDIX C

The BLUE LTD System at the University of Michigan

C.1 Introduction

Linear transformer drivers (LTDs) [128, 129, 130, 131] are an innovative and compact pulsed power technology under extensive investigation around the world [132, 133, 70, 134, 135, 136, 137, 138, 139, 140, 141, 142, 143, 144, 33, 145, 146, 147]. At the University of Michigan, a single-cavity LTD facility called MAIZE (Michigan Accelerator for Inductive Z-pinch Experiments) has been operational for over a decade [70, 33, 144]. MAIZE is a very low-impedance driver (∼0.1 Ω) and is capable of generating a current pulse that rises from 0 to 1 MA in as little as 100 ns into a matched load. To complement the single-cavity MAIZE facility, a four-cavity LTD facility called BLUE (Bestowed LTD from the Ursa minor Experiment) is under construction. The 1.25 m-diameter cavities used for BLUE were originally fabricated at the Institute of High Current Electronics (IHCE) in Tomsk, Russia, before becoming the basis for the 21-cavity Ursa Minor facility [138, 139] at Sandia National Laboratories (SNL). Ursa Minor has since been dismantled and repurposed. The original four IHCE cavities are now part of the BLUE facility at the University of Michigan.

Figure C.1 shows the BLUE experimental bay in the Plasma, Pulsed Power, and Microwave Lab (PPML) at the University of Michigan. A concrete brick wall was arranged around the cavities to contain radiation produced by the facility, including neutrons from deuterium pinches. The white steel rack suspends the cavities on their sides and allows the cavities to be stacked in series. The rack has rails that allow the cavities to glide into position. A motorized overhead crane can remove individual cavities and place them on a purpose-built wooden stand for servicing. Either 1, 2, 3, or 4 cavities can be stacked in series so that the driver impedance and driver voltage can be varied, and the effects of this variation on load performance can be investigated. The coupling of many stacked LTD cavities is important for future conceptual accelerators like Z-300 and Z-800 [141], which will require thousands of LTD cavities combined in both series and parallel configurations.

The donation from SNL included the empty metal cavities themselves as well as some of the fundamental internal elements, such as the spark-gap switches, the capacitors, the insulators, the

anode transmission line framework, and the Metglas cores. Auxiliary equipment had to be built from scratch, including the high-voltage charging circuitry, the control systems, the trigger pulse generator, and the core reset/pre magnetization pulse generator.

The remainder of this paper is organized as follows. In Sec. C.2, the assembly of the first (prototype) BLUE LTD cavity is described. In Section C.3, the auxiliary systems are described. In Sec. C.4, results are presented from experiments where the cavity was fired in two architectures: (1) as a single-stage bipolar Marx generator without ferromagnetic cores (Fig. C.1(a)) and (2) as a true linear transformer driver with ferromagnetic cores and a pre magnetization pulse generator to reset/magnetize those cores (Fig. C.1(b)). Both architectures were tested with a dummy resistive load. In Sec. C.5, results are presented from experiments where BLUE was used to drive a high-power microwave (HPM) device known as a magnetically-insulated line oscillator (MILO). In these BLUE-driven MILO experiments, 1.19-GHz microwave oscillations were successfully generated.

C.2 The Prototype BLUE Cavity

Images of the first completed BLUE cavity are presented in Figs. C.1 and C.2. In Figs. C.1(a) and C.2, a clear polycarbonate lid was in use, which enables the interior components to be observed during operation. The plastic lid also eliminates the parasitic current path around the LTD case [33], and thus all of the current is driven through the load at the center of the machine. Because the parasitic current path is eliminated, ferromagnetic cores were not required nor installed in Figs. C.1(a) and C.2 (i.e., the cavity was in a bipolar Marx generator configuration). As our testing evolved, the clear plastic lid was eventually replaced with a metal lid, and thus pre magnetized ferromagnetic cores became a requirement (see Section C.3.5 for a discussion on the LTD cores).

Referring to Fig. C.2, each BLUE cavity is comprised of 10 "bricks," where each brick consists of two 100 kV, 20-nF capacitors (General Atomics Part # 35467) and a single 200 kV (±100 kV) spark-gap switch (L3Harris Model # 40264-200kV). A photograph of an L3Harris spark-gap switch is presented in Fig. C.3. Each switch was refurbished and tested with ten nominal discharges in the PPML "brick-tester" before installation in the BLUE cavity. Switch pre-fires were rarely observed in either the brick tester or in BLUE—only one definite pre-fire event was confirmed in the ~100 shots performed thus far on the first cavity.

Each BLUE cavity also consists of a transmission line framework for mounting the bricks in the cavities, large plastic insulator disks for separating the anode and cathode sides of the cavity, charging and triggering circuitry (such as HV resistors, inductors, and cable feedthroughs), switch gas lines, and diagnostics.

The trigger inductors (each ~2 μH) were installed between the main trigger bus line and the UV-pins/mid-planes of the L3Harris switches. Due to the finite capacitance of a switch mid-
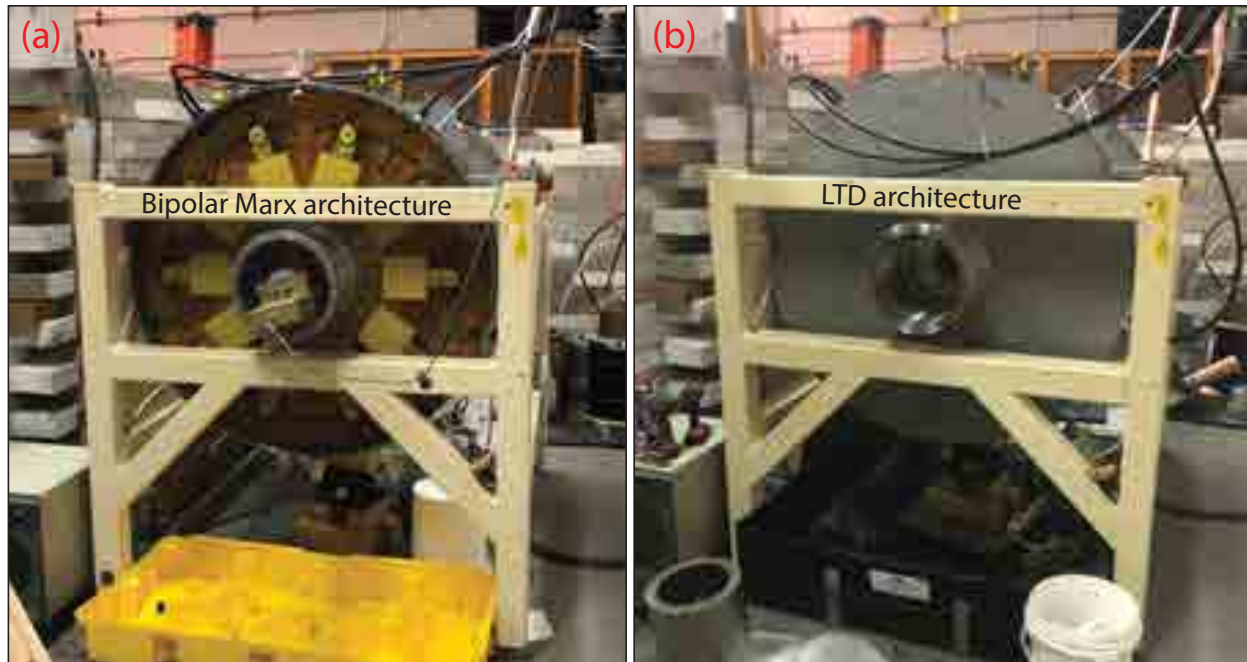
Figure C.1: The BLUE experimental bay in the Plasma, Pulsed Power, and Microwave Lab (PPML) at the University of Michigan, with the prototype BLUE cavity configured as: (a) a bipolar Marx generator with a clear plastic lid; and (b) as a linear transformer driver with a steel lid.

plane ($\sim$7 pF), the trigger inductors serve to amplify the trigger pulse and reduce the jitter of the switch [145]. They also provide some isolation between switches during the breakdown process. The bronze-colored trigger inductors can be seen attached to the switches in Fig. C.2.

Bipolar LTD cavities such as MAIZE and BLUE require both a positive and negative high-voltage charging supply. The open-circuit output voltage of the cavity is equal to the difference between the positive and negative values. Since these values usually have the same magnitude, the open-circuit output voltage is usually twice the "charge voltage." For example, a ± 100 kV charge voltage results in a 200 kV open-circuit output voltage. The spark-gap switches are bipolar as well, holding off both charge polarities from each other, until a trigger pulse on the grounded mid-plane electrode breaks down the switch. Each L3Harris switch also includes a "UV-pin." Upon triggering, the pin creates a small spark at the switch mid-plane. The spark floods the switch gas with photo-ionizing UV light, thus reducing the breakdown jitter [148, 149]. In a typical bipolar LTD cavity, the switch electrodes (and charging side of the capacitors) are chained together around the cavity through charging resistors or charging inductors (see Fig. C.2).

A high "rep-rate" (rate of repetitively charging and firing) is desired for various experimental platforms on BLUE (e.g., HPM experiments and dense plasma focus neutron source experiments). Thus, dual Spellman 12-kW power supplies were acquired. They allow a theoretical rep-rate >1 Hz, as long as the charging impedance is kept low. However, having a small charging impedance
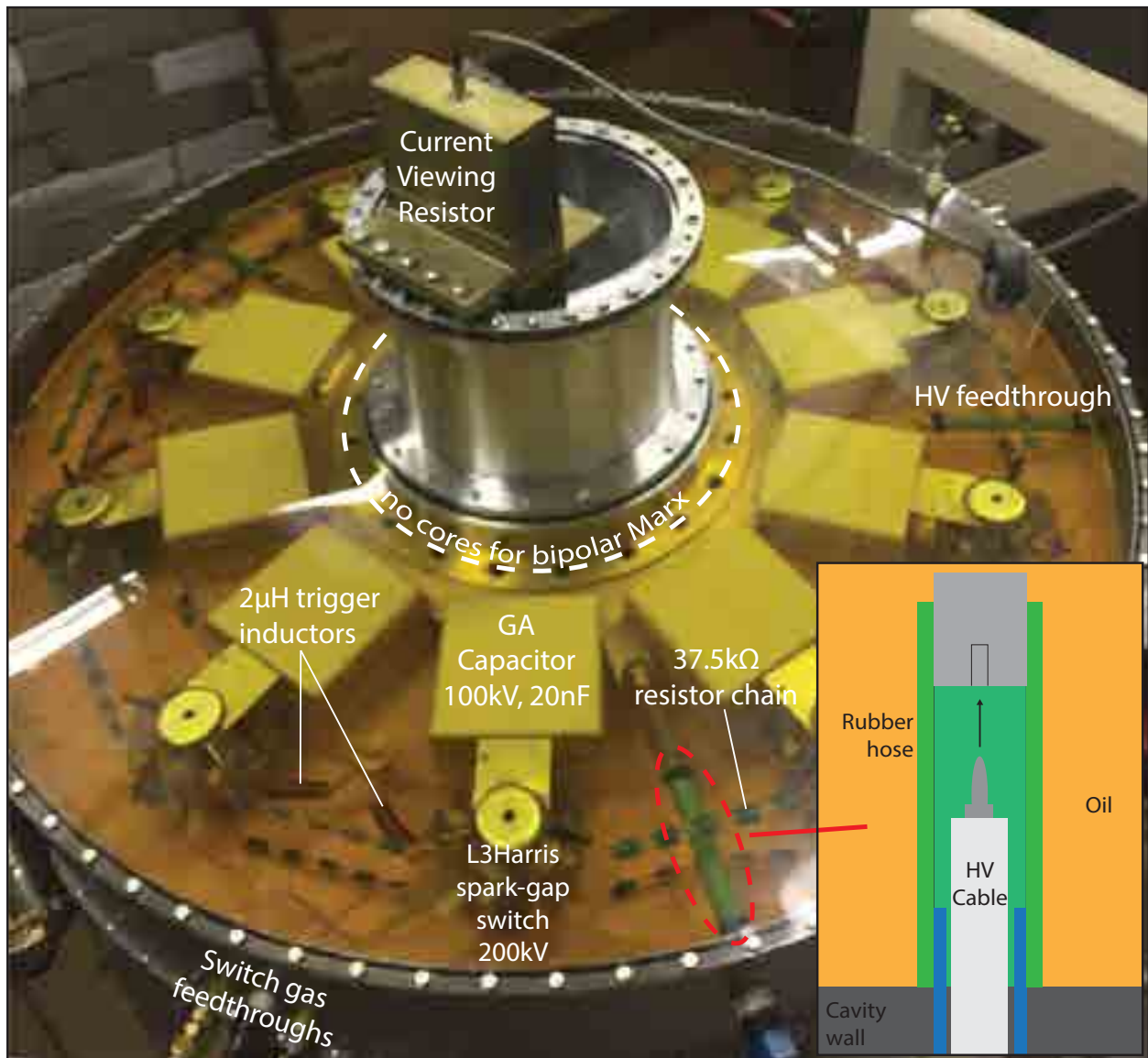
Figure C.2: The first assembled BLUE cavity, shown here with a clear polycarbonate lid and no ferromagnetic cores (i.e., the cavity is in a single-stage bipolar Marx generator configuration). The cavity is filled with transformer oil. The small vacuum chamber on top of the cavity houses the resistive load. The brass structure on top of the chamber is the current viewing resistor (CVR). Plug-in feedthroughs with 3D-printed parts allow high-voltage cables to be easily disconnected from the cavity without removing the lid or draining the transformer oil.

Figure C.3: An L3Harris spark-gap switch with brass electrodes, capable of operation at 200 kV ($\pm$100 kV) and up to 200 psi gas fill. These switches are used in the MAIZE and BLUE LTD systems at the University of Michigan. In this image, the switch is shown with a shorting wire between the UV-pin and mid-plane. In the BLUE cavity, the shorting wires are replaced with 3 mΩ resistor chains for proper operation of the UV-pin.

between each brick may lead to degradation of the L3Harris spark-gaps during pre-fire events, due to excessive current draw from neighboring bricks. HVR resistor chains were assembled to serve as the charging impedance between each brick. Ultimately, a 37.5-kΩ total resistance for each chain was chosen as a compromise between brick isolation and fast charging time. These HVR chains limit undesired pre-fire currents through adjacent bricks to <2.7 A. Considering the 20-nF capacitors used in BLUE, the RC time constant of this charging impedance is 750 μs.

Five high-voltage cables are fed into each BLUE cavity: one for each charge polarity, one for a trigger pulse, and one for each pre magnetization pulse polarity. Since the BLUE cavities must be moved back and forth between the servicing test stand and the side mounting stacking rack, it was desired for the HV cables to be able to be unplugged from the cavity without the need to open the cavity or drain the transformer oil. To this end, a novel plug-in connection was developed utilizing SLA 3D-printed parts. This HV feedthrough connection is depicted in Fig. C.2. The cavity dimensions limited the length of the feedthroughs, making the DC charge cables especially prone to arcing. Luckily, it was found that the arcing could be eliminated by partially filling the feedthroughs with a dielectric grease.

Figure C.4: Arduino Uno (ATmega328P-based) control panel for semi-autonomous control of the BLUE charging and firing sequence, as well as other system functions.

C.3 Auxiliary Systems

C.3.1 Control Panel

To streamline the firing sequence of the BLUE system, a consolidated and intuitive control interface was desired. The firing sequence includes monitoring safety interlocks, operating the Spellman high-voltage power supplies, operating high-voltage Ross relays for isolation/grounding, and generating the fire command logic pulse. Semi-autonomous control of the firing sequence and other system functions minimizes manual input and allows for faster rep-rating of the facility.

Figure C.4 shows the control panel assembled for BLUE. The panel is semi-autonomous, using the programmable Arduino Uno board (which is based on the ATmega328P 8-bit microcontroller). The best electrical resilience was obtained with the Ruggeduino-SE, a ruggedized version of the Uno manufactured by Rugged Circuits.

The panel is capable of rep-rating BLUE by automatically controlling the charging sequence as fast as possible. The only user input required is pressing the button to fire the machine. The panel has many other features as well, including monitoring for pre-fire events, automatic purging of the switch gas, and control of the pre magnetization pulse generator.

C.3.2   HV Ross Relay Barrel

Three high-voltage relays (produced by Ross Engineering Corporation) are used to connect/disconnect the cavity capacitors from the charging supplies. They also provide passive grounding in the event of an emergency abort or unexpected power loss. Operation of the three relays is handled by the Arduino-based control panel. The relays must be submerged in transformer oil to prevent arcing, so a 20-gallon steel drum was used to house the three relays, as shown in Fig. C.5. The drum also contains two 50-kΩ ceramic dump resistors, which absorb the energy stored in the cavity(s) upon abort. High-voltage feedthroughs similar to those developed for the prototype BLUE cavity allow up to five positive and five negative cables to plug into the barrel.

C.3.3   200 kV Trigger Pulse Generator

The L3Harris spark-gap switches require a high-voltage pulse as a trigger. The pulse is applied to the mid-plane, distorting the field in the switch enough to breakdown the pressurized gas (dry "zero" air) in the switch. A very fast $\frac{dV}{dt}$ on the rising edge of the pulse is desired to minimize the jitter of a single switch and the jitter between multiple switches receiving the same trigger pulse. The pulse should also have a macroscopic amount of energy ($\gg 1$ J) to ensure robust triggering of many switches in parallel (up to 40 switches with all four BLUE cavities in operation).

To achieve a large $\frac{dV}{dt}$, a single bipolar brick, charged in parallel with the LTD cavities, is used to trigger the cavities. This gives a trigger voltage equal to twice the charge voltage (also equal to a single cavity's open-circuit output voltage). The trigger brick is housed in a 10-gallon steel drum with high-voltage plug-in feedthroughs similar to those used on the prototype BLUE cavity and Ross relay barrel. Positive or negative trigger output may be chosen by grounding the opposite polarity. The trigger pulse generator barrel is shown in Fig. C.6.

The brick used in the trigger generator is identical to those used in the BLUE cavities, consisting of two 20-nF capacitors and a L3Harris spark-gap switch. The single spark-gap switch in the trigger generator is itself triggered by a PT55 pulse generator, which is mounted to the top of the barrel, as shown in Fig. C.6. See Sec. C.3.4 for further discussion of the PT55.

C.3.4   300-V Pulse Generator (PT003 Replacement)

The Pacific Atlantic Electronics (PAE) PT55 module (see Fig. C.7), which is no longer in production, uses a rare krytron switch to produce a +50 kV output pulse with a risetime of less than 2 ns. The module requires a low-power +7 kVDC charge voltage and a positive 250–300 V trigger pulse. PT55s are compact, low-jitter, and very useful in a pulsed-power laboratory, namely for triggering spark-gap switches. The single L3Harris spark-gap switch used in the BLUE trigger pulse generator (and also used in the MAIZE and BLUE LTD cavities) can be reliably triggered by

Figure C.5: A 20-gallon oil drum contains the three Ross HV relays used in the charging circuit. The relays are operated by the control panel (see Sec. C.3.1 and Fig. C.4) during the charging sequence. The large copper-sulfate dump resistors in this photograph were ultimately replaced with 50-kΩ ceramic resistors.

Figure C.6: The 10-gallon oil drum containing the trigger pulse generating brick, which is charged in parallel with the BLUE LTD cavities and triggered by the PT55 pulse generator mounted to the top of the drum.

Figure C.7: The Pacific Atlantic Electronics PT55 module with a +7 kVDC power supply and the newly developed +300 V pulse generator (PT003 replacement). Together, these modules can produce a +50 kV output pulse with <10 ns jitter from a logic-level (+5 V) input pulse.

a PT55 pulse, even when the switch is being operated at full voltage (200 kV). Several PT55s of varying condition are stockpiled in the PPML.

The PT55 draws <1 mA from its +7 kVDC power supply, so the charge voltage can be provided by a small 12-V DC-DC module (see Fig. C.7). By contrast, the PT55's positive 250–300 V input trigger pulse is not so trivial to produce. Thus, the defunct PAE company also offered the PT003, a small solid-state device that, when given a +100 VDC charge voltage and a logic-level (+5 V) trigger pulse, produces a positive 250–300 V output pulse suitable for triggering the PT55. For minimal jitter, the PT003 had a <10 ns risetime, as shown in Fig. C.8.

Unfortunately, the PPML supply of PT003s has dwindled much faster than the supply of PT55s. Since PT55s continue to be used around the lab, including for the BLUE trigger pulse generator, a suitable replacement for the PT003 had to be procured. With no inexpensive commercial options, the new/replacement module described in Figs. C.7–C.9 was developed, with inspiration from the 200-V spark-gap trigger circuit in Ref. [150].

The circuit of the new +300 V pulse generator is shown in Fig. C.9. Six small film capacitors in parallel, totaling 6 nF, are charged to -300 V with a small, commercially available 12-V DC-DC module. Five enhancement-type, P-channel MOSFETs (PMOS) in parallel (Nexperia BSP230,135) are used as a low-side switch to rapidly connect the -300 V to ground when triggered. Multiple capacitors and PMOS elements are used in parallel to minimize the inductance and resistance of the circuit. Triggering the PMOS elements produces a +300 V pulse into 50 Ω on the opposite side of
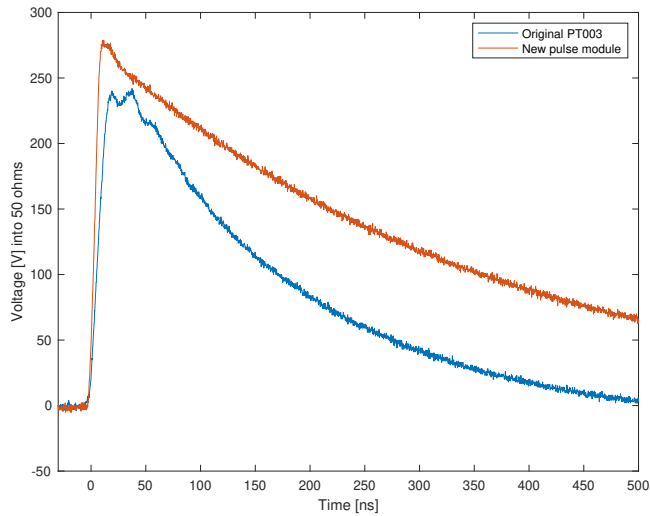
Figure C.8: Output pulses from an original PAE PT003 (blue) and the new +300 V pulse generator (orange) into 50 Ω, when given a +5 V TTL trigger signal

the capacitors. The over-damped pulse has an approximately 200 ns e-folding decay time, similar to the original PT003 (see Fig. C.8).

To trigger the PMOS elements in this configuration, a negative voltage pulse must be applied to the gates. It was found in testing that a positive 10–20 V pulse, produced by a commercial BNC pulse generator, could be inverted with a low-leakage-inductance pulse transformer, and thus trigger the PMOS elements. However, the gate input capacitance of the PMOS elements, with several in parallel, is significant. The inverted pulse from the BNC pulse generator, even at the maximum +20 V amplitude, was unable to draw enough instantaneous current from the gates to achieve the desired risetime and amplitude.

To trigger the PMOS elements more strongly with only a logic-level (+5 V) pulse, an NPN transistor (Diodes Inc. ZXTN25020DGTA) was added to the circuit. A 10-nF capacitor is charged to +20 V from an additional DC-DC converter. This capacitor is discharged to ground via the transistor upon receipt of a positive logic-level pulse. Closure of the transistor switch produces a -20 V pulse on the output of the capacitor, which is fed to the PMOS gates. The addition of the NPN transistor to the circuit produced the desired amplitude and risetime to reliably trigger the PT55 with jitter $<$10 ns (see Fig. C.8).

C.3.5   Pre magnetization Pulse Generator for Resetting BLUE's Ferromagnetic Cores

In an LTD cavity, there is a parasitic path that the discharge current can take along the inner surface of the LTD's metallic case [33]. This parasitic path is in parallel with the load. To limit the current that takes this parasitic path (and thus force the current through the load as desired), LTD
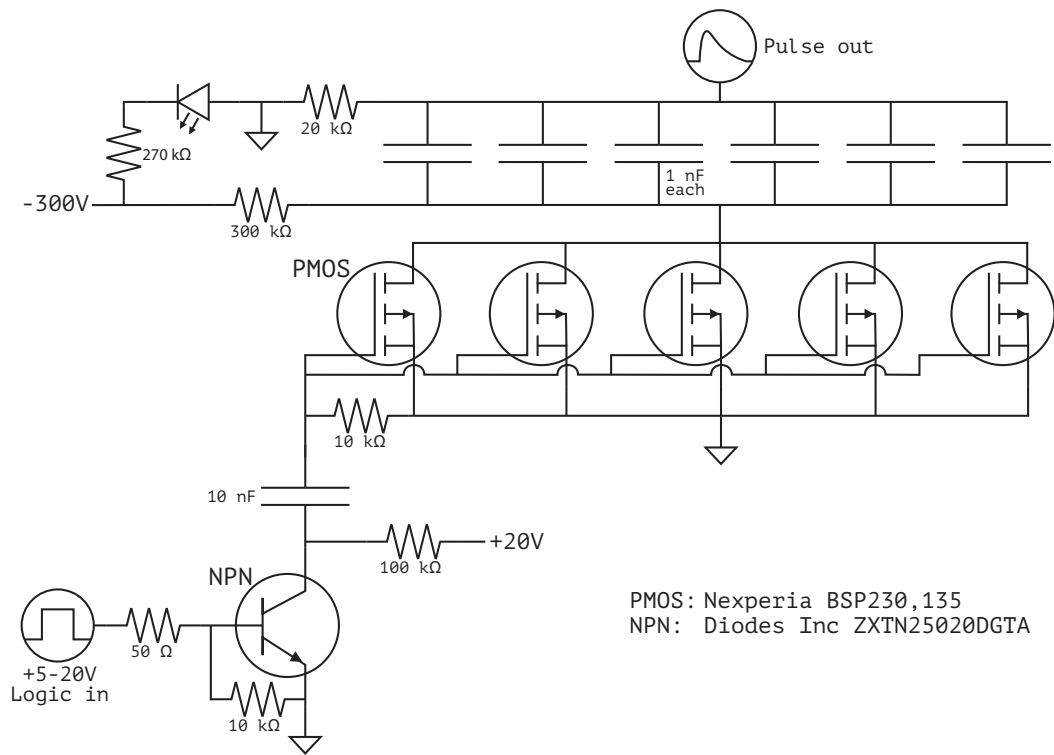
Figure C.9: Circuit diagram of the +300 V pulse generator designed to trigger the PT55 mounted to the BLUE trigger pulse generator. The +20 V and -300 V are provided with small 12 V DC-DC converters. This generator replaces the defunct PT003 module.

cavities usually include two ferromagnetic cores (an upper core and a lower core) within the loop formed by the parasitic current path.

The ferromagnetic cores typically consist of thin iron or Metglas tape, which is laminated with a dielectric film, wound into large rings, and potted in epoxy resin. Since the parasitic current path encloses the cores, generation of a parasitic current drives magnetization of the cores. Since the cores are made of thin strips of semi-resistive material with high magnetic permeability $\mu \gg \mu_0$, there is a high inductance associated with the parasitic path, which minimizes the fraction of current taking this path. In addition, there is a resistive effect due to eddy currents generated during magnetization of the cores, which appears at high-frequency [36]. Energy losses in the cores during an LTD discharge are often modeled with a static (and many times empirically determined) resistance in parallel with the load. To model lower-frequency pulses around the cores, such as the core resetting/pre magnetization discharge, an initial resistance that reduces rapidly after several microseconds is appropriate.

Due to magnetic hysteresis in the cores, the parasitic current from repeated cavity discharges eventually saturates the magnetic domains in the cores in a direction that reduces the effective permeability of the cores and thus reduces the impedance of the parasitic current path. To recover the maximum effective impedance for the parasitic current path, the alignment of the magnetic domains must be reset (reversed) back into their ideal direction for an LTD discharge. This can be done by applying a pre magnetization pulse to the cavity. This "pre mag" pulse drives a current in the LTD's metallic case that runs in a direction opposite to that of the parasitic current generated during an LTD discharge. The pre mag pulse can be applied using a much lower voltage and generating a much lower peak current than that of an LTD discharge, but the pre mag pulse must then be applied over a proportionally longer timescale. The pre mag pulse can be applied anytime between LTD discharges, but it is typically done before installation of the experimental load, since the pre mag pulse can ruin sensitive loads by driving modest currents through the load over long timescales.

The "volt-second product" of the cores is the parameter that defines the magnetic saturation properties of the cores. It can be roughly calculated from the material properties and geometry of the cores. From previous literature on the cavities (during the development of Ursa Minor) [151], the volt-second product of the cores used in the BLUE cavities is estimated to be around 20 mV·s. This figure makes intuitive sense: one can think about the volt-second product as if each core must "hold-off" the 100 kV pulse from half of the cavity for at least 200 ns (the typical experimental time). It also gives an estimate of the required pre mag pulse duration for saturation. For example, if the pre mag pulse voltage is 600 V, then saturation can be expected after a pulse duration of 33 μs. Reference [151] also recommends a pre magnetizing current of at least 1.5 kA to reach saturation in the Ursa Minor/BLUE cores.
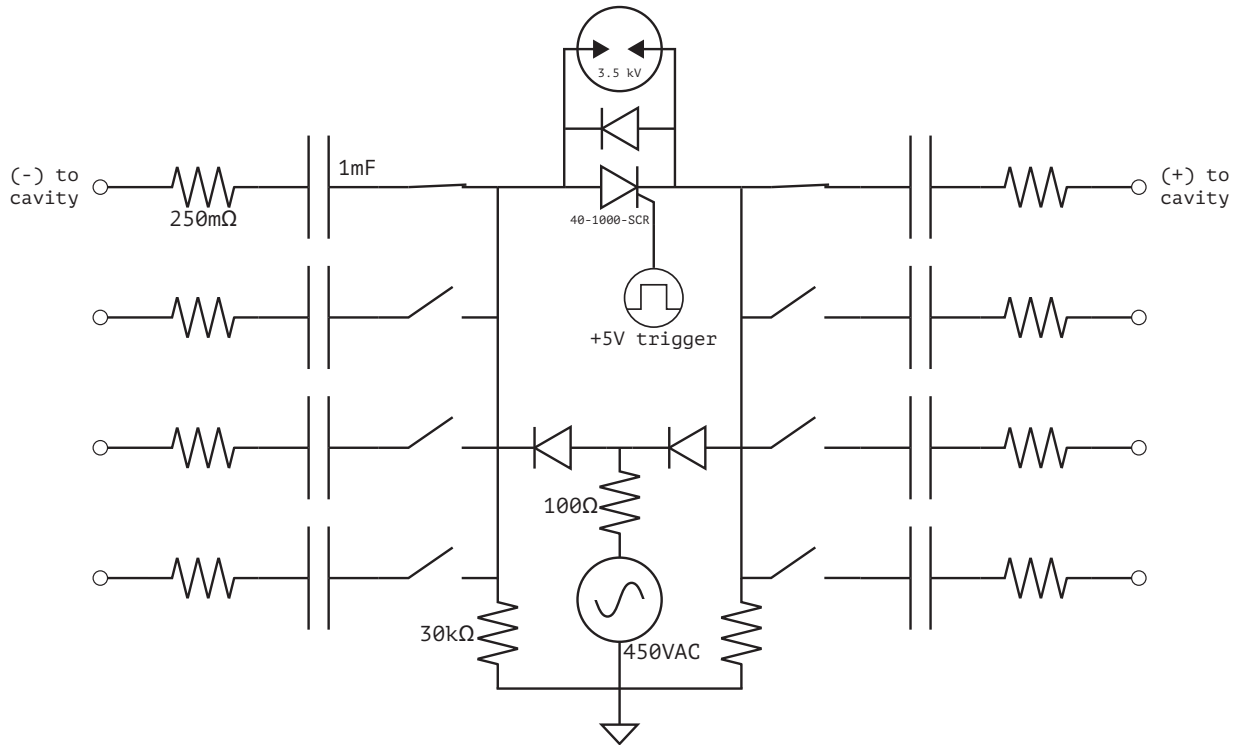
Figure C.10: Circuit diagram of the pre magnetization pulse generator for resetting the ferromagnetic cores on BLUE. In this diagram, only the output to the first cavity is enabled.

After exploratory modeling in LTspice, a relatively simple RC discharge was chosen to generate the required pulse while minimizing cost and complexity of the pre mag system. As shown in Fig. C.10, eight resistor-capacitor combinations are needed to provide a positive and negative channel for each of the four cavities. The capacitors (which can be individually disconnected from the circuit via screw-in breakers) are charged by a double-rectified 450-VAC transformer to (theoretically) ± 636 V. In reality, the capacitors charge to about 610 V due to leakage through the passive dump resistors. After charging is complete, a high-power, push-pull thyristor (Behlke HTS 40-1000-SCR) discharges the positive and negative channels to each other in a low-side bipolar fashion, similar to the operation of a bipolar LTD brick. In each channel, the resulting output pulse of the 1 mF capacitor is sent through a short length of nichrome wire acting as a high-power 250 mΩ resistor, over-damping the pulse, before it is sent to the cavity. An internal photograph of the pre magnetization pulse generator constructed for BLUE is shown in Fig. C.11.

Output current pulses from a single channel of the pre magnetization pulse generator were measured with a Pearson coil (see Fig. C.12). When the cores have already been saturated in the desired direction (i.e., the pre mag generator has already been successfully fired in preparation for an LTD discharge), the pre mag current pulse into the cavity is nearly identical to the pulse into a short-circuit load, indicating that the cavity has a very low impedance for the direction of
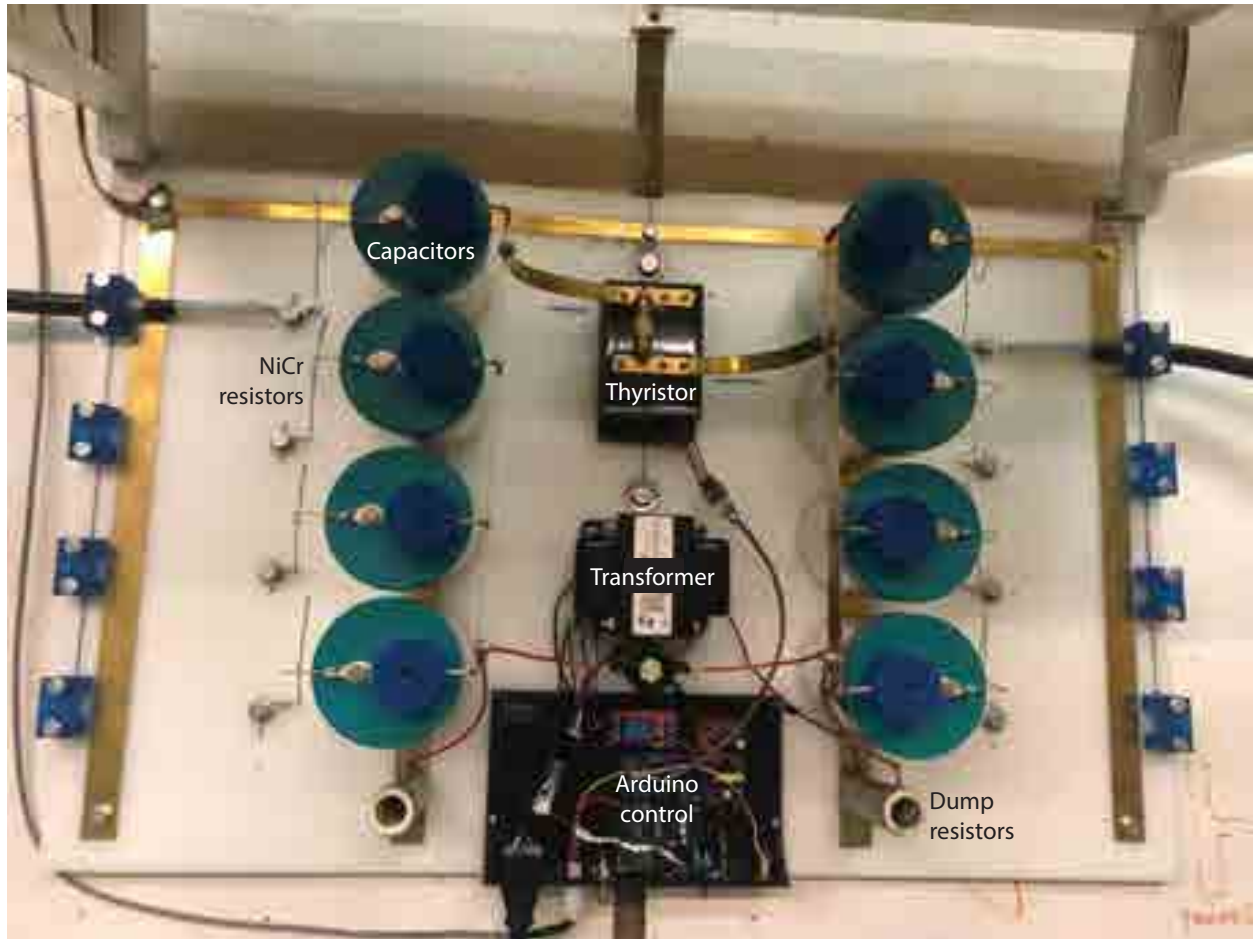
Figure C.11: Photograph of the internal components of the pre magnetization pulse generator constructed for resetting the ferromagnetic cores on BLUE. This photograph shows the generator's four positive and four negative output channels. The dark blue 3D-printed plastic structures on top of the capacitors are the screw-in breakers for connecting individual channels. In this photograph, only the cables to the first cavity are attached.
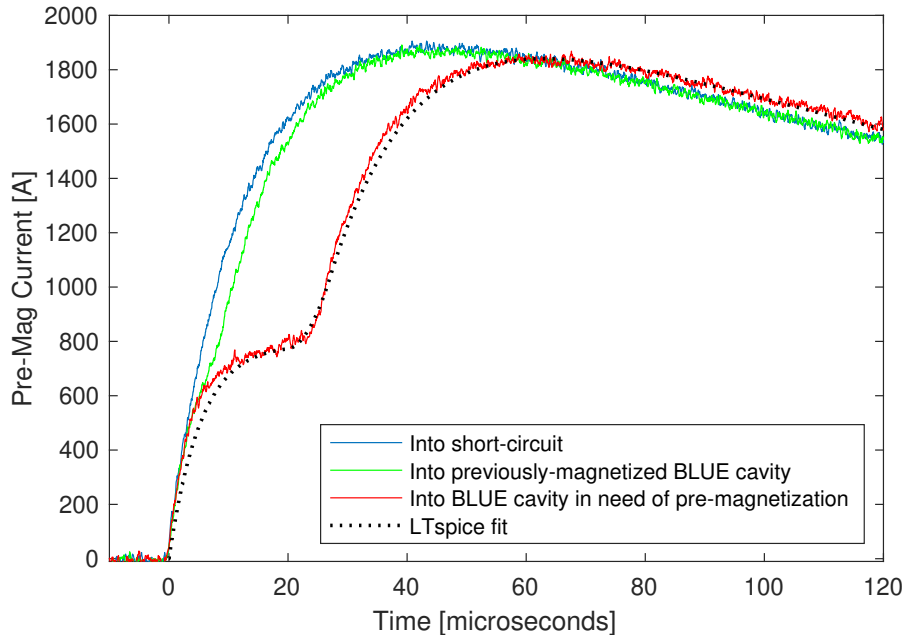
Figure C.12: Output current waveforms from a single channel of the pre magnetization pulse generator into three load scenarios: (1) into a short-circuit load (blue); (2) into the cavity for the case where the cores have already been reset/pre magnetized (green); and (3) into the cavity for the case where the cores need to be reset/pre magnetized (red). Also shown is a waveform produced by an LTspice model fine-tuned to closely match the experimental results.

the pre mag current pulse (and thus a high impedance for the direction of the parasitic current pulse during an LTD discharge). When the cores are saturated in the undesired direction (i.e., the cores are in need of a resetting pre mag pulse), a notch in the waveform of the pre mag current is observed (see Fig. C.12). This notch is the result of the initially high impedance of the cavity (for the direction of the pre mag current) dropping rapidly in the first ∼25 μs of the pulse. Note that 25 μs is consistent with the rough estimate of 33 μs from the volt-second product of the cores. This notch was predicted via LTspice modeling prior to the first experimental tests of the system. The LTspice pre mag model was then fine-tuned to nearly replicate the experimental results, as shown in Fig. C.12. The dynamic impedance seen by the pre mag generator is both inductive and resistive, with the resistive component being due to the eddy current effect mentioned previously. However, only the resistive component was tuned (modulated in time) to nearly replicate the experimental results with LTspice. Note that a tuned inductance (modulated in time) could also have been used to obtain results that agree well with experiments, so this tuning method does not necessarily provide the exact temporal behavior of the cores' effective inductance or resistance values.

The effects of successful pre magnetization on the main LTD cavity discharge can be seen in load current measurements taken when the cavity is fired into a resistive load. This is discussed in

Sec. C.4.2. In general, pre magnetization of the cavity increases the amplitude of the LTD's main discharge current by 10–20% and extends the duration of positive current into the load.

There is a large issue to be aware of in designing a pre magnetization pulse generator for LTDs. Since (ideally) the pre mag cables remain attached to the cavity during an LTD discharge, the high-voltage, high-frequency pulse from the main discharge can travel back to the pre mag generator, potentially damaging medium-voltage electronics such as the charging diodes or, more importantly, the thyristor. Two thyristors on BLUE's pre mag system were damaged during LTD discharges, despite attempts to protect them with metal-oxide varistors (MOVs) and an over-voltage spark-gap placed directly across the thyristor terminals (see Fig. C.10). Transient-voltage-suppression (TVS) diodes and/or better spark-gaps may provide more effective protection from the fast transients, but this has yet to be demonstrated experimentally. For now, triggered spark-gaps are recommended as a more robust alternative to thyristors for a pre mag system switch.

C.4   Resistive Load Testing of the Prototype BLUE Cavity

C.4.1   Bipolar Marx Generator Configuration

The prototype cavity was first tested with a polycarbonate lid, as shown in Figs. C.1(a) and C.2. This allows for internal visual access during testing. It also eliminates the parasitic current path and thus the need for ferromagnetic cores. This effectively puts the cavity into a bipolar Marx generator architecture, rather than a LTD architecture. This coreless configuration is closely related to an LTD spinoff concept known as the impedance matched Marx generator (IMG) [152].

A dummy resistive load for the cavity was fabricated using an arrangement of spare ceramic resistors. The resistance of the load was approximately $1\,\Omega$, while the inductance was estimated to be greater than 100 nH. An image of the cavity mounted on its side (i.e., mounted in the white, cavity-stacking support rack) and firing into the resistive load is shown in Fig. C.13.

A current-viewing resistor (CVR) was installed in series with the resistive load to obtain calibrated load current data. However, the anode (front/top) side of BLUE's load region must be grounded for an oscilloscope to properly monitor the CVR signal. This became problematic with the polycarbonate lid installed on the cavity's front/top side, because in this case, the cathode becomes the grounded end of BLUE's load region. This occurs because BLUE's central cathode stalk is in direct contact with the metal lid on the back (bottom) side of the cavity, which is in contact with the bulk of the metal cavity, the vacuum pumps, and the grounded steel frame that supports the cavity. Operating the cavity in this configuration also resulted in troublesome arcing from the anode to the steel frame (see Fig. C.13). As a result of these issues, the data acquired from the CVR was garbled and not representative of the true load current. For this reason, current measurements are not presented for the cavity in the bipolar Marx configuration.

151
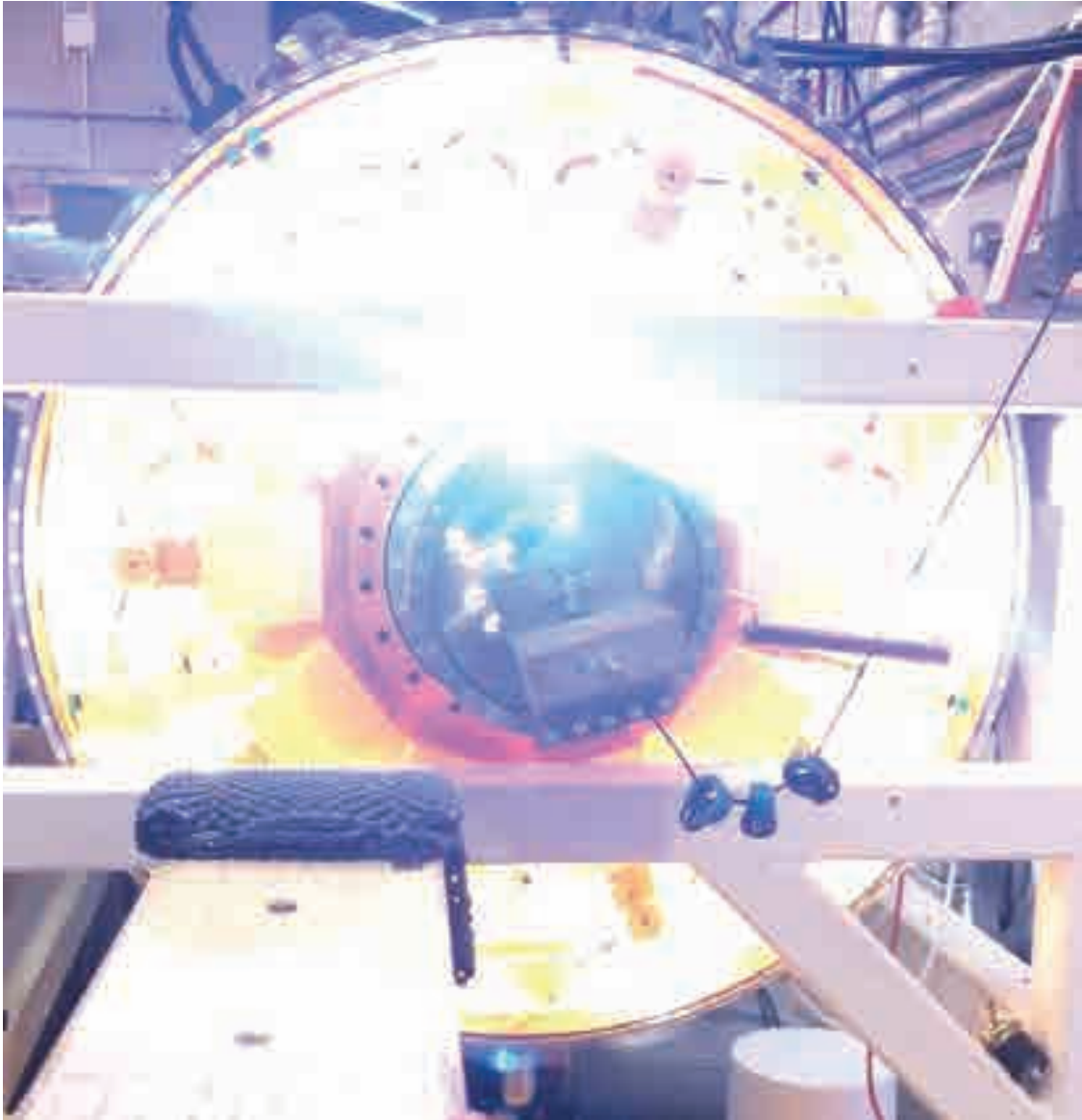
Figure C.13: The prototype BLUE cavity mounted on its side and firing into a resistive load in the bipolar Marx generator configuration (i.e., using the clear plastic lid and thus not using ferromagnetic cores). The bright flash is an undesirable arc to the white, steel support frame.

The aforementioned issues could be remedied by placing the polycarbonate lid on the back side of the cavity and isolating the cathode from the vacuum pump systems with a ceramic break. Other coreless configurations that could work include those described in Refs. [152, 153]. However, to avoid delays in commissioning the BLUE facility, the decision was made to move on to testing the cavity in its original LTD configuration - i.e., replacing the polycarbonate lid on the cavity's front side with the original steel lid, installing the ferromagnetic cores, and implementing the core reset/pre mag system.

C.4.2 Linear Transformer Driver Configuration

Replacing the polycarbonate lid with the original steel lid and inserting the ferromagnetic cores transforms the cavity back into the traditional LTD configuration (see Fig. C.1(b)). The pre mag pulse generator is now desired to magnetize the cores in the proper direction prior to an LTD shot, thus minimizing the current taking the parasitic path (see Sec. C.3.5).

A new, higher-quality resistive load (using new HVR APC ceramic disk resistors) was fabricated for BLUE in the LTD architecture. One of the motivations for doing this was that the simple cylindrical geometry of these disk resistors allows the load inductance to be more precisely estimated. The new load was also designed to have a variable resistance of 0.5–4 Ω by stacking multiple disk resistors in series. For the experiments reported herein, the load resistance was 1.5 Ω, and the load inductance was estimated to be $\approx$110 nH.

Figures C.14 and C.15 show experimental current traces from the prototype BLUE cavity in the LTD configuration. These traces were acquired by the CVR. Figure C.14 shows the current traces at varying charge voltages: $\pm$50 kV, $\pm$60 kV, and $\pm$70 kV. Figure C.14 also shows the effects of pre magnetization on the load current. Without pre magnetization, the load current is smaller in amplitude and shorter in duration, as significant current begins to leak into the parasitic current path around the time of peak current.

Figure C.15 shows good agreement between an experimentally measured current trace and the current trace generated by an LTspice simulation of the discharge. In this case, the charge voltage was $\pm$70 kV. The larger amplitude of the experimental trace before $t \approx 80$ ns is likely due to imperfect modeling of the core behavior and thus current losses to the parasitic current path.

From these initial calibration and pre magnetization experiments, a simple circuit model was semi-empirically developed for BLUE. The model is illustrated schematically in Fig. C.16. The values to be used in the circuit model are provided in Table C.1. In the central column of Table C.1, formulas are provided for calculating the circuit element values as a function of the number of cavities, N_{cav}. In the rightmost column of Table C.1, approximate values are given for a single cavity—i.e., with $N_{cav} = 1$.
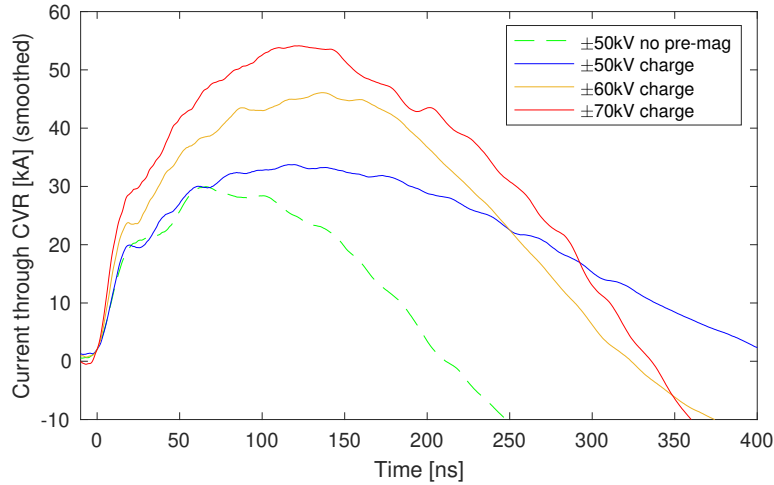
Figure C.14: Nominal experimental current traces from the prototype BLUE cavity configured as an LTD at different charge voltages, acquired using a current-viewing resistor (CVR). The data have been smoothed to reduce high-frequency noise. The resistive load has resistance and inductance values of approximately 1.5 Ω and 110 nH, respectively.
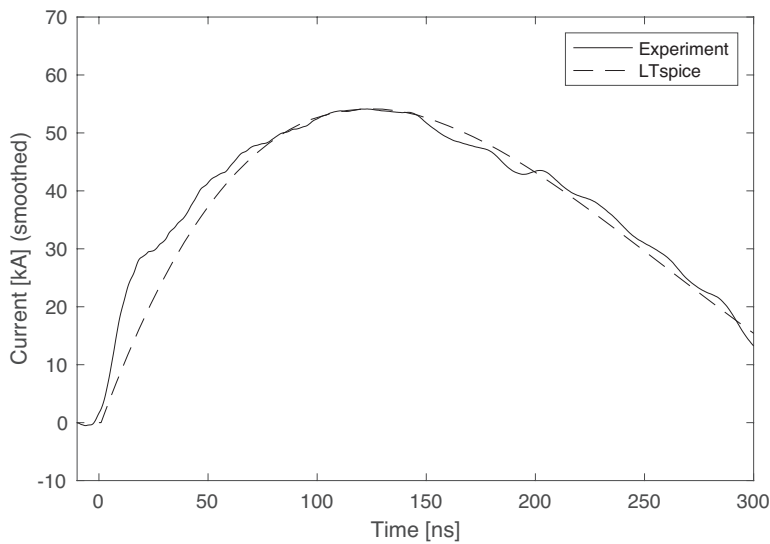
Figure C.15: Experimental current trace from the prototype BLUE cavity configured as an LTD at ± 70 kV charge voltage into a resistive and inductive load. The experimental curve has been smoothed to remove high-frequency noise. Also plotted for comparison is the current trace from an LTspice simulation of the discharge. In the simulation, the load resistance was 1.5 Ω and the load inductance was 110 nH, which is in good agreement with the estimated load resistance and inductance based on geometry.
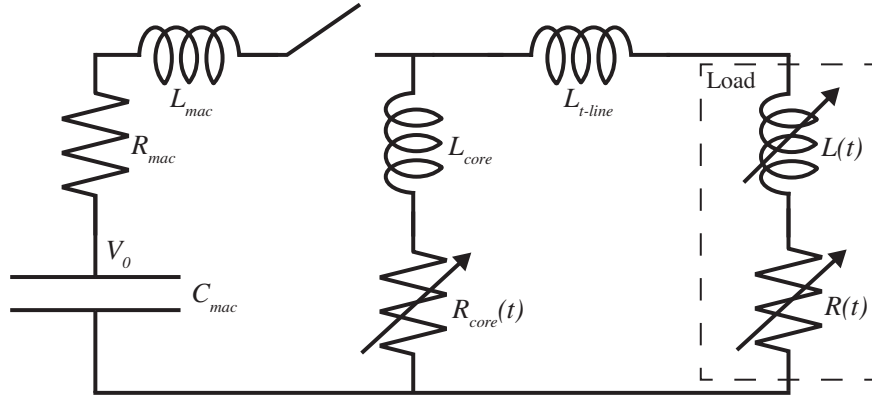
Figure C.16: A simple circuit model of the BLUE LTD facility. Formulas for the circuit elements, along with approximate values for a single cavity, are provided in Table C.1.

Circuit Variable	Formula	Approximate Value for $N_{\mathrm{cav}} = 1$
C_{mac}	$5\,C_{\mathrm{cap}}/N_{\mathrm{cav}}$	100 nF
V_0	$2\,|V_{\mathrm{charge}}| \cdot N_{\mathrm{cav}}$	200 kV max.
R_{mac}	$R_{\mathrm{brick}}N_{\mathrm{cav}}/10$	4–60 mΩ
L_{mac}	$L_{\mathrm{brick}}N_{\mathrm{cav}}/10$	22 nH
L_{core}	$L_{0,\mathrm{core}}N_{\mathrm{cav}}$	950 nH
$R_{\mathrm{core}}(t)$	$R_{0,\mathrm{core}}(t) \cdot N_{\mathrm{cav}}$	0.50 Ω (for $t \ll 10\mu s$)
$L_{\mathrm{t\text{-}line}}$	$L_{\mathrm{t\text{-}line}}$	$\sim$16 nH for chamber loads
Z_{mac}	$\sqrt{L_{\mathrm{mac}}/C_{\mathrm{mac}}}$	0.47 Ω

Table C.1: Formulas for the simple circuit elements shown in Fig. C.16. The approximate values provided in the rightmost column are for a single cavity—i.e., with $N_{\mathrm{cav}} = 1$. $L_{\mathrm{t\text{-}line}}$ is the inductance of the transmission line to the load, which can vary depending on the installed hardware. A transmission line to the chamber procured for Z-pinch experiments has an inductance of $\approx$16 nH. Z_{mac} is the machine impedance.

C.5   Testing a Magnetically Insulated Line Oscillator (MILO) on BLUE

The first physics load to be mounted on the prototype BLUE cavity was a high-power microwave (HPM) device known as a magnetically insulated line oscillator (MILO) [154]. An LTD paired with such a device can represent a very compact HPM source, desirable in many applications. To our knowledge, Ref. [155] presents the first demonstration of a compact LTD being used to drive an HPM source – in this case, the HPM source was a coaxial vircator.

The MILO driven with BLUE is a crossed-field HPM device [156] that, in this case, operates in a coaxial, axisymmetric geometry (see Fig. C.17(a)). In a MILO, the drive current produces a magnetic field that insulates the anode from electrons emitted at the cathode. Thus, external magnetic field coils are not required to operate a MILO, as they are in the case of other crossed-field devices (e.g., magnetrons). For the cylindrical MILO shown in Fig. C.17, the insulating magnetic field is azimuthal, $\mathbf{B} = B_\theta \, \hat{\boldsymbol{\theta}}$, and the driving electric field is radial $\mathbf{E} = E_r \, \hat{\boldsymbol{r}}$. Electrons emitted radially outward from the velvet-covered central cathode are turned by the magnetic field and begin to drift axially through the periodic slow wave structure (SWS) at a velocity of $\mathbf{v}_{\mathrm{drift}} = \mathbf{E} \times \mathbf{B}/B^2$ (see Fig. C.17(b)).

The MILO mounted to BLUE is shown in Fig. C.17(c). This MILO was previously tested by the Air Force Research Laboratory (AFRL) in Albuquerque, NM [158, 159, 160, 161]. In these tests, the MILO was driven by the Sandia National Laboratories 500 kV, 5-Ω, 300–600 ns IMP pulser [160, 161]. Note that the IMP pulser has remarkably similar drive characteristics to the full 4-cavity BLUE facility. Operation of this MILO has been simulated recently by D. A. Packard *et al.* [157] (see also Fig. C.17(b)).

While the specific details of our BLUE MILO experiments are left for a future publication, the preliminary demonstration of microwave generation is provided here. In Fig. C.18, voltage signals are presented from three B-dot probes located in the SWS of the MILO. Also shown is a Rogowski coil signal, integrated and calibrated to give the total current entering the MILO. The charge voltage for the shot was ± 70 kV (140 kV open-circuit). Microwave oscillations at a frequency of 1.187-GHz are observed for approximately 80 ns (during the period of 65–145 ns).

The oscillations are well-sampled for Fourier analysis and are distinct from background noise. Plotted in the bottom pane of Fig. C.18 are smoothed, normalized FFTs of the B-dot data, as well as normalized FFTs from CST simulations at different drive voltages [157]. The experimental frequency of 1.187 GHz is consistent with beam-loaded π mode operation in these particle-in-cell simulations. The differences between the experimental and simulated FFTs are due primarily to imperfect experimental geometries (leading to slight differences in the center frequencies of the FFT peaks) and disparate sampling windows (leading to differences in the widths of the FFT peaks). Regarding the disparate sampling windows, the simulations produced oscillations for
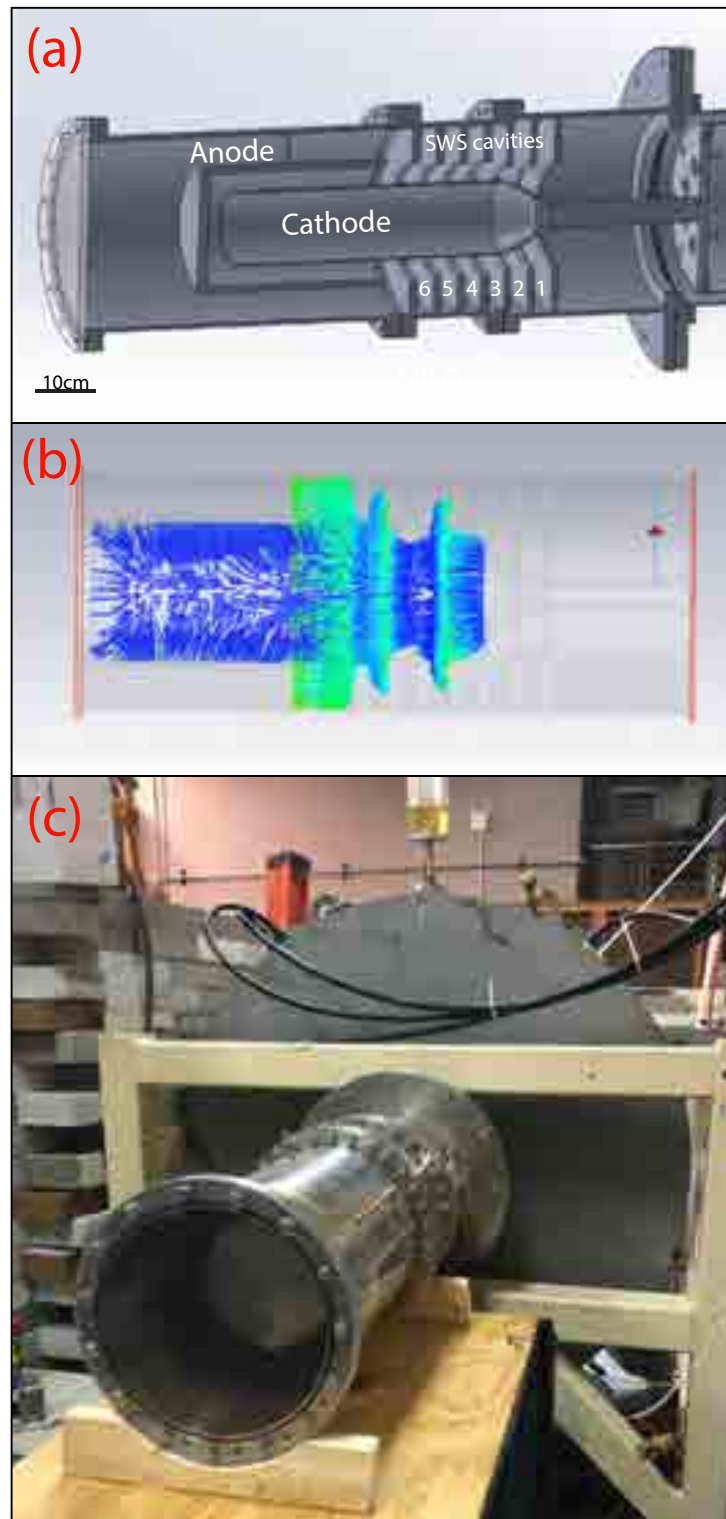
Figure C.17: (a) Cross-section of the MILO HPM device. (b) CST particle-in-cell simulation of the MILO in π mode operation, with the simulated electrons (blue/green) bunching into well-formed spoke-like structures in the SWS [157]. (c) The MILO mounted to the prototype BLUE cavity.
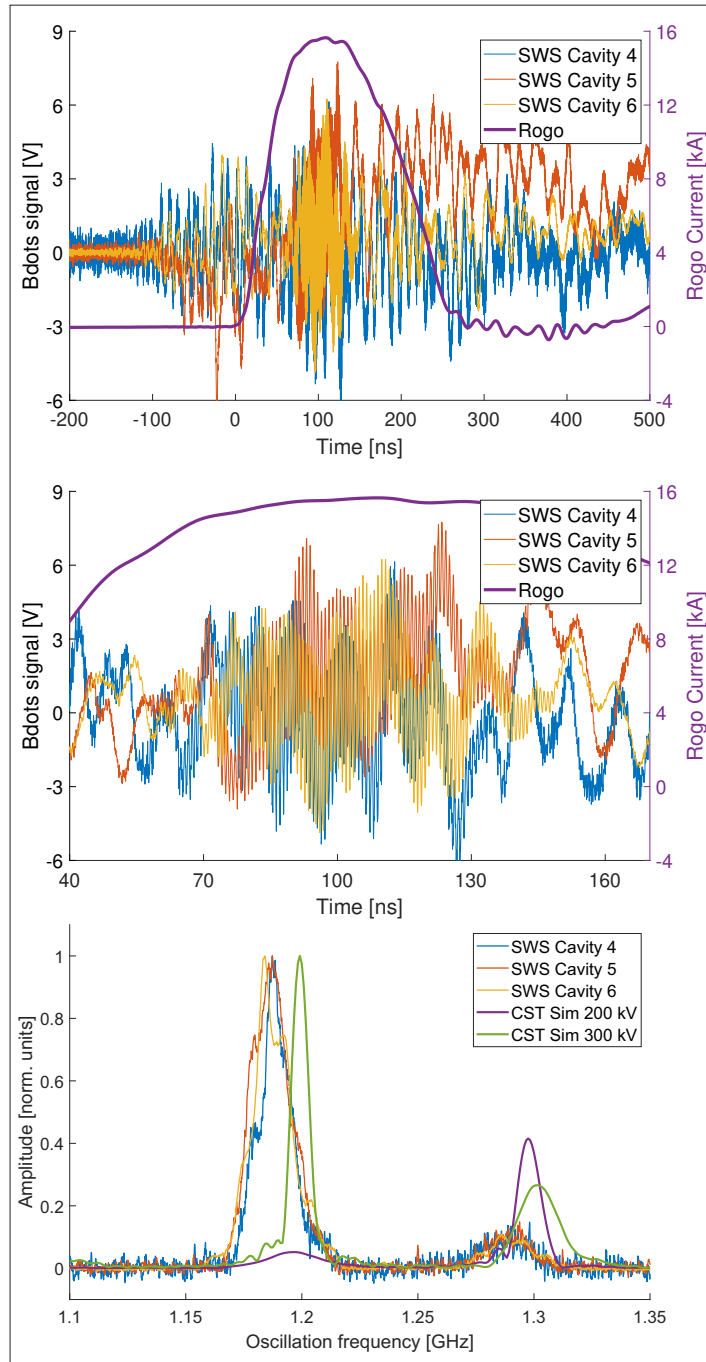
Figure C.18: Voltage signals from three B-dot probes in the slow-wave structure of the MILO during a discharge of the BLUE prototype cavity with a charge voltage of ±70 kV (top and middle). Also plotted is the load current into the MILO, which was measured using a calibrated Rogowski coil. Microwave oscillations at a frequency of 1.187 GHz are observed for approximately 80 ns (during the period of 65–145 ns). The oscillations are well-sampled for Fourier analysis and comparison with simulation (bottom). Plotted are smoothed, normalized FFTs of the B-dot data, as well as normalized FFTs from CST simulations in Ref. [157] at different drive voltages.

~150 ns, whereas the experiments produced oscillations for 80 ns. This results in the simulated FFTs having narrower peaks than the experimental FFTs, due to the uncertainties associated with the time-bandwidth product [162].

The excitation of the oscillations in the experiment for approximately 80 ns is remarkable given the relatively low drive voltage applied ($V_0 = 2\,|V_{\text{charge}}| = 140$ kV) and the very low driver impedance of just a single BLUE LTD cavity (0.5 Ω). In simulation, similar oscillations were predicted only at higher voltages (see Fig. C.18). Future experiments are planned to characterize the RF output power as a function of the applied drive voltage. The drive voltage will be varied (increased) by increasing the number of BLUE cavities stacked together in series, since $V_0 = 2\,|V_{\text{charge}}| \cdot N_{\text{cav}}$ (see Table C.1).

C.6   Summary

The first prototype cavity of the BLUE LTD facility at the University of Michigan is now operational. The components to make three more identical cavities have been procured, and construction of the second cavity has begun. A modular system like BLUE will allow future studies of LTD cavity coupling and pulse shaping [163, 164]. This informs the design of next generation LTD-based super-accelerators like Z-300 and Z-800 [141], which could likely demonstrate ignition of a nuclear fusion target using the MagLIF concept [39].

Beyond studies of pulsed-power technology, BLUE is capable of driving a wide variety of physics loads. A MILO HPM source has been successfully driven to produce microwaves, and a large diameter vacuum chamber with many diagnostic ports has been prepared to house various Z-pinch and X-pinch loads. The authors are excited to offer this new facility and capability to the pulsed-power, HPM, and HEDP communities.

BIBLIOGRAPHY

[1] John D Lawson. Some criteria for a power producing thermonuclear reactor. *Proceedings of the physical society. Section B*, 70(1):6, 1957.

[2] David Chandler. MIT-designed project achieves major advance toward Fusion Energy. `https://news.mit.edu/2021/MIT-CFS-major-advance-toward-fusion-energy-0908`. Accessed 2021-09-08.

[3] M Greenwald, D Whyte, P Bonoli, Z Hartwig, J Irby, B LaBombard, E Marmar, J Minervini, M Takayasu, J Terry, et al. The high-field path to practical fusion energy. *PSFC Report PSFC/RR-18-2*, 2018.

[4] Cary Forest. The physics basis for a $Q \approx 1$ high-field, compact, axisymmetric mirror. *Bulletin of the American Physical Society*, 2022.

[5] JA Alonso, I Calvo, D Carralero, JL Velasco, JM García-Regaña, I Palermo, and D Rapisarda. Physics design point of high-field stellarator reactors. *Nuclear Fusion*, 62(3):036024, 2022.

[6] BJ Sporer. Analysis of Two Fusion Reactor Designs Based on Magnetic Electrostatic Plasma Confinement. *Journal of Fusion Energy*, 41(1):5, 2022.

[7] AB Zylstra, OA Hurricane, DA Callahan, AL Kritcher, JE Ralph, HF Robey, JS Ross, CV Young, KL Baker, DT Casey, et al. Burning plasma achieved in inertial fusion. *Nature*, 601(7894):542–548, 2022.

[8] AB Zylstra, AL Kritcher, OA Hurricane, DA Callahan, JE Ralph, DT Casey, A Pak, OL Landen, B Bachmann, KL Baker, et al. Experimental achievement and signatures of ignition at the National Ignition Facility. *Physical Review E*, 106(2):025202, 2022.

[9] DB Sinars, MA Sweeney, CS Alexander, DJ Ampleford, T Ao, JP Apruzese, C Aragon, DJ Armstrong, KN Austin, TJ Awe, et al. Review of pulsed power-driven high energy density physics research on Z at Sandia. *Physics of Plasmas*, 27(7):070501, 2020.

[10] Jyllian Kemsley. Plutonium Studies Begin At National Ignition Facility. *Chemical & Engineering News*, 93(23), 2015.

[11] M Dunne, EI Moses, P Amendt, T Anklam, A Bayramian, E Bliss, B Debs, R Deri, T Diaz de la Rubia, B El-Dasher, et al. Timely delivery of laser inertial fusion energy (LIFE). *Fusion Science and Technology*, 60(1):19–27, 2011.

160

[12] Pravesh Patel, Markus Roth, Todd Ditmire, Gabriel Schaumann, Gilles Cheriaux, L Jarrott, Stefano Atzeni, Javier Honrubia, Andrea Hannasch, Florian Wasser, et al. The Focused Energy roadmap for Inertial Fusion Energy. *Bulletin of the American Physical Society*, 2022.

[13] Peter J. Turchi, Sherry D. Frese, and Michael H Frese. Stabilized Liner Compressor for Low-Cost Controlled Fusion at Megagauss Field Levels. *IEEE Transactions on Plasma Science*, 45(10):2800–2809, 2017.

[14] RC Kirkpatrick, IR Lindemuth, DC Barnes, RJ Faehl, PT Sheehey, and CE Knapp. Progress toward understanding magnetized target fusion (MTF). Technical report, Los Alamos National Lab.(LANL), Los Alamos, NM (United States), 2001.

[15] Review of controlled fusion power at megagauss field levels, author=Turchi, PJ, booktitle=2018 16th International Conference on Megagauss Magnetic Field Generation and Related Topics (MEGAGAUSS), pages=1–8, year=2018, organization=IEEE.

[16] CL Nehl, RJ Umstattd, WR Regan, Scott C Hsu, and PB McGrath. Retrospective of the ARPA-E ALPHA fusion program. *Journal of Fusion Energy*, 38:506–521, 2019.

[17] M Kaur, LJ Barbano, EM Suen-Lewis, JE Shrock, AD Light, MR Brown, and David A Schaffner. Measuring the equations of state in a relaxed magnetohydrodynamic plasma. *Physical Review E*, 97(1):011202, 2018.

[18] EB Hooper, CW Barnes, PM Bellan, MR Brown, JC Fernandez, TK Fowler, DN Hill, TR Jarboe, LL LoDestro, HS McLean, et al. The Spheromak path to fusion energy. *Lawrence Livermore National Laboratory, UCRL-ID-130429*, 1998.

[19] DN Hill and R Hazeltine. Report of the FESAC Toroidal Alternates Panel. *US Department of Energy, Washington DC*, 2008.

[20] Chris Grabowski, James Degnan, Mark Babineau, Frank Camacho, Sean Coffey, Gordon Coulter, Matt Domonkos, Don Gale, Bernard Martinez, Jerry Parker, et al. Frc compression heating experiment (frchx) at afrl. In *2007 16th IEEE International Pulsed Power Conference*, volume 2, pages 1728–1731. IEEE, 2008.

[21] Staged Magnetic Compression of FRC Targets to Fusion Conditions, author=Slough, J and Campbell, B and Kirtley, D and Milroy, R and Pihl, C and Votroubek, G, journal=ALPHA Annual Review, year=2016.

[22] H Gota, MW Binderbauer, T Tajima, A Smirnov, S Putvinski, M Tuszewski, SA Dettrick, DK Gupta, S Korepanov, RM Magee, et al. Overview of C-2W: high temperature, steady-state beam-driven field-reversed configuration plasmas. *Nuclear Fusion*, 61(10):106039, 2021.

[23] Qizhi Sun, Xianjun Yang, Yuesong Jia, Lulu Li, Dongfan Fang, Xiaoming Zhao, Weidong Qin, Zhengfen Liu, Wei Liu, Jun Li, et al. Formation of field reversed configuration (FRC) on the Yingguang-I device. *Matter and Radiation at Extremes*, 2(5):263–274, 2017.

[24] TP Intrator, Jaeyoung Y Park, James H Degnan, I Furno, Chris Grabowski, SC Hsu, Edward L Ruden, PG Sanchez, J Martin Taccetti, M Tuszewski, et al. A high-density field reversed configuration plasma for magnetized target fusion. *IEEE transactions on plasma science*, 32(1):152–160, 2004.

[25] MW Binderbauer, HY Guo, M Tuszewski, S Putvinski, L Sevier, D Barnes, N Rostoker, MG Anderson, R Andow, L Bonelli, et al. Dynamic formation of a hot field reversed configuration with improved confinement by supersonic merging of two colliding high-β compact toroids. *Physical review letters*, 105(4):045003, 2010.

[26] Loren C Steinhauer. Review of field-reversed configurations. *Physics of Plasmas*, 18(7):070501, 2011.

[27] DR Welch, SA Cohen, TC Genoni, and AH Glasser. Formation of field-reversed-configuration plasma with punctuated-betatron-orbit electrons. *Physical review letters*, 105(1):015002, 2010.

[28] Alan L Hoffman, Larry N Carey, Edward A Crawford, Dennis G Harding, Terence E DeHart, Kenneth F McDonald, John L McNeil, Richard D Milroy, John T Slough, Ricardo Maqueda, et al. The large-s field-reversed configuration experiment. *Fusion Technology*, 23(2):185–207, 1993.

[29] Hiroshi Gota and Michl W Binderbauer. Nuclear fusion research by Tri Alpha Energy. *Purazuma, Kaku Yugo Gakkai-Shi*, 93(1):24–27, 2017.

[30] PJ Turchi, AL Cooper, DJ Jenkins, and EP Scannell. A LINUS Fusion Reactor Design Based on Axisymmetric Implosion of Tangentially-Injected Liquid Metal. Technical report, NAVAL RESEARCH LAB WASHINGTON DC, 1981.

[31] Stephen A Slutz and Matthew R Gomez. Fusion gain from cylindrical liner-driven implosions of field reversed configurations. *Physics of Plasmas*, 28(4):042707, 2021.

[32] Michel Laberge. Magnetized target fusion with a spherical tokamak. *Journal of Fusion Energy*, 38(1):199–203, 2019.

[33] R. D. McBride, W. A. Stygar, M. E. Cuneo, D. B. Sinars, M. G. Mazarakis, J. J. Leckbee, M. E. Savage, B. T. Hutsel, J. D. Douglass, M. L. Kiefer, B. V. Oliver, G. R. Laity, M. R. Gomez, D. A. Yager-Elorriaga, S. G. Patel, B. M. Kovalchuk, A. A. Kim, P.-A. Gourdain, S. N. Bland, S. Portillo, S. C. Bott-Suzuki, F. N. Beg, Y. Maron, R. B. Spielman, D. V. Rose, D. R. Welch, J. C. Zier, J. W. Schumer, J. B. Greenly, A. M. Covington, A. M. Steiner, P. C. Campbell, S. M. Miller, J. M. Woolstrum, N. B. Ramey, A. P. Shah, B. J. Sporer, N. M. Jordan, Y. Y. Lau, and R. M. Gilgenbach. A Primer on Pulsed Power and Linear Transformer Drivers for High Energy Density Physics Applications. *IEEE Transactions on Plasma Science*, 46(11):3928–3967, 2018.

[34] JH Degnan, DJ Amdahl, M Domonkos, C Grabowski, EL Ruden, WM White, GA Wurden, TP Intrator, J Sears, T Weber, et al. Flux and magnetized plasma compression driven by Shiva Star. In *2012 14th International Conference on Megagauss Magnetic Field Generation and Related Topics (MEGAGAUSS)*, pages 1–9. IEEE, 2012.

[35] David Alexander Yager-Elorriaga, Matthew R Gomez, Daniel Edward Ruiz, Stephen A Slutz, Adam James Harvey-Thompson, Christopher Ashley Jennings, PF Knapp, PF Schmit, Matthew Robert Weis, Thomas J Awe, et al. An overview of magneto-inertial fusion on the Z machine at Sandia National Laboratories. *Nuclear Fusion*, 62(4):042015, 2022.

[36] Alexander Andreevich Kim, MG Mazarakis, VI Manylov, VA Vizir, and WA Stygar. Energy loss due to eddy current in linear transformer driver cores. *Physical Review Special Topics-Accelerators and Beams*, 13(7):070401, 2010.

[37] BJ Sporer, AP Shah, GV Dowhan, RV Shapovalov, DA Packard, M Wisher, JJ Leckbee, KJ Hendricks, BW Hoff, YY Lau, et al. Multicavity linear transformer driver facility for Z-pinch and high-power microwave research. *Physical Review Accelerators and Beams*, 24(10):100402, 2021.

[38] WA Stygar, TJ Awe, JE Bailey, NL Bennett, EW Breden, EM Campbell, RE Clark, RA Cooper, ME Cuneo, JB Ennis, et al. Conceptual designs of two petawatt-class pulsed-power accelerators for high-energy-density-physics experiments. *Physical Review Special Topics-Accelerators and Beams*, 18(11):110401, 2015.

[39] SA Slutz, WA Stygar, MR Gomez, KJ Peterson, AB Sefkow, DB Sinars, RA Vesey, EM Campbell, and R Betti. Scaling magnetized liner inertial fusion on Z and future pulsed-power accelerators. *Physics of Plasmas*, 23(2):022702, 2016.

[40] PF Schmit, AL Velikovich, RD McBride, and GK Robertson. Controlling Rayleigh-Taylor instabilities in magnetically driven solid metal shells by means of a dynamic screw pinch. *Physical review letters*, 117(20):205001, 2016.

[41] KR LeChien, WA Stygar, ME Savage, PE Wakeland, V Anaya, MJ Baremore, DE Bliss, R Chavez, GD Coombs, JP Corley, et al. 6.1-MV, 0.79-MA laser-triggered gas switch for multimodule, multiterawatt pulsed-power accelerators. *Physical Review Special Topics-Accelerators and Beams*, 13(3):030401, 2010.

[42] TD Pointon, HC Harjes, ME Savage, DE Bliss, and RW Lemke. Pulse shaping of the load current on the Z accelerator. In *Digest of Technical Papers. PPC-2003. 14th IEEE International Pulsed Power Conference (IEEE Cat. No. 03CH37472)*, volume 1, pages 175–178. IEEE, 2003.

[43] Andrew J Porwitzky, Christopher T Seagle, and Brian J Jensen. Zero to 1,600 m/s in 40 microns: Sensitive pulse shaping for materials characterization on Z. *Procedia engineering*, 204:337–343, 2017.

[44] SA Slutz, MC Herrmann, RA Vesey, AB Sefkow, DB Sinars, DC Rovang, KJ Peterson, and ME Cuneo. Pulsed-power-driven cylindrical liner implosions of laser preheated fuel magnetized with an axial field. *Physics of Plasmas*, 17(5):056303, 2010.

[45] Patrick K Rambo, Ian C Smith, John L Porter, Michael J Hurst, C Shane Speas, Richard G Adams, Antonio J Garcia, Ellis Dawson, Benjamin D Thurston, Colleen Wakefield, et al. Z-Beamlet: a multikilojoule, terawatt-class laser system. *Applied optics*, 44(12):2421–2430, 2005.

[46] DD Ryutov, DC Barnes, BS Bauer, JH Hammer, CW Hartman, RC Kirkpatrick, IR Lindemuth, V Makhin, PB Parks, DB Reisman, et al. Particle and heat transport in a dense wall-confined MTF plasma (theory and simulations). *Nuclear fusion*, 43(9):955, 2003.

[47] DD Ryutov. On drift instabilities in magnetized target fusion devices. *Physics of Plasmas*, 9(9):4085–4088, 2002.

[48] AL Velikovich, JL Giuliani, and ST Zalesak. Magnetic flux and heat losses by diffusive, advective, and Nernst effects in MagLIF-like plasma. In *AIP Conference Proceedings*, volume 1639, pages 59–62. American Institute of Physics, 2014.

[49] MM Basko, AJ Kemp, and J Meyer-ter Vehn. Ignition conditions for magnetized target fusion in cylindrical geometry. *Nuclear Fusion*, 40(1):59, 2000.

[50] LJ Perkins, BG Logan, GB Zimmerman, and CJ Werner. Two-dimensional simulations of thermonuclear burn in ignition-scale inertial confinement fusion targets under compressed axial magnetic fields. *Physics of Plasmas*, 20(7):072708, 2013.

[51] Ronald C Kirkpatrick. Ignition and burn in a small magnetized fuel target. *arXiv preprint arXiv:1404.1784*, 2014.

[52] SA Slutz, CA Jennings, TJ Awe, GA Shipley, BT Hutsel, and DC Lamppa. Auto-magnetizing liners for magnetized inertial fusion. *Physics of Plasmas*, 24(1):012704, 2017.

[53] Gabriel A Shipley, Thomas James Awe, Brian Thomas Hutsel, Stephen A Slutz, Derek C Lamppa, John B Greenly, and Trevor M Hutchinson. Megagauss-level magnetic field production in cm-scale auto-magnetizing helical liners pulsed to 500 kA in 125 ns. *Physics of Plasmas*, 25(5):052703, 2018.

[54] Gabriel A Shipley, Thomas James Awe, Brian Thomas Hutsel, John B Greenly, Christopher Ashley Jennings, and Stephen A Slutz. Implosion of auto-magnetizing helical liners on the Z facility. *Physics of Plasmas*, 26(5):052705, 2019.

[55] Gabriel A Shipley, Thomas J Awe, Brian T Hutsel, and David A Yager-Elorriaga. On the initiation and evolution of dielectric breakdown in auto-magnetizing liner experiments. *Physics of Plasmas*, 29(3):032701, 2022.

[56] Gabriel A Shipley, Christopher Ashley Jennings, and Paul F Schmit. Design of dynamic screw pinch experiments for magnetized liner inertial fusion. *Physics of Plasmas*, 26(10):102702, 2019.

[57] Electromagnetic Simulation Solvers and CAD Compatibility. CST Studio Suite.

[58] David Alexander Yager-Elorriaga, YY Lau, Peng Zhang, Paul C Campbell, Adam M Steiner, Nicholas M Jordan, Ryan D McBride, and Ronald M Gilgenbach. Evolution of sausage and helical modes in magnetized thin-foil cylindrical liners driven by a Z-pinch. *Physics of Plasmas*, 25(5):056307, 2018.

[59] Paul C Campbell, TM Jones, JM Woolstrum, NM Jordan, PF Schmit, JB Greenly, WM Potter, ES Lavine, BR Kusse, DA Hammer, et al. Stabilization of liner implosions via a dynamic screw pinch. *Physical Review Letters*, 125(3):035001, 2020.

[60] Paul C Campbell, TM Jones, JM Woolstrum, NM Jordan, PF Schmit, AL Velikovich, JB Greenly, WM Potter, ES Lavine, BR Kusse, et al. Liner implosion experiments driven by a dynamic screw pinch. *Physics of Plasmas*, 28(8):082707, 2021.

[61] Matthew R Gomez, Stephen A Slutz, Adam B Sefkow, Daniel B Sinars, Kelly D Hahn, Stephanie B Hansen, Eric C Harding, Patrick F Knapp, Paul F Schmit, Christopher A Jennings, et al. Experimental demonstration of fusion-relevant conditions in magnetized liner inertial fusion. *Physical review letters*, 113(15):155003, 2014.

[62] TJ Awe, RD McBride, CA Jennings, DC Lamppa, MR Martin, DC Rovang, SA Slutz, ME Cuneo, AC Owen, DB Sinars, et al. Observations of modified three-dimensional instability structure for imploding z-pinch liners that are premagnetized with an axial field. *Physical review letters*, 111(23):235005, 2013.

[63] Adam B Sefkow, SA Slutz, JM Koning, MM Marinak, KJ Peterson, DB Sinars, and RA Vesey. Design of magnetized liner inertial fusion experiments using the Z facility. *Physics of Plasmas*, 21(7):072711, 2014.

[64] G Zimmerman, D Kershaw, D Bailey, and J Harte. LASNEX code for inertial confinement fusion. Technical report, California Univ, 1977.

[65] RC Davidson and NA Krall. Anomalous transport in high-temperature plasmas with applications to solenoidal fusion systems. *Nuclear Fusion*, 17(6):1313, 1977.

[66] RD Milroy and JU Brackbill. Numerical studies of a field-reversed theta-pinch plasma. *The Physics of Fluids*, 25(5):775–783, 1982.

[67] MC Jones, DJ Ampleford, ME Cuneo, R Hohlfelder, CA Jennings, DW Johnson, B Jones, MR Lopez, J MacArthur, JA Mills, et al. X-ray power and yield measurements at the refurbished Z machine. *Review of Scientific Instruments*, 85(8):083501, 2014.

[68] J Schwarz, RA Vesey, DJ Ampleford, MA Schaeuble, AL Velikovich, JL Giuliani, A Esaulov, A Dasgupta, and B Jones. A model for K-shell X-ray yield from magnetic implosions at Sandia's Z machine. *Physics of Plasmas*, 29(10):103101, 2022.

[69] Thomas James Awe, Kyle J Peterson, Edmund P Yu, Ryan D McBride, Daniel B Sinars, Matthew R Gomez, Christopher Ashley Jennings, Matthew R Martin, Stephen E Rosenthal, DG Schroen, et al. Experimental demonstration of the stabilizing effect of dielectric coatings on magnetically accelerated imploding metallic liners. *Physical Review Letters*, 116(6):065001, 2016.

[70] R. M. Gilgenbach, M. R. Gomez, J. C. Zier, W. W. Tang, D. M. French, Y. Y. Lau, M. G. Mazarakis, M. E. Cuneo, M. D. Johnston, B. V. Oliver, T. A. Mehlhorn, A. A. Kim, and V. A. Sinebryukhov. MAIZE: a 1 MA LTD-Driven Z-Pinch at The University of Michigan. *AIP Conference Proceedings*, 1088(1):259–262, 2009.

[71] ExOne. What is Binder Jetting? `https://www.exone.com/en-US/Resources/case-studies/what-is-binder-jetting`. Accessed: 2023-05-09.

[72] Xometry Europe. Direct Metal Laser Sintering (DMLS) 3D printing: Technology overview. `https://xometry.eu/en/direct-metal-laser-sintering-dmls-3d-printing-technology-overview/`, August 2021. Accessed: 2023-05-09.

[73] Sculpteo. 3D Printing with Metal Casting. `https://www.sculpteo.com/en/materials/metal-casting-material/#:~:text=Lost%2Dwax%20casting%20is%20an,replica%20of%20the%20finished%20product.` Accessed: 2023-05-09.

[74] Formlabs. Resin Family: Tough and Durable. `https://formlabs.com/materials/tough-durable/`. Accessed: 2023-05-09.

[75] DC Rovang, DC Lamppa, ME Cuneo, AC Owen, J McKenney, DW Johnson, S Radovich, RJ Kaye, RD McBride, CS Alexander, et al. Pulsed-coil magnet systems for applying uniform 10–30 T fields to centimeter-scale targets on Sandia's Z facility. *Review of Scientific Instruments*, 85(12):124701, 2014.

[76] A Kramida, K Olsen, and Yu Ralchenko. NIST LIBS database. *National Institute of Standards and Technology, US Department of Commerce*, 2019.

[77] John Greenly, Matthew Martin, Isaac Blesener, David Chalenski, Patrick Knapp, and Ryan McBride. The Role of Flux Advection in the Development of the Ablation Streams and Precursors of Wire Array Z-pinches. In *AIP Conference Proceedings*, volume 1088, pages 53–56. American Institute of Physics, 2009.

[78] G Tabak, E Bell, R Duggan, D Liang, L Mehr, H Moore, A Novick, L Ransohoff, P-A Gourdain, W Potter, et al. Measuring magnetic fields stronger than 100 Teslas using miniature b-dot probes on COBRA. In *2014 IEEE 41st International Conference on Plasma Sciences (ICOPS) held with 2014 IEEE International Conference on High-Power Particle Beams (BEAMS)*, pages 1–1. IEEE, 2014.

[79] Ryan D McBride, David E Bliss, Matthew R Gomez, Stephanie B Hansen, Matthew R Martin, Christopher Ashley Jennings, Stephen A Slutz, Dean C Rovang, Patrick F Knapp, Paul F Schmit, et al. Implementing and diagnosing magnetic flux compression on the Z pulsed power accelerator. Technical report, Sandia National Lab.(SNL-NM), Albuquerque, NM (United States), 2015.

[80] Clayton Myers, Jack Hare, David Ampleford, Carlos Aragon, Jeremy Chittenden, Anthony Colombo, Aidan Crilly, Rishabh Datta, Aaron Edens, Will Fox, et al. Development of the MARZ platform (Magnetically Ablated Reconnection on Z) to study astrophysically relevant radiative magnetic reconnection in the laboratory. Technical report, Sandia National Lab.(SNL-NM), Albuquerque, NM (United States), 2021.

[81] FW Grover. Inductance calculations: working tables and formulas, 2004.

[82] Chris Grabowski, James H Degnan, Jerald V Parker, J Frank Camacho, Sean K Coffey, Rachel K Delaney, Matthew T Domonkos, Thomas P Intrator, Alan G Lynn, John McCullough, et al. Parallel Triggering and Conduction of Rail-Gap Switches in a High-Current Low-Inductance Crowbar Switch. *IEEE Transactions on Plasma Science*, 44(10):1997–2012, 2016.

[83] Francis F Chen et al. *Introduction to plasma physics and controlled fusion*, volume 1. Springer, 1984.

[84] TS Green. An investigation of the theta pinch using magnetic pick-up loops. *Nuclear Fusion*, 2(1-2):92, 1962.

[85] JP Chittenden, SV Lebedev, CA Jennings, SN Bland, and A Ciardi. X-ray generation mechanisms in three-dimensional simulations of wire array Z-pinches. *Plasma Physics and Controlled Fusion*, 46(12B):B457, 2004.

[86] Andrea Ciardi, Sergey V Lebedev, Adam Frank, Eric G Blackman, Jeremy P Chittenden, CJ Jennings, David J Ampleford, SN Bland, Simon C Bott, J Rapley, et al. The evolution of magnetic tower jets in the laboratory. *Physics of Plasmas*, 14(5):056501, 2007.

[87] SP Lyon and JD Johnson. SESAME: The Los Alamos National Laboratory Equation of State Database. Technical Report Technical Report No. LA-UR-92-3407, Los Alamos National Laboratory, 1992. unpublished.

[88] MP Desjarlais, JD Kress, and LA Collins. Electrical conductivity for warm, dense aluminum plasmas and liquids. *Physical Review E*, 66(2):025401, 2002.

[89] James M Stone, Dimitri Mihalas, and Michael L Norman. ZEUS-2D: A radiation magnetohydrodynamics code for astrophysical flows in two space dimensions. III-The radiation hydrodynamic algorithms and tests. *The Astrophysical Journal Supplement Series*, 80:819, 1992.

[90] Andrew S Richardson. 2019 NRL plasma formulary. Technical report, US Naval Research Laboratory, 2019.

[91] Loren C Steinhauer. Improved analytic equilibrium for a field-reversed configuration. *Physics of Fluids B: Plasma Physics*, 2(12):3081–3085, 1990.

[92] E Garate, I Allfrey, S Putvinski, G Snitchler, E Trask, J Schroeder, J Romero, TAE Team, et al. Dynamic Separatrix Control in C-2U. In *APS Division of Plasma Physics Meeting Abstracts*, volume 2015, pages BP12–026, 2015.

[93] M Tuszewski. Field reversed configurations. *Nuclear Fusion*, 28(11):008, 1988.

[94] AL Hoffman and JT Slough. Field reversed configuration lifetime scaling based on measurements from the large s experiment. *Nuclear Fusion*, 33(1):27, 1993.

[95] Weston M Stacey. *Fusion: An introduction to the physics and technology of magnetic confinement fusion*. John Wiley & Sons, 2010.

[96] AJ Crilly, NPL Niasse, AR Fraser, DA Chapman, KM McLean, SJ Rose, and JP Chittenden. SpK: A fast atomic and microphysics code for the high-energy-density regime. *arXiv preprint arXiv:2211.16464*, 2022.

[97] TC Simonen. Summary of results from the Tandem Mirror Experiment (TMX). Technical report, Lawrence Livermore National Lab., CA (USA), 1981.

[98] Harold Grad. Plasma trapping in cusped geometries. *Physical Review Letters*, 4(5):222, 1960.

[99] James L Tuck. A new plasma confinement geometry. *Nature*, 187(4740):863–864, 1960.

[100] Thomas J McGuire. Compact Fusion Reactor, CFR. *Physics of Plasmas*, 22:070901, 2015.

[101] Nicholas A Krall, Michael Coleman, K Maffei, J Lovberg, R Jacobsen, and Robert W Bussard. Forming and maintaining a potential well in a quasispherical magnetic trap. *Physics of Plasmas*, 2(1):146–158, 1995.

[102] Jaeyoung Park, Nicholas A Krall, Paul E Sieck, Dustin T Offermann, Michael Skillicorn, Andrew Sanchez, Kevin Davis, Eric Alderson, and Giovanni Lapenta. High-energy electron confinement in a magnetic cusp configuration. *Physical Review X*, 5(2), 2015.

[103] Thomas J Dolan. Magnetic electrostatic plasma confinement. *Plasma physics and controlled fusion*, 36(10):1539, 1994.

[104] Jaeyoung Park. Polywell - A Path to Electrostatic Fusion. EMC2, 16th US-Japan Workshop on Fusion Neutron Sources for Nuclear Assay and Alternate Applications, October 2014.

[105] AD Komarov, OA Lavrentiev, VA Naboka, VA Potapenko, and IA Stepanenko. Electrostatic Plasma Confinement in the Yupiter-1A Electromagnetic Trap. *Ukrainskij Fizicheskij Zhurnal*, 25(5):776–780, 1980.

[106] Thomas J Dolan. Prospects of Magnetic Electrostatic Plasma Confinement. In *Current Trends in International Fusion Research*, pages 197–209. Springer, 1997.

[107] OA Lavrent'ev, VA Maslov, SV Germanova, MG Nozdrachov, VP Oboznyj, and BA Shevchuk. Modeling of a Starting Mode of Thermonuclear Reactor "Elemag". *Fusion science and technology*, 47(1T):224–227, 2005.

[108] AA Ware and JE Faulkner. Electrostatic plugging of open-ended magnetic containment systems. *Nuclear Fusion*, 9(4):353, 1969.

[109] Carlos Romero-Talamás, Ian Abel, John Ball, Debjyoti Basu, Brian Beaudoin, Leah Dorsey, Nathan Eschbach, Adil Hassam, Timothy Koeth, Zachary Short, et al. Overview of the Centrifugal Mirror Fusion Experiment (CMFX). *Bulletin of the American Physical Society*, 2021.

[110] GF Abdrashitov, AV Beloborodov, VI Volosov, VV Kubarev, Yu S Popov, and Yu N Yudin. Hot rotating plasma in the PSP-2 experiment. *Nuclear Fusion*, 31(7):1275, 1991.

[111] AJ Creely, MJ Greenwald, SB Ballinger, D Brunner, J Canik, J Doody, T Fülöp, DT Garnier, R Granetz, TK Gray, et al. Overview of the SPARC tokamak. *Journal of Plasma Physics*, 86(5), 2020.

[112] C Forest, J Anderson, B Mumgaard, and D Whyte. The Wisconsin HTS Axisymmetric Mirror (WHAM). *ARPA-E BETHE Kickoff Virtual Workshop*, August 2020.

[113] Hongyu Bai, Mark D Bird, Lance D Cooley, Iain R Dixon, Kwang Lok Kim, David C Larbalestier, William S Marshall, Ulf P Trociewitz, Hubertus W Weijers, Dmytro V Abraimov, et al. The 40 T Superconducting Magnet Project at the National High Magnetic Field Laboratory. *IEEE Transactions on Applied Superconductivity*, 30(4):1–5, 2020.

[114] Yukikazu Iwasa and Seungyong Hahn. First-cut design of an all-superconducting 100-T direct current magnet. *Applied Physics Letters*, 103(25):253507, 2013.

[115] Q&A session with Brandon Sorbom of Commonwealth Fusion Systems, APS Division of Plasma Physics Meeting 2020.

[116] EE Yushmanov. The power gain factor Q of an ideal magneto-electrostatic fusion reactor. *Nuclear Fusion*, 20(1):3, 1980.

[117] The ITER Organization. Facts & Figures. `https://www.iter.org/factsfigures`, 2021. Accessed 2021-11-14.

[118] TJ Dolan and BL Stansfield. Fusion reaction rate from truncated Maxwellian distributions. Technical report, Univ. of Quebec, Varennes, 1973.

[119] RH Cohen, ME Rensink, TA Cutler, and AA Mirin. Collisional loss of electrostatically confined species in a magnetic mirror. *Nuclear Fusion*, 18(9):1229, 1978.

[120] SA Vdovin, SB Germanova, Oleg A Lavrent'ev, VA Maslov, MG Nozdrachev, VP Obozniy, VI Petrenko, and NN Sappa. Plasma accumulation and confinement in the Jupiter-2M multicusp electromagnetic trap. *Proceedings All Union Conference on Open Traps*, pages 70–81, 1990.

[121] VP Pastukhov. Classical transport processes in a magnetoelectrostatic trap. *Fizika Plazmy*, 4(3):560–569, 1978.

[122] OA Lavrent'ev. Diffusion loss of particles and energy in a one-slit electromagnetic trap. *Ukrainskij Fizicheskij Zhurnal*, 26(9):1466–1472, 1981.

[123] Fabricating ITER's first wall. `https://www.neimagazine.com/features/featurefabricating-iters-first-wall-4551656/`. Accessed: 2021-04-06.

[124] J Uhlíř, M Mareček, M Straka, L Szatmáry, Z Nový, P Sláma, P Svoboda, and P Toman. Experimental verification of selected processes devoted to MSR fuel cycle technology. June 2016.

[125] Yuhu Zhai, Peter Titus, Charles Kessel, and Laila El-Guebaly. Conceptual magnet design study for fusion nuclear science facility. *Fusion Engineering and Design*, 135:324–336, 2018.

[126] Hannu Rajainmaki, Arnaud Foussat, Jesus Rodriguez, David Evans, John Fanthome, Marcello Losasso, and Victor Diaz. The ITER pre-compression rings–A first in cryogenic composite technology. In *AIP Conference Proceedings*, volume 1574, pages 92–99. American Institute of Physics, 2014.

[127] J Knaster, W Baker, L Bettinali, C Jong, K Mallick, C Nardi, H Rajainmaki, P Rossi, and L Semeraro. Design Issues of the Pre-compression Rings of ITER. In *AIP Conference Proceedings*, volume 1219, pages 145–154. American Institute of Physics, 2010.

[128] B. M. Koval'chuk, V. A. Vizir', A. A. Kim, E. V. Kumpyak, S. V. Loginov, A. N. Bastrikov, V. V. Chervyakov, N. V. Tsoi, P. Monjaux, and D. Kh'yui. Fast primary storage device utilizing a linear pulse transformer. *Russian Physics Journal*, 40(12):1142–1153, Dec 1997.

[129] A. A. Kim, B. M. Kovalchuk, E. V. Kumpjak, and N. V. Zoi. 0.75 MA, 400 ns rise time LTD stage. In *Digest of Technical Papers. 12th IEEE International Pulsed Power Conference. (Cat. No.99CH36358)*, volume 2, pages 955–958, June 1999.

[130] M. G. Mazarakis and R. B. Spielman. A compact, high-voltage e-beam pulser. In *Digest of Technical Papers. 12th IEEE International Pulsed Power Conference. (Cat. No.99CH36358)*, volume 1, pages 412–415, June 1999.

[131] A. A. Kim and B. M. Kovalchuk. High Power Direct Driver For Z-Pinch Loads. In G. Mesyats, B. Kovalchuk, and G. Remnev, editors, *Proceedings of the 12th Symposium on High Current Electronics (part of the First International Congress on Radiation Physics, High Current Electronics, and Modification of Materials)*, page 263, Tomsk, Russia, 2000. Institute of High Current Electronics.

[132] W. A. Stygar, M. E. Cuneo, D. I. Headley, H. C. Ives, R. J. Leeper, M. G. Mazarakis, C. L. Olson, J. L. Porter, T. C. Wagoner, and J. R. Woodworth. Architecture of petawatt-class z-pinch accelerators. *Phys. Rev. ST Accel. Beams*, 10(3):030401, 2007.

[133] A. A. Kim, M. G. Mazarakis, V. A. Sinebryukhov, B. M. Kovalchuk, V. A. Visir, S. N. Volkov, F. Bayol, A. N. Bastrikov, V. G. Durakov, S. V. Frolov, V. M. Alexeenko, D. H. McDaniel, W. E. Fowler, K. LeChien, C. Olson, W. A. Stygar, K. W. Struve, J. Porter, and R. M. Gilgenbach. Development and tests of fast 1-MA linear transformer driver stages. *Phys. Rev. ST Accel. Beams*, 12:050402, May 2009.

[134] W. A. Stygar, W. E. Fowler, K. R. LeChien, F. W. Long, M. G. Mazarakis, G. R. McKee, J. L. McKenney, J. L. Porter, M. E. Savage, B. S. Stoltzfus, D. M. Van De Valde, and J. R. Woodworth. Shaping the output pulse of a linear-transformer-driver module. *Phys. Rev. ST Accel. Beams*, 12:030402, Mar 2009.

[135] Michael G. Mazarakis, William E. Fowler, Alexander A. Kim, Vadim A. Sinebryukhov, Sonrisa T. Rogowski, Robin A. Sharpe, Dillon H. McDaniel, Craig L. Olson, John L. Porter,

Kenneth W. Struve, William A. Stygar, and Joseph R. Woodworth. High current, 0.5-MA, fast, 100-ns, linear transformer driver experiments. *Phys. Rev. ST Accel. Beams*, 12:050401, May 2009.

[136] M. G. Mazarakis, W. E. Fowler, K. L. LeChien, F. W. Long, M. K. Matzen, D. H. McDaniel, R. G. McKee, C. L. Olson, J. L. Porter, S. T. Rogowski, K. W. Struve, W. A. Stygar, J. R. Woodworth, A. A. Kim, V. A. Sinebryukhov, R. M. Gilgenbach, M. R. Gomez, D. M. French, Y. Y. Lau, J. C. Zier, D. M. VanDevalde, R. A. Sharpe, and K. Ward. High-Current Linear Transformer Driver Development at Sandia National Laboratories. *IEEE Trans. Plasma Sci.*, 38(4):704–713, April 2010.

[137] A. A. Kim, M. G. Mazarakis, V. I. Manylov, V. A. Vizir, and W. A. Stygar. Energy loss due to eddy current in linear transformer driver cores. *Phys. Rev. ST Accel. Beams*, 13:070401, Jul 2010.

[138] Joshua Leckbee, Steve Cordova, Bryan Oliver, Timothy Webb, Martial Toury, Michel Caron, Rodolphe Rosol, Bill Bui, Tobias Romero, and Derek Ziska. Linear transformer driver (LTD) research for radiographic applications. In *2011 IEEE Pulsed Power Conference*, pages 614–618. IEEE, 2011.

[139] J. J. Leckbee, T. D. Pointon, S. R. Cordova, B. V. Oliver, T. J. Webb, M. Toury, M. Caron, and D. W. Droemer. Commissioning and power flow studies of the 2.5-MeV Ursa Minor LTD. In *2012 IEEE International Power Modulator and High Voltage Conference (IPMHVC)*, pages 169–173. IEEE, June 2012.

[140] A. A. Kim, M. G. Mazarakis, V. A. Sinebryukhov, S. N. Volkov, S. S. Kondratiev, V. M. Alexeenko, F. Bayol, G. Demol, and W. A. Stygar. Square pulse linear transformer driver. *Phys. Rev. ST Accel. Beams*, 15:040401, Apr 2012.

[141] W. A. Stygar, T. J. Awe, J. E. Bailey, N. L. Bennett, E. W. Breden, E. M. Campbell, R. E. Clark, R. A. Cooper, M. E. Cuneo, J. B. Ennis, D. L. Fehl, T. C. Genoni, M. R. Gomez, G. W. Greiser, F. R. Gruner, M. C. Herrmann, B. T. Hutsel, C. A. Jennings, D. O. Jobe, B. M. Jones, M. C. Jones, P. A. Jones, P. F. Knapp, J. S. Lash, K. R. LeChien, J. J. Leckbee, R. J. Leeper, S. A. Lewis, F. W. Long, D. J. Lucero, E. A. Madrid, M. R. Martin, M. K. Matzen, M. G. Mazarakis, R. D. McBride, G. R. McKee, C. L. Miller, J. K. Moore, C. B. Mostrom, T. D. Mulville, K. J. Peterson, J. L. Porter, D. B. Reisman, G. A. Rochau, G. E. Rochau, D. V. Rose, D. C. Rovang, M. E. Savage, M. E. Sceiford, P. F. Schmit, R. F. Schneider, J. Schwarz, A. B. Sefkow, D. B. Sinars, S. A. Slutz, R. B. Spielman, B. S. Stoltzfus, C. Thoma, R. A. Vesey, P. E. Wakeland, D. R. Welch, M. L. Wisher, and J. R. Woodworth. Conceptual designs of two petawatt-class pulsed-power accelerators for high-energy-density-physics experiments. *Phys. Rev. ST Accel. Beams*, 18:110401, Nov 2015.

[142] Lin Zhou, Zhenghong Li, Zhen Wang, Chuan Liang, Mingjia Li, Jianmin Qi, and Yanyun Chu. Design of a 5-MA 100-ns linear-transformer-driver accelerator for wire array Z-pinch experiments. *Phys. Rev. Accel. Beams*, 19:030401, Mar 2016.

[143] A.A. Kim, B.M. Kovalchuk, V.A. Kokshenev, A.V. Shishlov, N.A. Ratakhin, V.I. Oreshkin, V.V. Rostov, V.I. Koshelev, and V.F. Losev. Review of high-power pulsed systems at the

Institute of High Current Electronics. *Matter and Radiation at Extremes*, 1(4):201–206, 2016.

[144] P. C. Campbell, J. M. Woolstrum, F. Antoulinakis, T. M. Jones, D. A. Yager-Elorriaga, S. M. Miller, N. M. Jordan, Y. Y. Lau, R. M. Gilgenbach, and R. D. McBride. Diagnostic and Power Feed Upgrades to the MAIZE Facility. *IEEE Trans. Plasma Sci.*, 46(11):3973–3981, Nov 2018.

[145] J. D. Douglass, B. T. Hutsel, J. J. Leckbee, T. D. Mulville, B. S. Stoltzfus, M. L. Wisher, M. E. Savage, W. A. Stygar, E. W. Breden, J. D. Calhoun, M. E. Cuneo, D. J. De Smet, R. J. Focia, R. J. Hohlfelder, D. M. Jaramillo, O. M. Johns, M. C. Jones, A. C. Lombrozo, D. J. Lucero, J. K. Moore, J. L. Porter, S. D. Radovich, S. A. Romero, M. E. Sceiford, M. A. Sullivan, C. A. Walker, J. R. Woodworth, N. T. Yazzie, M. D. Abdalla, M. C. Skipper, and C. Wagner. 100 GW linear transformer driver cavity: Design, simulations, and performance. *Phys. Rev. Accel. Beams*, 21:120401, Dec 2018.

[146] A. A. Kim and M. G. Mazarakis. The Story of the LTD Development. *IEEE Transactions on Plasma Science*, 48(4):749–756, 2020.

[147] F. Conti, J. C. Valenzuela, V. Fadeev, N. Aybar, D. B. Reisman, A. Williams, G. Collins, J. Narkis, M. P. Ross, F. N. Beg, and R. B. Spielman. MA-class linear transformer driver for Z-pinch research. *Phys. Rev. Accel. Beams*, 23:090401, Sep 2020.

[148] JR Woodworth, JA Alexander, FR Gruner, WA Stygar, MJ Harden, JR Blickem, GJ Dension, FE White, LM Lucero, HD Anderson, et al. Low-inductance gas switches for linear transformer drivers. *Physical Review Special Topics-Accelerators and Beams*, 12(6):060401, 2009.

[149] Joseph Ray Woodworth, William A Stygar, Lawrence F Bennett, Michael Gerrassimos Mazarakis, HD Anderson, MJ Harden, JR Blickem, FR Gruner, and R White. New low inductance gas switches for linear transformer drivers. *Physical Review Special Topics-Accelerators and Beams*, 13(8):080401, 2010.

[150] J. Yan, S. Parker, T. Gheorghiu, N. Schwartz, S. Theocharous, and S. N. Bland. Miniature solid-state switched spiral generator for the cost effective, programmable triggering of large scale pulsed power accelerators. *Phys. Rev. Accel. Beams*, 24:030401, Mar 2021.

[151] Alexandra A Kim, Alexander N Bastrikov, Sergey N Volkov, Vjacheslav G Durakov, Boris M Kovalchuk, and Vadim A Sinebryukhov. Development of the ultra-fast LTD stage. In *2002 14th International Conference on High-Power Particle Beams (BEAMS)*, volume 1, pages 81–84. IEEE, 2002.

[152] WA Stygar, KR LeChien, MG Mazarakis, ME Savage, BS Stoltzfus, KN Austin, EW Breden, ME Cuneo, BT Hutsel, SA Lewis, et al. Impedance-matched Marx generators. *Physical Review Accelerators and Beams*, 20(4):040402, 2017.

[153] P.-A. Gourdain, M. Evans, P. Efthimion, R. Ellis, W. Fox, H. R. Hasson, H. Ji, R. V. Shapovalov, J. R. Young, and I. West-Abdallah. Coreless Fast Pulsed-Power Drivers. *IEEE Transactions on Plasma Science*, 49(7):2161–2165, 2021.

[154] Raymond W. Lemke and M. Collins Clark. Theory and simulation of high-power microwave generation in a magnetically insulated transmission line oscillator. *Journal of Applied Physics*, 62(8):3436–3440, 1987.

[155] Boris M Kovalchuk, Sergey D Polevin, Ruslan V Tsygankov, and Andrey A Zherlitsyn. S-band coaxial vircator with electron beam premodulation based on compact linear transformer driver. *IEEE transactions on plasma science*, 38(10):2819–2824, 2010.

[156] James Benford, John A. Swegle, and Edl Schamiloglu. *High Power Microwaves*. Taylor & Francis Group, 2nd edition, 2007.

[157] Drew A Packard, Anna Cooleybeck, Nicholas M Jordan, Brendan J Sporer, Alexander E Mazarakis, YY Lau, Ronald M Gilgenbach, and Ryan D McBride. HFSS and CST Simulations of a GW-Class MILO. *IEEE Transactions on Plasma Science*, 48(6):1894–1901, 2020.

[158] Steve E. Calico, M. Collins Clark, Raymond W. Lemke, and Michael C. Scott. Experimental and theoretical investigations of a magnetically insulated line oscillator (MILO). In Howard E. Brandt, editor, *Intense Microwave Pulses III*, volume 2557, pages 50–59. International Society for Optics and Photonics, SPIE, 1995.

[159] Raymond W Lemke, Steve E Calico, and M Collins Clark. Investigation of a load-limited, magnetically insulated transmission line oscillator (MILO). *IEEE Transactions on Plasma Science*, 25(2):364–374, 1997.

[160] MD Haworth, G Baca, J Benford, T Englert, K Hackett, KJ Hendricks, D Henley, M LaCour, RW Lemke, David Price, et al. Significant Pulse-Lengthening in a Multigigawatt Magnetically Insulated Transmission Line Oscillator. *IEEE Transactions on Plasma Science*, 26(3):312–319, 1998.

[161] M.D. Haworth, J.W. Luginsland, and R.W. Lemke. Evidence of a new pulse-shortening mechanism in a load-limited MILO. *IEEE Transactions on Plasma Science*, 28(3):511–516, 2000.

[162] Dennis Gabor. Theory of communication. Part 1: The analysis of information. *Journal of the Institution of Electrical Engineers-Part III: Radio and Communication Engineering*, 93(26):429–441, 1946.

[163] WA Stygar, WE Fowler, KR LeChien, FW Long, MG Mazarakis, GR McKee, JL McKenney, John L Porter, ME Savage, BS Stoltzfus, et al. Shaping the output pulse of a linear-transformer-driver module. *Physical Review Special Topics-Accelerators and Beams*, 12(3):030402, 2009.

[164] Alexander Andreevich Kim, MG Mazarakis, VA Sinebryukhov, SN Volkov, SS Kondratiev, VM Alexeenko, F Bayol, G Demol, and WA Stygar. Square pulse linear transformer driver. *Physical Review Special Topics-Accelerators and Beams*, 15(4):040401, 2012.

[165] Michael A Lieberman and Allan J Lichtenberg. Principles of plasma discharges and materials processing. *MRS Bulletin*, 30(12):899–901, 1994.

[166] Saul Dushman, JM Lafferty, and RN Peacock. Scientific Foundations of Vaccum Technique. *Journal of The Electrochemical Society*, 110(3):77C, 1963.

[167] Alan L Hoffman, Richard D Milroy, John T Slough, and Loren C Steinhauer. Formation of field-reversed configurations using scalable, low-voltage technology. *Fusion technology*, 9(1):48–57, 1986.